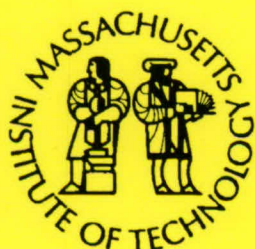


**Massachusetts Institute of Technology
Woods Hole Oceanographic Institution**



**Joint Program
in Oceanography/
Applied Ocean Science
and Engineering**



DOCTORAL DISSERTATION

**Slip on Ridge Transform Faults:
Insights From Earthquakes and Laboratory Experiments**

by

Margaret S. Boettcher

June 2005

DISTRIBUTION STATEMENT A
Approved for Public Release
Distribution Unlimited

**Slip on Ridge Transform Faults:
Insights from Earthquakes and Laboratory Experiments**

by

Margaret S. Boettcher

Sc.B., Brown University, 1998

Submitted in partial fulfillment of the requirements for the degree of

Doctor of Philosophy

at the

MASSACHUSETTS INSTITUTE OF TECHNOLOGY

and the

WOODS HOLE OCEANOGRAPHIC INSTITUTION

June, 2005

©MMV Margaret S. Boettcher

All rights reserved.

The author hereby grants to MIT and WHOI permission to reproduce paper and electronic copies of this thesis in whole or in part and to distribute them publicly.

Signature of Author *Margaret Boettcher*

Joint Program in Oceanography

Massachusetts Institute of Technology

and Woods Hole Oceanographic Institution

March 22, 2005

Certified by *Thomas H. Jordan*

Dr. Thomas H. Jordan

Thesis Supervisor

Certified by *Jeffrey J. McGuire*

Dr. Jeffrey J. McGuire

Thesis Supervisor

Certified by *Gregory Hirth*

Dr. Gregory Hirth

Thesis Supervisor

Accepted by *Gregory Hirth*

Dr. Gregory Hirth

Chair, Joint Committee for Marine Geology and Geophysics

Associate Scientist

Woods Hole Oceanographic Institution

**Slip on Ridge Transform Faults:
Insights from Earthquakes and Laboratory Experiments**

by

Margaret S. Boettcher

Submitted to the Department of Marine Geology and Geophysics,
Massachusetts Institute of Technology–Woods Hole Oceanographic Institution,
Joint Program in Oceanography
on March 22, 2005, in partial fulfillment of the
requirements for the degree of
Doctor of Philosophy

Abstract

The relatively simple tectonic environment of mid-ocean ridge transform fault (RTF) seismicity provides a unique opportunity for investigation of earthquake and faulting processes. We develop a scaling model that is complete in that all the seismic parameters are related to the RTF tectonic parameters. Laboratory work on the frictional stability of olivine aggregates shows that the depth extent of oceanic faulting is thermally controlled and limited by the 600°C isotherm. Slip on RTFs is primarily aseismic, only 15% of the tectonic offset is accommodated by earthquakes. Despite extensive fault areas, few large earthquakes occur on RTFs, and few aftershocks follow the large events. Standard models of seismicity, in which all earthquakes result from the same seismic triggering process, do not describe RTF earthquakes. Instead, large earthquakes appear to be preceded by an extended fault preparation process marked by abundant foreshocks within 1 hour and 15 km of the mainshocks. In our experiments normal force vibrations, such as seismic radiation from nearby earthquakes, can weaken and potentially destabilize steadily creeping faults. Integrating the rheology, geology, and seismicity of RTFs, we develop a synoptic model to better understand the spatial distribution of fault strength and stability and provide insight into slip accommodation on RTFs.

Acknowledgments

It has truly been an honor to be a part of the MIT/WHOI Joint Program. I have gained so much from both institutions and have very much enjoyed my time spent both on and off the Cape. My incredible team of advisors— Tom Jordan, Jeff McGuire, Greg Hirth, and Chris Marone— have made graduate school successful and fun with their constant guidance, support, and friendship throughout the last six years. Each has shared with me his extensive knowledge base and individual approach to problem solving. Tom and Chris, in particular, have been extremely generous with their hospitality and long-distance encouragement. I want to especially thank Tom for giving me so much of his time, working with me at his home in Southern California and in offices, bookstores, and restaurants around the country. Chris and Greg have encouraged my experimental inclinations and have both patiently helped me in the lab. I have found Greg's "jack of all trades, master of one" approach very appealing and I want to thank him for guiding me towards that goal. Jeff deserves special thanks for the seismology that he has taught (and will teach!) me and for his patience, during the many times when I delayed my work with him to finish previous projects. I am also grateful to my other committee members, Don Forsyth and Maria Zuber, who have provided many insightful comments over the past few months. Additionally, John Collins deserves thanks for his guidance during my first few years and for taking me on my only research cruise. Finally, I could not have accomplished my laboratory experiments without the equipment, space, and expertise of Brian Evans and Xiaohui Xiao at MIT, Glenn Gaetani at WHOI, and Kevin Frye at MIT/Penn State.

I have been fortunate to spend time (at both work and play) with so many wonderful and unique EAPS and G&G students over these past six years. I owe much to Frederik and Mark and to the other students who came before me including Eliza, Mike, Astri, Jen, Keli, Laurent, Oded. I have also benefited scientifically from and thoroughly enjoyed my time with the current students, especially Rhea, Mea, Jeff, Brian, Jessica, Kristy, Trish, Rose, Andrea, Matt J, Dave, Emily, Clare, Matt M, Nick, Lili. Mea is the best officemate ever. She has always been extremely helpful, especially during the last few months of finishing up my thesis, and I want to thank her for all our walks to the beach over the years when we both needed a break. Rhea also deserves special thanks for so many things (including bringing me to Samoa). Grad school would never have been the same without her and it has been a great experience to start and finish together. Additionally all my friends and housemates in Woods Hole and Boston have made these six years incredibly enjoyable- Linda, Rhea, Heidi, Mea, Alison, Cara, Jeff, Brian, Mark, Adam, Joe, Sarah, Jessica, Charlie, Emily, Oscar, Jim, Dirk, Heather, Kristy, Jonathan, Adam, Rose, Luc, Tracy, Patty, and Boa. In particular, Linda's sense of adventure, her support, and the endless hours we have spent chatting have been some of my favorite times during these past six years.

Most of all I want to express my gratitude towards my family. My brother, Dave, is an amazing person in all senses and I can't wait to see what he chooses to do next. My parents have always been full of encouragement and support and they have provided me with every opportunity I could want. I am lucky to be part of such a wonderful family.

Finally, I have also been fortunate in that I have been supported by many fellowships throughout my tenure including funding from the Deep Ocean Earth Institute Fellowship, MIT Presidential Fellowship, NSF Fellowship, and WHOI Academic Programs Office— and I want to thank Julia, Marsha, John, and Judy for all their help throughout the years.

Contents

1	Introduction	9
2	Earthquake Scaling Relations for Mid-Ocean Ridge Transform Faults*	15
3	Earthquake Clustering on East Pacific Rise Transform Faults	37
3.1	Introduction	37
3.2	Foreshock sequences and short-term earthquake predictability on Earth Pacific Rise transform faults*	38
3.3	Supplementary Information Accompanying: Foreshock sequences and short-term earthquake predictability on East Pacific Rise transform faults	44
3.3.1	Foreshocks and Aftershocks on EPR Faults	44
3.3.2	Declustering	46
3.3.3	Sensitivity to Parameter Choices	47
3.3.4	Estimation of α and n	49
3.3.5	Prediction Space-Time Windows	50
4	Olivine Friction at the Base of Oceanic Seismogenic Zones	51
4.1	Introduction	52
4.2	Experimental Design	52
4.3	Results	53
4.3.1	Strength	54
4.3.2	Stability	56
4.3.3	Volumetric Strain	57
4.3.4	Microstructural Observations	58
4.4	Discussion	61

4.5	Conclusions	65
5	Effects of Normal-Stress Variation on the Strength and Stability of Creeping Faults*	67
6	A Synoptic Model of Ridge Transform Fault Seismicity	83
6.1	Introduction	84
6.2	The Rheology of Oceanic Transform Faults	84
6.2.1	Brittle Deformation I: Olivine	85
6.2.2	Brittle Deformation II: Serpentine	86
6.2.3	Brittle Deformation III: Gabbro	89
6.2.4	Ductile Flow	89
6.2.5	Thermal Modeling	90
6.2.6	Maximum Fault Strength	93
6.3	Case Study I: The Blanco Transform Fault System	96
6.3.1	Blanco Seismicity	96
6.3.2	Blanco Thermal Structure	102
6.3.3	Strength of the Blanco RTF	102
6.3.4	Fit of Blanco Seismicity to the Synoptic Model	104
6.4	Case Study II: The Romanche Transform Fault	107
6.4.1	Fit of Romanche Seismicity to the Synoptic Model	110
6.5	Synoptic Model Evaluation and Implications	111
6.6	Summary	114

Chapter 1

Introduction

How slip is accommodated on major faults, whether through seismic slip, steady aseismic fault creep, or episodic aseismic transients, remains a central problem of tectonics. This topic encompasses a number of basic questions, including: (1) How do seismic and aseismic deformation couple and partition to accommodate slip on major faults? (2) What effect does this partitioning have on seismic hazard? (3) How predictable are large earthquakes? (4) How do earthquakes nucleate, and what role do foreshocks play in the earthquake nucleation process? (5) What are the stress levels on seismogenic faults and how do they relate to earthquake stress drops? (6) What physical mechanisms control near- and far-field dynamic triggering of seismicity by large earthquakes? and (7) Are small-scale phenomena relevant to large-scale fault slip and earthquake rupture? These questions are the focus of much current research including the work presented in this thesis.

Earthquake science is historically divided into four broadly defined fields: (1) seismological and geodetic observation and modeling of individual earthquakes and their interactions with the surrounding stress field, (2) large-scale geodetic study of interseismic tectonic deformations, (3) quantification of past fault slip through on-land and oceanic field geology, and (4) experimental and theoretical study of fault and rock mechanics. More recently, advances in earthquake science have come through system-wide studies, and the realization that faulting and earthquakes are integrally connected with each other, with neighboring faults, and with the surrounding fault zone. In this thesis I have taken the latter approach, coupling understanding of earthquake processes from seismic observations with laboratory-based insight into the mechanics of fault friction.

In discussing the state of earthquake science thirteen years ago, *Scholz* [1992] elucidated the divide between seismologists and rock mechanicians in their traditional views on stick-slip theory of earthquakes:

...since seismology will always be an important part of the study of earthquakes, this revolution (from the descriptive asperity model to a quantitative rate and state dependent model of friction) will only be resolved when seismologists have embraced the new view, and this will only take place over a prolonged period as the education of a new generation of seismologists encompasses the discipline of rock mechanics.

This thesis represents a move towards this unification of the earthquake science disciplines, presenting an integrated view of fault slip and earthquake behavior on a relatively simple faulting environment.

The focus of this thesis is primarily on the strike-slip faults that offset mid-ocean ridge spreading centers, ridge transform faults (RTFs). These faults are far from land-based seismic networks, so the location and source parameters of their seismicity are more poorly determined than for many continental faults. However, at least on a global basis their tectonic parameters are better constrained, with a length given by the distance between two spreading segments and a slip rate determined by present day plate motions. RTFs are generally long lived structures with cumulative displacements that far exceed their lengths, as evidenced by the continuity of ocean-crossing fracture zones. The compositional structure of the oceanic lithosphere is more homogeneous than continental crust, and its thermal structure, and consequently its fault rheology, should be more predictable from known plate kinematics. Moreover, RTFs on the East Pacific Rise comprise some of the fastest slipping faults on Earth. The largest earthquakes on the EPR are small, with maximum magnitude of about 6.5, and thus a complete seismic cycle takes less than 10 years, compared with more than 100 years required for a full seismic cycle on the San Andreas Fault, making it possible to observe an entire cycle of faulting and earthquake slip with a relatively short seismic catalog. Owing to the relative simplicity of the mid-ocean environment, RTF seismicity may be more amenable to interpretation in terms of the dynamics of faulting and less contingent on its geologic history than the better studied continental strike-slip faults. A thorough review of previous work on RTF faulting and

seismicity is given in the introduction to Chapter 2 and is contrasted with a simplified model of continental strike-slip seismicity in Appendix A of Chapter 2.

In Chapter 2 we present a comprehensive scaling model for RTF seismicity based on 41 years of data from approximately 17,000 km of fault length. This model is complete in the sense that all seismic parameters scale with the two tectonic control variables, length and slip rate. In contrast to fully-coupled continental strike-slip faults, RTF slip is primarily aseismic. The depth extent of oceanic faulting is thermally controlled and limited by the 600°C isotherm (as shown in Chapter 4). Thus, depending on the thermal model used, a maximum of 15% of the known tectonic offset on RTFs is accommodated by earthquakes and the remaining 85% or more occurs as steady sliding or slow creep events. Despite extensive seismogenic areas RTF earthquakes are small, rarely greater than $M = 7.0$, even for the largest faults. We find that the rupture area of the largest expected earthquakes scales with fault area to the one-half power. As such, on average larger RTFs have bigger earthquakes but smaller seismic productivities and these parameters trade off in such a way to maintain constant seismic coupling.

The standard models of earthquake triggering developed for Southern California, in which all earthquakes initiate in the same manner, do not describe RTF seismicity. In Chapters 2 and 3 we investigate the temporal and spatial clustering of earthquakes on RTFs. We find that RTF earthquakes are followed by very few aftershocks, approximately 15 times fewer than the number observed on continental strike-slip faults. In contrast, about four times more foreshocks precede earthquakes of magnitude 5.5 or greater on East Pacific Rise RTFs than precede earthquakes on faults in Southern California. The foreshocks are separated from the mainshocks by less than 15 km and 1 hour. Thus, the larger events on RTFs are more predictable than the smaller ones that are typically not preceded by foreshocks. The differences in clustering statistics between RTFs and faults in Southern California allow us to reject the hypothesis that all sizes of RTF earthquakes initiate in the same way.

The frictional behavior of olivine, which is a primary component of the oceanic lithosphere, strongly influences faulting on RTFs. Chapter 4 presents an experimental investigation of olivine friction motivated by the observation that RTF seismic parameters are thermally controlled (from the scaling relations derived in Chapter 2). In our experiments, we observed a transition from velocity-weakening (potentially unstable) to velocity-

strengthening (stable) frictional behavior at about 1000°C. Based on Bowden and Tabor's asperity hypothesis, we speculate that plastic yielding of the asperities at high temperatures stabilizes frictional sliding of the bulk sample. We scale our laboratory results to the temperature and strain rate conditions on RTFs and find a maximum earthquake nucleation depth of approximately 600°C for these faults.

Chapter 5 is a second study of earthquake nucleation and triggering, conducted experimentally on simulated fault gouge. We found that high-amplitude, low-frequency, normal-force vibrations, such as seismic radiation from an earthquake on a nearby fault, can weaken and potentially destabilize steadily creeping faults. Our experimental results are systematic and can be modeled with rate and state dependent constitutive friction laws. The simulated faults recover to their steady-state frictional strength following the vibrations, suggesting that no permanent damage is done to the fault zone. Thus, both Chapters 3 and 5 suggest that for faults characterized by aseismic slip, probabilities of earthquake nucleation are increased during and immediately following (less than 1 hour) changes in fault stressing rate.

Finally, in Chapter 6 we combine results of the previous chapters with additional constraints from regional geology, thermal modeling, and prior laboratory studies of fault rheology into a self-consistent model that can be tested against future observations. With this synoptic model we construct two-dimensional maps of the maximum yield stress and frictional behavior on RTFs. By comparing these predictions to observed seismicity patterns, we evaluate where this synoptic model is successful and where unmodeled effects are significant.

While this thesis represents significant progress in the understanding of many issues central to earthquake science, including: (1) the partitioning of fault slip into seismic (potentially damaging) and aseismic (stable) components, (2) the relationship between fault dimension and the size of the largest earthquake, (3) the effects of pressure, temperature, strain rate, and cumulative offset on shear localization and earthquake size distributions, (4) the effects of dynamic stressing on frictional strength of faults, and (5) determining whether the nucleation processes of small and large earthquakes are the same, it leaves us with many questions for future study. A primary one comes from the result that RTFs are characterized by low seismic coupling. We have documented the very different seismic characteristics of RTFs compared with continental strike-slip faults, however the reason for this difference

remains unclear. Why is so much of the slip on RTFs aseismic? Serpentine, whose velocity-strengthening frictional behavior is often thought to accommodate much of the aseismic slip, accounts for significantly less than 85% of the area above the 600°C isotherm. What aspect of the rheology or fault dynamics controls this partitioning on RTFs? Is aseismic slip comprised of subseismic transients, which we have suggested may be responsible for the abundance of foreshocks found on these faults, or is it primarily steady creep? Furthermore, if subseismic transients are common on RTFs, and are the trigger of most large earthquakes, then is it possible that such a process exists on continental strike-slip faults? Could such indicators of large earthquakes be less frequent on the continents and possibly have longer time constants, thus be more difficult to observe?

These questions and others raised throughout the thesis, can be best addressed with improved data sets. Ocean bottom seismometer deployments on RTFs combined with new seafloor geodetic technology and continued hydroacoustic monitoring will allow for rapid progress in understanding the mechanics of faulting on RTFs and whether similar processes should be expected on continental faults.

Chapter 2

Earthquake Scaling Relations for Mid-Ocean Ridge Transform Faults*

Abstract

A mid-ocean ridge transform fault (RTF) of length L , slip rate V , and moment release rate \dot{M} can be characterized by a seismic coupling coefficient $\chi = A_E/A_T$, where $A_E \sim \dot{M}/V$ is an effective seismic area and $A_T \propto L^{3/2}V^{-1/2}$ is the area above an isotherm T_{ref} . A global set of 65 RTFs with a combined length of 16,410 km is well described by a linear scaling relation (1) $A_E \propto A_T$, which yields $\chi = 0.26 \pm 0.05$ for $T_{\text{ref}} = 600^\circ\text{C}$. Therefore, nearly 3/4 of the slip above the 600°C isotherm must be accommodated by subseismic mechanisms, and this slip partitioning does not depend systematically on either V or L . RTF seismicity can be fit by a truncated Gutenberg-Richter distribution with a slope $\beta = 2/3$ in which the cumulative number of events N_0 and the upper-cutoff moment $M_C = \mu D_C A_C$ depend on A_T . Data for the largest events are consistent with a self-similar slip scaling, $D_C \propto A_C^{1/2}$, and a square-root areal scaling (2) $A_C \propto A_T^{1/2}$. If (1) and (2) apply, then moment balance requires that the dimensionless seismic productivity, $\nu_0 \propto \dot{N}_0/A_TV$, should scale as $\nu_0 \propto A_T^{-1/4}$, which we confirm using small events. Hence, the frequencies of both small and large earthquakes adjust with A_T to maintain constant coupling. RTF scaling relations appear to violate the single-mode hypothesis, which states that a fault patch is either fully seismic or fully aseismic and thus implies $A_C \leq A_E$. The heterogeneities in the stress distribution and fault structure responsible for (2) may arise from a thermally regulated, dynamic balance between the growth and coalescence of fault segments within a rapidly evolving fault zone.

*Published as: M. S. Boettcher and T. H. Jordan, Earthquake scaling relations for mid-ocean ridge transform faults, *J. Geophys. Res.*, v. 109, B12302, doi:1029/2004JB003110. Reproduced with permission from the American Geophysical Union.

Earthquake scaling relations for mid-ocean ridge transform faults

M. S. Boettcher

Marine Geology and Geophysics, MIT/WHOI Joint Program, Woods Hole, Massachusetts, USA

T. H. Jordan

Department of Earth Sciences, University of Southern California, Los Angeles, California, USA

Received 24 March 2004; revised 8 July 2004; accepted 30 July 2004; published 9 December 2004.

[1] A mid-ocean ridge transform fault (RTF) of length L , slip rate V , and moment release rate \dot{M} can be characterized by a seismic coupling coefficient $\chi = A_E/A_T$, where $A_E \sim \dot{M}/V$ is an effective seismic area and $A_T \propto L^{3/2}V^{-1/2}$ is the area above an isotherm T_{ref} . A global set of 65 RTFs with a combined length of 16,410 km is well described by a linear scaling relation (1) $A_E \propto A_T$, which yields $\chi = 0.15 \pm 0.05$ for $T_{\text{ref}} = 600^\circ\text{C}$. Therefore about 85% of the slip above the 600°C isotherm must be accommodated by subseismic mechanisms, and this slip partitioning does not depend systematically on either V or L . RTF seismicity can be fit by a truncated Gutenberg-Richter distribution with a slope $\beta = 2/3$ in which the cumulative number of events N_0 and the upper cutoff moment $M_C = \mu D_C A_C$ depend on A_T . Data for the largest events are consistent with a self-similar slip scaling, $D_C \propto A_C^{1/2}$, and a square root areal scaling (2) $A_C \propto A_T^{1/2}$. If relations 1 and 2 apply, then moment balance requires that the dimensionless seismic productivity, $\nu_0 \propto \dot{N}_0/A_T V$, should scale as $\nu_0 \propto A_T^{-1/4}$, which we confirm using small events. Hence the frequencies of both small and large earthquakes adjust with A_T to maintain constant coupling. RTF scaling relations appear to violate the single-mode hypothesis, which states that a fault patch is either fully seismic or fully aseismic and thus implies $A_C \leq A_E$. The heterogeneities in the stress distribution and fault structure responsible for relation 2 may arise from a thermally regulated, dynamic balance between the growth and coalescence of fault segments within a rapidly evolving fault zone.

INDEX TERMS: 7230 Seismology: Seismicity and seismotectonics; 8123 Tectonophysics: Dynamics, seismotectonics; 8150 Tectonophysics: Plate boundary—general (3040); 3035 Marine Geology and Geophysics: Midocean ridge processes; **KEYWORDS:** earthquakes, scaling relations, fault mechanics

Citation: Boettcher, M. S., and T. H. Jordan (2004), Earthquake scaling relations for mid-ocean ridge transform faults, *J. Geophys. Res.*, 109, B12302, doi:10.1029/2004JB003110.

1. Introduction

[2] How slip is accommodated on major faults remains a central problem of tectonics. Although synoptic models of fault slip behavior have been constructed [e.g., Sibson, 1983; Yeats *et al.*, 1997; Scholz, 2002], a full dynamical theory is not yet available. Some basic observational issues are (1) the partitioning of fault slip into seismic and aseismic components, including the phenomenology of steady creep [Schulz *et al.*, 1982; Wesson, 1988], creep transients (silent earthquakes) [Sacks *et al.*, 1978; Linde *et al.*, 1996; Heki *et al.*, 1997; Hirose *et al.*, 1999; Dragert *et al.*, 2001; Miller *et al.*, 2002], and slow earthquakes [Kanamori and Cipar, 1974; Okal and Stewart, 1982; Beroza and Jordan, 1990]; (2) the scaling of earthquake slip with rupture dimensions, e.g., for faults with large aspect ratios, whether slip scales

with rupture width [Romanowicz, 1992, 1994; Romanowicz and Ruff, 2002], length [Scholz, 1994a, 1994b; Hanks and Bakun, 2002], or something in between [Mai and Beroza, 2000; P. Somerville, personal communication, 2003]; (3) the outer scale of faulting, i.e., the relationship between fault dimension and the size of the largest earthquake [Jackson, 1996; Schwartz, 1996; Ward, 1997; Kagan and Jackson, 2000]; (4) the effects of cumulative offset on shear localization and the frequency-magnitude statistics of earthquakes, in particular, characteristic earthquake behavior [Schwartz and Coppersmith, 1984; Wesnousky, 1994; Kagan and Wesnousky, 1996]; and (5) the relative roles of dynamic and rheologic (quenched) structures in generating earthquake complexity (Gutenberg-Richter statistics, Omori's Law) and maintaining stress heterogeneity [Rice, 1993; Langer *et al.*, 1996; Shaw and Rice, 2000].

[3] A plausible strategy for understanding these phenomena is to compare fault behaviors in different tectonic environments. Continental strike-slip faulting, where the

observations are most comprehensive, provides a good baseline. Appendix A summarizes one interpretation of the continental data, which we will loosely refer to as the "San Andreas Fault (SAF) model," because it owes much to the abundant information from that particular fault system. Our purpose is not to support this particular interpretation (some of its features are clearly simplistic and perhaps wrong) but to use it as a means for contrasting the behavior of strike-slip faults that offset two segments of an oceanic spreading center. These ridge transform faults (RTFs) are the principal subject of our study.

[4] RTFs are known to have low seismic coupling on average [Brune, 1968; Davies and Brune, 1971; Frohlich and Apperson, 1992; Okal and Langenhorst, 2000]. Much of the slip appears to occur aseismically, and it is not clear which parts of the RTFs, if any, are fully coupled [Bird et al., 2002]. Given the length and linearity of many RTFs, the earthquakes they generate tend to be rather small; since 1976, only one event definitely associated with an RTF has exceeded a moment-magnitude (m_w) of 7.0 (Harvard Centroid-Moment Tensor Project, 1976–2002, available at <http://www.seismology.harvard.edu/projects/CMT>) (Harvard CMT). Slow earthquakes are common on RTFs [Kanamori and Stewart, 1976; Okal and Stewart, 1982; Beroza and Jordan, 1990; Ihlmlé and Jordan, 1994]. Many slow earthquakes appear to have a compound mechanism comprising both an ordinary (fast) earthquake and an infraseismic event with an anomalously low rupture velocity (quiet earthquake); in some cases, the infraseismic event precedes, and apparently initiates, the fast rupture [Ihlmlé et al., 1993; Ihlmlé and Jordan, 1994; McGuire et al., 1996; McGuire and Jordan, 2000]. Although the latter inference remains controversial [Abercrombie and Ekström, 2001, 2003], the slow precursor hypothesis is also consistent with episodes of coupled seismic slip observed on adjacent RTFs [McGuire et al., 1996; McGuire and Jordan, 2000; Forsyth et al., 2003].

[5] The differences observed for RTFs and continental strike-slip faults presumably reflect their tectonic environments. When examined on the fault scale, RTFs reveal many of the same complexities observed in continental systems: segmentation, braided strands, stepovers, constraining and releasing bends, etc. [Pockalny et al., 1988; Embley and Wilson, 1992; Yeats et al., 1997; Ligi et al., 2002]. On a plate tectonic scale, however, RTFs are generally longer lived structures with cumulative displacements that far exceed their lengths, as evidenced by the continuity of ocean-crossing fracture zones [e.g., Cande et al., 1989]. Moreover, the compositional structure of the oceanic lithosphere is more homogeneous, and its thermal structure is more predictable from known plate kinematics [Turcotte and Schubert, 2001]. Owing to the relative simplicity of the mid-ocean environment, RTF seismicity may therefore be more amenable to interpretation in terms of the dynamics of faulting and less contingent on its geologic history.

[6] In this paper, we investigate the phenomenology of oceanic transform faulting by constructing scaling relations for RTF seismicity. As in many other published studies, we focus primarily on earthquake catalogs derived from teleseismic data. Because there is a rich literature on the subject, we begin with a detailed review of what has been previously learned and express the key results in a consistent mathe-

matical notation (see notation section). We then proceed with our own analysis, in which we derive new scaling relations based on areal measures of faulting. We conclude by using these relations to comment on the basic issues laid out in this introduction.

2. Background

[7] Oceanic and continental earthquakes provide complementary information about seismic processes. On the one hand, RTFs are more difficult to study than continental strike-slip earthquakes because they are farther removed from seismic networks; only events of larger magnitude can be located, and their source parameters are more poorly determined. On the other hand, the most important tectonic parameters are actually better constrained, at least on a global basis. An RTF has a well-defined length L , given by the distance between spreading centers, and a well-determined slip rate V , given by present-day plate motions. Moreover, the thermal structure of the oceanic lithosphere near spreading centers is well described by isotherms that deepen according to the square root of age.

[8] Brune [1968] first recognized that the average rate of seismic moment release could be combined with L and V to determine the effective thickness (width) of the seismic zone, W_E . For each earthquake in a catalog of duration Δt_{cat} , he converted surface wave magnitude m_S into seismic moment M and summed over all events to obtain the cumulative moment ΣM . Knowing that M divided by the shear modulus μ equals rupture area times slip, he obtained a formula for the effective seismic width

$$W_E = \frac{\Sigma M}{\mu L V \Delta t_{\text{cat}}} \quad (1)$$

In his preliminary analysis, Brune [1968] found values of W_E in the range 2–7 km. A number of subsequent authors have applied Brune's procedure to direct determinations of M as well as to m_S catalogs [Davies and Brune, 1971; Burr and Solomon, 1978; Solomon and Burr, 1979; Hyndman and Weichert, 1983; Kawaski et al., 1985; Frohlich and Apperson, 1992; Sobolev and Rundquist, 1999; Okal and Langenhorst, 2000; Bird et al., 2002]. The data show considerable scatter with the effective seismic widths for individual RTFs varying from 0.1 to 8 km.

[9] Most studies agree that W_E increases with L and decreases with V , but the form of the scaling remains uncertain. Consider the simple, well-motivated hypothesis that the effective width is thermally controlled, which appeared in the literature soon after quantitative thermal models of the oceanic lithosphere were established [e.g., Burr and Solomon, 1978; Kawaski et al., 1985]. If the seismic thickness corresponds to an isotherm, then it should deepen as the square root of lithospheric age, implying $W_E \propto L^{1/2} V^{-1/2}$ and $\Sigma M \propto L^{3/2} V^{1/2}$ [e.g., Okal and Langenhorst, 2000]. However, two recent studies have suggested that W_E instead scales exponentially with V [Frohlich and Apperson, 1992; Bird et al., 2002], while another proposes that ΣM scales exponentially with L [Sobolev and Rundquist, 1999]. The most recent papers, by Langenhorst and Okal [2002] and Bird et al. [2002], do not explicitly test the thermal scaling of W_E .

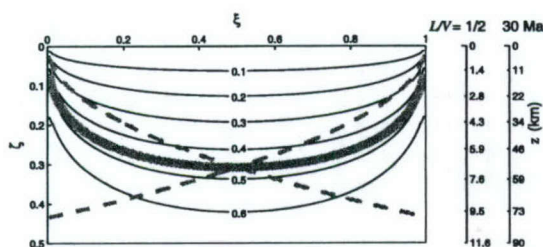


Figure 1. Thermal area of contact, A_T , is the fault area above a reference isotherm T_{ref} . Temperatures of the plates bounding the fault are assumed to evolve as $T_0 \text{erf}[\zeta\xi^{-1/2}]$ and $T_0 \text{erf}[\zeta(1-\xi)^{-1/2}]$, where T_0 is the mantle potential temperature, $\xi = x/L$ and $\zeta = 2/\sqrt{8\kappa L/V}$ are nondimensionalized length and depth, and κ is the thermal diffusivity. Fault isotherms T/T_0 (thin curves) are calculated by averaging the two plate temperatures, which reach a maximum depth in kilometers at $z_{\text{max}} = 2\sqrt{\kappa L/V} \text{erf}^{-1}(T_{\text{ref}}/T_0)$. Our model assumes a reference isotherm of $T_{\text{ref}}/T_0 = 0.46$ (thick gray line), or $T_{\text{ref}} = 600^\circ\text{C}$ for $T_0 = 1300^\circ\text{C}$; the corresponding plate isotherms are plotted as dashed lines. Depth axes for $L/V = 0.5$ Ma and 30 Ma (right side, in kilometers), calculated for an assumed diffusivity of $\kappa = 10^{-12} \text{ km}^2/\text{s}$, bound the plate ages spanned by the RTF data set.

[10] An important related concept is the fractional seismic coupling, defined as the ratio of the observed seismic moment release to the moment release expected from a plate tectonic model [Scholz, 2002]:

$$\chi = \frac{\Sigma M_{\text{obs}}}{\Sigma M_{\text{ref}}} \quad (2)$$

Previous authors have made different assumptions in calculating the denominator of equation (2). In our study, we specified ΣM_{ref} in terms of a “thermal area of contact,” A_T , which we obtained from a standard algorithm: the thermal structure of an RTF is approximated by averaging the temperatures of the bounding plates computed from a two-dimensional half-space cooling model [e.g., Engeln et al., 1986; Stoddard, 1992; Okal and Langenhorst, 2000; Abercrombie and Ekström, 2001]. The isotherms and particular parameters of the algorithm are given in Figure 1. A_T is just the area of a vertical fault bounded from below by a chosen isotherm, T_{ref} , and its scaling relation is $A_T \propto L^{3/2}V^{-1/2}$. We define the average “thermal thickness” for this reference isotherm by $W_T \equiv A_T/L$. The cumulative moment release is $\Sigma M_{\text{ref}} = \mu L W_T V \Delta t_{\text{ent}}$, so equations (1) and (2) imply that χ is simply the ratio of W_E to W_T .

[11] The seismic coupling coefficient has the most direct interpretation if the reference isotherm T_{ref} corresponds to the brittle-plastic transition defined by the maximum depth of earthquake rupture [Scholz, 2002]. In this case, the value $\chi = 1$ quantifies the notion of “full seismic coupling” used in section 1. The focal depths of oceanic earthquakes do appear to be bounded by an isotherm, although estimates range from 400°C to 900°C [Wiens and Stein, 1983; Trehu and Solomon, 1983; Engeln et al., 1986; Bergman and

Solomon, 1988; Stein and Pelayo, 1991]. Ocean bottom seismometer (OBS) deployments [Wilcock et al., 1990] and teleseismic studies using waveform modeling and slip inversions [Abercrombie and Ekström, 2001] tend to favor temperatures near 600°C . We therefore adopt this value as our reference isotherm. Actually, what matters for seismic coupling is not the absolute temperature, but its ratio to the mantle potential temperature T_0 . We choose $T_{\text{ref}}/T_0 = 0.46$, so that a reference isotherm of 600°C implies $T_0 = 1300^\circ\text{C}$, a typical value supported by petrological models of mid-ocean spreading centers [e.g., Bowan and White, 1994].

[12] Previous studies have shown that the χ values for RTFs are generally low. Referenced to the 600°C isotherm, most yield global averages of 10–30%, but again there is a lot of variability from one RTF to another. High values ($\chi > 0.8$) have been reported for many transform faults in the Atlantic Ocean [Kanamori and Stewart, 1976; Muller, 1983; Wilcock et al., 1990], whereas low values ($\chi < 0.2$) are observed for Eltanin and other transform faults in the Pacific [Kawaski et al., 1985; Okal and Langenhorst, 2000]. The consensus is for a general decrease in χ with spreading rate [Kawaski et al., 1985; Sobolev and Rundquist, 1999; Bird et al., 2002; Rundquist and Sobolev, 2002].

[13] By definition, low values of χ imply low values of the effective coupling width, W_E . However, is the actual RTF coupling depth that shallow? Several of the pioneering studies suggested this possibility [Brune, 1968; Davies and Brune, 1971; Burr and Solomon, 1978; Solomon and Burr, 1979]. From Sleep’s [1975] thermal model, Burr and Solomon [1978] obtained an average coupling depth corresponding to the 150°C isotherm ($\pm 100^\circ\text{C}$), and they supported their value with Stesky et al.’s [1974] early work on olivine deformation. Given the direct evidence of seismic rupture at depths below the 400°C isotherm, cited above, and experiments that show unstable sliding at temperatures of 600°C or greater [Pinkston and Kirby, 1982; Boettcher et al., 2003], this “shallow isotherm” hypothesis no longer appears to be tenable [Bird et al., 2002].

[14] However, the low values of χ could imply that RTFs have “thin, deep seismic zones,” bounded from above by an isotherm in the range 400 – 500°C and from below by an isotherm near 600°C . Alternatively, the seismic coupling of RTFs may not depend solely on temperature; it might be dynamically maintained or depend on some type of lateral compositional variability. If so, does the low seismic coupling observed for RTFs represent a single-mode distribution of seismic and creeping patches, as in Appendix A, or does a particular patch sometimes slip seismically and sometimes aseismically?

[15] The low values of χ reflect the paucity of large earthquakes on RTFs, which can be characterized in terms of an upper cutoff magnitude. Like most other faulting environments, RTFs exhibit Gutenberg-Richter (GR) frequency-size statistics over a large range of magnitudes; that is, they obey a power law scaling of the form $\log N \propto -bm \propto -\beta \log M$, where N is the cumulative number above magnitude m and $\beta = (2/3)b$. The upper limit of the scaling region is specified by a magnitude cutoff m_C or an equivalent moment cutoff M_C , representing the “outer scale” of fault rupture. A variety of truncated GR distributions are available [Molnar, 1979; Anderson and Luco, 1983; Main and Burton, 1984; Kagan, 1991, 1993; Kagan and Jackson,

2000; Kagan, 2002a], but they all deliver a scaling relation of the form $\Sigma M \propto M_C^{1-\beta}$.

[16] The β values of individual transform faults are difficult to constrain owing to their remoteness and the correspondingly high detection thresholds of global catalogs. OBS deployments have yielded β values in the range 0.5–0.7 [Trehu and Solomon, 1983; Lilwall and Kirk, 1985; Wilcock *et al.*, 1990], while teleseismic studies of regional RTF seismicity have recovered values from 0.3 to 1.1 [Francis, 1968; Muller, 1983; Dziak *et al.*, 1991; Okal and Langenhorst, 2000]. The most recent global studies disagree on whether β is constant [Bird *et al.*, 2002] or depends on V [Langenhorst and Okal, 2002]. This observational issue is closely linked to theoretical assumptions about how RTF seismicity behaves at large magnitudes. Bird *et al.* [2002] adopted the truncated GR distribution of Kagan and Jackson [2000] (a three-parameter model); they showed that the Harvard CMT data set for the global distribution of RTFs is consistent with the self-similar value $\beta = 2/3$, and they expressed the seismicity variations among RTFs in terms of a cutoff moment M_C . They concluded that $\log M_C$ decreases quadratically with V . On the other hand, Langenhorst and Okal [2002] fit the data by allowing β to vary above and below an “elbow moment” that was also allowed to vary with V (a four-parameter model); they concluded that below the elbow, β increases linearly with V , while the elbow moment itself varies as approximately $V^{-3/2}$.

3. Seismicity Model

[17] We follow Bird *et al.* [2002] and adopt the three-parameter seismicity model of Kagan and Jackson [2000], in which an exponential taper modulates the cumulative GR distribution [see also Kagan, 2002a]:

$$N(M) = N_0 \left(\frac{M_0}{M} \right)^\beta \exp \left(-\frac{M_0 - M}{M_C} \right). \quad (3)$$

M_0 is taken to be the threshold moment above which the catalog can be considered complete, and N_0 is the cumulative number of events above M_0 during the catalog interval Δt_{cat} . At low moment, N scales as $M^{-\beta}$, while above the outer scale M_C this cumulative number decays exponentially. We will refer to an event with moment M_C as an “upper cutoff earthquake”; larger events will occur, but with an exponentially decreasing probability. The total moment released during Δt_{cat} is obtained by integrating the product of M and the incremental distribution $n(M) = -dN/dM$,

$$\begin{aligned} \Sigma M &= \int_{M_0}^{\infty} M n(M) dM \\ &= N_0 M_0^\beta M_C^{1-\beta} \Gamma(1-\beta) e^{M_0/M_C}. \end{aligned}$$

Assuming $M_0 \ll M_C$, we obtain

$$\Sigma M \approx N_0 M_0^\beta M_C^{1-\beta} \Gamma(1-\beta). \quad (4)$$

For $\beta = 2/3$, the gamma function is $\Gamma(1/3) = 2.678 \dots$

[18] Substituting equation (4) into equation (1) yields the formula for the effective seismic thickness W_E . In order to avoid equating small values of χ with shallow coupling depths, we multiply W_E by the total RTF length L to cast the analysis in terms of an effective seismic area A_E . We average over seismic cycles and equate an RTF moment rate with its long-catalog limit, $\dot{M} \equiv \lim_{\Delta t_{\text{cat}} \rightarrow \infty} \Sigma M / \Delta t_{\text{cat}}$. This reduces equation (1) to the expression

$$A_E = \dot{M} / (\mu V). \quad (5)$$

The effective area is thus the total seismic potency, M/μ , per unit slip, averaged over many earthquake cycles.

[19] Similarly, the outer scale of fault rupture can be expressed in terms of upper cutoff moment, $M_C = \mu A_C D_C$, where A_C is the rupture area and D_C is the average slip of the upper cutoff earthquake. In this notation, the long catalog limit of equation (4) can be written $\dot{M} = \dot{N}_0 M_0^\beta M_C^{1-\beta} \Gamma(1-\beta)$, where \dot{N}_0 is the average number of events with moment above M_0 per unit time. We employ a nondimensionalized version of this event rate parameter, which we call the seismic productivity:

$$\nu_0 = \frac{\dot{N}_0 M_0}{\mu A_T V}. \quad (6)$$

The seismic productivity is the cumulative event rate normalized by the rate of events of moment M_0 needed to attain full seismic coupling over the thermal area of contact A_T . For the RTFs used in this study, $M_C \gg M_0$, so that $\nu_0 \ll 1$. With these definitions, our model for the seismic coupling coefficient becomes

$$\chi = A_E / A_T = \nu_0 (M_C / M_0)^{1-\beta} \Gamma(1-\beta). \quad (7)$$

4. Data

[20] We delineated the RTFs using altimetric gravity maps [Smith and Sandwell, 1997], supplemented with T phase locations from the U.S. Navy Sound Surveillance System (SOSUS) of underwater hydrophones [Dziak *et al.*, 1996, 2000; R. P. Dziak, SOSUS locations for events on the western Blanco Transform Fault, personal communication, 1999]. Like other strike-slip faults, RTFs show many geometric complexities, including offsets of various dimensions (see section 1 for references), so that the definition of a particular fault requires the choice of a segmentation scale. Given the resolution of the altimetry and seismicity data, we chose offsets of 35 km or greater to define individual faults. Fault lengths L for 78 RTFs were calculated from their end-point coordinates, and their tectonic slip rates were computed from the NUVEL-1 plate velocity model [DeMets *et al.*, 1990]. We winnowed the fault set by removing any RTF with $L < 75$ km and $A_T < A_T^{\text{min}} = 350$ km². This eliminated small transform faults with uncertain geometry or seismicity measures significantly contaminated by ridge crest normal faulting. The resulting fault set comprised 65 RTFs with a combined length of 16,410 km (Figure 2).

4.1. Seismicity Catalogs

[21] We compiled a master list of RTF seismicity by collating hypocenter and magnitude information from the

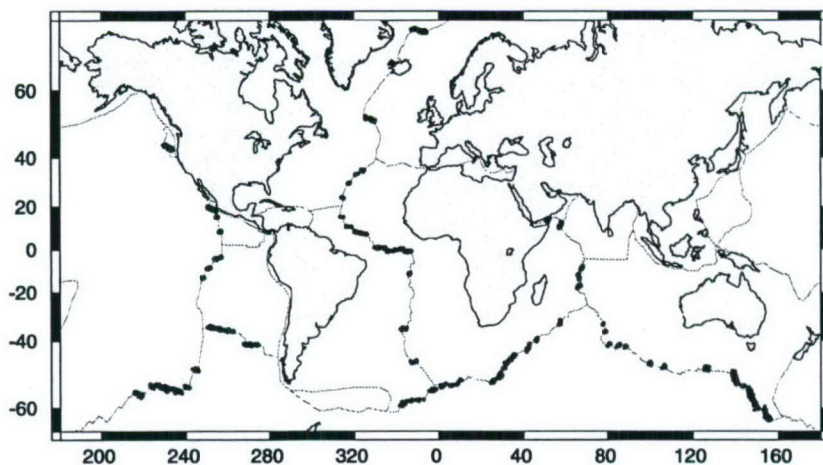


Figure 2. Global distribution of the 65 mid-ocean ridge transform faults (RTFs) used in this study. The faults were selected to have $L > 75$ km and $A_T > 350$ km² and have been delineated by plotting all associated earthquakes from the ISC m_s and Harvard CMT catalogs (black dots). The cumulative fault length is 16,410 km.

Harvard CMT and the International Seismological Center (ISC) online bulletin (1964–1999, available at <http://www.isc.ac.uk>) catalogs. We created an earthquake catalog for each RTF comprising all events with locations (ISC epicenters for 1964–1999, CMT epicentroids for 2000–2002) that fell within a region extending 80 km on either side of the fault or 50 km from either end. To avoid overlap in the cases where faults were close together, we reduced the radii of the semicircular regions capping the fault ends until each earthquake was associated with a unique RTF. The tectonic parameters and seismicity compilations for individual RTFs are summarized in Appendix B.

[22] Three types of magnitude data were included in our catalogs, body wave (m_b) and surface wave (m_s) magnitudes from the ISC (1964–1999) and moment magnitude (m_w) from the Harvard CMT (1976–2002). Using the moment tensors from the latter data set, we further winnowed the catalog of events whose null axis plunges were less than 45° in order to eliminate normal-faulting earthquakes. Normal-faulting events without CMT solutions could not be culled from the m_b and m_s data sets, although their contributions to the total moment are probably small. The three magnitude distributions for the 65 RTFs indicate average global network detection thresholds at $m_b = 4.7$, $m_s = 5.0$, and $m_w = 5.4$, with slightly higher thresholds for m_b and m_w in the Southern Ocean, at 4.8 and 5.6, respectively. We use the higher threshold values in our analysis to avoid any geographic bias.

[23] The location uncertainties for RTF events depend on geographic position, but for events larger than the m_s threshold of 5.0, the seismicity scatter perpendicular to the fault traces has an average standard deviation of about 25 km. The spatial window for constructing the fault catalogs was chosen to be sufficiently wide to comprise essentially all of the CMT events with appropriately oriented strike-slip mechanisms. Increasing the window dimensions by 20% only increased the total number of events with $m_w > 5.6$ from 548 to 553 (+0.9%) and their

cumulative CMT strike-slip moment from 1.205×10^{21} N m to 1.212×10^{21} N m (+0.6%).

[24] A potentially more significant problem was the inclusion of seismicity near the RTF end points, where the transition from spreading to transform faulting is associated with tectonic complexities [Behn *et al.*, 2002]. However, completely eliminating the semicircular window around the fault ends only decreased the event count to 517 (−5.7%) and the cumulative moment to 1.162×10^{21} N m (−3.6%), which would not change the results of our scaling analysis.

[25] Some large earthquakes with epicenters near ridge-transform junctures actually occur on intraplate fracture zones, rather than the active RTF. Including these in the RTF catalogs can bias estimates of the upper cutoff magnitude, m_c . A recent example is the large ($m_w = 7.6$) earthquake of 15 July 2003 east of the Central Indian Ridge, which initiated near the end of a small (60 km long) RTF and propagated northeastward away from the ridge-transform junction [Bohnenstiehl *et al.*, 2004]. A diagnostic feature of this type of intraplate event is a richer aftershock sequence, distinct from the depleted aftershock sequences typical of RTFs (see section 4.3). An example that occurred during the time interval of our catalog, the $m_w = 7.2$ event of 26 August 1977, was located on the fracture zone 130 km west of the Bullard (A) RTF fracture zone. This event and its three aftershocks ($m_b \geq 4.8$) were excluded from our data set by our windowing algorithm. We speculate that the anomalously large ($m \approx 8$) earthquake of 10 November 1942, located near the end of the Andrew Bain RTF in the southwest Indian Ocean [Okal and Stein, 1987] was a fracture zone event, rather than an RTF earthquake as assumed in some previous studies [e.g., Langenhorst and Okal, 2002; Bird *et al.*, 2002].

4.2. Calibration of Surface Wave Magnitude

[26] The calibration of surface wave magnitude m_s to seismic moment M for oceanic environments has been discussed by Burr and Solomon [1978], Kawaski *et al.*

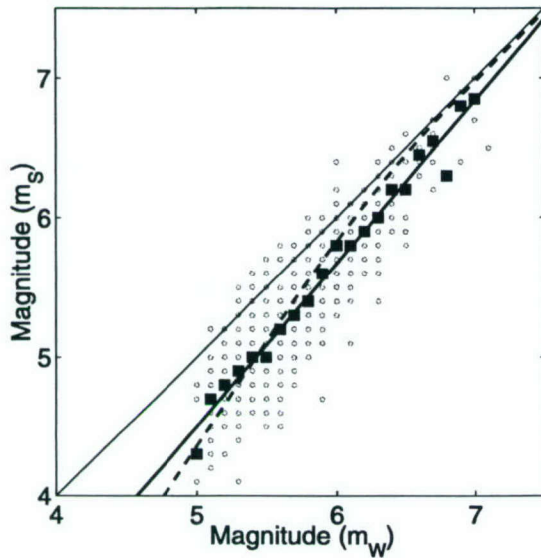


Figure 3. Calibration of ISC surface wave magnitudes to Harvard moment magnitudes. Magnitudes sampled by the data are shown as small circles. The regression line, $m_S = 1.17 m_W - 1.34$ (thick solid line), provides a better fit to the median values of m_S (solid squares) than the nonlinear relation of Ekström and Dziewonski [1988] (dashed line).

[1985], and Ekström and Dziewonski [1988]. Ekström and Dziewonski derive an empirical relationship to calibrate ISC surface wave magnitudes to CMT moments, and they list the various factors to explain why regional subsets might deviate from a global average. On a m_S - m_W plot (Figure 3), the medians for our data agree with their global curve at low magnitudes but fall somewhat below for $m_W \geq 6$. Overall, the data are better matched by a linear fit to the medians: $m_S = 1.17 m_W - 1.34$. We used this linear relationship to convert the ISC values of m_S to seismic moment.

[27] With this calibration, the total moment release rates for all RTFs in our data set are 4.39×10^{19} N m/yr for the 36-year m_S catalog and 4.72×10^{19} N m/yr for the 25.5-year m_W catalog. The 10% difference, as well as the scatter in the ratio of the two cumulative moments for individual RTFs, is consistent with the fluctuations expected from observational errors and the Poisson (time-independent) model of seismicity employed in our statistical treatment. The Poisson model ignores any clustering associated with foreshock-main shock-aftershock sequences, which are known to introduce bias in the analysis of continental seismicity [e.g., Aki, 1956; Knopoff, 1964; Gardner and Knopoff, 1974].

4.3. Aftershock Productivity

[28] RTF earthquakes generate very few aftershocks, however. Defining an aftershock as an event of lower magnitude that occurred within 30 days and 100 km of a main shock, we counted aftershocks above a magnitude threshold m_0 . Figure 4 compares the average count per main shock with similar data for strike-slip earthquakes in south-

ern California [Kisslinger and Jones, 1991] and Japan [Yamanaka and Shimazaki, 1990]. The data can be described by an aftershock law of the form

$$\log N_{\text{after}} = \alpha(m_{\text{main}} - m_0 - \Delta m_{\text{after}}). \quad (8)$$

The triggering exponent α is a fundamental scaling parameter of the Epidemic Type Aftershock Sequence (ETAS) model [Kagan and Knopoff, 1991; Ogata, 1988; Guo and Ogata, 1997; Helmstetter and Sornette, 2002]; the offset Δm_{after} is related to the magnitude decrement of the largest probable aftershock, given by Báth's law to be about 1.2 [Felzer et al., 2002; Helmstetter and Sornette, 2003a]. The continental data in Figure 4 yield $\alpha \approx 0.8$, which agrees with previous studies [Utsu, 1969; Yamanaka and Shimazaki, 1990; Guo and Ogata, 1997; Helmstetter and Sornette, 2003a], and $\Delta m_{\text{after}} \approx 0.9$, consistent with the data for southern California [Felzer et al., 2002; Helmstetter, 2003].

[29] In the case of RTFs, the aftershock productivity is so low that the data for the smallest main shock magnitudes approach background seismicity (Figure 4). RTF earthquakes are consistent with $\alpha = 0.8$ and yield $\Delta m_{\text{after}} \approx 2.2$, much larger than the continental value. In other words, the key parameter of the ETAS model, the "branching ratio" $n = 10^{-\alpha \Delta m_{\text{after}} b / (b - \alpha)}$, which is the average over all main shock magnitudes of the mean number of events triggered by a main shock [Helmstetter and Sornette, 2002], is more than an order of magnitude less for RTF seismicity than the critical value of unity approached by continental strike-slip faulting. If the ETAS model holds for RTF seismicity, then the low branching ratio ($n \approx 0.1$) implies that most ($\sim 90\%$) RTF earthquakes are driven by tectonic loading and subseismic slip, rather than triggered by other seismic events [Helmstetter and Sornette, 2003b]. This observation underlines a central difference between RTF seismicity and the SAF model.

5. Scaling Analysis

[30] The RTFs are arrayed according to their fault lengths L and slip velocities V in Figure 5. The data set spans about an order of magnitude in each of these tectonic variables. The seismicity of an individual RTF is represented by its "cumulative moment magnitude," obtained by plugging ΣM from the Harvard CMT catalog into Kanamori's [1977] definition of moment magnitude:

$$m_{\Sigma} = \frac{2}{3}(\log \Sigma M - 9.1). \quad (9)$$

There were only 11 RTFs with $m_{\Sigma} \geq 7.0$; five were in the central Atlantic, including the Romanche transform fault, which had the largest CMT moment release ($m_{\Sigma} = 7.46$). The catalogs were too short to allow a robust estimation for individual faults with lower seismicity levels; therefore we grouped the data into bins spanning increments of the geologic control variables, L , V , and A_T . For each control variable, we adjusted the boundaries of the bins so that the subsets sampled the same numbers of events, more or less, and were numerous enough to estimate the seismicity parameters. After some experimentation, we settled on four subsets, each containing an average of about 130 and

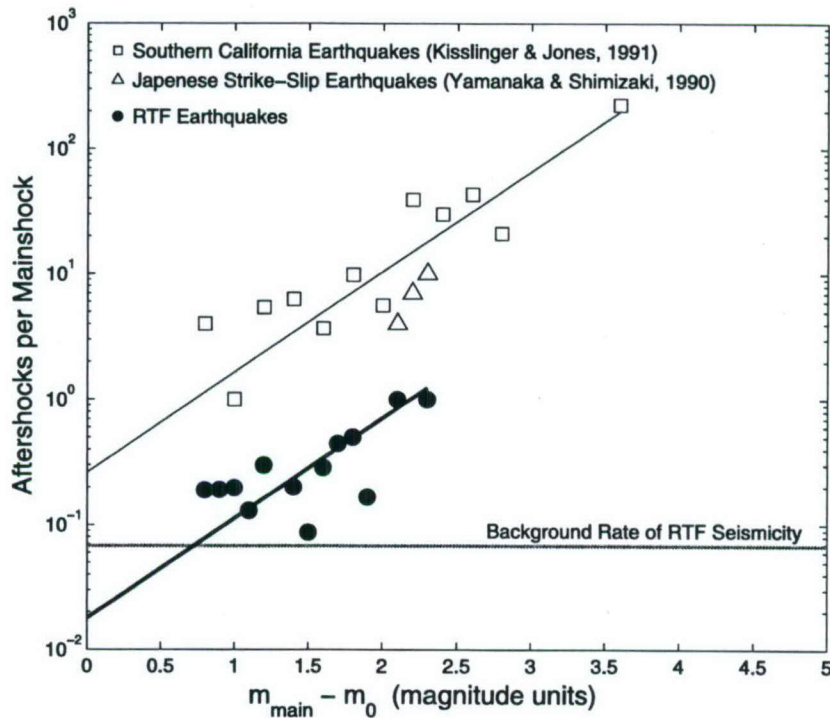


Figure 4. Average number of aftershocks above a magnitude threshold m_0 for each main shock plotted against $m_{\text{main}} - m_0$ for earthquakes on RTFs (solid symbols) and continental strike-slip faults (open symbols). RTF aftershocks were defined as events with an ISC m_b greater than or equal to $m_0 = 4.8$ that occurred within 30 days and 100 km of a main shock. The continental data sets were compiled by Kisslinger and Jones [1991] and Yamanaka and Shimazaki [1990] using local magnitude thresholds of $m_0 = 4.0$ and 4.5 , respectively. Both continental and RTF aftershocks are consistent with a slope $\alpha = 0.8$ (inclined lines), but the latter are about 1.3 orders of magnitude less frequent than the former. Note that at low main shock magnitudes, RTF aftershock rates approach background seismicity (horizontal line).

190 earthquakes for the m_W and m_S catalogs, respectively. The boundaries of the subsets are indicated in Figure 5.

5.1. Seismicity Parameters

[31] We estimated the seismicity parameters by fitting equation (3) to the data subsets using a maximum likelihood method. Event frequencies were binned in 0.1 increments of $\log M$ for the Harvard CMT data and 0.1 increments of m_S for the ISC data. The random variable representing the observed number of earthquakes, n_k , in each bin of moment width ΔM_k was assumed to be Poisson distributed with an expected value, $\bar{n}_k \approx -\Delta M_k dN(M_k)/dM$, where the cumulative distribution $N(M)$ was specified by equation (3). This yielded the likelihood function:

$$\text{Lik}(\beta, M_C) = \sum_k \left\{ \ln \left[n_k N_0 \left(\frac{\beta}{M_k} + \frac{1}{M_C} \right) \left[\frac{M_k}{M_0} \right]^{-\beta} \right] \right. \\ \cdot \exp \left[-\frac{M_0 - M_k}{M_C} \right] - N_0 \left(\frac{\beta}{M_k} + \frac{1}{M_C} \right) \left[\frac{M_k}{M_0} \right]^{-\beta} \\ \cdot \exp \left[-\frac{M_0 - M_k}{M_C} \right] - \ln(n_k!) \left. \right\}. \quad (10)$$

Our procedure followed Smith and Jordan's [1988] analysis of seamount statistics, but it differed from most treatments

of earthquake frequency-size data [e.g., Aki, 1965; Bender, 1983; Ogata, 1983; Frohlich and Davis, 1993; Kagan and Jackson, 2000; Wiemer and Wyss, 2000], which take the GR distribution or its truncated modification as the underlying probability function (compare equation (10) with equation (12) of Kagan and Jackson [2000]).

[32] The method is illustrated in Figure 6, where it has been applied to the m_W and m_S catalogs collated for all RTFs used in this study. On the basis of the seismicity roll-off at low magnitudes, we fixed the threshold magnitudes at 5.6 for m_W and 5.5 for recalibrated m_S . The maximum likelihood estimator for N_0 is the cumulative number of events observed above the corresponding threshold moments M_0 (531 and 750, respectively). Figures 6c and 6d contour the likelihood functions for the other two parameters, the power law exponent β and upper cutoff moment M_C . The two catalogs give very similar estimates: $\beta = 0.72$, $M_C = 1.42 \times 10^{19}$ N m ($m_C = 6.70$) for the Harvard CMT catalog, and $\beta = 0.70$, $M_C = 1.58 \times 10^{19}$ N m ($m_C = 6.73$) for the recalibrated ISC catalog. The 95% confidence region for each estimate includes the other estimate, as well as the maximum likelihood estimate obtained by fixing β at the self-similar value of 2/3. Our results thus agree with those of Bird *et al.* [2002], who found RTF seismicity to be consistent with

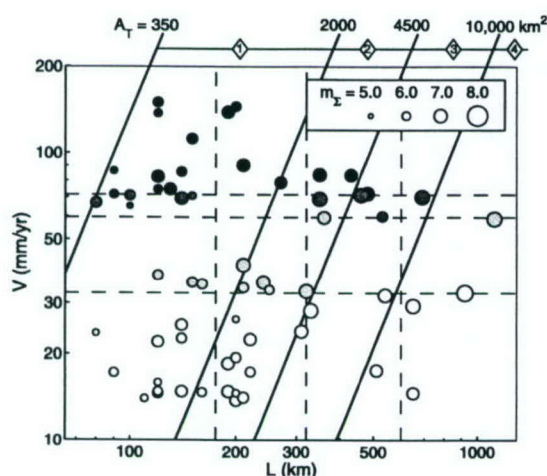


Figure 5. Distribution of fault lengths L and slip rates V for the 65 RTFs used in this study (circles). The symbols have been sized according to the cumulative moment magnitude m_c , defined by equation (9), and shaded based on the four slip rate bins separated by horizontal dashed lines. Values separating the fault length bins (vertical dashed lines) and the thermal area bins (inclined solid lines) used in our scaling analysis are also shown.

self-similar scaling below the upper cutoff moment. The self-similar assumption yields conditional values of M_C that differ by only 1% between the two catalogs (diamonds in Figure 6).

[33] The truncated GR model provides an adequate fit to the global RTF data sets. It slightly underestimates the frequency of the largest earthquakes, predicting only one event of magnitude 7 or larger compared to the three observed in both catalogs; however, the discrepancy is not statistically significant even at a low (74%) confidence level. The Harvard CMT catalog also shows a modest depletion of events just below M_C , but this feature is not evident in the ISC data.

[34] Maximum likelihood estimates of total seismic moment ΣM , upper cutoff moment M_C , and seismic productivity ν_0 derived from binned data allow us to investigate how these parameters are distributed with fault length L and slip velocity V (see Appendix C for figures and additional details). Because the catalogs are relatively short, the scatter in the individual fault data is large, especially for the smaller faults. Some variation may also be due to recent changes in plate motion, which may affect the geometry and possibly the thermal structure of an RTF. The maximum likelihood estimates, which correctly average over the Poissonian variability of the catalogs, are more systematic. ΣM and M_C increase with L , whereas ν_0 decreases. The correlations in V suggest weak positive trends in ΣM and ν_0 and a weak negative trend in M_C . A proper interpretation of these correlations must account for any correlation between the two tectonic variables.

[35] According to the thermal scaling hypothesis, the seismicity parameters should depend on fault length and

slip rate through the thermal area of contact, A_T (Figure 1). We sorted the data into the A_T bins shown in Figure 5 and estimated the seismicity parameters for the four subgroups. Figures 7 and 8 show the results for the Harvard CMT catalog. The estimates for $\beta = 2/3$ (numbered diamonds) fall within the 50% confidence regions for the unconstrained estimates (shaded areas) in all four bins (Figure 8a), again consistent with self-similar scaling below the cutoff moment. There is more scatter in the A_T binned estimates from the ISC catalog, but self-similar scaling is still acceptable at the 95% confidence level. We therefore fixed β at $2/3$ and normalized the seismicity models for the four A_T groups according to equation (6). The seismicity models obtained from both catalogs indicate that as A_T increases, the upper cutoff moment M_C increases and the seismic productivity ν_0 decreases, while the area under the curve stays about the same (e.g., Figure 8b). These statements can be quantified in terms of scaling relations involving the three areal measures A_T , A_E , and A_C .

5.2. Seismic Coupling

[36] We computed the effective seismic area $A_E = LW_E$ from equation (1) assuming the shear modulus, $\mu = 44.1$ GPa, which is the lower crustal value from the Preliminary Reference Earth Model (PREM) [Dziewonski and Anderson, 1981]. On plots of A_E versus A_T (Figure 9),

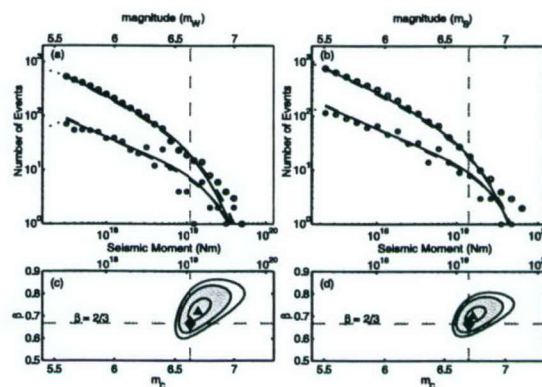


Figure 6. Global frequency-moment distributions for RTF earthquakes from (a) the Harvard CMT catalog and (b) recalibrated ISC catalog, with corresponding log likelihood maps (Figures 6c and 6d) for the model parameters. Numbers of events in discrete m_w bins (open circles) and cumulative numbers of events (solid circles) are fit with a three-parameter tapered GR distribution (dashed lines) and a tapered GR distribution with a low-moment slope fixed at $\beta = 2/3$ (solid lines). In both cases the upper cutoff moment M_C is taken at the best fit value. Triangles are the maximum likelihood solutions; contours show the 99%, 95%, and 50% confidence regions. For both catalogs, the solutions constrained by $\beta = 2/3$ (diamonds) lie within the 95% confidence contours of the unconstrained solution (shaded regions), and m_C for the two solutions are within a tenth of a magnitude unit. The threshold moment magnitude m_0 was set at 5.6 for CMT data and 5.5 for recalibrated ISC data.

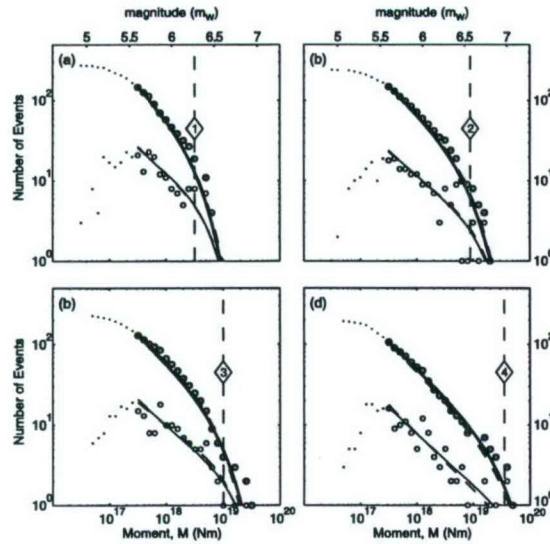


Figure 7. Frequency-moment distributions derived from the Harvard CMT catalog by binning RTFs according to the A_T divisions shown at the top of Figure 5: (a) 350–2000 km², (b) 2000–4500 km², (c) 4500–10,000 km², and (d) >10,000 km². Numbers of events in discrete m_w bins (open circles) and cumulative numbers of events (solid circles) are fit by maximum likelihood procedure with a three-parameter tapered GR distribution (dashed lines) and a tapered GR distribution with a low-moment slope fixed at $\beta = 2/3$ (solid lines). Dots show data below the threshold moment magnitude of $m_0 = 5.6$. Vertical dashed lines are the maximum likelihood estimates of M_C for $\beta = 2/3$.

the data for individual small faults scatter by as much as 2 orders of magnitude, but the maximum likelihood values for the binned data form linear arrays consistent with a constant coupling coefficient. To test the constant χ hypothesis, we constructed the likelihood function for the parameters of a more general scaling law,

$$A_E/A_E^* = (A_T/A_T^*)^\psi, \quad (11)$$

where A_E^* and A_T^* are reference values. The maximum likelihood estimates of the scaling exponent are $\psi = 1.03^{+0.20}_{-0.14}$ for the m_w data and $\psi = 0.87^{+0.17}_{-0.11}$ for the m_s data (here and elsewhere the uncertainties delineate the 95% confidence regions). Both data sets are consistent with $\psi = 1$; moreover, with the exponent fixed at unity, both give the same value of the coupling coefficient, $\chi = A_E^*/A_T^* = 0.15^{+0.02}_{-0.02}$ and $0.15^{+0.03}_{-0.01}$, respectively.

[37] Therefore our results support the simplest version of the thermal scaling hypothesis: the long-term cumulative moment release depends on the tectonic parameters L and V only through the thermal relation $A_E \propto A_T \propto L^{3/2}V^{-1/2}$. The constant χ model agrees well with the data (Figure C1), except at large V where the data fall below the model. This discrepancy is due in part to the weak negative correlation between L and V , evident in Figure 5. As a check, we compensated the values of ΣM for thermal scaling and

replotted them against L and V ; the maximum likelihood estimates for the rebinned data showed no significant residual trends.

5.3. Upper Cutoff Earthquake

[38] To calculate the rupture area $A_C = L_C W_C$ of the upper cutoff earthquake from its seismic moment $M_C = \mu A_C D_C$, some assumption must be made about how the average slip D_C scales with the rupture length L_C and width W_C . Given the continuing controversy over the slip scaling for large strike-slip earthquakes (see introduction), we considered a scaling relation of form

$$D_C = \frac{\Delta\sigma}{\mu} L_C^\lambda W_C^{1-\lambda}, \quad (12)$$

where $0 \leq \lambda \leq 1$ and $\Delta\sigma$ is the static stress drop, which we took to be independent of earthquake size. The various

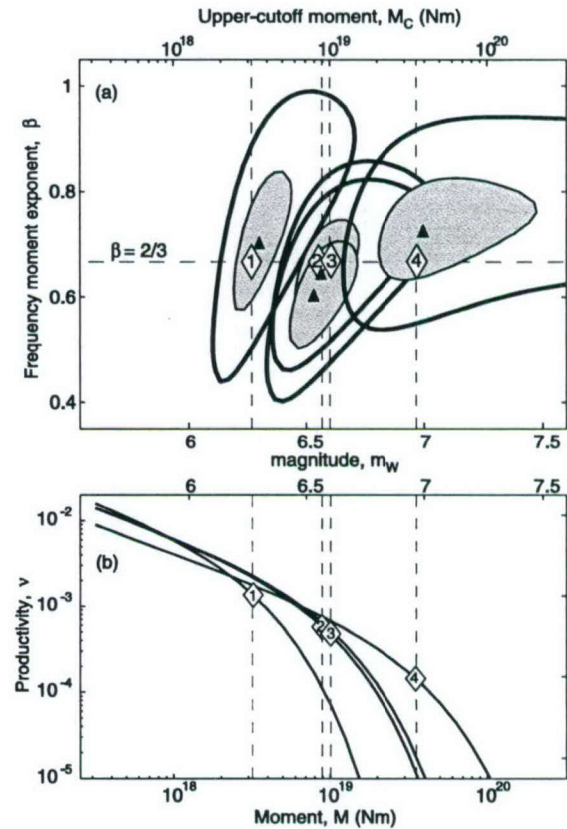


Figure 8. (a) Parameter estimates and (b) frequency-moment distributions derived from the A_T -binned data of Figure 7. Log likelihood maps in Figure 8a show the upper cutoff moment M_C and low-moment slope β corresponding to the four A_T bins. Triangles are the maximum likelihood solutions; contours show the 95% and 50% confidence regions. The solutions constrained by $\beta = 2/3$ (diamonds) lie within the 50% confidence contours of the unconstrained solution (shaded regions), and M_C for the two solutions are within a tenth of a magnitude unit.

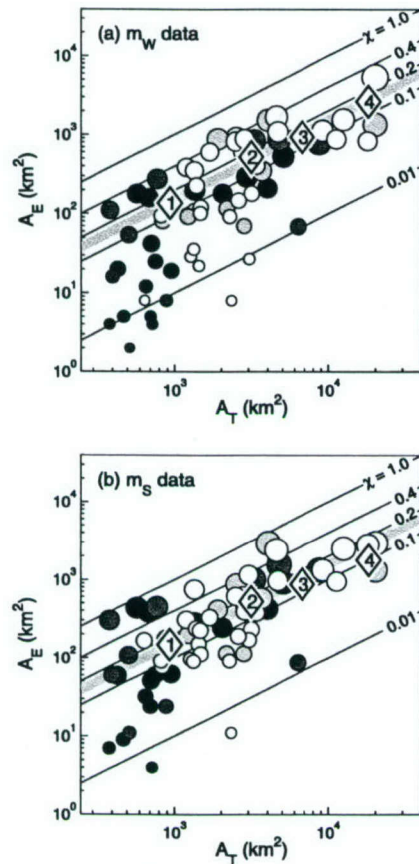


Figure 9. Effective seismic area A_E versus thermal area of contact A_T for (a) the Harvard CMT catalog and (b) recalibrated ISC m_S catalog. Symbols show data for individual RTFs (circles) and maximum likelihood estimates from the A_T -binned data for $\beta = 2/3$ (numbered diamonds). The data bins, as well as the circle sizes and shading, are given in Figure 5; fits are shown in Figures 7 and 8. The abscissa values for the diamonds are the averages of A_T in each bin weighted by the plate tectonic moment release rate $\mu A_T V$. Thin lines correspond to the seismic coupling factors χ for $T_{\text{ref}} = 600^\circ\text{C}$. The maximum likelihood values are consistent with a simple linear scaling $A_E \sim A_T$ (Table 1) and $\chi = 0.15$ (thick gray line).

models extant in the literature correspond to different values of the scaling exponent λ . The W model preferred by Romanowicz [1992, 1994] and Romanowicz and Ruff [2002] is given by $\lambda = 0$, whereas the L model preferred by Scholz [1982], Shimazaki [1986], Scholz [1994a, 1994b], Pegler and Das [1996], Wang and Ou [1998], Shaw and Scholz [2001], and Hanks and Bakun [2002] corresponds to $\lambda = 1$. The intermediate value, $\lambda = 1/2$, specifies the self-similar slip scaling advocated for large continental strike-slip earthquakes by Bodin and Brune [1996], Mai and

Beroza [2000], and P. Somerville (personal communication, 2003), here called the S model. As noted in Appendix A, the best data for continental regions, including the large strike-slip events in Izmit, Turkey (1999), and Denali, Alaska (2002), tend to favor the S model (P. Somerville, personal communication, 2003). Langenhorst and Okal [2002] adopted the W model for their analysis of RTF seismicity; however, for large RTF earthquakes, no independent observations of fault slip and rupture dimensions are available to constrain λ .

[39] On the basis of the rupture depth observations cited previously and the success of thermal scaling in explaining the ΣM data, we assumed the vertical extent of faulting during large earthquakes scales with the average thermal thickness $W_T \equiv A_T/L$,

$$W_C = \eta W_T. \quad (13)$$

Here η is a constant whose value is unimportant to the scaling analysis but presumably lies between χ (thin seismic zone) and unity (thick seismic zone). From equation (12), the upper cutoff area can then be expressed as

$$A_C = (M_C/\Delta\sigma)^{\frac{1}{1+\gamma}} (\eta W_T)^{\frac{\gamma}{1+\gamma}}. \quad (14)$$

[40] Figure 10 displays the data on plots of A_C versus A_T for $\lambda = 1/2$ (S model) assuming a constant stress drop of $\Delta\sigma = 3$ MPa. The maximum likelihood estimates for the four A_T bins again form linear arrays, but the slopes are significantly less than unity. We fit the data with the scaling relation

$$A_C/A_C^* = (A_T/A_T^*)^\gamma \quad (15)$$

and obtained maximum likelihood estimates and 95% confidence regions for the upper cutoff scaling exponent $\gamma = 0.54^{+0.29}_{-0.32}$ for the m_W catalog and $\gamma = 0.54^{+0.33}_{-0.34}$ for the m_S catalog. Varying the slip-scaling exponent λ gave values of γ that ranged from 0.30 to 0.61, depending on the data set (Figure 11). In all cases, the data are consistent with $\gamma = 1/2$, which we adopted as our model value for upper cutoff scaling.

[41] Under the constraints of our model (e.g., constant $\Delta\sigma$, γ), the seismicity data can, in principle, determine the slip-scaling exponent λ . Combining the conductive cooling equation with equations (14) and (15) yields a general relation between the upper cutoff moment and the RTF tectonic parameters: $M_C \propto L^{(\lambda+1)(3\gamma/2) - \lambda + 1/2} V^{-(\lambda+1)(\gamma/2) + \lambda - 1/2}$. For $\gamma = 1/2$ we find

W model	$M_C \propto L^{5/4} V^{-3/4},$	
S model	$M_C \propto L^{9/8} V^{-3/8},$	(16)
L model	$M_C \propto L.$	

The L model thus implies that the cutoff moment M_C is proportional to the tectonic fault length and independent of

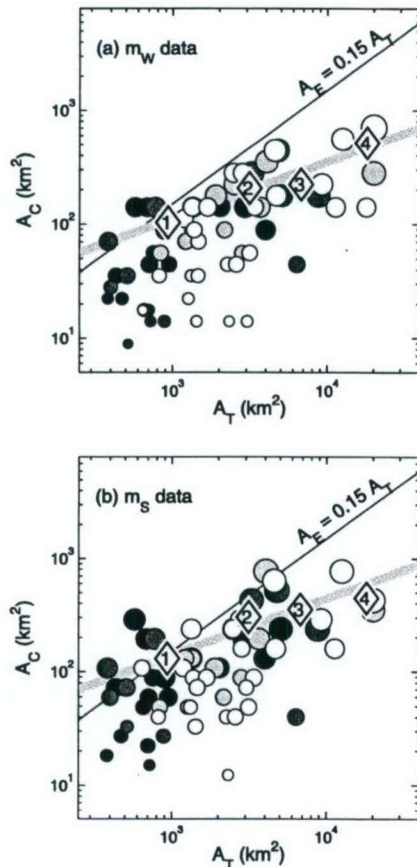


Figure 10. Upper cutoff area A_C versus thermal area of contact A_T for (a) the Harvard CMT catalog and (b) recalibrated ISC m_S catalog. Symbols show largest earthquakes for individual RTFs (circles) and maximum likelihood estimates from the A_T -binned data for $\beta = 2/3$ (numbered diamonds). The data bins, as well as the circle sizes and shading, are given in Figure 5; fits are shown in Figures 7 and 8. Calculations assume $A_C = (M_C/\Delta\sigma)^{2/3}$, corresponding to the S model of slip scaling ($\lambda = 1/2$), and a constant stress drop of $\Delta\sigma = 3$ MPa. The abscissa values for the diamonds are the averages of A_T in each bin weighted by the plate tectonic moment release rate $\mu A_T V$. The maximum likelihood values are consistent with the scaling relation $A_C \sim A_T^{1/2}$ (Table 1); the best fit (thick gray line) crosses the scaling relation for effective seismic area (thin black line) at $A_T^* = 555$ km² (Figure 10a) and $A_T^* = 862$ km² (Figure 10b).

the tectonic slip rate. Decreasing λ introduces a negative dependence on V , while maintaining an approximate proportionality between M_C and L .

[42] The L -binned estimates of M_C (Figures C2a and C2c) do show near proportionality, although they cannot resolve the small differences among the models in equation (16). The negative trends in the V -binned estimates of M_C , seen in both the m_W and m_S data sets (Figure C2b and C2d), are

more diagnostic, favoring $\lambda < 1$. After compensating for the scalings $\lambda = 1/2$ and $\gamma = 1/2$, we found that the residual correlations of M_C in L and V were negligible, so we adopted the S model for our subsequent calculations. However, given the uncertainties and restrictive modeling assumptions, neither the L nor W end-member models can be firmly rejected with the data in hand.

5.4. Seismic Productivity

[43] The parameter in the truncated GR distribution most accurately estimated by the seismicity data is N_0 , the total number of events above the moment threshold M_0 . Its value depends primarily on the more numerous smaller earthquakes and is therefore insensitive to the upper cutoff behavior. Its normalized version, the seismic productivity ν_0 , can be related to the other seismicity parameters through equation (7):

$$\nu_0 = \chi (M_0/M_C)^{1-\beta} / \Gamma(1-\beta). \quad (17)$$

The right-hand side of equation (17) can be evaluated directly from the scaling relations we have already derived: $\nu_0 \propto A_T^{-\gamma(\lambda+1)(1-\beta)+\psi-1}$. The preferred exponents ($\psi = 1$, $\beta = 2/3$, $\gamma = 1/2$, $\lambda = 1/2$) in our scaling model given in equations (3), (11), (12), and (15) therefore imply

$$\nu_0 \propto A_T^{-1/4} \propto L^{-3/8} V^{1/8}. \quad (18)$$

Because the form of this scaling relation has been determined primarily from the frequency of large earthquakes, the data on ν_0 provide an independent test of the model.

[44] Figure 12 plots the ν_0 observations against A_T . Unlike the other seismicity parameters, the scaling of ν_0 is insensitive to the magnitude moment calibration. We can therefore use the uncalibrated m_b catalog, as well as the m_W and calibrated m_S catalogs, in evaluating the model. All three data sets show a decrease in ν_0 very close to the model-predicted trend of $A_T^{-1/4}$ (gray lines). The data in

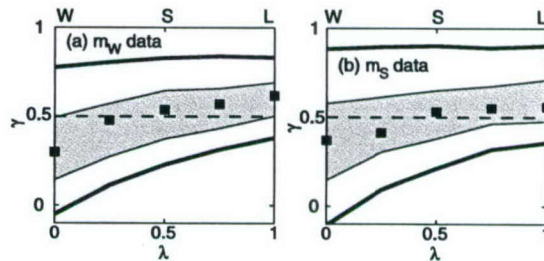


Figure 11. Maximum likelihood estimates (solid squares) of the characteristic area scaling exponent γ conditional on the slip-scaling exponent λ , obtained from (a) the Harvard CMT catalog and (b) recalibrated ISC m_S catalog. The best estimates for both catalogs cross the model value $\gamma = 1/2$ (dashed line) near $\lambda = 1/2$, which is our preferred exponent for slip scaling (S model). The end-member W and L models of slip scaling are also consistent with $\gamma = 1/2$ at the 50% confidence level (shaded band). Thick lines delineate 95% confidence region for the conditional estimate.

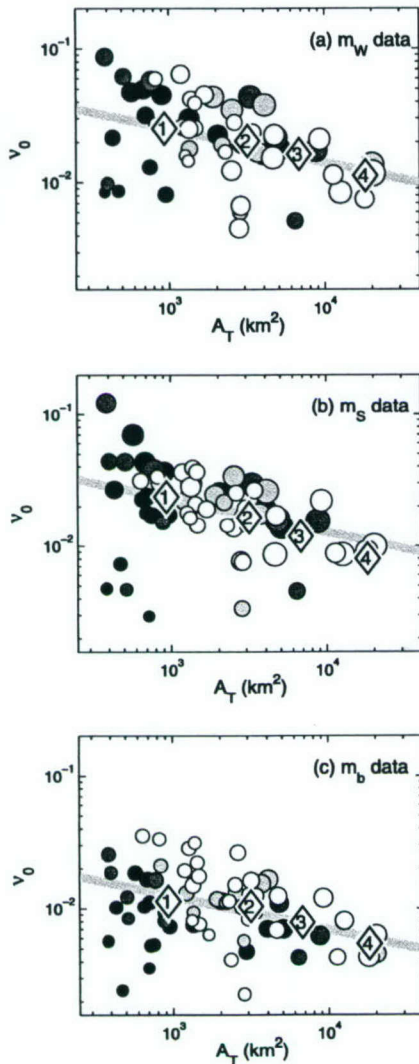


Figure 12. Seismic productivity ν_0 versus thermal area of contact A_T for (a) the Harvard CMT catalog, (b) recalibrated ISC m_S catalog, and (c) ISC m_b catalog. Symbols show normalized event counts for individual RTFs (circles) and maximum likelihood estimates from the A_T -binned data for $\beta = 2/3$ (numbered diamonds). The data bins, as well as the circle sizes and shading, are given in Figure 5; fits are shown in Figures 7 and 8. The magnitude threshold for the ISC m_b catalog was set at 4.8, providing significantly more events (2278) than either the Harvard CMT catalog (548) or the recalibrated ISC m_S catalog (890). The abscissa values for the diamonds are the averages of A_T in each bin weighted by the plate tectonic moment release rate $\mu A_T V$. The data are consistent with $\nu_0 \sim A_T^{-1/4}$ (thick gray lines), providing an independent check on the scaling model of Table 1.

Figure C3 are also consistent with the scalings in equation (18), although the increase in V is too weak to be resolved. When we compensated the data for this scaling, we found no significant residual trends in either L or V .

[45] We have come to a rather interesting result: on average, larger transform faults have bigger earthquakes but smaller seismic productivities. Through some poorly understood mechanism, the distributions of both small and large earthquakes adjust with the fault area in a way that maintains a constant coupling coefficient χ .

6. Discussion

[46] Our preferred scaling model for RTF seismicity is summarized in Table 1. As a final consistency check, we synthesized a frequency-moment distribution from the model and compared it with the M_W data from the global RTF catalog (Figure 13). The only data used to construct the synthetic distribution were the observed fault lengths L and the slip rates V computed from the NUVEL-1 plate motions; the synthetic distribution was calibrated to the seismicity catalog only through the scaling relations for the upper cutoff moment M_C and the cumulative number of events N_0 . The agreement between the synthetic and observed seismicity in Figure 13 is at least as good as the direct fit of the three-parameter model (cf. Figure 6). This global test corroborates the scaling relations inferred from subsets of the data.

[47] The linear thermal scaling relation, $A_E \propto A_T$, implies that seismic coupling χ is independent of L and V . A constant χ would be expected, for example, if the fault rheology were governed by thermally activated transitions from stable to unstable sliding. The simplest model is a “thin” seismic zone, in which both the top and the bottom of the zone conform to isotherms, the area between the isotherms is seismically fully coupled, and the average seismic thickness is thus equal to the effective thickness W_E . An RTF in this configuration conforms to the single-mode hypothesis, which states that a fault patch is either fully seismic or fully aseismic (Appendix A). For typical tectonic values of $L = 300$ km and $V = 40$ mm/yr, W_E is only about 1.7 km. If we follow Burr and Solomon [1978] in taking the upper boundary of the seismic zone to be the seafloor (Figure 14a), we are stuck with an implausibly shallow basal isotherm ($\sim 100^\circ\text{C}$). As Bird et al. [2002] have pointed out, a thin, shallow seismic zone is inconsistent with observed earthquake focal depths and laboratory experiments.

[48] An alternative is a thin, deep seismic zone. Fixing the basal isotherm at 600°C yields an upper boundary for a fully coupled zone at about 520°C (Figure 14b). This boundary

Table 1. Scaling Model for RTF Seismicity^a

Relation	Seismic Parameter	Scaling With A_T , L , and V
A	seismic coupling	$\chi \propto \text{const} (\approx 0.15 \text{ for } T_{\text{ref}} = 600^\circ)$
B	effective area	$A_E \propto A_T \propto L^{3/2} V^{-1/2}$
C	cumulative moment	$\Sigma M \propto A_T V \propto L^{3/2} V^{1/2}$
D	upper cutoff area	$A_C \propto A_T^{1/2} \propto L^{3/4} V^{-1/4}$
E	upper cutoff slip	$D_C \propto A_T^{1/4} \propto L^{3/8} V^{-1/8}$
F	upper cutoff moment	$M_C \propto A_T^{3/4} \propto L^{9/8} V^{-3/8}$
G	seismic productivity	$\nu_0 \propto A_T^{-1/4} \propto L^{-3/8} V^{1/8}$
H	cumulative number	$N_0 \propto A_T^{3/4} V \propto L^{9/8} V^{5/8}$

^aThe RTF seismicity data are consistent with the exponents $\beta = 2/3$, $\psi = 1$, $\gamma = 1/2$, and $\lambda = 1/2$, defined in equations (3), (11), (12), and (15), which imply this set of scaling relations.

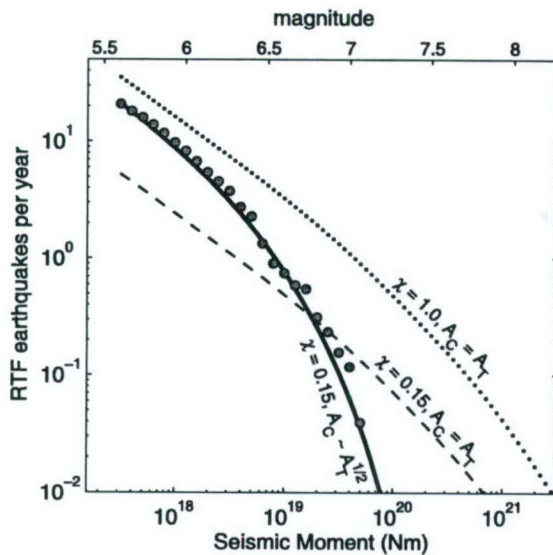


Figure 13. Comparison of the cumulative frequency-moment distribution from the Harvard CMT catalog (solid circles) with three models. The seismicity data are the same as in Figure 6a. The models combine the global distribution of RTF tectonic parameters with seismicity scaling relations; i.e., each fault is assumed to generate seismicity according to equation (3) with $\beta = 2/3$ and the other parameters scaled to its observed fault length L and slip rate V . The dotted curve shows a fully coupled model ($\chi = 1$) with an upper cutoff area equal to the thermal area of contact ($A_C = A_T$). The dashed curve is a similar model with a coupling factor reduced to the observed value ($\chi = 0.15$). The solid curve is a model that satisfies this constraint plus the observed scaling relation $A_C = 3.5 A_T^{1/2}$. The good fit obtained by the latter corroborates the scaling model of Table 1.

could be related to the stability of serpentinite. Many authors have implicated hydrated ultramafic minerals of the serpentine group in the promotion of subseismic slip. Serpentinized peridotites are commonly dredged from RTFs [Tucholke and Lin, 1994; Cannat *et al.*, 1995], and serpentinized Franciscan rocks outcrop on the creeping section of the San Andreas Fault [Allen, 1968]. Lizardite and chrysotile, the most common serpentine minerals in oceanic rocks, are stable up to temperatures of about 500°C [O'Hanley *et al.*, 1989]. Velocity-strengthening behavior (stable sliding) has been observed in room temperature laboratory experiments on serpentinite at plate-tectonic slip speeds ($< 5 \times 10^{-9}$ m/s) [Reinen *et al.*, 1994]. The presence of serpentinite may therefore inhibit the shallow nucleation of RTF earthquakes.

[49] However, it is unlikely that earthquake ruptures remain confined to a thin, deep seismic zone. Reinen *et al.* [1994] found that serpentinite transforms to velocity-weakening behavior at moderately higher slip rates (10^{-8} – 10^{-7} m/s), so earthquakes nucleating within a thin, deep seismic zone could propagate into, and perhaps all the way through, any shallow serpentinite-rich layer. Seismic slip and aseismic creep are both observed during experiments on a

single, laboratory sample of serpentinite and can be reproduced with spring-slider simulations using a multimechanism constitutive model [Reinen, 2000a, 2000b]. This behavior violates the single-mode hypothesis but is consistent with finite source inversions for large RTF earthquakes

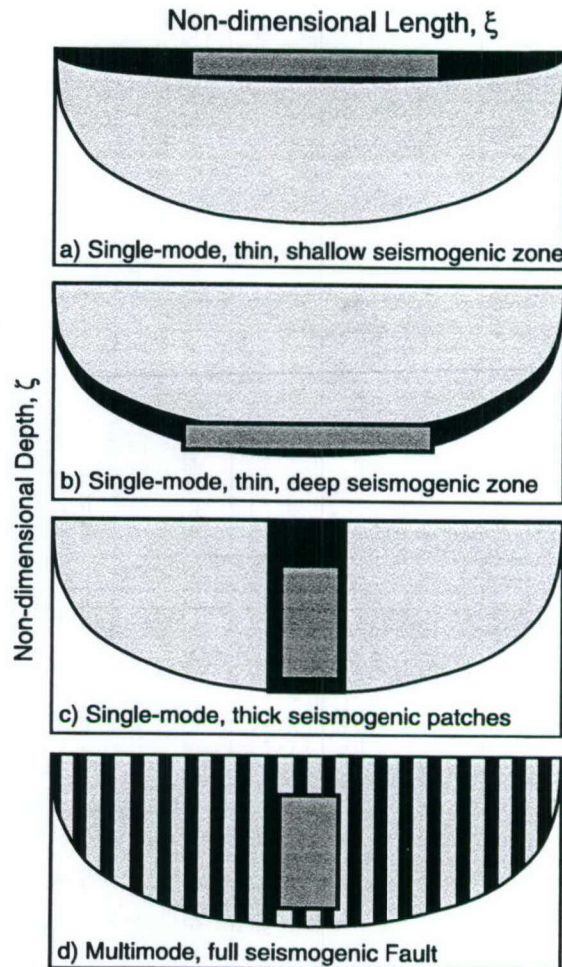


Figure 14. (a)–(c) Schematic models of the RTF seismogenic zone that conform to the scaling relations of Table 1. Models in Figures 14a–14c obey the single-mode hypothesis; the black regions show the fully coupled fault area, equal to A_E , and the light gray regions show the area that slips subseismically, equal to $A_E - A_T$. The medium gray rectangles superposed on the seismogenic zones represent the area of the upper cutoff earthquake, A_C , here scaled to an RTF of intermediate size ($A_T = 2000 \text{ km}^2$, $A_E = 300 \text{ km}^2$, $A_C = 155 \text{ km}^2$). The thin, shallow seismogenic zone in Figure 14a and thin, deep seismogenic zone in Figure 14b are bounded by isotherms, whereas the seismogenic zone in Figure 14c is laterally separated into thick patches. (d) Illustration of a multimode model in which slip can occur seismically or subseismically over the entire thermal area of contact.

Table 2. Oceanic Transform Fault Earthquake Stress Drops

Fault	Date	M , 10^{18} N m	L , km	W_T , ^a km	$\Delta\sigma$, MPa	References
Romanche	14 March 1994	50	112 ^b	22	0.4	McGuire et al. [2002a]
Romanche	14 March 1994	40	70–120 ^c	30 ^c	0.2–0.4	Abercrombie and Ekström [2001]
Mendocino	1 Sept. 1994	39	75 ^b	20 ^c	0.7	McGuire et al. [2002b]
Romanche	18 May 1995	22	77 ^b	22	0.3	McGuire et al. [2002b]
Blanco	2 June 2000	2.5	75 ^d	10	0.1	Bohnenstiehl et al. [2002]

^aWhen not otherwise marked, W_T is taken from the thermal widths listed in Table B1.

^b L is computed from second moments of the moment tensor.

^c L and W_T are from slip model calculated from waveform inversion.

^d L is inferred from distribution of aftershocks.

^e W_T for the Mendocino is inferred from the earthquake focal depth calculations of Oppenheimer et al. [1993].

[Abercrombie and Ekström, 2001; McGuire et al., 2002b], which indicate that the rupture width of an upper cutoff event, W_C , is probably closer to the full thermal thickness W_T than to W_E .

[50] We therefore consider models in which the seismic zone is wider than W_E but laterally patchy. The area of this zone, which we denote A_S , measures the part of the fault where seismic moment release occurs, so the single-mode hypothesis used in the thin zone models can be expressed by the statement

$$A_S = A_E \quad (19)$$

(single-mode hypothesis). If we make the reasonable assumption that the width of the seismic zone is equal to the width ruptured by the largest probable earthquake ($W_S = W_C$) and use the notation of equation (13) to write the effective length of the seismic zone as $L_S = A_S/\eta W_T$, then the single-mode hypothesis implies $L_S = (\chi/\eta)L$. Assuming $\eta \approx 1$, as inferred from the finite source inversions, $L_S \approx \chi L$, which means that earthquake ruptures on a typical RTF would be confined to only about one sixth of the total fault length (Figure 14c). This model can, in principle, be assessed from the along-strike distribution of RTF ruptures, but the uncertainties in epicenter locations and their relationship to rupture extent preclude a definitive result.

[51] A more diagnostic test of the single-mode hypothesis comes from the requirement that the area ruptured by an upper cutoff earthquake A_C be accommodated within the area of the seismic zone A_S and thus within the effective seismic area A_E :

$$A_C \leq A_E \quad (20)$$

(single-mode hypothesis). The observation that $1/2 \approx \gamma < \psi \approx 1$ implies that the power laws (11) and (15) must cross, so we can choose the fiducial point A_T^* such that $A_C^* = A_E^*$. In order to maintain inequality (20) below this crossover, there must be a break in the A_C or A_E scaling relation, or in both, at A_T^* . No obvious scale break is observed in Figures 9 and 10 within the data range $350 \text{ km}^2 \leq A_T \leq 21,000 \text{ km}^2$. The single-mode hypothesis thus implies that A_T^* lies outside this range.

[52] The location of the crossover depends on the stress drop. Our preferred scaling model ($\gamma = 1/2$, $\lambda = 1/2$) gives

$$A_T^* = \hat{A}_T^* (\Delta\hat{\sigma}/\Delta\sigma)^{4/3}, \quad (21)$$

where \hat{A}_T^* is computed assuming a reference stress drop of $\Delta\hat{\sigma}$. For $\Delta\hat{\sigma} = 3 \text{ MPa}$, we obtained the central estimates $\hat{A}_T^* = 555 \text{ km}^2$ from the m_W catalog, and $\hat{A}_T^* = 862 \text{ km}^2$ from the

m_S catalog (cf. Figure 10). Few estimates are available for the static stress drops of RTF earthquakes. This is not too surprising, because the standard teleseismic method for recovering stress drop relies on inferring fault rupture dimensions from aftershock sequences, which cannot be applied to most RTFs owing to the paucity of their aftershocks (Figure 4). An exception is the 27 October 1994 Blanco earthquake, whose small aftershocks were delineated by Bohnenstiehl et al. [2002] using SOSUS T phase data. We combined their inferred rupture dimension of 75 km with a thermal width of $W_T = 10 \text{ km}$ and the Harvard CMT moment to obtain $\Delta\sigma = 0.1 \text{ MPa}$ (Table 2). The rupture dimensions of a few RTF earthquakes were also available from recent teleseismic waveform inversions. McGuire et al. [2002a, 2002b] estimated the second spatial moments of three large events on the Romanche transform fault, which gave us stress drops of 0.3–0.4 MPa. Similar results were found for the 14 March 1994 earthquake using the finite source model published by Abercrombie and Ekström [2001].

[53] These data suggest that the stress drops for RTF earthquakes are on the order of 1 MPa or less, so equation (21) implies $A_T^* \geq 4.3 \hat{A}_T^*$. Taking into account the estimation uncertainties for \hat{A}_T^* yields $A_T^* > 480 \text{ km}^2$ (m_W catalog) and $> 710 \text{ km}^2$ (m_S catalog) at the 95% confidence level. We conclude that the crossover should lie within our data range, but does not, and therefore that the simple power laws derived from the fits shown in Figures 9 and 10 are inconsistent with the single-mode hypothesis. In other words, the rupture areas of large earthquakes on the smaller RTFs appear to be bigger than their effective seismic areas, at least on average.

[54] While there are significant uncertainties in the various parameters and assumptions underlying this test (e.g., constant stress drop), the results are consistent with the inferences drawn by Reinen [2000a] from her laboratory data and supports the multimode model shown in Figure 14d in which seismic and subseismic slip can occur on the same fault patch.

7. Conclusions

[55] The RTF scaling relations in Table 1 are complete in the sense that every variable in our seismicity model has been scaled to the two tectonic control parameters fault length L and slip velocity V . The seismicity depends on the fault length and width (depth) only through the thermal area of contact $A_T \propto L^{3/2} V^{-1/2}$, i.e., all of the scaling relations can be written in terms of A_T and V . We have validated this model using multiple seismicity catalogs and an interlock-

ing set of constraints. In particular, the seismic productivity $\nu_0 \propto N_0/A_T V$ was determined indirectly from the data on the larger earthquakes through the moment balance equation (17), as well as directly from counts of (mostly small) earthquakes. These nearly independent estimates of the productivity scaling both deliver relation G of Table 1.

[56] Our scaling model is remarkable in its simplicity and universality. As shown by *Bird et al.* [2002] and confirmed here, RTF earthquakes are well described by a truncated Gutenberg-Richter distribution with a self-similar slope, $\beta = 2/3$. Integrating over this distribution yields a linear thermal scaling for the effective seismic area (relation B), which implies that the seismic coupling coefficient χ is also independent of the tectonic parameters (relation A). Thus, while the moment release rates vary by more than an order of magnitude from one fault to another, the seismic coupling for a long, slow fault is, on average, the same as for a short, fast fault. Stated another way, the partitioning between seismic and subseismic slip above T_{ref} does not vary systematically with the maximum age of the lithosphere in contact across the fault, which ranges from about 1 Ma to 45 Ma.

[57] Our results do not support the oft stated view that χ decreases with V [e.g., *Bird et al.*, 2002; *Rundquist and Sobolev*, 2002]. In our model, V governs seismicity only as a tectonic loading rate and through the thermal area of contact (e.g., relations C and H). While laboratory experiments clearly indicate a dependence of fault friction on loading rate, no rate-dependent effects are obvious in the RTF seismicity, and we require no systematic variation in fault properties from slow to fast mid-ocean ridges (e.g., a decrease in the amount of serpentinization with V , as suggested by *Bird et al.* [2002]).

[58] As a global mean, our estimate of seismic coupling is in line with previous studies of RTF seismicity. For a basal reference isotherm $T_{ref} = 600^\circ\text{C}$, the data yield $\chi \approx 15\%$ ($\pm 5\%$ standard error). If no seismic slip occurs below this reference isotherm, then nearly six sevenths of the slip above it must be accommodated by subseismic mechanisms not included in the cataloged moment release: steady aseismic creep, silent earthquakes, and infraseismic (quiet) events.

[59] Relation B suggests that temperature is the main variable controlling the distribution of seismic and subseismic slip. However, by combining relations B and D with observations of low stress drop, we find that the area ruptured by the largest expected earthquake exceeds the effective seismic area ($A_C > A_E$) for the smaller RTFs. This inequality violates the "single-mode hypothesis," which states that a fault patch is either fully seismic or fully aseismic. If this inference is correct, then the small value of χ and its lack of dependence on L and V cannot simply reflect the thermal state of the faulting; some sort of temperature-dependent mechanics must govern the multi-mode partitioning of seismic and subseismic slip.

[60] A dynamical rather than structural control of ridge transform faulting is underscored by a basic conclusion of our study: on average, larger RTFs have bigger earthquakes but smaller seismic productivities, and the two corresponding seismicity parameters, A_C and ν_0 , trade off to maintain constant seismic coupling. Moreover, the areal scaling of the biggest RTF earthquakes (relation D) is

characterized by an exponent that lies halfway between the zero value implied by a constant upper cutoff moment (advocated for global seismicity by *Kagan* [2002b]) and the unit value of a simple linear model. An increase of A_C with A_T is hardly surprising, since larger faults should support larger earthquakes, but the square root scaling indicates heterogeneities in stress and/or fault structure (e.g., segmentation) that act to suppress the expected linear growth of A_C with A_T (see comparison in Figure 13).

[61] These heterogeneities might plausibly arise from a dynamical instability in the highly nonlinear mechanics of fault growth. Fault lengths in various tectonic settings are observed to increase in proportion to cumulative slip, $L \propto \Sigma D$ [*Elliott*, 1976; *Cowie and Scholz*, 1992; *Cowie*, 1998], and the coalescence of neighboring faults leads to the localization of displacement on smoother, longer faults with larger earthquakes [*Stirling et al.*, 1996; *Scholz*, 2002]. In the case of RTFs, where the cumulative displacements can reach thousands of kilometers, the tendency toward localization must be counterbalanced by mechanical instabilities that prevent "ridge-to-ridge" ruptures and maintain the relation D over order-of-magnitude variations in L and V .

[62] This mechanics is no doubt intrinsically three-dimensional, involving interactions among multiple strands within the transform fault system. Extensional relay zones and intratransform spreading centers develop due to changes in plate motion [*Bonatti et al.*, 1994; *Pockalny et al.*, 1997; *Ligi et al.*, 2002]. Some RTF earthquake sequences show ruptures on parallel faults offset by tens of kilometers [*McGuire et al.*, 1996; *McGuire and Jordan*, 2000; *McGuire et al.*, 2002a], which may reflect the cross-strike dimension of the system. A power law distribution of faults below this outer scale may explain the self-similar GR distribution observed for small earthquakes, as well as the self-similar slip distribution inferred for large earthquakes (relation E). However, the earthquake-mediated stress interactions among these faults must be very weak to satisfy the low branching ratio ($n \approx 0.1$) we observed for RTF aftershock sequences. In other words, the subseismic slip that accounts for nearly 85% of the total moment release also drives about 90% of rupture nucleation.

[63] Given the evidence for slow precursors to many large RTF earthquakes [*Jhmlé and Jordan*, 1994; *McGuire et al.*, 1996; *McGuire and Jordan*, 2000], we speculate that the seismogenic stresses on ridge transform faults may be primarily regulated by slow transients, rather than the fast ruptures that dominate continental strike-slip faults. In this view, most ordinary (loud) earthquakes on RTFs would simply be "aftershocks" of quiet or silent events.

Appendix A: San Andreas Fault Model

[64] According to this hypothetical model of continental strike-slip faulting, essentially all permanent strain within the seismogenic zone occurs as seismic slip (i.e., the faults are seismically "fully coupled" [*Brune*, 1968; *Kiratzis*, 1993; *Stein and Hanks*, 1998]) except along rare creeping segments where most of the strain is accommodated aseismically [*Schulz et al.*, 1982; *Thatcher*, 1990; *Scholz*, 2002]. This behavior, which we refer to as the "single-mode hypothesis," is maintained in the transition from the locked to creeping sections, which are populated with isolated,

Table B1. Tectonic and Seismic Data for Oceanic Ridge Transform Faults

Fault Reference	Name	Latitude	Longitude	L, km	V_r mm/yr	m_b	m_s	m_w	ΣM_i 10^{18} N m	χ	W_{T_1} km	z_{Tmax} km	A_{T_1} km^2	A_{E_2} km^2	A_{C_2} km^2
<i>Mid-Atlantic Ridge</i>															
1	Jan Mayen	71.3	350.9	220	17.3	6.0	5.6	6.0	3.5	0.06	14.5	17.2	3148	180	52
2	Charlie Gibbs (A)	52.7	326.6	220	22.4	5.9	6.5	6.7	15.4	0.22	12.7	15.1	2762	612	288
3	Charlie Gibbs (B)	52.2	329.1	120	15.9	5.2	5.4	5.4	0.4	0.02	11.5	13.6	1430	22	12
4	Oceanographer	35.1	324.4	120	22.0	5.7	6.0	6.3	9.6	0.33	9.7	11.5	1188	387	111
5	Hayes	33.6	321.4	140	22.6	5.8	5.8	6.1	3.1	0.08	10.3	12.2	1470	120	71
6	Atlantis	30.1	317.6	80	23.6	5.8	6.0	5.5	0.2	0.01	7.7	9.2	643	8	17
7	Kane	23.8	314.4	140	25.2	6.1	6.4	6.4	10.0	0.26	9.6	11.4	1339	353	147
8	15°20'	15.4	314.2	200	26.4	5.8	4.9	5.4	0.2	0.00	11.4	13.5	2323	8	14
9	Vema	10.9	317.7	330	28.2	6.1	6.9	6.9	53.2	0.37	14.0	16.6	4573	1679	462
10	Doldrums	7.6	323.1	650	29.3	6.3	7.0	7.0	51.0	0.12	19.3	22.9	12562	1549	565
11	St Paul	0.6	332.4	540	31.9	6.1	6.5	6.6	40.1	0.12	16.9	20.1	9225	1119	236
12	Romanche	-0.3	339.4	920	32.5	6.2	6.7	7.1	195.0	0.27	21.8	25.9	20058	5327	700
13	Chain	-1.2	345.5	320	33.0	6.3	7.0	6.8	56.4	0.38	12.7	15.1	4050	1521	354
14	Ascension	-11.7	346.3	160	35.0	5.3	6.1	6.2	4.2	0.08	8.6	10.3	1350	108	93
15	MAR 35S	-35.4	343.5	240	35.5	6.0	6.4	6.6	36.6	0.37	10.6	12.6	2503	916	221
16	Falkland	-47.2	348.1	250	33.4	5.3	5.9	6.0	2.6	0.02	11.2	13.3	2810	70	58
<i>Juan De Fuca</i>															
17	Blanco	43.8	231.5	360	59.4	6.1	6.3	6.4	23.3	0.10	10.1	12.0	3660	348	149
<i>East Pacific Rise</i>															
18	Rivera	19.0	252.6	460	71.2	6.1	6.8	6.9	70.4	0.18	10.4	12.4	4771	880	440
19	Orozco	15.2	255.0	90	86.5	5.1	5.1	5.6	0.3	0.01	4.2	5.0	384	4	24
20	Clipperton ^a	10.2	256.0	90	105.3	5.7	6.5	6.6	19.8	0.53	3.7	4.4	313	167	213
21	Siquiros	8.4	256.5	150	111.9	5.2	5.7	5.9	5.3	0.06	4.7	5.6	712	42	43
22	Quebrada	-3.8	256.8	120	137.4	5.2	5.3	5.6	0.7	0.01	3.9	4.6	474	5	23
23	Discovery ^a	-4.0	255.8	70	137.9	5.1	5.8	6.0	6.3	0.19	3.0	3.5	214	41	56
24	Gofar	-4.5	254.6	190	138.8	5.9	5.9	6.2	16.9	0.12	4.8	5.7	902	108	86
25	Yaquina ^a	-6.2	252.8	60	141.4	5.1	5.2	5.5	0.5	0.02	2.6	3.0	142	3	18
26	Wilkes	-9.0	251.0	200	145.0	5.3	5.7	5.9	3.1	0.02	4.8	5.7	954	19	42
27	Garrett	-13.4	248.2	120	149.8	5.3	5.8	5.8	3.5	0.05	3.7	4.3	434	20	35
<i>Chile Rise</i>															
28	Chile	-35.5	256.8	1120	58.8	5.8	6.6	6.7	88.7	0.07	17.9	21.3	20064	1342	296
29	Valdivia	-41.5	271.2	530	60.0	5.6	5.5	5.9	4.6	0.01	12.1	14.4	6379	69	44
<i>Pacific Antarctic Ridge</i>															
30	Menard	-49.6	244.7	210	90.5	5.9	6.1	6.4	20.0	0.15	6.3	7.5	1347	197	142
31	Vaquier ^a	-53.1	241.8	80	87.2	5.3	5.6	5.8	2.2	0.07	4.0	4.7	322	22	34
32	Raitt	-54.5	240.5	140	85.8	5.6	5.9	6.0	2.4	0.03	5.3	6.3	756	25	58
33	Heezen	-55.7	235.5	350	83.8	5.7	6.3	6.4	27.4	0.10	8.4	9.9	2927	291	139
34	Tharp	-54.6	229.0	430	83.5	5.6	6.1	6.2	19.8	0.05	9.3	11.0	3991	211	95
35	Hollister	-54.4	223.9	120	82.5	5.6	6.5	6.4	16.6	0.31	4.9	5.8	577	179	146
36	Herron ^a	-56.5	220.8	60	79.7	5.5	5.7	5.9	1.2	0.07	3.5	4.2	210	14	42
37	Udintsev	-56.5	217.6	270	78.8	5.8	6.0	6.4	16.0	0.09	7.6	9.0	2034	181	141
<i>America Antarctic Ridge</i>															
38	Bullard (A)	-59.1	342.8	90	17.2	5.4	5.5	5.8	1.8	0.11	9.3	11.0	822	94	37
39	Bullard (B)	-58.2	348.1	510	17.5	6.0	6.2	6.4	17.2	0.08	22.1	26.3	11334	872	144
40	Conrad	-55.7	356.7	190	18.5	5.7	6.4	6.7	17.0	0.33	13.1	15.6	2480	816	290
<i>South West Indian Ridge</i>															
41	Bouvet	-54.2	1.9	200	13.8	5.8	6.5	6.6	11.3	0.24	15.4	18.3	3017	730	210
42	Islas Orcadas	-54.2	6.1	110	14.0	5.8	5.6	5.6	0.5	0.02	11.5	13.7	1266	29	22
43	Shaka	-53.5	9.3	210	14.1	5.7	5.9	6.4	6.4	0.12	15.9	18.9	3393	403	137
44	Du Toit	-53.0	25.5	120	14.6	5.2	5.9	6.2	3.8	0.17	11.7	13.9	1378	228	95
45	Andrew Bain	-50.1	30.0	650	14.6	6.8	6.7	6.4	13.6	0.05	27.4	32.6	17944	826	150
46	Marion	-46.6	33.7	120	14.7	5.4	5.6	5.8	0.6	0.03	11.5	13.6	1323	36	34
47	Prince Edward	-45.4	35.1	160	14.7	5.5	5.5	5.9	1.5	0.04	13.7	16.3	2264	92	41
48	Eric Simpson ^a	-43.5	39.3	60	14.8	5.5	6.4	6.7	14.0	1.79	8.1	9.6	469	839	270
49	Discovery II (A)	-43.4	41.6	140	14.8	5.4	5.9	6.4	10.1	0.36	12.4	14.7	1682	606	139
50	Discovery II (B)	-41.9	42.5	190	14.8	5.7	6.2	6.7	14.7	0.31	14.7	17.5	2831	883	288
51	Indomed	-39.5	46.1	120	14.8	5.9	5.8	5.8	1.7	0.07	11.8	14.1	1461	101	38
52	Atlantis II	-32.8	57.0	200	14.6	5.7	5.8	5.4	0.4	0.01	5.2	18.0	3035	27	15
<i>Central Indian Ridge</i>															
53	Gemino ^a	-22.9	69.2	60	47.3	5.3	5.2	5.2	0.2	0.01	4.5	5.3	253	3	8
54	Marie Celeste	-17.4	65.9	210	40.8	5.6	6.0	6.5	40.4	0.46	9.2	10.9	1899	880	173
55	Argo	-13.7	66.3	120	37.6	5.6	5.6	6.0	3.4	0.10	7.2	8.6	838	81	50
56	CIR 12°12'	-11.9	65.7	150	35.5	6.0	6.1	6.1	3.7	0.08	8.3	9.9	1221	92	62
57	Vema II	-8.9	67.5	210	34.0	5.6	5.7	6.2	4.4	0.05	10.2	12.2	2169	116	79

Table B1. (continued)

Fault Reference	Name	Latitude	Longitude	L , km	V , mm/yr	m_b	m_s	m_w	ΣM , 10^{18} N m	χ	W_T , km	z_{max} , km	A_T , km ²	A_E , km ²	A_C , km ²
<i>Gulf of Aden</i>															
58	Alula Fartak	13.9	51.7	200	19.4	5.9	5.5	5.9	3.2	0.06	13.1	15.5	2588	147	47
59	Owen	11.5	57.5	310	23.9	6.2	6.2	6.5	29.2	0.23	14.9	17.7	4682	1085	162
<i>South East Indian Ridge</i>															
60	Ter Tholen	-33.2	77.8	100	65.2	5.5	5.4	5.2	0.1	0.00	5.1	6.1	518	2	9
61	Zeewolf ^a	-35.4	78.5	70	66.4	5.0	4.9	5.3	0.2	0.01	4.1	4.9	272	3	11
62	Amsterdam	-36.6	78.6	80	67.0	5.7	6.0	6.1	8.3	0.29	4.6	5.5	386	110	67
63	Boomerang ^a	-37.4	78.2	40	67.2	5.2	6.0	5.7	0.6	0.05	3.3	3.9	139	7	29
64	Hillegom's Hole ^a	-38.5	78.6	40	67.8	5.7	6.3	6.4	9.8	0.97	3.2	3.8	132	128	150
65	Vlamingh	-41.5	80.2	140	69.4	5.8	6.3	6.4	21.5	0.35	5.7	6.8	777	275	154
66	Geelvinck	-41.7	85.0	150	70.8	5.6	5.3	5.4	0.6	0.01	5.9	7.1	888	8	15
67	SEIR 88E	-42.0	88.3	90	71.7	5.4	5.7	5.7	1.3	0.04	4.5	5.4	401	16	30
68	SEIR 96E (A) ^a	-45.6	96.1	70	73.9	5.8	6.2	6.3	9.7	0.42	4.0	4.7	281	117	100
69	SEIR 96E (B) ^a	-46.5	95.9	50	74.0	5.3	5.7	5.7	1.6	0.12	3.3	3.9	156	20	27
70	SEIR 100E	-47.8	99.8	130	74.7	5.5	6.3	6.4	13.3	0.23	5.4	6.4	686	159	139
71	SEIR 107E	-48.8	106.5	130	75.3	5.2	5.2	5.5	0.4	0.01	5.4	6.4	705	5	16
72	SEIR 114E ^a	-50.0	114.1	70	75.4	5.3	5.4	5.4	0.4	0.02	4.0	4.7	277	4	15
73	Euroka	-49.2	126.1	120	74.6	5.3	5.6	5.5	1.0	0.02	5.3	6.3	657	12	19
74	Birubi	-49.3	127.4	130	74.4	5.6	5.0	5.4	0.3	0.01	5.5	6.5	723	4	14
75	George V	-52.0	139.8	480	72.0	5.9	6.4	6.5	42.8	0.10	10.6	12.6	5071	528	191
76	SEIR 143E	-54.5	143.8	100	71.0	5.4	5.8	5.8	4.3	0.11	4.9	5.9	511	54	37
77	Tasman	-57.8	147.7	690	70.1	5.8	6.4	6.5	60.9	0.09	12.8	15.2	8773	772	195
78	Balleny	-61.5	154.4	350	69.0	5.7	6.7	6.7	64.3	0.25	9.3	11.0	3275	829	270
Total	-	-	-	17,230	-	-	-	-	1270	-	-	-	215,978	30,186	9646

^aRTF has been excluded from general analysis because $L < 75$ km or $A_T < 350$ km².

fully coupled patches surrounded by continuously creeping material [e.g., *Lindh and Boore*, 1981; *Harris and Segall*, 1987; *Nadeau and Johnson*, 1998; *Sammis and Rice*, 2001; *Waldhauser and Ellsworth*, 2002]. Slow strain transients with time constants of hours to days (silent earthquakes) do occur, but they are small and infrequent and appear to be associated with the creeping parts [*Gladwin et al.*, 1994; *Linde et al.*, 1996; *Thurber and Sessions*, 1998]. Slow earthquakes (seismic events with anomalous low-frequency excitation suggestive of low rupture velocities) are also rare [*Kanamori and Hauksson*, 1992; *Ihmlé and Jordan*, 1994]; the large events that have been studied in detail show rupture velocities that approach (or sometimes exceed) the shear wave speed [e.g., *Aki*, 1968; *Beroza*, 1991; *Wald et al.*, 1996; *Bouchon et al.*, 2000]. Fault area is fractally distributed within the volume of continental crust [*Turcotte*, 1986; *Aviles et al.*, 1987; *King et al.*, 1988; *Hirata*, 1989; *Power and Tullis*, 1995; *Ouilleon et al.*, 1996]; as the displacement increases, this distribution evolves through a process of strain localization to produce smoother, longer faults with larger characteristic earthquakes [*Wesnousky*, 1990; *Stirling et al.*, 1996]. According to this hypothesis, geologic structure plays a dominant role in determining earthquake complexity. This complexity is reflected in aftershock sequences, which follow a modified version of Omori's law [*Utsu*, 1961; *Reasenber and Jones*, 1989; *Kisslinger and Jones*, 1991] and conform to Båth's law, namely, that the largest aftershock is about 1.2 magnitude units lower than the main shock [*Båth*, 1965; *Felzer et al.*, 2002; *Helmstetter and Sornette*, 2003a]. The largest earthquakes result from event cascades that involve the propagation of faulting across segment boundaries and are thus larger than the characteristic earthquakes for individual segments [*Jackson*, 1996; *Ward*, 1997]. The best data indicate that the slip displacement D scales with the rupture length L and width W as $S = \sqrt{LW}$ (the self-similar or

S model), even for large earthquakes that rupture through the entire seismogenic zone [*Mai and Beroza*, 2000; *P. Somerville*, personal communication, 2003].

Appendix B: RTF Tectonic Parameters and Seismic Data

[65] Table B1 is a compilation of observed and calculated measures of RTF location, size, and seismicity. Latitude and longitude values indicate the midpoint of each RTF. V was calculated from the NUVEL-1 plate velocity model [*DeMets et al.*, 1990]. Magnitudes are the maximum value reported in the 36 year (1964–1999) ISC catalog (for m_b and m_s data), or the 25.5 year (June 1976 to January 2002) CMT catalog (for m_w data). ΣM indicates the total moment release reported by the CMT catalog for each RTF. The reference isotherm $T_{ref} = 600^\circ\text{C}$ was used to compute χ , W_T , z_{max} , and A_T . A stress drop of $\Delta\sigma = 3$ MPa was assumed in the calculation of A_C . Faults were split into multiple segments if there was an offset ≥ 35 km.

Appendix C: Scaling of Seismic Parameters With L and V

[66] Figures C1–C3 display how the seismicity parameters total moment release ΣM , upper cutoff earthquake moment M_C , and seismic productivity ν_0 are distributed with the tectonic parameters fault length L and slip rate V . The diamonds correspond to the maximum likelihood estimates derived from the binned Harvard CMT data with $m_0 = 5.6$ and $\beta = 2/3$; the circles are the observations for individual RTFs. In calculating the ordinate values for the maximum likelihood estimates, we weighted the individual faults by their theoretical moment rates, which are proportional to VA_T . In comparisons with the maximum likelihood estimates of M_C , we used the largest seismic moment

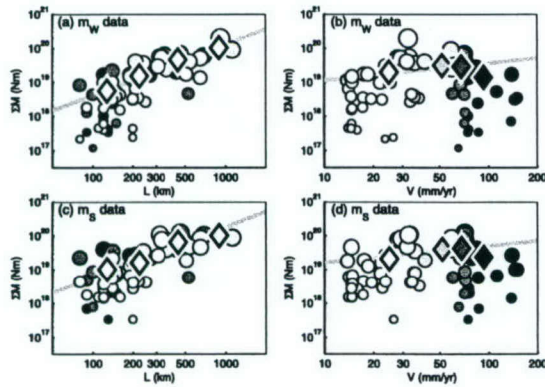


Figure C1. (left) Total seismic moment ΣM versus fault length L and (right) slip rate V for (top) the Harvard CMT catalog and (bottom) recalibrated ISC m_S catalog. Points show cumulative moments for individual RTFs (circles) and maximum likelihood estimates obtained by fitting equation (4) to the binned data (diamonds). The data bins, as well as the circle sizes and shading, are given in Figure 5. The abscissa values for the diamonds are the averages of L and V in each bin weighted by the plate tectonic moment release rate $\mu A_T V$. Solid lines correspond to the model scaling relation, $\Sigma M \sim L^{3/2} V^{1/2}$ (Table 1).

observed on an individual RTF. The maximum likelihood estimates of the seismic parameters show systematic correlations with fault length, and less convincing trends with slip velocity. As discussed in the text, a proper interpretation

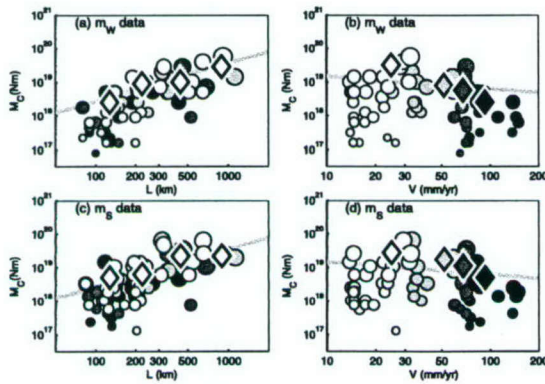


Figure C2. Upper cutoff moment M_C versus (left) fault length L and (right) slip rate V for (top) the Harvard CMT catalog and (bottom) recalibrated ISC m_S catalog. Points show the largest earthquakes for individual RTFs (circles) and maximum likelihood estimates obtained by fitting equation (4) to the binned data (diamonds). The data bins, as well as the circle sizes and shading, are given in Figure 5. The abscissa values for the diamonds are the averages of L and V in each bin weighted by the plate tectonic moment release rate $\mu A_T V$. Solid lines correspond to the model scaling relation, $M_C \sim L^{9/8} V^{-3/8}$, given in Table 1.

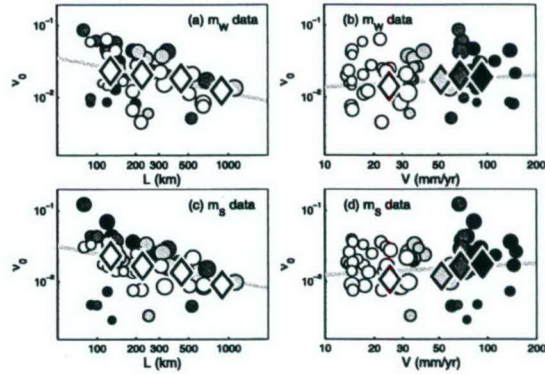


Figure C3. Seismic productivity, $\nu_0 = \dot{N}_0 M_0 / (\mu V A_T)$, versus (left) fault length L and (right) slip rate V for (top) the Harvard CMT catalog and (bottom) recalibrated ISC m_S catalog. Points show normalized event counts for individual RTFs (circles) and maximum likelihood estimates obtained by fitting equation (4) to the binned data (diamonds). The data bins, as well as the circle sizes and shading, are given in Figure 5. The ν_0 values from both catalogs have been normalized to a threshold moment magnitude of $m_0 = 5.6$. The abscissa values for the diamonds are the averages of L and V in each bin weighted by the plate tectonic moment release rate $\mu A_T V$. Solid lines correspond to the model scaling relation, $\nu_0 \sim L^{-3/8} V^{1/8}$ (Table 1).

of these relationships must account for any covariance of L and V .

Notation

- A_C upper cutoff area (M_C rupture area).
- A_E effective seismic area (area displaced by the observed moment release rate per unit tectonic slip).
- A_S total fault area from which seismic moment is released.
- A_T thermal area above isotherm T_{ref} .
- b slope of Gutenberg-Richter distribution.
- D_C average slip of upper cutoff earthquake.
- ΣD cumulative slip.
- L fault length.
- L_C fault length ruptured by M_C .
- L_S effective seismic zone length (A_S/W_S).
- m_b body wave magnitude.
- m_C upper cutoff magnitude.
- m_{main} main shock magnitude.
- m_S surface wave magnitude.
- m_W moment magnitude.
- m_0 catalog completeness threshold magnitude.
- m_Σ cumulative moment magnitude.
- Δm_{after} magnitude decrement of largest probable after-shock.
- M earthquake moment.
- \dot{M} moment release rate.
- M_C upper cutoff moment (largest probable earthquake).
- M_0 catalog completeness threshold moment.

ΔM_k	moment width of the k th bin.
ΣM	total moment release.
n	ETAS branching ratio.
n_k	number of events in the k th bin.
N	cumulative number of earthquakes.
N_{after}	number of aftershocks with $m_0 \leq m \leq m_{\text{main}}$.
N_0	number of events above M_0 .
\bar{N}_0	average N_0 per unit time.
Δt_{cat}	duration of earthquake catalog.
T_0	mantle potential temperature.
T_{ref}	temperature of a reference isotherm.
V	tectonic slip rate.
W_C	down-dip width ruptured by M_C .
W_E	effective seismic width (A_E/L).
W_S	down-dip width of A_S .
W_T	average depth to T_{ref} (A_T/L).
x	along strike position.
z	down-dip position.
z_{max}	maximum depth to T_{ref} .
α	ETAS parameter describing aftershock rate changes with m_{main} .
β	low moment slope of the moment-frequency distribution ($\beta = 2/3b$).
γ	A_C to A_T scaling exponent.
ζ	nondimensional depth.
η	scale factor between W_C and W_T .
κ	thermal diffusivity.
λ	slip scaling exponent.
μ	shear modulus.
ν_0	seismic productivity.
ξ	nondimensional length.
$\Delta\sigma$	stress drop.
$\Delta\hat{\sigma}$	constant stress drop value.
χ	seismic coupling coefficient.
ψ	A_E to A_T scaling exponent.

[67] **Acknowledgments.** We thank J. McGuire and G. Hirth for helpful discussions. Comments from reviewers R. Abercrombie, D. Forsyth, and C. Frohlich helped to clarify the paper. M.B. was supported by a NSF Graduate Research Fellowship, a MIT Presidential Fellowship, and the WHOI DOEI Fellowship. This research was supported by the Southern California Earthquake Center. SCEC is funded by NSF Cooperative Agreement EAR-0106924 and USGS Cooperative Agreement 02HQAG0008. This is SCEC contribution 768 and the Woods Hole Oceanographic Institution contribution 11132.

References

- Abercrombie, R., and G. Ekström (2001), Earthquake slip on oceanic transform faults, *Nature*, **410**, 74–77.
- Abercrombie, R. E., and G. Ekström (2003), A reassessment of the rupture characteristics of oceanic transform earthquakes, *J. Geophys. Res.*, **108**(B5), 2225, doi:10.1029/2001JB000814.
- Aki, K. (1956), Some problems in statistical seismology, *J. Seismol. Soc. Jpn.*, **8**, 205–228.
- Aki, K. (1965), Maximum likelihood estimate of b in the formula $\log n = a - bm$ and its confidence limits, *Bull. Earthquake Res. Inst. Univ. Tokyo*, **43**, 237–239.
- Aki, K. (1968), Seismic displacements near a fault, *J. Geophys. Res.*, **73**, 5959–5976.
- Allen, C. R. (1968), The tectonic environments of seismically active and inactive areas along the San Andreas Fault system, in *Proceedings of a Conference on the Geologic Problems of the San Andreas Fault System*, pp. 70–82, Stanford Univ. Press, Stanford, Calif.
- Anderson, J. G., and J. E. Luco (1983), Consequences of slip rate constraints on earthquake occurrence relation, *Bull. Seismol. Soc. Am.*, **73**, 471–496.
- Aviles, C. A., C. H. Scholz, and J. Boatwright (1987), Fractal analysis applied to characteristic segments of the San Andreas Fault, *J. Geophys. Res.*, **92**, 331–344.
- Báth, M. (1965), Lateral inhomogeneities in the upper mantle, *Tectonophysics*, **2**, 483–514.
- Behn, M. D., J. Lin, and M. T. Zuber (2002), Evidence for weak oceanic transform faults, *Geophys. Res. Lett.*, **29**(24), 2207, doi:10.1029/2002GL015612.
- Bender, B. (1983), Maximum likelihood method estimation of b values for magnitude grouped data, *Bull. Seismol. Soc. Am.*, **73**, 831–851.
- Bergman, E. A., and S. C. Solomon (1988), Transform fault earthquakes in the North Atlantic: Source mechanisms and depth of faulting, *J. Geophys. Res.*, **93**, 9027–9057.
- Beroza, G. (1991), Near-source modeling of the Loma Prieta earthquake: Evidence for heterogeneous slip and implications for earthquake hazard, *Bull. Seismol. Soc. Am.*, **81**, 1603–1621.
- Beroza, G. C., and T. H. Jordan (1990), Searching for slow and silent earthquakes using free oscillations, *J. Geophys. Res.*, **95**, 2485–2510.
- Bird, P., Y. Y. Kagan, and D. D. Jackson (2002), Plate tectonics and earthquake potential of spreading ridges and oceanic transform faults, in *Plate Boundary Zones, Geodyn. Ser.*, vol. 30, edited by S. Stein and J. T. Freymueller, pp. 203–218, AGU, Washington, D. C.
- Bodin, P., and J. M. Brune (1996), On the scaling of slip with rupture length for shallow strike-slip earthquakes: Quasi-static models and dynamic rupture propagation, *Bull. Seismol. Soc. Am.*, **86**, 1292–1299.
- Boettcher, M. S., G. Hirth, and B. Evans (2003), Olivine friction at the base of the seismogenic zone, *Eos Trans. AGU*, **84**(46), Fall Meet. Suppl., Abstract T41C-0231.
- Bohnenstiehl, D. R., M. Tolstoy, R. P. Dziak, C. G. Fox, and D. K. Smith (2002), Aftershock sequences in the mid-ocean ridge environment: An analysis using hydroacoustic data, *Tectonophysics*, **354**, 49–70.
- Bohnenstiehl, D. R., M. Tolstoy, and E. Chapp (2004), Breaking into the plate: A 7.6 M_w fracture-zone earthquake adjacent to the Central Indian Ridge, *Geophys. Res. Lett.*, **31**, L02615, doi:10.1029/2003GL018981.
- Bonatti, E., M. Ligi, L. Gasperini, A. Peyve, Y. Raznitsin, and Y. Chen (1994), Transform migration and vertical tectonics at the Romanche fracture zone, equatorial Atlantic, *J. Geophys. Res.*, **99**, 21,779–21,802.
- Bouchon, M., N. Toksoz, H. Karabulut, M.-P. Bouin, M. Dietrich, M. Aktar, and M. Edie (2000), Seismic imaging of the Izmit rupture inferred from near-fault recordings, *Geophys. Res. Lett.*, **27**, 3013–3016.
- Bowan, J., and R. S. White (1994), Variation with spreading rate of oceanic crustal thickness and geochemistry, *Earth Planet. Sci. Lett.*, **121**, 435–449.
- Brune, J. N. (1968), Seismic moment, seismicity, and rate of slip along major fault zones, *J. Geophys. Res.*, **73**, 777–784.
- Burr, N. C., and S. C. Solomon (1978), The relationship of source parameters of oceanic transform earthquakes to plate velocity and transform length, *J. Geophys. Res.*, **83**, 1193–1205.
- Cande, S., J. LaBrecque, R. Larson, W. Pitman III, X. Golovchenko, and W. Haxby (1989), Magnetic lineations of world's ocean basins (map), technical report, Am. Assoc. of Pet. Geol., Tulsa, Okla.
- Cannat, M., et al. (1995), Thin crust, ultramafic exposures, and rugged faulting patterns at the Mid-Atlantic Ridge (22°–24°N), *Geology*, **23**, 49–52.
- Cowie, P. A. (1998), Normal fault growth in three-dimensions in continental and oceanic crust, in *Faulting and Magmatism at Mid-Ocean Ridges*, *Geophys. Monogr. Ser.*, vol. 106, edited by W. R. Buck et al., pp. 325–348, AGU, Washington, D. C.
- Cowie, P. A., and C. H. Scholz (1992), Physical explanation for displacement-length relationship for faults using a post-yield fracture mechanics model, *J. Struct. Geol.*, **14**, 1133–1148.
- Davies, G. F., and J. N. Brune (1971), Regional and global fault slip rates from seismicity, *Nature Phys. Sci.*, **229**, 101–107.
- DeMets, C., R. G. Gordon, D. F. Angus, and S. Stein (1990), Current plate motions, *Geophys. J. Int.*, **101**, 425–478.
- Dragert, H., K. Wang, and T. S. James (2001), A silent slip event on the deeper Cascadia subduction interface, *Science*, **292**, 1525–1528.
- Dziak, R. P., C. G. Fox, and R. W. Embley (1991), Relationship between the seismicity and the geologic structure of the Blanco Transform Fault Zone, *Mar. Geophys. Res.*, **13**(3), 203–208.
- Dziak, R., C. Fox, R. Embley, J. Lupton, G. Johnson, W. Chadwick, and R. Koski (1996), Detection of and response to a probable volcanogenic T -wave event swarm on the western Blanco Transform Fault Zone, *Geophys. Res. Lett.*, **23**, 873–876.
- Dziak, R. P., C. Fox, R. Embley, J. Nabelek, J. Braunmiller, and R. Koski (2000), Recent tectonics of the Blanco Ridge, eastern Blanco Transform Fault Zone, *Mar. Geophys. Res.*, **21**(5), 423–450.
- Dziewonski, A. M., and D. L. Anderson (1981), Preliminary Reference Earth Model, *Phys. Earth Planet. Inter.*, **25**, 297–356.
- Ekström, G., and A. M. Dziewonski (1988), Evidence of bias in estimations of earthquake size, *Nature*, **332**, 319–323.
- Elliott, D. (1976), The energy balance and deformation mechanisms of thrust sheets, *Philos. Trans. R. Soc. London, Ser. A*, **283**, 289–312.

- Embley, R. W., and D. S. Wilson (1992), Morphology of the Blanco Transform Fault Zone-NE Pacific—Implications for its tectonic evolution, *Mar. Geophys. Res.*, **14**(1), 25–45.
- Engeln, J. F., D. A. Weins, and S. Stein (1986), Mechanisms and depths of Atlantic transform earthquakes, *J. Geophys. Res.*, **91**, 548–577.
- Felzer, K. R., T. W. Becker, R. E. Abercrombie, G. Ekström, and J. R. Rice (2002), Triggering of the 1999 M_w 7.1 Hector Mine earthquake by aftershocks of the 1992 M_w 7.3 Landers earthquake, *J. Geophys. Res.*, **107**(B9), 2190, doi:10.1029/2001JB000911.
- Forsyth, D. W., Y. Yang, M. Mangriotis, and Y. Shen (2003), Coupled seismic slip on adjacent oceanic transform faults, *Geophys. Res. Lett.*, **30**(12), 1618, doi:10.1029/2002GL016454.
- Francis, T. J. G. (1968), The detailed seismicity of mid-ocean ridges, *Earth Planet. Sci. Lett.*, **4**(1), 39–46.
- Frohlich, C., and K. D. Apperson (1992), Earthquake focal mechanisms, moment tensors, and the consistency of seismic activity near plate boundaries, *Tectonics*, **11**(2), 279–296.
- Frohlich, C., and S. Davis (1993), Teleseismic b values; or, much ado about 1.0, *J. Geophys. Res.*, **98**, 631–644.
- Gardner, J., and L. Knopoff (1974), Is the sequence of earthquakes in southern California, with aftershocks removed, Poissonian?, *Bull. Seismol. Soc. Am.*, **64**, 1363–1367.
- Gladwin, M. T., R. L. Gwyther, R. H. G. Hart, and K. S. Breckenridge (1994), Measurements of the strain field associated with episodic creep events on the San Andreas Fault at San Juan Bautista, California, *J. Geophys. Res.*, **99**, 4559–4565.
- Guo, Z., and Y. Ogata (1997), Statistical relations between the parameters of aftershocks in time, space, and magnitude, *J. Geophys. Res.*, **102**, 2857–2873.
- Hanks, T. C., and W. H. Bakun (2002), A bilinear source-scaling model for $m - \log a$ observations, *Bull. Seismol. Soc. Am.*, **92**, 1841–1846.
- Harris, R. A., and P. Segall (1987), Detection of a locked zone at depth on the Parkfield, California, segment of the San Andreas Fault, *J. Geophys. Res.*, **92**, 7945–7962.
- Heki, K., S. Miyazake, and H. Tsuji (1997), Silent fault slip following an interplate thrust earthquake at the Japan trench, *Nature*, **386**, 595–598.
- Helmstetter, A. (2003), Is earthquake triggering driven by small earthquakes?, *Phys. Rev. Lett.*, **91**(5), doi:10.1103/PhysRevLett.91.058501.
- Helmstetter, A., and D. Sornette (2002), Subcritical and supercritical regimes in epidemic models of earthquake aftershocks, *J. Geophys. Res.*, **107**(B10), 2237, doi:10.1029/2001JB001580.
- Helmstetter, A., and D. Sornette (2003a), Bath's law derived from the Gutenberg-Richter law and from aftershock properties, *Geophys. Res. Lett.*, **30**(20), 2069, doi:10.1029/2003GL018186.
- Helmstetter, A., and D. Sornette (2003b), Importance of direct and indirect triggered seismicity in the ETAS model of seismicity, *Geophys. Res. Lett.*, **30**(11), 1576, doi:10.1029/2003GL017670.
- Hirata, T. (1989), Fractal dimension of fault systems in Japan: Fractal structure in rock fracture geometry at various scales, *Pure Appl. Geophys.*, **131**, 157–170.
- Hirose, H., K. Hirahara, F. Kimata, N. Fujii, and S.-I. Miyazake (1999), A slow thrust slip event following the two 1996 Hyuganada earthquakes beneath the Bungo Channel, southwest Japan, *Geophys. Res. Lett.*, **26**, 3237–3240.
- Hyndman, R. D., and D. H. Weichert (1983), Seismicity and rates of relative plate motion on the plate boundaries of western North America, *Geophys. J. R. Astron. Soc.*, **72**, 59–82.
- Ihmlé, P. F., and T. H. Jordan (1994), Teleseismic search for slow precursors to large earthquakes, *Science*, **266**, 1547–1551.
- Ihmlé, P. F., P. Harabaglia, and T. H. Jordan (1993), Teleseismic detection of a slow precursor to the Great 1989 Macquarie Ridge earthquake, *Science*, **261**, 177–182.
- Jackson, D. D. (1996), The case for huge earthquakes, *Seismol. Res. Lett.*, **67**(1), 3–5.
- Kagan, Y. Y. (1991), Seismic moment distribution, *Geophys. J. Int.*, **106**, 123–134.
- Kagan, Y. Y. (1993), Statistics of characteristic earthquakes, *Bull. Seismol. Soc. Am.*, **83**, 7–24.
- Kagan, Y. Y. (2002a), Seismic moment distribution revisited: I. Statistical results, *Geophys. J. Int.*, **148**, 520–541.
- Kagan, Y. Y. (2002b), Seismic moment distribution revisited: II. Moment conservation principle, *Geophys. J. Int.*, **149**, 731–754.
- Kagan, Y. Y., and D. D. Jackson (2000), Probabilistic forecasting of earthquakes, *Geophys. J. Int.*, **143**, 438–453.
- Kagan, Y. Y., and L. Knopoff (1991), Stochastic synthesis of earthquake catalogs, *J. Geophys. Res.*, **96**, 2853–2862.
- Kagan, Y. Y., and S. Wesnously (1996), The Gutenberg-Richter or characteristic earthquake distribution, Which is it? Discussion and reply, *Bull. Seismol. Soc. Am.*, **86**, 274–291.
- Kanamori, H. (1977), The energy release in great earthquakes, *J. Geophys. Res.*, **82**, 2981–2987.
- Kanamori, H., and J. J. Cipar (1974), Focal process of the Great Chilean earthquake May 22, 1960, *Phys. Earth Planet. Inter.*, **9**, 128–136.
- Kanamori, H., and E. Hauksson (1992), A slow earthquake in the Santa Maria basin, California, *Bull. Seismol. Soc. Am.*, **82**, 2087–2096.
- Kanamori, H., and G. Stewart (1976), Mode of strain release along the Gibbs Fracture Zone, Mid-Atlantic Ridge, *Phys. Earth Planet. Inter.*, **11**, 312–332.
- Kawaski, I., Y. Kawahara, I. Takata, and N. Kosugi (1985), Mode of seismic moment release at transform faults, *Tectonophysics*, **118**, 313–327.
- King, G. C. P., R. S. Stein, and J. B. Rundle (1988), The growth of geological structures by repeated earthquakes: 1. Conceptual framework, *J. Geophys. Res.*, **93**, 13,307–13,318.
- Kiratzis, A. A. (1993), A study on the active crustal deformation of the North and East Anatolian fault zones, *Tectonophysics*, **225**, 191–203.
- Kisslinger, C., and L. M. Jones (1991), Properties of aftershock sequences in southern California, *J. Geophys. Res.*, **96**, 11,947–11,958.
- Knopoff, L. (1964), Statistics of earthquakes in southern California, *Bull. Seismol. Soc. Am.*, **54**, 1871–1873.
- Langenhorst, A. R., and E. A. Okal (2002), Correlation of beta-value with spreading rate for strike-slip earthquakes of the mid-oceanic ridge system, in *Plate Boundary Zones, Geodyn. Ser.*, vol. 30, edited by S. Stein and J. T. Freymueller, pp. 191–202, AGU, Washington, D. C.
- Langer, J. S., J. M. Carlson, C. R. Myers, and B. E. Shaw (1996), Slip complexity in dynamic models of earthquake faults, *Proc. Natl. Acad. Sci. U.S.A.*, **93**, 3825–3829.
- Ligi, M., E. Bonatti, L. Gasperini, and A. N. Poliakov (2002), Oceanic broad multifault transform plate boundaries, *Geology*, **30**(1), 11–14.
- Lilwall, R., and R. Kirk (1985), OBS observations on the Charlie Gibbs Fracture Zone, *Geophys. J. R. Astron. Soc.*, **80**, 195–208.
- Linde, A. T., M. T. Gladwin, M. J. Johnson, R. L. Gwyther, and R. G. Bilham (1996), A slow earthquake sequence on the San Andreas Fault, *Nature*, **383**, 65–68.
- Lindh, A. G., and D. M. Boore (1981), Control of rupture by fault geometry during the 1966 Parkfield earthquake, *Bull. Seismol. Soc. Am.*, **71**, 95–116.
- Mai, P. M., and G. Beroza (2000), Source scaling properties from finite-fault rupture models, *Bull. Seismol. Soc. Am.*, **90**, 604–615.
- Main, I. G., and P. W. Burton (1984), Information theory and the earthquake frequency-magnitude distribution, *Bull. Seismol. Soc. Am.*, **74**, 1409–1426.
- McGuire, J. J., and T. H. Jordan (2000), Further evidence for the compound nature of slow earthquakes: The Prince Edward Island earthquake of April 28, 1997, *J. Geophys. Res.*, **105**, 7819–7827.
- McGuire, J. J., P. F. Ihmlé, and T. H. Jordan (1996), Time-domain observations of a slow precursor to the 1994 Romache Transform earthquake, *Science*, **274**, 82–85.
- McGuire, J. J., T. H. Jordan, and J. Lin (2002a), Complexities of transform fault plate boundaries in the oceans, in *Plate Boundary Zones, Geodyn. Ser.*, vol. 30, edited by S. Stein and J. T. Freymueller, pp. 219–241, AGU, Washington, D. C.
- McGuire, J. J., L. Zhao, and T. H. Jordan (2002b), Predominance of unilateral rupture for a global catalog of large earthquakes, *Bull. Seismol. Soc. Am.*, **92**, 3309–3317.
- Miller, M. M., T. Melbourne, D. J. Johnson, and W. Q. Sumner (2002), Periodic slow earthquakes from the Cascadia subduction zone, *Science*, **295**, 2423.
- Molnar, P. (1979), Earthquake recurrence intervals and plate tectonics, *Bull. Seismol. Soc. Am.*, **69**, 115–133.
- Muller, J. (1983), Earthquake source parameters, seismicity, and tectonics of North Atlantic transform faults, Ph.D. thesis, Mass. Inst. of Technol., Cambridge.
- Nadeau, R., and L. R. Johnson (1998), Seismological studies at Parkfield. vi: Moment release rates and estimates of source parameters for small repeating earthquakes, *Bull. Seismol. Soc. Am.*, **88**, 790–814.
- Ogata, Y. (1983), Estimation of the parameters in the modified Omori formula for aftershock frequencies by maximum likelihood procedure, *J. Phys. Earth*, **31**, 115–124.
- Ogata, Y. (1988), Statistical models for earthquake occurrence and residual analysis for point processes, *J. Am. Stat. Assoc.*, **83**, 9–27.
- O'Hanley, D. S., J. V. Chernosky, and F. J. Wicks (1989), The stability of lizardite and chrysotile, *Can. Mineral.*, **27**, 483–493.
- Okal, E. A., and A. R. Langenhorst (2000), Seismic properties of the Eltanin Transform System, South Pacific, *Phys. Earth Planet. Inter.*, **119**, 185–208.
- Okal, E. A., and S. Stein (1987), The 1942 Southwest Indian Ocean Ridge earthquake: Largest ever recorded on an oceanic transform, *Geophys. Res. Lett.*, **14**, 147–150.
- Okal, E. A., and L. M. Stewart (1982), Slow earthquakes along oceanic fracture zones: evidence for asthenospheric flow away from hotspots?, *Earth Planet. Sci. Lett.*, **57**, 75–87.

- Oppenheimer, D., et al. (1993), The Cape Mendocino, California, earthquakes of April 1992: Subduction at the triple junction, *Science*, **261**, 433–438.
- Ouilleon, G., C. Castaing, and D. Sornette (1996), Hierarchical geometry of faulting, *J. Geophys. Res.*, **101**, 5477–5487.
- Pegler, G., and S. Das (1996), Analysis of the relationship between seismic moment and fault length for large crustal strike-slip earthquakes between 1977–92, *Geophys. Res. Lett.*, **23**, 905–908.
- Pinkston, J., and S. H. Kirby (1982), Experimental deformation of dunite under conditions appropriate to the lithosphere, *Eos Trans. AGU*, **63**, 1094.
- Pockalny, R., R. Detrick, and P. Fox (1988), Morphology and tectonics of the Kane transform from Sea Beam bathymetry data, *J. Geophys. Res.*, **93**, 3907–3939.
- Pockalny, R. A., P. J. Fox, D. J. Fornari, K. C. Macdonald, and M. R. Perfit (1997), Tectonic reconstruction of the Clipperton and Siqueiros Fracture Zones: Evidence and consequences of plate motion change for the last 3 Myr, *J. Geophys. Res.*, **102**, 3167–3181.
- Power, W. L., and T. E. Tullis (1995), A review of the fractal character of natural fault surfaces with implications for friction and the evolution of fault zones, in *Fractals in the Earth Sciences*, edited by P. Lapointe and C. Barton, pp. 89–105, Plenum, New York.
- Reasenber, P. A., and L. M. Jones (1989), Earthquake hazard after a mainshock in California, *Science*, **243**, 1173–1176.
- Reinen, L. A. (2000a), Slip styles in a spring-slider model with a laboratory-derived constitutive law for serpentinite, *Geophys. Res. Lett.*, **27**, 2037–2040.
- Reinen, L. A. (2000b), Seismic and aseismic slip indicators in serpentinite gouge, *Geology*, **28**(2), 135–138.
- Reinen, L. A., J. D. Weeks, and T. E. Tullis (1994), The frictional behavior of lizardite and antigorite serpentinites: Experiments, constitutive models, and implications for natural faults, *Pure Appl. Geophys.*, **143**, 317–385.
- Rice, J. R. (1993), Spatiotemporal complexity of slip on a fault, *J. Geophys. Res.*, **98**, 9885–9907.
- Romanowicz, B. (1992), Strike-slip earthquakes on quasi-vertical transcurrent faults: Inferences for general scaling relations, *Geophys. Res. Lett.*, **19**(5), 481–484.
- Romanowicz, B. (1994), Comment on “A reappraisal of large earthquake scaling” by C. Scholz, *Bull. Seismol. Soc. Am.*, **84**, 1675–1676.
- Romanowicz, B., and L. J. Ruff (2002), On moment-length scaling of large strike slip earthquakes and the strength of faults, *Geophys. Res. Lett.*, **29**(12), 1604, doi:10.1029/2001GL014479.
- Rundquist, D., and P. Sobolev (2002), Seismicity of mid-ocean ridges and its geodynamic implications: A review, *Earth Sci. Rev.*, **58**, 143–161.
- Sacks, I., S. Suyehiro, A. T. Linde, and J. A. Snoke (1978), Slow earthquakes and stress redistribution, *Nature*, **275**, 599–602.
- Sammis, C. G., and J. R. Rice (2001), Repeating earthquakes as low-stress-drop events at a border between locked and creeping fault patches, *Bull. Seismol. Soc. Am.*, **91**, 532–537.
- Scholz, C. H. (1982), Scaling laws for large earthquakes: Consequences for physical models, *Bull. Seismol. Soc. Am.*, **72**, 1–14.
- Scholz, C. H. (1994a), A reappraisal of large earthquake scaling, *Bull. Seismol. Soc. Am.*, **84**, 215–218.
- Scholz, C. H. (1994b), Reply to comments on “A reappraisal of large earthquake scaling” by C. Scholz, *Bull. Seismol. Soc. Am.*, **84**, 1677–1678.
- Scholz, C. H. (2002), *The Mechanics of Earthquakes and Faulting*, 2nd ed., Cambridge Univ. Press, New York.
- Schulz, S. S., G. M. Mavko, R. O. Burford, and W. D. Stuart (1982), Long-term fault creep observations in central California, *J. Geophys. Res.*, **87**, 6977–6982.
- Schwartz, D. (1996), The case against huge earthquakes, *Seismol. Res. Lett.*, **67**(3), 3–5.
- Schwartz, D. P., and K. J. Coppersmith (1984), Fault behavior and characteristic earthquakes: Examples from the Wasatch and San Andreas fault zones, *J. Geophys. Res.*, **89**, 5681–5698.
- Shaw, B. E., and J. R. Rice (2000), Existence of continuum complexity in the elastodynamics of repeated fault ruptures, *J. Geophys. Res.*, **105**, 791–810.
- Shaw, B. E., and C. H. Scholz (2001), Slip-length scaling in large earthquakes: Observations and theory and implications for earthquake physics, *Geophys. Res. Lett.*, **28**, 2991–2994.
- Shimazaki, K. (1986), Small and large earthquakes: The effects of the thickness of the seismogenic layer and the free surface, in *Earthquake Source Mechanics*, *Geophys. Monogr. Ser.*, vol. 37, edited by S. Das et al., pp. 209–216, AGU, Washington, D. C.
- Sibson, R. H. (1983), Continental fault structure and the shallow earthquake source, *J. Geol. Soc. London*, **140**, 741–767.
- Sleep, N. H. (1975), Formation of the oceanic crust: Some thermal constraints, *J. Geophys. Res.*, **80**, 4037–4042.
- Smith, D. K., and T. H. Jordan (1988), Seamount statistics in the Pacific Ocean, *J. Geophys. Res.*, **93**, 2899–2918.
- Smith, W. H. F., and D. T. Sandwell (1997), Global seafloor topography from satellite altimetry and ship depth soundings, *Science*, **277**, 1957–1962.
- Sobolev, P., and D. V. Rundquist (1999), Seismicity of oceanic and continental rifts—A geodynamic approach, *Phys. Earth Planet. Inter.*, **111**, 253–266.
- Solomon, S. C., and N. C. Burr (1979), The relationship of source parameters of ridge-crest and transform earthquakes to the thermal structure of oceanic lithosphere, *Tectonophysics*, **55**, 107–126.
- Stein, R. C., and T. C. Hanks (1998), $M \geq 6$ earthquakes in southern California during the twentieth century: No evidence for a seismicity or moment deficit, *Bull. Seismol. Soc. Am.*, **88**, 635–652.
- Stein, S., and A. Pelayo (1991), Seismological constraints on stress in the oceanic lithosphere, *Philos. Trans. R. Soc. London, Ser. A*, **337**, 53–72.
- Stesky, R. M., W. F. Brace, D. K. Riley, and P.-Y. F. Robin (1974), Friction in faulted rock at high temperature and pressure, *Tectonophysics*, **23**, 177–203.
- Stirling, M. W., S. G. Wesnousky, and K. Shimazaki (1996), Fault trace complexity, cumulative slip, and the shape of the magnitude-frequency distribution for strike-slip faults: A global survey, *Geophys. J. Int.*, **124**, 833–868.
- Stoddard, P. R. (1992), On the relation between transform fault resistance and plate motion, *J. Geophys. Res.*, **97**, 17,637–17,650.
- Thatcher, W. (1990), Present-day crustal movements and the mechanics of cyclic deformation, in *San Andreas Fault System*, California, edited by R. Wallace, *U. S. Geol. Surv. Prof. Pap.*, **1515**, 189–205.
- Thurber, C., and R. Sessions (1998), Assessment of creep events as potential earthquake precursors: Application to the creeping section of the San Andreas Fault, California, *Pure Appl. Geophys.*, **152**, 685–705.
- Trehu, A., and S. Solomon (1983), Earthquakes in the Orozco Transform Zone: Seismicity, source mechanism, and tectonics, *J. Geophys. Res.*, **88**, 8203–8225.
- Tucholke, B. E., and J. Lin (1994), A geological model for the structure of ridge segments in slow-spreading ocean crust, *J. Geophys. Res.*, **99**, 11,937–11,958.
- Turcotte, D. L. (1986), A fractal model for crustal deformation, *Tectonophysics*, **132**, 261–269.
- Turcotte, D. L., and G. Schubert (2001), *Geodynamics, Application of Continuum Physics to Geological Problems*, Cambridge Univ. Press, New York.
- Utsu, T. (1961), A statistical study on the occurrence of aftershocks, *Geophys. Mag.*, **30**, 521–605.
- Utsu, T. (1969), Aftershocks and earthquake statistics, I, Some parameters which characterize an aftershock sequence and their interaction, *J. Fac. Sci. Hokkaido Univ., Ser.*, **7**(3), 129–195.
- Wald, D., T. Heaton, and K. Hudnut (1996), The slip history of the 1994 Northridge, California, earthquake determined from strong-motion, teleseismic, GPS, and leveling data, *Bull. Seismol. Soc. Am.*, **86**, S49–S70.
- Waldhauser, F., and W. L. Ellsworth (2002), Fault structure and mechanics of the Hayward Fault, California, from double-difference earthquake locations, *J. Geophys. Res.*, **107**(B3), 2054, doi:10.1029/2000JB000084.
- Wang, J.-H., and S.-S. Ou (1998), On scaling of earthquake faults, *Bull. Seismol. Soc. Am.*, **88**, 758–766.
- Ward, S. N. (1997), More on m_{max} , *Bull. Seismol. Soc. Am.*, **87**, 1199–1208.
- Wesnousky, S. G. (1990), Seismicity as a function of cumulative geologic offset: Some observations from southern California, *Bull. Seismol. Soc. Am.*, **80**, 1374–1381.
- Wesnousky, S. G. (1994), The Gutenberg-Richter or characteristic earthquake distribution, which is it?, *Bull. Seismol. Soc. Am.*, **84**, 1940–1959.
- Wesson, R. L. (1988), Dynamics of fault creep, *J. Geophys. Res.*, **93**, 8929–8951.
- Wiemer, S., and M. Wyss (2000), Minimum magnitude of completeness in earthquake catalogs: Examples from Alaska, the western United States, and Japan, *Bull. Seismol. Soc. Am.*, **90**, 859–869.
- Wiens, D. A., and S. Stein (1983), Age dependence of oceanic intraplate seismicity and implications for lithospheric evolution, *J. Geophys. Res.*, **88**, 6455–6468.
- Wilcock, W., G. Purdy, and S. Solomon (1990), Microearthquake evidence for extension across the Kane Transform Fault, *J. Geophys. Res.*, **95**, 15,439–15,462.
- Yamanaka, Y., and K. Shimazaki (1990), Scaling relationship between the number of aftershocks and the size of the main shock, *J. Phys. Earth*, **38**, 305–324.
- Yeats, R. S., C. R. Allen, and K. E. Sieh (1997), *The Geology of Earthquakes*, Oxford Univ. Press, New York.

M. S. Boettcher, MIT/WHOI Joint Program, Woods Hole Oceanographic Institution, Woods Hole, MA 02543, USA. (margaret@who.edu)
 T. H. Jordan, Department of Earth Sciences, University of Southern California, Los Angeles, CA 90089-0740, USA. (tjordan@usc.edu)

Chapter 3

Earthquake Clustering on East Pacific Rise Transform Faults

Abstract

Earthquake clustering properties of mid-ocean ridge transform faults (RTFs) are distinct from those of continental transform faults. Approximately 15 times fewer aftershocks follow RTF earthquakes, while RTFs are preceded by about four times more foreshocks. Because of their high ratio of foreshocks to aftershocks, RTF earthquakes cannot be explained by standard models of seismic triggering, in which there is no fundamental distinction between foreshocks, mainshocks, and aftershocks. Here we present a retrospective analysis of six years of hydroacoustic data from the fastest slipping faults within the hydrophone array of the National Oceanic and Atmospheric Pacific Marine Environmental Laboratory. We demonstrate that foreshock sequences on East Pacific Rise transform faults can be used to achieve statistically significant short-term prediction of large earthquakes (magnitude $M > 5.4$) with good spatial (15 km) and temporal (1 hr) resolution. The predictability of East Pacific Rise transform earthquakes is consistent with a model in which slow slip transients trigger earthquakes, enrich their low-frequency radiation, and accommodate much of the subseismic plate motion.

3.1 Introduction

Is there hope of short-term prediction of the eventual size of an earthquake from the first signs of its initiation? The answer to this question depends on which of the two proposed models better represents earthquake nucleation, the cascade model or pre-slip model [e.g. *Dodge et al.*, 1996]. In the cascade model, earthquakes are triggered through a self-similar process in which stress heterogeneities cause a cascade of small patches to fail consecutively, concentrating stress at the hypocenter of the mainshock, and finally triggering the main

event. According to the cascade model, no aspect of the nucleation process scales with size of the eventual earthquake, and therefore prediction of the largest events based on precursory phenomena is not possible without perfect knowledge of fault zone constitutive laws and stress distributions. In contrast, the pre-slip model suggests that a magnitude-dependent fault preparation process triggers the mainshock and any foreshocks.

Much controversy exists concerning which model of earthquake nucleation is more representative. The pre-slip model is favored by *Dodge et al.* [1996]; *Yamaoka et al.* [1999], and *Umino et al.* [2002], who all investigated the temporal and spatial distribution of foreshocks preceding large earthquakes, while *Abercrombie and Mori* [1996]; *Kilb and Gomberg* [1999] and *Feltzer et al.* [2004] favor the cascade model to describe foreshock data. *Mori and Kanamori* [1996] studied earthquakes in Southern California and found no scaling between the moment release in nucleation phases and the total moment release. However, *Ellsworth and Beroza* [1998] analyzed the same earthquake sequence and determined that *Mori and Kanamori* [1996] could not accurately evaluate the existence and size of nucleation phases due to limitations of their data in terms of bandwidth and dynamic range. Thus, the data from California, Japan, and other well-instrumented continental fault systems have not yet provided a definitive answer as to which model better reflects earthquake nucleation.

Here we examine earthquake clustering on East Pacific Rise (EPR) transform faults. We find few aftershocks, consistent with our findings from Chapter 2, and many foreshocks. We show that the EPR data can not be fit by the Epidemic Type Aftershock Sequence (ETAS) model of triggered seismicity, which states that all earthquakes—whether they are foreshocks, mainshocks, or aftershocks—initiate in the same manner. Thus, we speculate that the abundant foreshocks that precede large $M > 5.5$ earthquakes, indicate that some type of fault preparation process occurs before large earthquakes on these mid-ocean ridge transform faults.

3.2 Foreshock sequences and short-term earthquake predictability on Earth Pacific Rise transform faults*

*Published as: J.J. McGuire, M.S. Boettcher, and T.H. Jordan, *Nature*, 434, 457-461, 2005. Reproduced with permission from the Nature Publishing Group 2005.

Foreshock sequences and short-term earthquake predictability on East Pacific Rise transform faults

Jeffrey J. McGuire¹, Margaret S. Boettcher² & Thomas H. Jordan³

¹Department of Geology and Geophysics, Woods Hole Oceanographic Institution, and ²MIT-Woods Hole Oceanographic Institution Joint Program, Woods Hole, Massachusetts 02543-1541, USA

³Department of Earth Sciences, University of Southern California, Los Angeles, California 90089-7042, USA

East Pacific Rise transform faults are characterized by high slip rates (more than ten centimetres a year), predominately aseismic slip and maximum earthquake magnitudes of about 6.5. Using recordings from a hydroacoustic array deployed by the National Oceanic and Atmospheric Administration, we show here that East Pacific Rise transform faults also have a low number of aftershocks and high foreshock rates compared to continental strike-slip faults. The high ratio of foreshocks to aftershocks implies that such transform-fault seismicity cannot be explained by seismic triggering models in which there is no fundamental distinction between foreshocks, mainshocks and aftershocks. The foreshock sequences on East Pacific Rise transform faults can be used to predict (retrospectively) earthquakes of magnitude 5.4 or greater, in narrow spatial and temporal windows and with a high probability gain. The predictability of such transform earthquakes is consistent with a model in which slow slip transients trigger earthquakes, enrich their low-frequency radiation and accommodate much of the aseismic plate motion.

On average, before large earthquakes occur, local seismicity rates show a significant increase¹. In continental regions, where dense regional seismic networks provide the best data, most foreshock studies^{2–4}, though not all⁵, are consistent with the hypotheses that earthquake nucleation is independent of magnitude and that foreshocks result from a general triggering process in which there is no fundamental distinction between foreshocks, mainshocks and aftershocks. The inability to distinguish foreshocks from the statistical fluctuations in the continental background seismicity severely limits their usefulness in predicting large earthquakes⁶.

It is unclear, however, whether these statements apply to other tectonic environments, or how aseismic processes affect earthquake triggering. Aseismic slip transients with timescales of days to months have recently been observed in the subduction zones of Japan^{7–9} and Cascadia¹⁰, using continuously monitored GPS arrays. The possibility that aseismic slip triggers large earthquakes on subduction megathrusts is especially intriguing given the observation¹¹ that a slow slip transient occurred 15 minutes before the great 1960 Chilean megathrust earthquake, which had a moment magnitude (M_w) of 9.5, the largest ever recorded. Notably, subduction zones are observed to have higher foreshock rates than continental regions¹².

Another tectonic environment in which aseismic processes are thought to exert a strong influence on fault behaviour is mid-ocean ridge transform faults (RTFs). Studies over the last several decades^{13–15} have shown that on average most of the slip on RTFs, up to about 85% (ref. 15), is aseismic. Moreover, the seismic component of slip occurs in earthquakes that are relatively small ($M_w \leq 7.2$) given the length of the faults^{14–16}. Many of the larger RTF earthquakes are slow events with anomalous low-frequency radiation^{17,18}. Low-frequency spectral analyses^{19,20} have indicated that slow RTF earthquakes are compound events comprising an ordinary rupture and a slow transient of comparable moment but much longer duration; in some cases, the slow component precedes, and presumably initiates, the main seismic component. Time-domain records of slow precursors to RTF earthquakes^{20,21} and episodes of coupled seismic slip observed on adjacent RTFs^{20,22}

support the inference of slow slip transients, but the subject remains controversial²³.

Hydroacoustic detection of foreshocks

Here we use data from a six-element hydroacoustic array deployed by the National Oceanic and Atmospheric Administration's Pacific Marine Environmental Laboratory (NOAA-PMEL) to examine anomalous foreshock sequences on East Pacific Rise (EPR) transform faults (Fig. 1). The NOAA-PMEL arrays^{24–26} routinely locate EPR earthquakes with acoustic source level (ASL) magnitudes (see Methods) M_{ASL} below 3, reducing the detection threshold by 1.5–2.0 magnitude units below global seismicity catalogues (see Methods). A reconnaissance study indicated that foreshocks in the last hour before large events are significantly more common on EPR transform faults than on strike-slip faults in the North Atlantic, Northeast Pacific or Southern California²⁷.

Figure 2 displays stacks of the seismicity in space-time windows centred on nine mainshocks that occurred on the Discovery and Gofar transform faults between May 1996 and December 2001. This set of mainshocks comprised all $M_w \geq 5.4$ earthquakes on these two faults recorded by the NOAA-PMEL array in the Harvard Centroid Moment Tensor (CMT) catalogue²⁸ that did not follow within 1 week and 100 km of another mainshock. The longer window (Fig. 2a) shows low background seismicity tens of hours before the mainshocks and the subsequent aftershock decay. The shorter window (Fig. 2b) reveals an accelerating rate of seismicity close to the mainshock epicentres during the hour immediately preceding the mainshock origin times.

Earthquake triggering model

The anomalous nature of the RTF foreshock activity can be quantified in terms of the Epidemic Type Aftershock Sequence (ETAS) model of triggered seismicity^{4,29,30}. ETAS is a marked point process model³¹ in which all earthquake magnitudes above a lower cutoff m_0 are independent samples of the Gutenberg–Richter (GR) probability distribution, $P(m) = 10^{-b(m-m_0)}$, where b is the slope of the distribution, and all earthquakes give birth to daughter events at

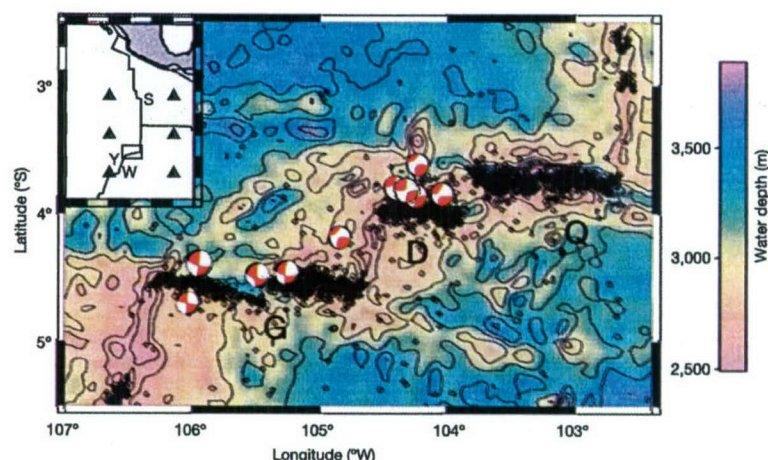


Figure 1 Map of the Quebrada (Q), Discovery (D), and Gofar (G) transform faults in the equatorial eastern Pacific, contoured with the bathymetry predicted from the satellite-derived gravity field⁴². Diamond symbols represent the acoustic radiator positions in the NOAA-PMEL seismicity catalogue for 1996–2001²⁴, and beachball symbols show the

focal mechanisms and centroid locations for the same period from the Harvard CMT catalogue. The inset map locates the EPR and Cocos ridge crests (black lines), the six NOAA hydrophones (triangles), the Wilkes (W), Yaquina (Y), and Siqueiros (S) transform faults, and the region of the main map (rectangle). The contour interval is 200 m.

an average rate of $\phi(m, t) = \rho(m)\psi(t)$, where t is time since the earthquake. This triggering rate is assumed to increase exponentially with magnitude, $\rho(m) = k \times 10^{\alpha(m-m_0)}$, where α is the triggering exponent, and to decay with time after a mother event according to the modified Omori law, $\psi(t) = \theta c^\theta / (c + t)^{1+\theta}$ (where $\theta > 0$). The constants k , θ and c are parameters that vary among regions. Renormalization for a single mainshock of magnitude m yields an average seismicity rate proportional to $N_a^{II}(m) = \frac{k}{1-n} 10^{\alpha(m-m_0)}$. N_a^{II} is the expected number of aftershocks of any magnitude (type-II aftershocks; that is, not constrained to be smaller than m), and the constant $n = \int_0^1 \rho(\mu) dP(\mu) = kb/(b-\alpha)$ is the branching ratio, which equals both the average number of directly triggered aftershocks per event and the fraction of the earthquake population

that is made up of triggered earthquakes³⁰. The aftershock rate decays with an effective Omori exponent⁴ $p = 1 + O(\theta)$.

In the ETAS model, the seismicity rate before a mainshock at $t = 0$ increases according to the inverse Omori law; that is, $\sim |t|^{-p'}$, where $p' = 1 + O(\theta)$, and the expected number of events of all magnitudes conditioned on the mainshock occurrence (type-II foreshocks) is independent⁴ of m . This conditional foreshock number can be approximated as the product of two factors: the probability that the mainshock is a triggered event, and the expected number of events in a cluster averaged over mainshock magnitude. The first is just the branching ratio n , and the second is the integral $\int_0^1 N_a^{II}(\mu) dP(\mu)$; therefore³⁰, $N_f^{II} \approx n^2/(1-n)$. To include only earthquakes smaller than the mainshock (type-I foreshocks), we multiply the integrand by the probability that no event in a cluster exceeds m and integrate over the appropriate magnitude range. If $k/(1-n)$ is small and m is large (conditions which apply to our data), then the extra probability factor is close to unity, and the results are $N_f^I \approx N_f^{II}[1 - 10^{-(b-\alpha)(m-m_0)}]$.

A similar modification to the aftershock number yields the foreshock/aftershock ratio:

$$\frac{N_f}{N_a} \approx n \left(\frac{b}{b-\alpha} \right) \left[\frac{10^{(b-\alpha)\Delta m_1^f} - 10^{(b-\alpha)\Delta m_2^f}}{10^{b\Delta m_1^f} - 10^{b\Delta m_2^f}} \right] \quad (1)$$

Here we have generalized the formula to count foreshocks in the magnitude range from $m - \Delta m_1^f$ to $m - \Delta m_2^f$ and aftershocks from $m - \Delta m_1^a$ to $m - \Delta m_2^a$, where $0 \leq \Delta m_2^a < \Delta m_1^a \leq m - m_0$. This approximation, which applies to large mainshocks, differs conceptually from the expression recently used by ref. 3 to explain the foreshock/aftershock ratios from global and regional catalogues (see Methods).

Anomalous foreshock activity

Earthquake populations on RTFs are well described by a tapered GR distribution having a low-magnitude slope $b \approx 1$ (refs 14, 15) similar to that of continental regions. The hydroacoustic catalogue for the EPR faults is consistent with this self-similar scaling, and its aftershock sequences decay according to Omori's law with³² $p \approx 1$, again similar to continental regions. However, global catalogues demonstrate that the aftershock productivity of large RTF earthquakes is lower than continental faults by approximately a factor of fifteen¹⁵ (Fig. 3). The low aftershock productivity combined with

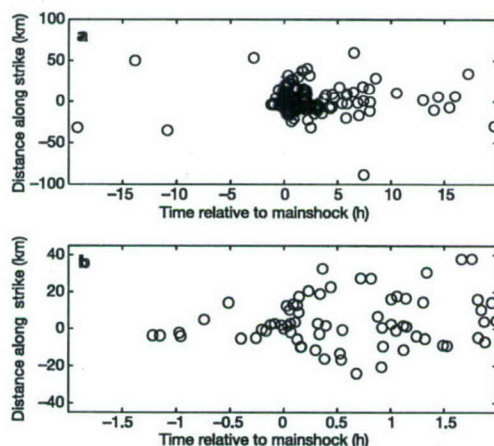


Figure 2 Space-time distribution of seismicity around the nine mainshocks ($M_w \geq 5.4$) on the Discovery and Gofar transform faults between May 1996 and December 2001, from the declustered Harvard CMT catalogue. **a**, Stack of all events from the NOAA-PMEL hydroacoustic catalogue with $M_{ASL} > 2.5$ (for $ASL > 207$) that were located within ± 100 km along strike and within ± 20 h of the mainshocks. Positive distance is west of the mainshock, and positive time is after the mainshock. **b**, Zoomed-in view of the same seismicity, showing foreshock activity within about 1 h and 15 km of the mainshocks.

the poor detection thresholds of global catalogues makes it difficult to constrain the values of n and α independently. A maximum-likelihood fit to the teleseismic RTF data yields a best-fit value of the triggering exponent $\alpha = 0.72$, and is consistent with the somewhat higher values found for California and Japan ($\alpha = 0.8$ – 1.0)^{33,34} (Fig. 3). Error bounds on the maximum-likelihood estimate are large, but aftershock counts using the hydroacoustic catalogue (points with horizontal bars in Fig. 3) also favour relatively high values of α and rule out values less than about 0.6 (see Supplementary Information).

The difference between oceanic and continental aftershocks primarily manifests itself in the intercept of the scaling relation, $k/(1 - n)$, which is offset by about a factor of fifteen (Fig. 3). The maximum-likelihood fit in Fig. 3 corresponds to a branching ratio, $n \approx 0.1$, compared to values approaching unity in continental seismic zones³⁵. As discussed in the Supplementary Information, the aftershock rate may be somewhat higher for the EPR faults, but we can say with a high degree of confidence that $n < 0.3$. In other words, according to the ETAS model, most RTF earthquakes (70–90%) would be primary events driven by aseismic plate-tectonic loading rather than aftershocks of previous earthquakes. Equation (1) with the maximum-likelihood estimate of α and n predicts that the foreshock/aftershock ratio for RTFs should be about an order of magnitude lower than that observed in continents.

Instead, the EPR transform faults that are well recorded by the NOAA-PMEL array give values of N_f/N_a that are an order of magnitude higher than observed in Southern California (Fig. 4). For both regions, we identified mainshocks as events in the Harvard CMT catalogue with $M_w \geq 5.4$ that did not follow within 1 week and 100 km of another mainshock (see Methods), and we compiled

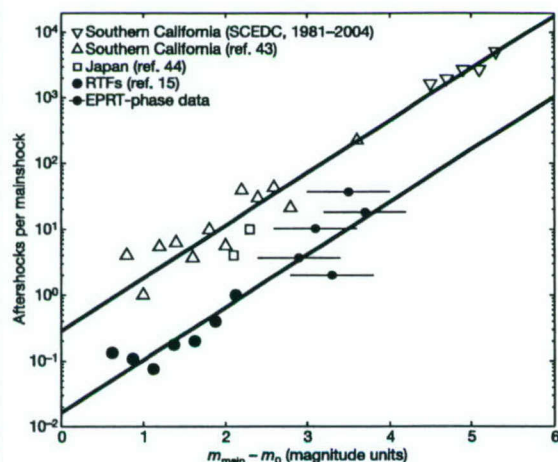


Figure 3 Aftershocks per mainshock, plotted against the difference between the mainshock magnitude m_{main} and the catalogue completeness threshold m_0 . RTF aftershocks (large filled circles) were defined as events with calibrated surface-wave magnitudes above $m_0 = 5.1$ that occurred within 14 days and 100 km of a $M_w \geq 5.6$ mainshock during the catalogue interval 1976–2001 (ref. 15). Southern California aftershocks from the SCEDC catalogue (open triangles) were defined as events above a local-magnitude (M_L) threshold of $m_0 = 2.0$ that occurred within 14 days and 100 km of a $M_L \geq 6.5$ mainshock during the interval 1981–2004. Aftershock counts from the EPR T-phase catalogue (small filled circles) are shown with error bars to account for uncertainties in m_0 ($2.0 \leq m_0 \leq 3.0$). The T-phase catalogue aftershocks were counted within 14 days and 30 km of the mainshocks. Previously published continental data sets (open triangles and squares) were compiled by Kisslinger and Jones⁴³ and Yamanaka and Shimazaki⁴⁴ using M_L thresholds of $m_0 = 4.0$ and 4.5 , respectively. Both RTF and continental aftershocks are consistent with a triggering exponent of $\alpha = 0.8$ (solid lines), but RTFs produce fewer aftershocks by a factor of fifteen.

foreshock and aftershock statistics from the NOAA-PMEL and the Southern California Earthquake Data Center (SCEDC) catalogues. We counted all events with local magnitudes (M_{SL} or M_L) up to 2.8 units smaller than the mainshock M_w in the 1-h interval before and the 5-h interval after the mainshock. Figure 4 compares the observed N_f/N_a for spatial windows of various radii with the predictions of equation (1), corrected for the finite sampling intervals (see Methods). The SCEDC statistics satisfy an ETAS model with $\alpha = 0.8$ – 0.9 , consistent with previous catalogue studies^{3,29}. However, foreshock rates from the NOAA-PMEL statistics are about two orders of magnitude greater than the ETAS predictions using the maximum-likelihood fit in Fig. 3. As shown in Fig. 4 and Supplementary Fig. S3, these results are robust with respect to the choice of windows and declustering procedures.

Therefore, we can reject the ETAS hypothesis that the clustering of foreshocks, mainshocks and aftershocks on RTFs can be described by the same seismic triggering mechanism. We infer that large earthquakes on EPR faults are preceded by an extended preparation process, possibly driven by subseismic transients (silent or quiet earthquakes), that can often be observed through foreshocks. This alternative hypothesis is consistent with the tightly localized distribution of the foreshocks about the mainshock in both space and time (Fig. 2 and Supplementary Fig. S4), which does not conform to the inverse-diffusive behaviour expected from the ETAS model⁴.

The correspondence of slow slip with foreshocks was suggested as early as 1976 by Kanamori and Stewart¹⁸, who noted a foreshock with a body-wave magnitude $m_b \approx 5$ about 500 s before the $M_w = 7$ slow earthquake on the Gibbs transform fault in the North Atlantic. More recently, McGuire *et al.* associated $m_b = 4.5$ – 5.0 foreshocks before the 1994 $M_w = 7.0$ Romanche²⁰ and 1997 $M_w = 6.8$ Prince Edward Island²¹ earthquakes with slow precursors observed at low frequencies. Forsyth *et al.*²² suggested

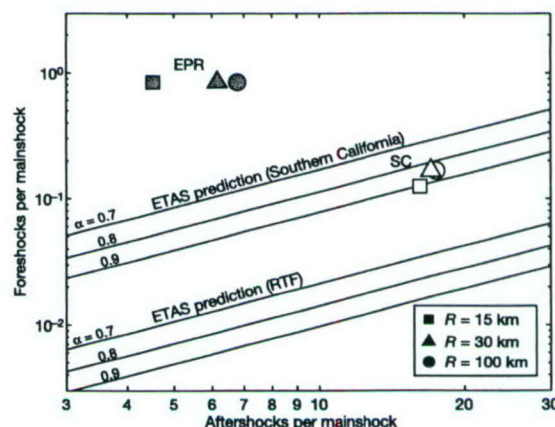


Figure 4 Foreshock and aftershock rates observed for EPR transform faults (solid symbols) and Southern California (open symbols) in regions of radius R about the mainshock. The data sets included 19 mainshocks ($M_w \geq 5.4$) on five transform faults (Discovery, Gofar, Wilkes, Yaquina and Siqueiros) from the declustered Harvard CMT catalogue for 1996–2001, and 24 mainshocks ($M_L \geq 5.4$) in Southern California from the declustered SCEDC catalogue for 1981–2003. Events with magnitudes up to 2.8 units below the mainshock magnitude were counted from the NOAA-PMEL and SCEDC catalogues in the 1-h window preceding and 5-h window following the mainshocks. These rates are compared with the N_f/N_a ratios from the ETAS model (equation (1)) for $\alpha = 0.7$ – 0.9 (solid lines), assuming $\Delta m_2^{f,a} = 0$, $\Delta m_1^{f,a} = 2.8$ and $b = 1$, with estimated branching ratios of $n = 0.8$ (Southern California) and $n = 0.1$ (RTF). The $\alpha = 0.8$ line for RTFs is close to the maximum-likelihood estimate from Fig. 3. Uncertainties in α and n allow shifts in the ETAS prediction upwards from the maximum-likelihood value by half an order of magnitude at most.

articles

that a subseismic slip process was responsible for a swarm of contemporaneous seismicity on the Anakena and Raraku transform faults of the southern EPR recorded by an ocean-bottom seismometer array in 1995. These and other examples³⁶ combined with the global aftershock depletion (Fig. 3) and the evidence for slow precursors to large earthquakes on RTFs worldwide¹⁹, indicate that the aseismic, foreshock-generating process on EPR faults may be prevalent throughout the mid-ocean-ridge system, including the slower-slipping, colder RTFs in the Atlantic and Indian oceans.

Short-term predictability of large earthquakes

The high rate of proximate foreshocks suggests a naive scheme for short-term earthquake prediction—we simply assume that every event is a foreshock of an impending large earthquake. We can formalize this scheme into a well-posed prediction algorithm³⁷: whenever we observe any RTF event above some ASL magnitude threshold m_0 within a specified RTF region, we issue an alert that an earthquake of moment magnitude greater than or equal to m_p will occur sometime during time window of length t_p immediately following the event and somewhere in a spatial window of radius r_p about the event's epicentre. Figure 5 illustrates this prediction algorithm for the parameter set [$m_0 = 2.5$ (M_{ASL}), $m_p = 5.4$ (M_W), $t_p = 1$ h, $r_p = 15$ km] by applying it retrospectively to the two most active EPR transform faults, Discovery and Gofar. Of the nine candidate earthquakes that occurred during the catalogue interval May 1996–November 2001, six were located within the space-time prediction windows (Fig. 5) and thus constitute successful predictions. There were three failures-to-predict and about 1,400 false alarms.

Although the false-alarm rate is quite high, all alarms taken together occupy only about 0.15% of the total space-time volume of about $250 \text{ km} \times 5.5 \text{ yr}$ (see Supplementary Information). We can relate $P(M|F)$, the probability of a mainshock M in the prediction window given the occurrence of a foreshock F , to $P(M)$, the probability of M in a random window of the same size, using the Bayes identity:

$$P(M|F) = P(M) \left[\frac{P(F|M)}{P(F)} \right] \quad (2)$$

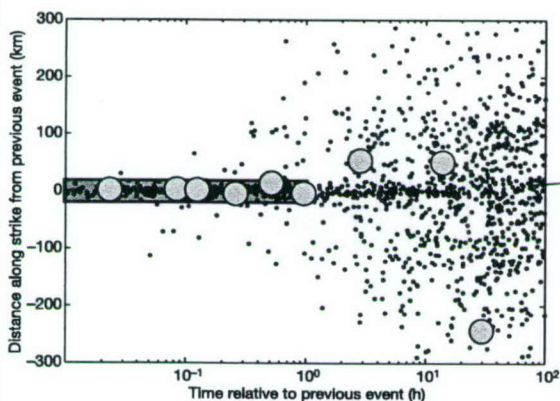


Figure 5 Retrospective application of the naive prediction algorithm described in the text to the NOAA-PMEL catalogue (May 1996–November 2001) for the Discovery and Gofar faults. Plot shows along-strike distance (positive to the west) and time of each earthquake relative to its previous event for all catalogued events with $M_{ASL} \geq 2.5$ ($ASL \geq 207$). Events were considered to be distinct if they were separated by more than 1 min from the previous event, to exclude redundancies. Six of the nine mainshocks identified from the declustered Harvard CMT catalogue (large circles) fall within the 1-h, ± 15 -km alert windows (shaded area) used in the prediction algorithm.

$P(F|M)$ is the fraction of mainshocks preceded by foreshocks, and $P(F)$ equals the fraction of the space-time volume occupied by alerts. The ratio of these probabilities (the term in square brackets) is the probability gain factor g of the prediction algorithm³⁷. Our retrospective analysis of the Discovery and Gofar faults gives $g = 450$. This performance can be compared to prediction experiments in California, where even highly optimized algorithms with many adjustable parameters are thought to achieve probability gains of 10–20 or less³⁸.

The performance relative to random chance can be evaluated using Molchan's³⁹ error diagram, which plots the failure-to-predict probability, $1 - P(F|M)$, against $P(F)$ (Fig. 6). Large sets of random alerts should fall close to the line $1 - P(F)$, corresponding to no probability gain ($g = 1$). Figure 6 shows that the Discovery–Gofar point lies well below the 99% confidence range for random chance; the probability of reproducing this performance with random alerts filling 0.15% of the space-time volume is less than one in ten million. Similar results were obtained by applying the algorithm retrospectively to the five active EPR transforms in the study area; nine of sixteen mainshocks were successfully predicted by alerts occupying 0.13% of the space-time volume, which gives $g = 340$ (Fig. 6, see Supplementary Discussion).

Our naive algorithm is far from optimal. For instance, raising the threshold magnitude m_0 from 2.5 to 3.4 (that is, increasing the ASL from 207 to 215) reduces the number of alarms in the Gofar–Discovery catalogue to 407 without changing $P(F|M)$, increasing g to about 1,000 (Fig. 6). More parameters could be added to improve the performance further.

Discussion

Mid-ocean ridges are far removed from urban centres on continents, so the direct societal value of short-term earthquake prediction on RTFs (assuming it could be operationally implemented using real-time, near-source monitoring) would be small. Nevertheless, the existence of short-term predictability in this tectonic environment—the main conclusion of this paper—is of considerable scientific interest, because it supports a physical linkage between foreshocks and mainshocks through stress changes driven by aseismic slip transients or some other fault preparation process

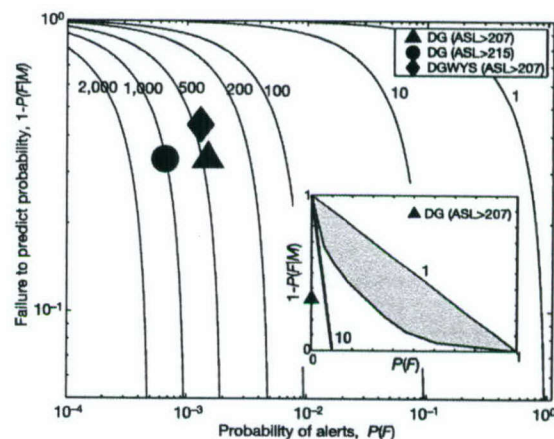


Figure 6 Molchan's³⁹ error diagram of the failure-to-predict probability $1 - P(F|M)$ against the probability of alerts $P(F)$ on a logarithmic scale, contoured with probability gain g (solid curves). Performance of the naive prediction algorithm is given for the Discovery and Gofar (DG) faults with $m_0 = 2.5$ (triangle) and $m_0 = 3.4$ (circle), and for the five active EPR faults (DGWYS) with $m_0 = 2.5$ (diamond). Inset diagram is the same plot on a linear scale, comparing the 99% confidence region for a random prediction of nine mainshocks (shaded area) with the first DG test (triangle).

such as hydrothermal flow or nearby magmatic activity.

To monitor RTFs geodetically will require a new generation of ocean-bottom instrumentation, a considerable technological challenge. But collecting such data may well be the best way to test the hypothesis that three anomalous aspects of RTF seismicity—large slip deficits, high foreshock activity and slow earthquakes—can be explained by aseismic fault-slip transients. Given the importance of understanding the fundamental mechanics of earthquake predictability, overcoming the technological hurdles should be worth the effort. □

Methods

We use the NOAA-PMEL hydroacoustic earthquake catalogue for the equatorial Pacific which began in 1996 (ref. 24). Their array (Fig. 1) records acoustic energy radiated into the water column by earthquakes and other sources (T-phases). T-phases propagate very efficiently in the low-velocity sound fixing and ranging (SOFAR) channel, and the array arrivals can be used to locate precisely where the energy entered the SOFAR channel. The standard errors in this source location are estimated to be ± 2 km, ± 10 s for the southern/northernmost faults (the Wilkes and Siqueiros faults) and are slightly smaller for the faults located in the centre of the array²⁴ (the Discovery and Gofar faults). A propagation model is used to convert the magnitude of the pressure signal at the hydrophones into an ASL (measured in decibels) at the source location. We used a conversion between ASL and magnitude, $M_{ASL} = 0.107ASL - 19.6$, obtained from the regression of the observed ASLs compiled in ref. 32 against the body-wave magnitudes of the International Seismological Centre (ISC) catalogue (<http://www.isc.ac.uk/>). Frequency-magnitude statistics indicate that the seismicity catalogues are approximately complete down to $ASL \approx 207-212$, or $M_{ASL} \approx 2.5-3.0$.

To prevent biases from ongoing aftershock sequences, we eliminated CMT catalogue earthquakes that occurred within 1 week and 100 km of a previous CMT earthquake from our analysis. Our declustering criterion eliminated only one earthquake with $M_w \approx 5.5$ from the Discovery-Gofar set and only two from the mainshock set for other three active RTFs within the NOAA-PMEL array. Moderate increases in the space and time windows did not disqualify additional events. Moreover, each of the three disqualifying events had a foreshock sequence distinct from the aftershock sequence of the preceding mainshock, consistent with the statistics in Fig. 4 (see Supplementary Fig. 2).

The time dependence of foreshock and aftershock rates in ETAS is controlled by Omori's law. Helmstetter *et al.*⁴ have demonstrated that the time-decay exponent p in the renormalized Omori law is not strictly a constant. When $p(m)$ has finite variance ($\alpha/b \leq 1/2$), p varies from $1 - \theta$ for $t \ll t^* = c(n/1 - n)^{1/\theta}$ to $1 + \theta$ for $t \gg t^*$. The theory breaks down for $\alpha/b > 1/2$, owing to the strong coupling between earthquake energy and seismicity rate, but the numerical simulations of ref. 4 indicate that the short-time value of p increases approximately linearly from $1 - \theta$ at $\alpha/b = 1/2$ to $1 + \theta$ as $\alpha/b \rightarrow 1$. For $\alpha/b = 0.8$, the Omori exponents can be approximated by $p^* \approx p \approx 1 + \theta$; hence, the requisite integrals are $\int_0^{t^*} \psi(\tau) d\tau \approx 1 - (c/\Delta t_a)^p$, where the approximation assumes $\Delta t_a \gg c$. Equation (1) can thus be corrected for the finite foreshock and aftershock sampling intervals, $\Delta t_f = 1$ h and $\Delta t_a = 5$ h, by multiplying its right-hand side by the ratio of these integrals. This ratio varies from 0.72 to 0.94 over the plausible range of parameters $c = 1$ s – 1 min, $\theta = 0-0.2$, so the correction is minor.

Equation (1) is a more general form of models used in previous studies^{3,12,40,41}. Feltzer *et al.*³ consider the case $\alpha = b$. Taking this limit in equation (1), we obtain $N_f/N_s \approx n(\ln 10) \left[\frac{\Delta m_f^2 - \Delta m_s^2}{10^{\Delta m_f^2} - 10^{\Delta m_s^2}} \right]$. For the magnitude ranges of ref. 3 ($\Delta m_f^2 = 1.0$, $\Delta m_s^2 = 0$; $\Delta m_f^2 = 1.0$, $\Delta m_s^2 = 0.4$), the ratio in brackets reproduces their foreshock/aftershock ratio of 0.134. The factor $n(\ln 10)$ missing in their equation (6) probably lies between 1 and 2 for continental and subduction-zone seismicity⁴⁰, so their formula provides an adequate approximation in most regions. For RTFs, however, the scaling of N_f/N_s with the branching ratio n is numerically important (see Fig. 4).

Received 3 September 2004; accepted 19 December 2005; doi:10.1038/nature03377.

- Jones, L. M. & Molnar, P. Some characteristics of foreshocks and their possible relationship to earthquake prediction and premonitory slip on faults. *J. Geophys. Res.* **84**, 3596–3608 (1979).
- Abercrombie, R. E. & Mori, J. Occurrence patterns of foreshocks to large earthquakes in the Western United States. *Nature* **381**, 303–307 (1996).
- Felzer, K., Abercrombie, R. E. & Ekström, G. A common origin for aftershocks, foreshocks, and multiplets. *Bull. Seismol. Soc. Am.* **94**(1), 88–98 (2004).
- Helmstetter, A., Sornette, D. & Grasso, J.-R. Mainshocks are aftershocks of conditional foreshocks: How do foreshock statistical properties emerge from aftershock laws. *J. Geophys. Res.* **108**, doi:10.1029/2002JB001991 (2003).
- Dodge, D. A., Ellsworth, W. E. & Beroza, G. C. Detailed observations of California foreshock sequences: Implications for the earthquake initiation process. *J. Geophys. Res.* **101**, 22371–22392 (1996).
- Geller, R. J., Jackson, D. D., Kagan, Y. Y. & Mulargia, F. Earthquakes cannot be predicted. *Science* **275**, 1616–1617 (1997).
- Hirose, H., Hirahara, K., Kimata, F., Fujii, N. & Miyazaki, S. A slow thrust slip event following the two 1996 Hyuganada earthquakes beneath the Bungo Channel, Southwest Japan. *Geophys. Res. Lett.* **26**, 3237–3240 (1999).
- Ozawa, S. *et al.* Detection and monitoring of ongoing aseismic slip in the Tokai region, central Japan. *Science* **298**, 1009–1012 (2002).
- Ozawa, S. *et al.* Characteristic silent earthquakes in the eastern part of the Boso peninsula, Central Japan. *Geophys. Res. Lett.* **30**, doi:10.1029/2002GL016665 (2003).
- Dragert, H., Wang, K. & James, T. S. A silent slip event on the deeper Cascadia subduction interface. *Science* **292**, 1525–1528 (2001).

- Kanamori, H. & Cipar, J. Focal process of the great Chilean earthquake. *Phys. Earth Planet. Inter.* **9**, 128–136 (1974).
- Reasenber, P. A. Foreshock occurrence before large earthquakes. *J. Geophys. Res.* **104**, 4755–4768 (1999).
- Brune, J. N. Seismic moment, seismicity, and rate of slip along major fault zones. *J. Geophys. Res.* **73**, 777–784 (1968).
- Bird, P., Kagan, Y. & Jackson, D. in *Plate Boundary Zones* (ed. Freymueller, S. S. a. l.) 203–218 (AGU, Washington DC, 2002).
- Boettcher, M. S. & Jordan, T. H. Earthquake scaling relations for mid-ocean ridge transform faults. *J. Geophys. Res.* **109**, doi:10.1029/2004JB003110 (2004).
- Bird, P. & Kagan, Y. Plate-tectonic analysis of shallow seismicity: Apparent boundary width, beta, corner magnitude, coupled lithosphere thickness, and coupling in 7 tectonic settings. *Bull. Seismol. Soc. Am.* **94**(6), 2380–2399 (2004).
- Perez-Campos, X., McGuire, J. J. & Beroza, G. C. Resolution of the slow earthquake/apparent stress paradox for oceanic transform fault earthquakes. *J. Geophys. Res.* **108**, doi:10.1029/2002JB002312 (2003).
- Kanamori, H. & Stewart, G. S. Mode of strain release along the Gibbs fracture zone, Mid-Atlantic Ridge. *Phys. Earth Planet. Inter.* **11**, 312–332 (1976).
- Ihmle, P. F. & Jordan, T. H. Teleseismic search for slow precursors to large earthquakes. *Science* **266**, 1547–1551 (1994).
- McGuire, J. J., Ihmlé, P. F. & Jordan, T. H. Time-domain observations of a slow precursor to the 1994 Romanche transform earthquake. *Science* **274**, 82–85 (1996).
- McGuire, J. J. & Jordan, T. H. Further evidence for the compound nature of slow earthquakes: The Prince Edward Island earthquake of April 28, 1997. *J. Geophys. Res.* **105**, 7819–7828 (2000).
- Forsyth, D. W., Yang, Y., Mangiotes, M.-D. & Shen, Y. Coupled seismic slip on adjacent oceanic transform faults. *J. Geophys. Res.* **30**, doi:10.1029/2002GL016454 (2003).
- Abercrombie, R. E. & Ekström, G. Earthquake slip on oceanic transform faults. *Nature* **410**, 74–77 (2001).
- Fox, C. G., Matsumoto, H. & Lau, T. K. Monitoring Pacific Ocean seismicity from an autonomous hydrophone array. *J. Geophys. Res.* **106**, 4183–4206 (2001).
- Fox, C. G. *et al.* Acoustic detection of seafloor spreading. *J. Geophys. Res.* **22**, 131–134 (1995).
- Smith, D. *et al.* Hydroacoustic monitoring of seismicity at the slow-spreading Mid-Atlantic Ridge. *Geophys. Res. Lett.* **29**, 10.1029/2001GL013912 (2002).
- McGuire, J. J. Immediate foreshock sequences of oceanic transform earthquakes on the East Pacific Rise. *Bull. Seismol. Soc. Am.* **93**, 948–952 (2003).
- Ekström, G., Dziewonski, A. M., Maternovskaya, N. N. & Nettles, M. Global seismicity of 2001: centroid-moment tensor solutions for 961 earthquakes. *Phys. Earth Planet. Inter.* **136**, 165–185 (2003).
- Helmstetter, A. & Sornette, D. Bath's law derived from the Gutenberg-Richter law and from aftershock properties. *Geophys. Res. Lett.* **30**, doi:10.1029/2003GL018186 (2003).
- Helmstetter, A. & Sornette, D. Importance of direct and indirect triggered seismicity in the ETAS model of seismicity. *Geophys. Res. Lett.* **30**, 4, doi:10.1029/2003GL017670 (2003).
- Ogata, Y. Statistical models for earthquake occurrence and residual analysis for point processes. *J. Am. Stat. Assoc.* **83**, 9–27 (1988).
- Bohnenstiehl, D. R., Tolstoy, M., Dziak, R. P., Fox, C. G. & Smith, D. Aftershocks in the mid-ocean ridge environment: An analysis using hydroacoustic data. *Tectonophysics* **354**, 49–70 (2002).
- Helmstetter, A. Is earthquake triggering driven by small earthquakes? *Phys. Rev. Lett.* **91**, 058501 (2003).
- Helmstetter, A., Kagan, Y. & Jackson, D. D. Importance of small earthquakes for stress transfers and earthquake triggering. *J. Geophys. Res.* (in press).
- Helmstetter, A. & Sornette, D. Subcritical and supercritical regimes in epidemic models of earthquake aftershocks. *J. Geophys. Res.* **107**, doi:10.1029/2001JB001580 (2002).
- Hanson, J. A. & Given, H. K. Accurate azimuth estimates from a large aperture hydrophone array using T-phase waveforms. *Geophys. Res. Lett.* **25**, 365–368 (1998).
- Aki, K. in *Earthquake Prediction* (eds Simpson, D. W. & Richards, P. G.) 556–574 (AGU, Washington DC, 1981).
- Keilis-Borok, V., Shebalin, P., Gabrielov, A. & Turcotte, D. Reverse tracing of short-term earthquake precursors. *Phys. Earth Planet. Inter.* **145**, 75–85 (2004).
- Molchan, G. M. Earthquake prediction as a decision-making problem. *Pure Appl. Geophys.* **149**, 233–247 (1997).
- Reasenber, P. A. & Jones, L. M. Earthquake hazards after a mainshock in California. *Science* **243**, 1173–1176 (1989).
- Reasenber, P. A. & Jones, L. M. Earthquake aftershocks: Update. *Science* **265**, 1251–1252 (1994).
- Sandwell, D. T. & Smith, W. H. F. Marine gravity anomaly from Geosat and ERS 1 satellite altimetry. *J. Geophys. Res.* **102**, 10039–10054 (1997).
- Kisslinger, C. & Jones, L. M. Properties of aftershock sequences in Southern California. *J. Geophys. Res.* **96**, 11947–11958 (1991).
- Yamanaka, Y. & Shimazaki, K. Scaling relationship between the number of aftershocks and the size of the main shock. *J. Phys. Earth* **38**, 305–324 (1990).

Supplementary Information accompanies the paper on www.nature.com/nature.

Acknowledgements We thank R. Dziak for answering questions about details of the hydroacoustic earthquake catalogues, D. Bohnenstiehl for suggestions on clarifying the manuscript, A. Helmstetter for her help in understanding ETAS, and V. Keilis-Borok, I. Zaliapin, and L. Jones for discussions of earthquake prediction algorithms. J.J.McG. was supported by the Frank and Lisina Hoch Fund. M.S.B. was supported by the Deep Ocean Exploration Institute at WHOI. This work was supported by the NSF, SCEC and USGS.

Competing interests statement The authors declare that they have no competing financial interests.

Correspondence and requests for materials should be addressed to J.J.McG. (jmcguire@whoi.edu).

3.3 Supplementary Information Accompanying: Foreshock sequences and short-term earthquake predictability on East Pacific Rise transform faults

3.3.1 Foreshocks and Aftershocks on EPR Faults

The NOAA hydroacoustic array in the equatorial eastern Pacific detects earthquakes from much of the Pacific basin, but only six RTFs are contained within the region for which the array has both its maximum detection ability and location accuracy. The tectonic parameters of these faults are given in Table 3.1. Global RTF scaling relations predict that the largest magnitude earthquake typically observed on this set of faults would be about $M_W = 6.3$ [Boettcher and Jordan, 2004]. The Quebrada transform has not produced any earthquakes large enough for inclusion in the Harvard CMT catalog during the operation of the T-phase array (Figure 3-1) and hence was not used in our foreshock analysis.

Table 3.1:

Fault	Latitude (°N)	Length (km)	Slip Velocity (mm/yr)	Seismic Coupling (%)
Siqueiros (S)	8.4	150	112	6
Quebrada (Q)	-3.8	120	137	1
Discovery (D)	-4.0	70	138	19
Gofar (G)	-4.5	190	139	12
Yaquina (Y)	-6.2	60	141	2
Wilkes (W)	-9.0	200	145	2

Tectonic Parameters of the RTFs considered in this study. Seismic coupling estimates are taken from Boettcher and Jordan [2004] for plate motion above the 600°C isotherm. The letters in parentheses following the fault names are used to refer to the various faults.

Table 3.2 lists all the earthquakes in both the Harvard CMT and NOAA catalogs for the EPR faults sorted by their magnitude. The events on the Yaquina, Wilkes, and Siqueiros transforms tend to be slightly smaller than the Discovery and Gofar events, but 3 of the 5 declustered mainshocks on these faults (i.e., events with $M_W = 5.4$ that did not follow within 1 week and 100 km of another mainshock) had foreshocks in the 1-hr \times 15-km window, consistent with the observations of Discovery and Gofar faults (6 of 9). Table 3.2 suggests that foreshocks are more likely for $M_W \geq 5.5$ events (8 of 13) than for $5.3 \leq M_W \leq 5.5$ events (2 of 6), but longer hydroacoustic catalogs will be required to confirm this trend.

Table 3.2:

CMT ID	Year	Day	Fault	MW	Nf	Na
080596D	1996	218	Y	5.3	0	3
051397A	1997	133	W	5.3	1	0
033199C	1999	090	W	5.3	0	5
042601D	2001	116	S	5.3	7*	9
072197B	1997	202	W	5.4	0	1
100898B	1998	281	W	5.4	0	4
102000B	2000	294	G	5.4	2	1
091899A	1999	261	G	5.5	0	5
091701D	2001	260	W	5.5	0	3
111099A	1999	314	Y	5.5	14	7
111598E	1998	319	D	5.5	1	7
081200B	2000	225	S	5.5	2	3
0730001B	2001	211	D	5.6	0	0
032597D	1997	084	G	5.6	1	0
042601C	2001	116	S	5.7	1	8
040797D	1997	097	G	5.7	0	1
082396D	1996	236	D	5.8	1*	5
051098C	1998	130	S	5.8	0	8
051198A	1998	131	S	5.8	11*	18
082396D	1996	236	D	5.9	3	2
062601H	2001	177	D	6.0	2	3
081597B	1997	227	G	6.2	2	12

EPR earthquakes in both the Harvard CMT and NOAA-PMEL Catalogs. Foreshocks and aftershocks are events within ± 15 km and 1 hour of a mainshock, based on NOAA-PMEL locations. The source fault for each earthquake are denoted by W (Wilkes), S (Siqueiros), Y (Yaquina), D (Discovery), G (Gofar). Events with an asterisk next to their foreshock counts are disqualified by the declustering algorithm used in the text; e.g., these mainshocks occurred within 1 week and 100 km of a previous mainshock. Table 3.3 contains two earthquakes on the Gofar fault from July, 2002, that are not yet included in the NOAA-PMEL catalog. Inspection of the seismograms from the GSN station PAYG on the Galapagos Islands indicates that these events were preceded by a $M_W = 5.0$ earthquake in the 1 hour beforehand (Figure 3-1). The ISC located the $M_W > 5.0$ events on the Gofar fault. The NOAA-PMEL locations for these (and smaller) foreshocks will constitute a prospective test of our prediction algorithm in the time period following our 1996-2001 training set.

Table 3.3:

CMT ID	Year	Day	MW	Fault	Nf	Na
061702B	2002	168	5.8	G	1	3
061702C	2002	168	6.0	G	2	2

Similar to Table 3.2, but for events occurring after the current end of the NOAA catalog. These earthquakes are shown in Figure 3-1.

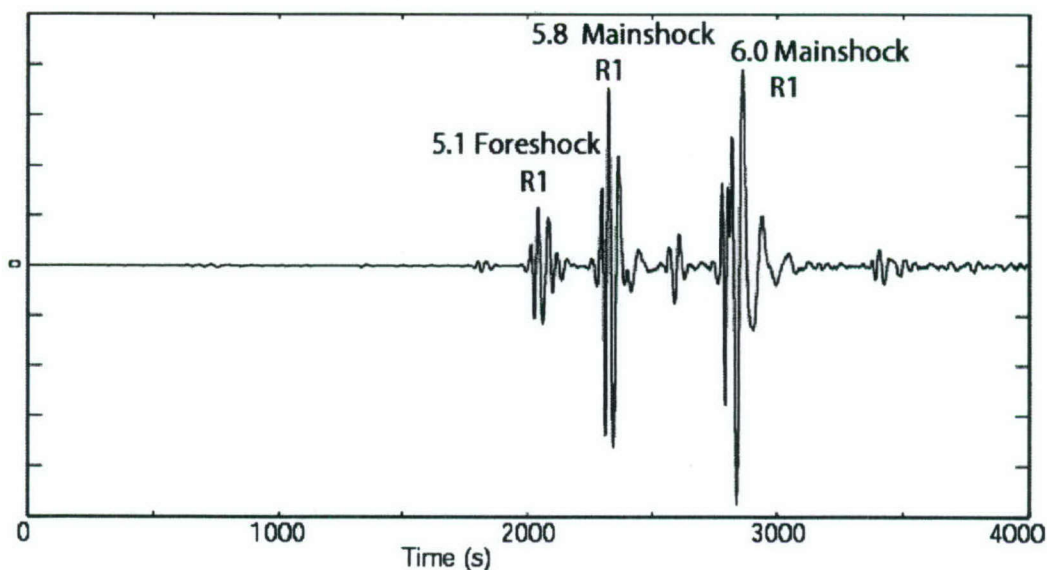


Figure 3-1: Vertical component seismogram from station PAYG (Galapagos) for a 4000-s period on June 17, 2002, when a series of large earthquakes ruptured the Gofar fault (epicentral distance ≈ 1000 km). The Rayleigh-wave arrivals are labeled for four earthquakes, the last two of which have moment magnitudes listed in the Harvard CMT catalog. The arrivals are nearly identical at low frequencies, suggesting all three events ruptured the Gofar fault.

3.3.2 Declustering

Three earthquakes in Table 3.2 were not used in either Figure 3-4 or 3-6 because they occur within 100 km and 1 week of a previous CMT earthquake, and thus their foreshock and aftershock counts are potentially elevated. While these events were disqualified to conform to standard catalog analysis, each event has a foreshock sequence that can be distinguished from the previous event's aftershock sequence. Figure 3-2 shows the clear clusters of activity before the two Siqueiros events that are spatially and temporally distinct from the previous aftershock sequence. Thus, the three disqualified events also show evidence of the extended (~ 1 hr) fault preparation process implied by the sequences in Figure 3-2. We did not attempt to decluster based on the ASL estimates provided by the NOAA-PMEL catalog because (1) these values show large scatter when correlated with surface-wave and moment magnitudes, and (2) for the typical aftershock sequence depicted in Figure 3-3, the difference in magnitude between the mainshock and largest aftershock (Båth's law [Båth, 1965]) is typically 2.4 units. Therefore only mainshocks larger than magnitude 5.0 would contribute aftershocks to the T-phase catalog, which has detection threshold of 2.5-3.0. Thus, the

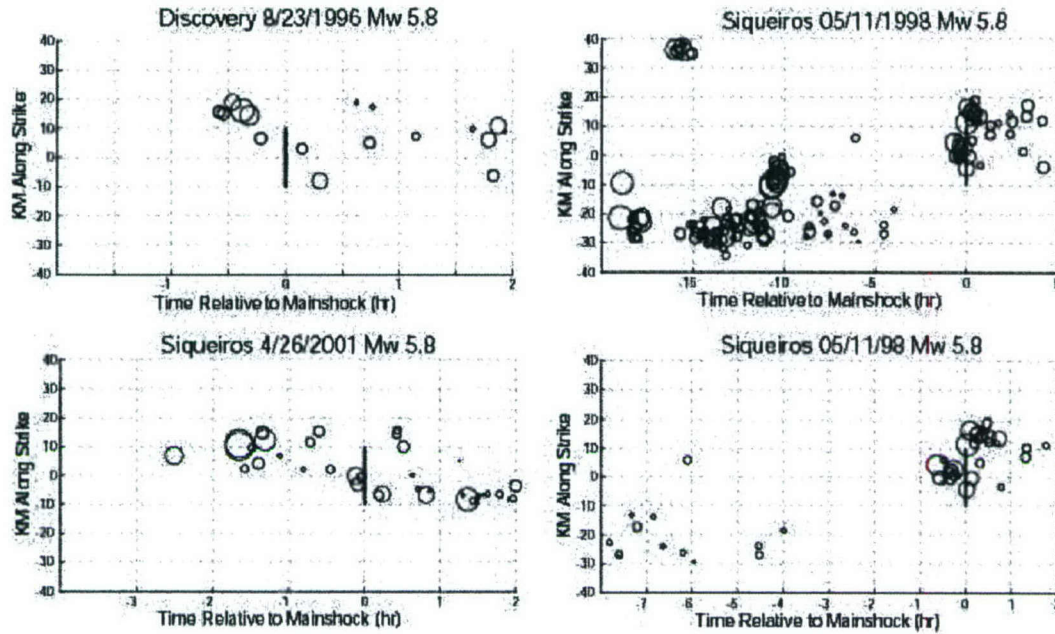


Figure 3-2: Space-time plots of the seismicity surrounding the 3 CMT catalog events that were excluded by our declustering procedure (see methods). The plot is shown at two different scales for the 5/11/98 event. The symbol size is scaled according to the ASL for each event. The two Siqueiros events show foreshock sequences in the last half-hour before the mainshock that appear to be distinct from the aftershock sequence of the preceding event.

foreshock counts in Table 3.2 are not likely to be contaminated by aftershocks triggered by events too small to be included in the CMT catalog.

3.3.3 Sensitivity to Parameter Choices

The observed foreshock/aftershock ratio in Figure 3-4 depends on the temporal and spatial windows. Although 30 km windows are probably best for minimizing bias in this ratio, the results were found to be insensitive to variations in window size from 15 to 100 km (Figure 3-4). Moreover, 30 kilometers corresponds to a clear drop-off in the spatial clustering in Figure 3-2A, as well as being about twice the expected rupture length of the largest ($M_W = 6.2$) mainshock in our dataset. We tested the dependence of the foreshock/aftershock ratio on time windows up to a month long (Figure 3-3). For Southern California events, the implied values of n were near 1, consistent with previous studies [Helmstetter, 2003; Helmstetter *et al.*, 2005], except for large foreshock time intervals, where foreshock counts were contaminated by background seismicity. Our conclusion that the foreshock/aftershock ratio for

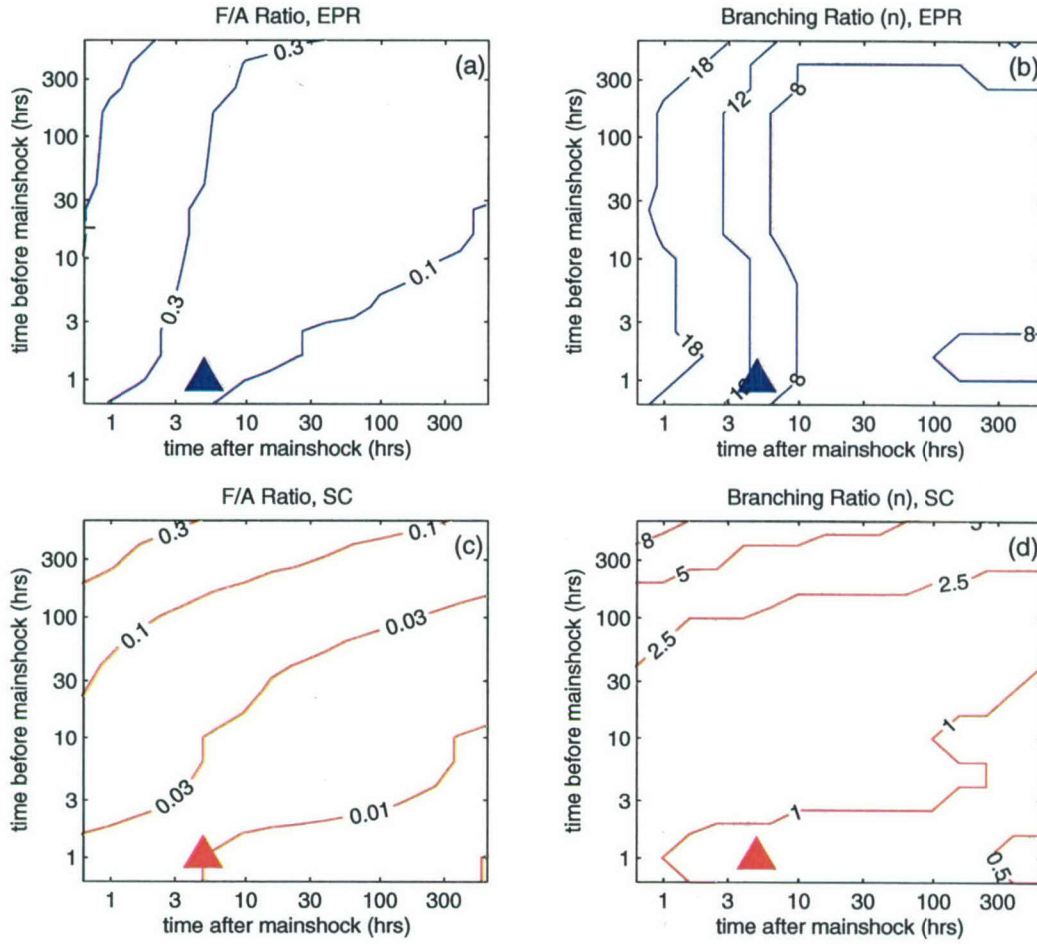


Figure 3-3: Effect of time-window length on the observed foreshock/aftershock ratio. Results are shown for the 19 mainshocks from 5 active EPR faults in (a) and the 24 mainshocks from Southern California (SC) in (c). Foreshocks and aftershocks were counted within 15 km of the mainshock and in the magnitude range 0 to 2.8 units below the mainshock M_W . EPR events were taken from the NOAA-PMEL catalog and SC events were taken from the SCEDC catalog. The branching ratios for EPR events in (b) and for SC events in (d) were calculated from Eqn. 1 assuming $\Delta m_2^{f,a} = 0$, $\Delta m_1^{f,a} = 2.8$, $b = 1$, and $\alpha = 0.8$. Triangles show the window lengths used in Figure 3-4.

EPR faults is substantially larger than that for Southern California is robust with respect to large variations in spatial and temporal window lengths (Figure 3-3).

3.3.4 Estimation of α and n

The lack of a uniform magnitude scale for measuring RTF earthquakes over a wide range of sizes introduces uncertainties into the estimates of n and α obtained from the magnitude dependence of aftershock rates. In Figure 3-3, we used M_W from the Harvard CMT catalog to measure mainshock magnitude and M_S values from the ISC catalog, recalibrated against M_W as was done in Chapter 2, to measure aftershock magnitude. A maximum-likelihood fit to these data gave $n \approx 0.1$ for the global RTF data set (for $\alpha = 0.72$), but the 95% confidence region of this fit is large. There are numerous mainshocks (more than 400 total) that control the end of the line at low values of $m_{\text{main}} - m_0$, but relatively few (about 20) with $m_{\text{main}} = m_0 > 1.5$ to pin the high end of the curve.

The NOAA-PMEL catalog can be used to estimate the number of aftershocks at much smaller magnitudes than the global catalogs, and thus to constrain α . We counted aftershocks on EPR transforms in the first day after the $M_W \geq 5.7$ mainshocks, obtaining an average value of 59 per mainshock. The appropriate value of $m_{\text{main}} - m_0$ to use with this frequency was highly uncertain, however, owing to the M_{ASL} uncertainty; according to published estimates, the detection threshold could be anywhere from about 1.8 [Fox *et al.*, 2001] to 2.9 [Bohnenstiehl *et al.*, 2002] with some claimed detections [Fox *et al.*, 2001] as small as $m_b = 0.5$. We determined a very conservative lower bound on α by assuming the NOAA-PMEL catalog is complete down to $M_W = 1.0$. Combining the EPR counts with the global RTF aftershock data from Figure 3-3 in the same maximum likelihood fit requires $\alpha > 0.6$. The EPR aftershock data do not provide a clear upper bound on α , and even permit values greater than one, but the combination of the EPR and global RTF datasets constrain n to be smaller than about 0.3. Another potential source of uncertainty is that the aftershock rates of EPR faults could be greater than the global RTF average. However, large earthquakes on the Blanco Transform of the Juan De Fuca Ridge also show similarly numerous small magnitude (hydroacoustically detected) aftershocks [Dziak *et al.*, 2000], suggesting that relatively large values of α characterize RTF behavior over a significant range in spreading rate.

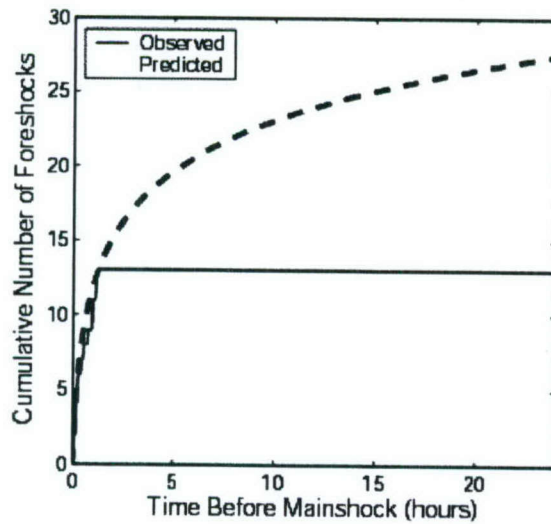


Figure 3-4: A comparison of the inverse Omori law for $p' = 1$ (dashed line) with the stacked foreshock sequences from Figure 3-3 (solid line). The inverse Omori law provides a reasonable fit to the foreshock rate in a 1-hr period before the mainshocks, but it is inconsistent with the lack of any measurable foreshock activity before 1 hr.

3.3.5 Prediction Space-Time Windows

The total space-time volume filled by the alerts was calculated by integrating the space-time window of each individual alert forward in time until either the time window expired or another earthquake occurred. This approach was necessary to avoid double counting many duplicate entries of small earthquakes in the catalog with origin times only a few seconds apart.

Chapter 4

Olivine Friction at the Base of Oceanic Seismogenic Zones

Abstract

The frictional properties at the base of the seismogenic zone in oceanic lithosphere are fundamental to our understanding of earthquake processes. While the composition of the oceanic lithosphere is probably the simplest and most well constrained of any seismogenic region on Earth, few data on its frictional properties exist. Here we investigate the strength and sliding stability of olivine aggregates at temperatures and effective pressures similar to those at the base of the seismogenic zone on a typical transform fault. We conducted triaxial compression tests on dry olivine powder (particle diameters of up to $60\text{ }\mu\text{m}$) using argon as a pore fluid medium at effective pressures P_{eff} between 50 and 300 MPa, temperatures T between 600°C and 1000°C , and displacement rates V from 0.06 to $60\text{ }\mu\text{m/s}$ (axial strain rates, $\dot{\epsilon} \approx 3 \times 10^{-6}\text{ s}^{-1}$ to $3 \times 10^{-3}\text{ s}^{-1}$). In each test deformation localized onto a narrow shear plane oriented between 30-45 degrees to the direction of axial compression. Sample strength increased linearly with P_{eff} , nearly independent of temperature. Rate-weakening behavior was found at $T \leq 800^{\circ}\text{C}$ and a transition to rate-strengthening behavior was observed at $T = 1000^{\circ}\text{C}$. We speculate that the pressure-dependent strength and temperature-dependent stability can be explained with Bowden and Tabor's asperity hypothesis. At high temperatures, plastic yielding at the asperity stabilizes frictional sliding of the bulk sample. As such, a greater tendency towards instability was found at lower temperatures and higher displacement rates. Rapid compaction occurred at the start of each experiment and was followed by deformation at approximately constant volume. Lower pressure experiments showed a tendency towards dilatant behavior at high strain and high loading rates and compaction at low loading rates. Extrapolation of our experimental data is consistent with seismic data, which show earthquake hypocenters limited by temperatures near the 600°C isotherm. Moreover, in scaling our laboratory results to the strain rate conditions present in the earth, we find approximately 600°C divides the velocity-weakening, seismogenic lithosphere from the velocity-strengthening region below.

4.1 Introduction

Comparison of depths of oceanic earthquakes with thermal models indicates that the seismicity is thermally bounded, with estimates of the limiting isotherm ranging from 400°C to 900°C [Wiens and Stein, 1983; Engeln *et al.*, 1986; Bergman and Solomon, 1988; Stein and Pelayo, 1991; Scholz, 2002]. The most recent studies of oceanic transform fault seismicity indicate that the 600°C isotherm approximately bounds the base of seismogenic zone [Wilcock *et al.*, 1990; Abercrombie and Ekström, 2001, 2003]. By contrast, previous experimental work on olivine friction showed a transition from unstable to stable sliding at significantly lower temperatures, $T \approx 200^\circ\text{C}$ [Stesky *et al.*, 1974; Stesky, 1978a, b]. Here we present a resolution to this apparent contradiction between the seismically obtained focal depths and the range of depths inferred from laboratory experiments.

In our experiments, we observe shear localization in aggregates of olivine grains and investigate the experimental conditions at which the stability of frictional sliding changes from velocity weakening to strengthening. We scale our laboratory results to geologic conditions using empirical flow laws, previously determined from creep tests on olivine single crystals [Kohlstedt and Goetze, 1974; Durham and Goetze, 1977; Goetze, 1978; Evans and Goetze, 1979; Bai *et al.*, 1991]. We then discuss the processes controlling the transition from unstable to stable deformation and the conditions at which the transition is likely to occur. The experimental results presented here are consistent with the direct seismological evidence of rupture depths of oceanic transform fault earthquakes.

4.2 Experimental Design

Deformation experiments were conducted in a servo-controlled, internally-heated, gas-medium apparatus from ‘Paterson Instruments’ [see Paterson, 1990; Xiao and Evans, 2003]. Crystals of San Carlos olivine ($\sim\text{Fo}_{91}$) were ground to a powder, producing a starting grain size of less than 60 μm . Samples were oven dried, then cold pressed at approximately 5 MPa into copper jackets 26 mm in length with inner and outer diameters of 10 mm and 11.2 mm respectively. Experiments were conducted at temperatures $600^\circ\text{C} \leq T \leq 1000^\circ\text{C}$ and effective pressures $50 \text{ MPa} \leq P_{\text{eff}} \leq 300 \text{ MPa}$, where P_{eff} is confining pressure minus pore pressure $P_{\text{eff}} = P_{\text{C}} - P_{\text{P}}$. Argon was used for both the confining and pore fluid media, and volumetric strain was measured with a volumometer.

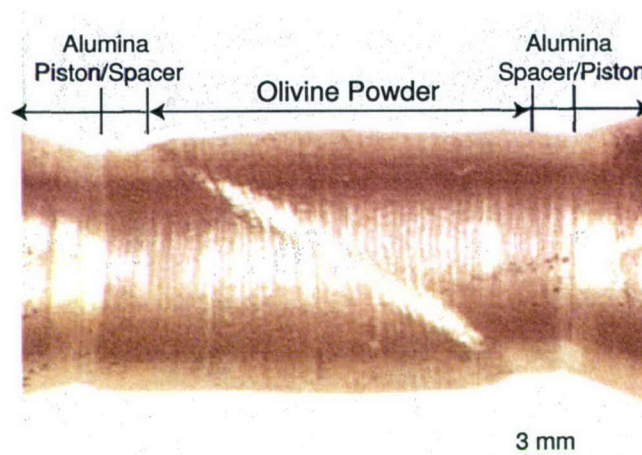


Figure 4-1: An initially cylindrical volume of olivine grains was deformed at $P_{\text{eff}} = 50 \text{ MPa}$, $T = 800^\circ\text{C}$, resulting in a localized shear zone oriented approximately 30 degrees to the shortening direction (horizontal in photograph). Sample assembly includes alumina (Al_2O_3) pistons (only piston tips are shown), 3 mm thick alumina spacers, and the sample of olivine powder. All parts of the assembly are enclosed within a copper jacket.

Prior to deformation, each sample was subject to an hour-long hot press at the experimental pressure and temperature conditions. Experiments were run at displacement rates $0.06 \mu\text{m/s} \leq V \leq 60 \mu\text{m/s}$, i.e. axial strain rates $3 \times 10^{-6} \text{ s}^{-1} \leq \dot{\epsilon} \leq 3 \times 10^{-3} \text{ s}^{-1}$. After deformation, samples were impregnated with epoxy, cut perpendicular to the shear zone, and thin sections were prepared to observe microstructures. Raw data in the form of load, axial displacement, and volumeter displacement were converted to differential stress, axial strain, and volumetric strain, assuming homogeneous deformation. For samples with no pore fluid pressure, stress was calculated assuming a constant sample volume, and for experiments in which volume changes were recorded, they were used to obtain differential stress. An example of a deformed sample is shown in Figure 4-1.

4.3 Results

The results of 13 triaxial deformation tests are summarized in Table 4.1. Experiments were reproducible, showing a variation in strength of less than 1% for tests conducted at the same conditions (e.g. OF-02 and OF-04 in Table 4.1 and Figure 4-2). All experiments were terminated prior to 5.5 mm of axial displacement. This constraint limited rotations of the stress field caused by buckling of the load column and ensured that the jacket separating

Table 4.1: Experimental Parameters

Name	T °C	P_{eff} MPa	P_C MPa	V $\mu\text{m/s}$	σ_{max}^b MPa	d_{max} mm	axial ϵ %	(a-b) -/+
OF-01	740	300	300	0.6	395	2.37	10.4	—
OF-02	800	300	300	0.6	510	4.22	20.8	—
OF-03 ^a	800	300	300	n/a	n/a	n/a	0	n/a
OF-04	800	300	310	0.6	495	4.56	21.4	—
OF-05	800	50	300	0.6, 6	125	2.66	14.1	—
OF-06	800	200	310	0.6, 6	370	3.39	16.1	—
OF-07	1000	200	300	0.6, 6	380	5.18	24.1	—, +
OF-08 ^a	1000	200	300	0.6	259	1.22	6.2	n/a
OF-11 ^a	1000	200	300	0.6	174	1.11	4.9	n/a
OF-12 ^a	1000	200	300	0.6	187	0.97	4.9	n/a
OF-13	800	100	300	0.06 - 60	205	4.80	23.8	—
OF-15	1000	100	300	0.06 - 60	225	4.11	22.6	—, +
OF-19	600	100	125	0.06 - 60	215	3.83	20.9	—

^aExperiment was stopped after little to no axial strain.

^bMaximum differential stress reached while subject to a loading rate of $V = 0.6 \mu\text{m/s}$.

the pore fluid from the confining pressure did not rupture. While the displacement range available in our experiments was restricted, the results display consistent behavior in both strength and volumetric strain.

4.3.1 Strength

The stress-displacement curves of Figure 4-2 show that sample strengths increased approximately linearly with increasing effective pressure. Samples deformed elastically for the first 0.1-0.2 mm of axial displacement. A period of work-hardening followed, which increased in duration with increasing pressure. In the higher pressure tests, $P_{\text{eff}} = 200$ & 300 MPa, work-hardening gave way to yielding and stick-slip instabilities at 3.0-3.5 mm. In lower pressure tests, $P_{\text{eff}} = 50$ & 100 MPa, the samples reached a steady-state frictional sliding stress at 1.7-2.7 mm of displacement, after undergoing a 10-15% decrease in strength. For all the data shown in Figure 4-2, sample strength eventually decreased with increasing loading rate, demonstrating rate-weakening behavior.

Sample strength showed little temperature dependence (Figure 4-3). After about 2.5 mm of axial displacement, the stress-displacement curves shown in Figure 4-3 all approach a differential stress of $\sigma_1 - \sigma_3 \approx 200$ MPa. However, temperature did effect the onset and

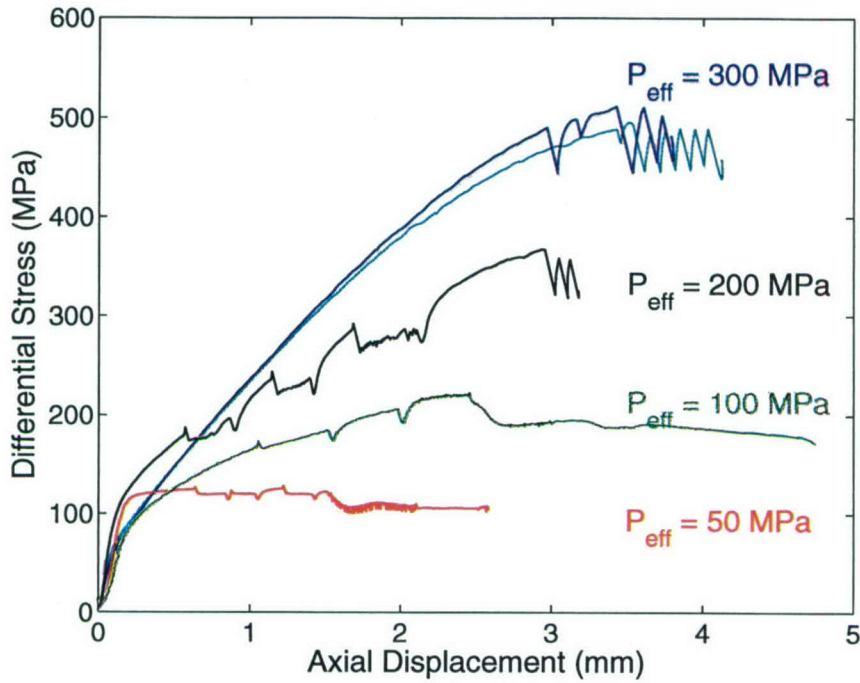


Figure 4-2: Linear increase in sample strength with effective pressure for experiments deformed at $T = 800^{\circ}\text{C}$. Steps in velocity between 0.6 and $6.0 \mu\text{m/s}$ were applied to the $P_{\text{eff}} = 50$ and 200 MPa tests and steps between $V = 0.06$ and $60 \mu\text{m/s}$ were performed during the $P_{\text{eff}} = 100$ MPa test. The $P_{\text{eff}} = 300$ MPa experiment was run at a constant loading rate of $V = 0.6 \mu\text{m/s}$. Note the similarity in the two strength profiles for experiments conducted at $P_{\text{eff}} = 300$ MPa.

rate of yielding. At higher temperatures yielding occurred at lower stress and the hardening rate was not as great. Thus the higher temperature tests required additional displacement to reach their eventual differential stress level.

Mohr circles in Figure 4-4 illustrate that a coefficient of friction $\mu = \tau/\sigma_n \approx 0.5$ fits our data well. The Mohr circles are drawn using the maximum differential stress reached while sliding at $V = 0.6 \mu\text{m/s}$ in each experiment and assuming $\sigma_3 = P_{\text{eff}}$ (Table 4.1). The linear fit between $\sigma_1 - \sigma_3$ and P_{eff} (Figure 4-4b) is consistent with $\mu = 0.5$. The nonlinear fit (also shown in Figure 4-4b) predicts a slight decrease in μ with P_{eff} , such that at low pressures $\mu > 0.5$ and high pressures μ decreases to ~ 0.4 . A decreasing coefficient of friction with increasing confining pressure has been previously observed for many rock types and by many researches [e.g. *Brace et al.*, 1966; *Shimada et al.*, 1983; *Evans et al.*, 1990; *Escartin et al.*, 1997].

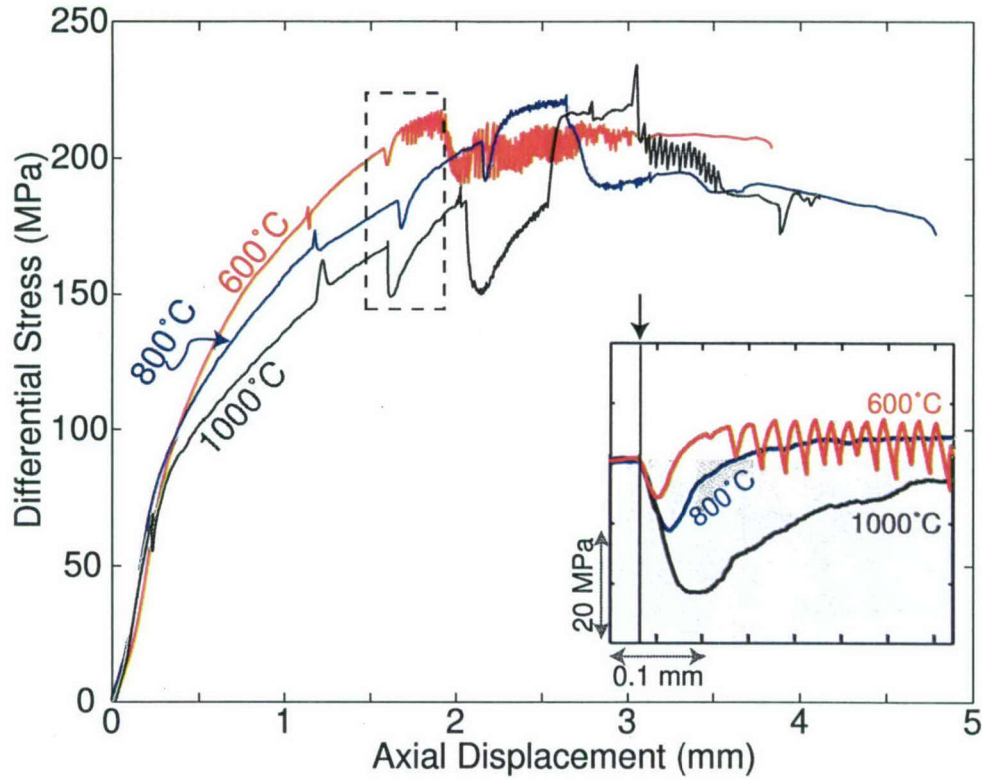


Figure 4-3: Temperature effect on the strength and stability of experiments conducted at $P_{\text{eff}} = 100$ MPa with loading rates, $0.06 \leq V \leq 60 \mu\text{m/s}$. Dashed box indicates the data plotted in the inset, where the work-hardening trend was removed and the data were shifted to the same initial strength. The arrow marks the step in loading rate from 6.0 to $0.6 \mu\text{m/s}$. Note the $T = 1000^\circ\text{C}$ data show velocity strengthening behavior (gray field), while at $T = 600^\circ\text{C}$ & 800°C the data are velocity weakening (white field).

4.3.2 Stability

The velocity-dependence of friction changes from rate-weakening to rate-strengthening as temperatures increase to $T = 1000^\circ\text{C}$. Order-of-magnitude steps in V were conducted in the $P_{\text{eff}} = 50, 100, \& 200$ MPa experiments to test the sign of the friction rate parameter, $a - b$, of the rate-state constitutive equations [Dieterich, 1979; Ruina, 1983; Marone, 1998]. In all experiments at $T \leq 800^\circ\text{C}$, potentially unstable, velocity-weakening ($a - b < 0$) behavior was observed. The rate-dependence at $T = 600^\circ\text{C}$, 800°C , & 1000°C is illustrated in the inset to Figure 4-3, which shows velocity-weakening behavior at $T = 600^\circ\text{C}$ and 800°C , with prominent stick-slip events evident at 600°C , and velocity strengthening behavior at $T = 1000^\circ\text{C}$. Another rate and state parameter D_C , which represents the distance over which a surface must slip following a step change in loading rate before friction evolves to a

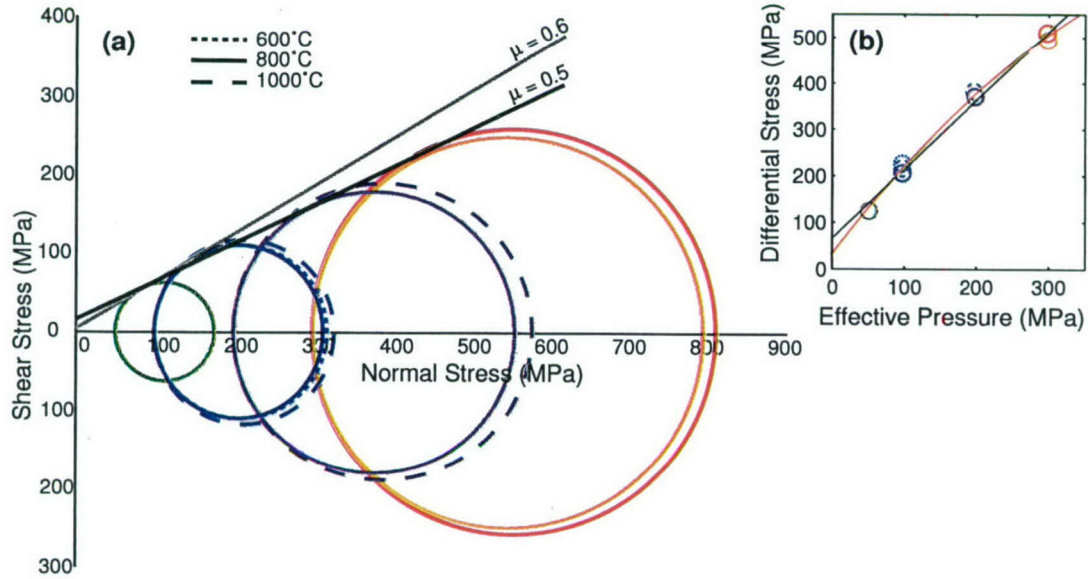


Figure 4-4: Differential strength increases with effective pressure. Data are shown for tests with $d_{\max} \geq 3$ mm (Table 4.1) at all temperatures. (a) Mohr circles, calculated with the maximum observed differential stress at $V = 0.6 \mu\text{m/s}$ show a coefficient of friction of $\mu \approx 0.5$ fits the data well. (b) Both linear (black) and nonlinear (red) least squares fits to the effective pressure and differential stress data.

new steady-state level, is also temperature dependent. The inset to Figure 4-3 shows that D_C varies from less than 0.1 mm at 600°C, to ~ 0.2 mm at 800°C, to ~ 3.6 mm at 1000°C.

The increased sliding stability at higher temperatures— a fundamental result of our study, is also shown in Figure 4-5, where higher pressure enhances the stabilizing effect of temperature on frictional sliding. At $P_{\text{eff}} = 200$ MPa the first velocity step, from $V = 0.6 \mu\text{m/s}$ to $V = 6.0 \mu\text{m/s}$, resulted in a 15% strength increase, compared to only a 5% increase at $P_{\text{eff}} = 100$ MPa. The same trend of greater $a - b$ with increased pressure can be seen throughout the initial $\sim 14\%$ of axial strain. In both $P_{\text{eff}} = 100$ & 200 MPa experiments frictional behavior abruptly changed from velocity strengthening to velocity weakening at $\sim 14\%$ axial strain, coincident with a loading rate increase from 0.6 to 6.0 $\mu\text{m/s}$.

4.3.3 Volumetric Strain

Correlating volumetric strain data, shown in Figures 4-5 & 4-6, with differential stress measurements allows us to infer the micromechanical processes taking place as the sample deforms. Compaction occurred at the start of all experiments while the samples work-

hardened. The compaction rate slowed as sample strength approached a constant level. Little to no further change in sample volume occurred after the strength decrease characteristic of high temperature and low pressure experiments. Only the lowest pressure sample, $P_{\text{eff}} = 50$ MPa, shown in Figure 4-6a, dilated appreciably. Dilation occurred during fast loading rates when the sample was weakest. Compaction occurred during slow loading rates, i.e. at higher stresses. After the drop in strength at about 8% axial strain, the sample underwent continued dilation. The compaction rate in higher pressure experiments changed with loading rate, compacting significantly faster at higher loading rates.

4.3.4 Microstructural Observations

Under continued loading, shear bands formed in the initially-homogeneous cylindrical volumes of olivine grains. These localized zones of deformation were oriented between 30 to 45 degrees to the greatest compressive stress σ_1 with a width dependent on P_{eff} and T . By conducting experiments at a range of experimental conditions we obtained microstructural fabrics at different stages of strain localization. The micrograph shown in Figure 4-7a illustrates the initiation of localization and grain size reduction within the shear zone. The 0.5-1.0 mm thick shear zone is the result of deformation at high effective pressure, where the sample remained in the first stage of deformation (work-hardening and compacting) for nearly 90% of the applied axial strain. In contrast, experiments conducted at lower pressures, such as that shown in panel 4-7b, developed highly-localized, fine-grained shear planes. The sample displayed in panel 4-7c was subject to the most axial strain and was deformed at high temperature and high pressure. Panel 4-7c shows a primary shear plane along with a number of secondary shear surfaces, indicating that a single slip surface does not always persist throughout deformation. From the thickness of the fine-grained particles, we estimate that most of the slip was accommodated by the right-most through-going shear plane, consistent with progressive strain localization. The series of shear planes is similar to those observed by *Beeler et al.* [1996], in much longer displacement tests with granitic samples, which showed migration of the primary shear surface as the experiment progressed. The limited microstructural evidence presented here suggests that localization is enhanced with increased displacement and lower pressures.

In summary, four distinct stages of deformation were observed for the olivine samples. At low strain, each experiment compacted, while increasing in strength along a work-hardening

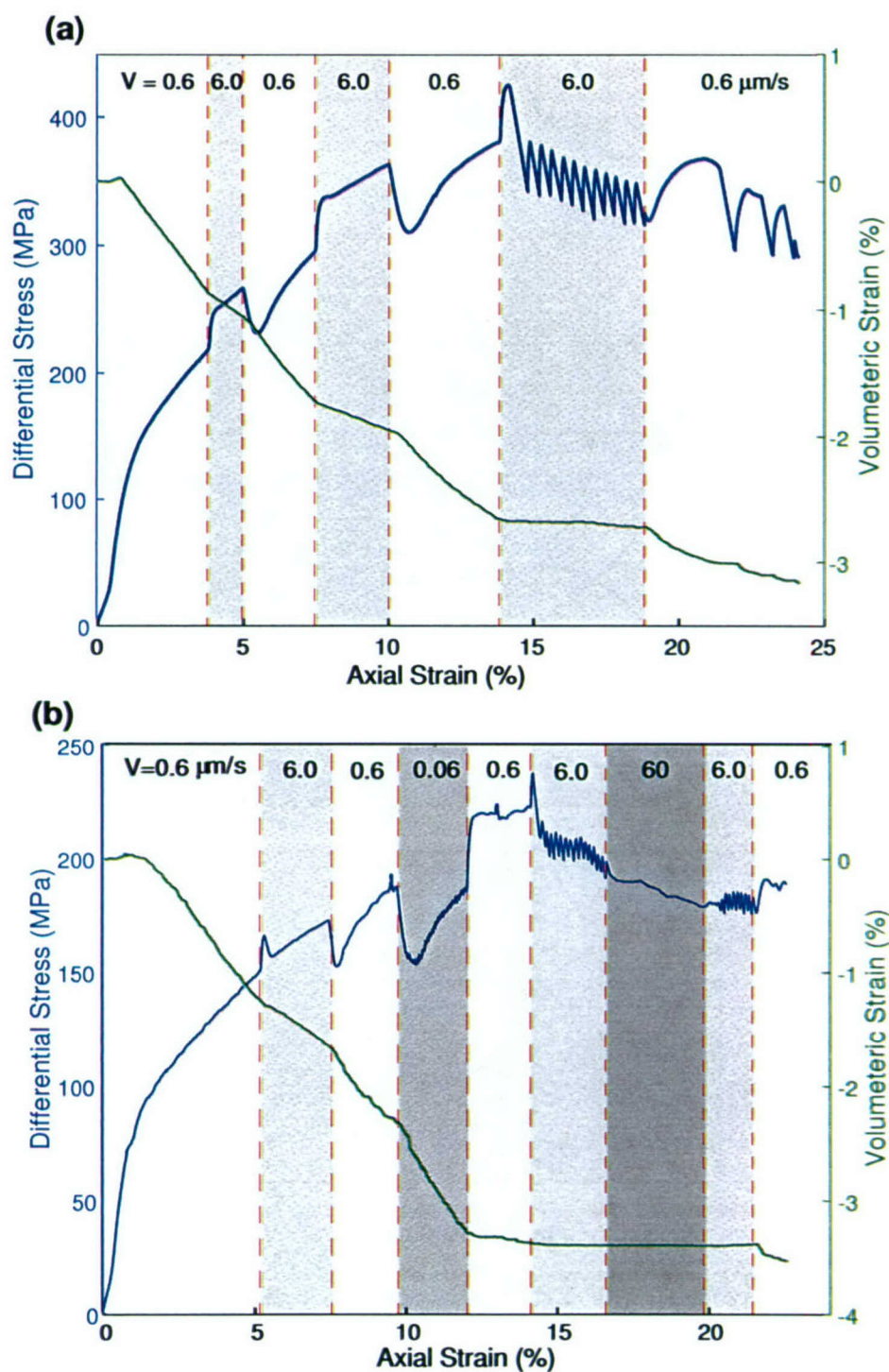


Figure 4-5: Differential stress (blue) and volumetric strain (green) data for experiments conducted at $T = 1000^\circ\text{C}$. (a) Experiment OF-07 at $P_{\text{eff}} = 200$ MPa. (b) Experiment OF-15 at $P_{\text{eff}} = 100$ MPa. Changes in loading rate, indicated with background color changes, are specified for each axial strain at the top of the plot. Note velocity-strengthening behavior is observed for the initial $\sim 14\%$ strain, followed by a change to velocity-weakening frictional conditions.

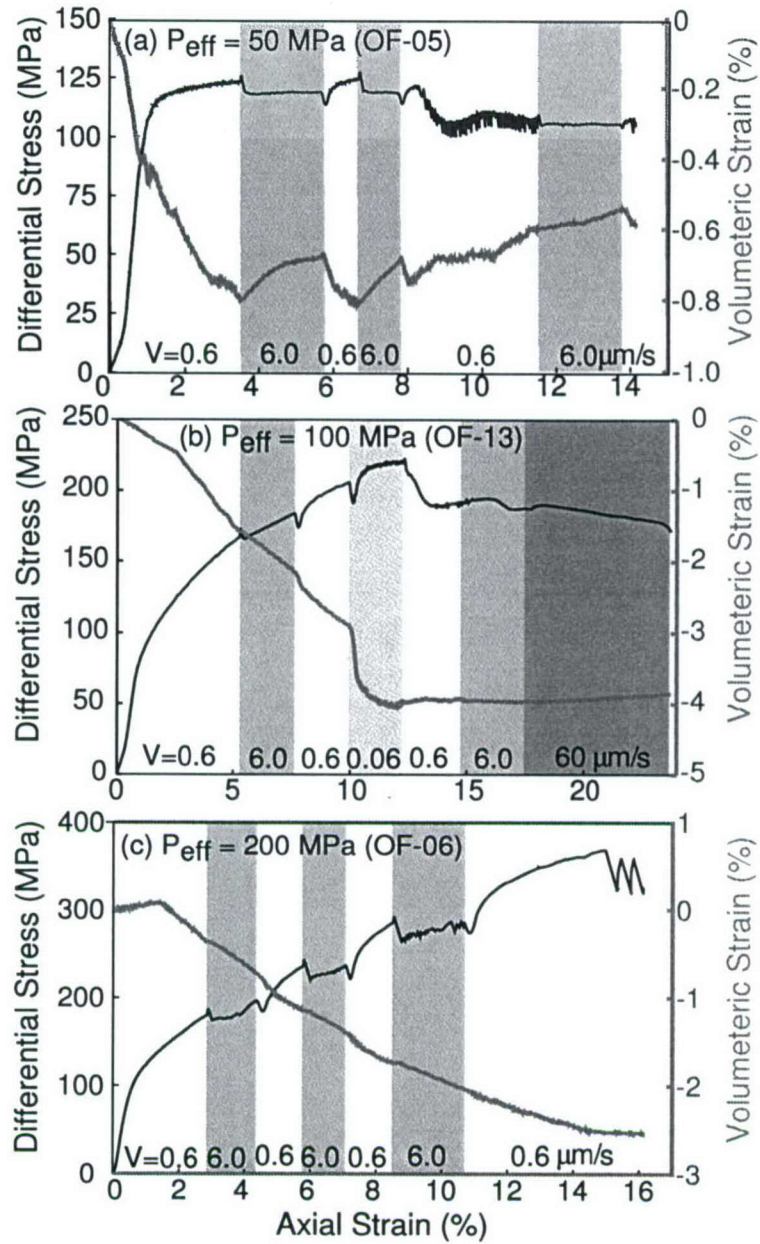


Figure 4-6: Differential stress (black curves) and volumetric strain (gray curves) for three samples deformed at $T = 800^\circ\text{C}$ and $P_{\text{eff}} =$ (a) 50 MPa, (b) 100 MPa, and (c) 200 MPa. Changes in loading rate (indicated with background color) show rate dependent effects of sample strength, compaction, and frictional behavior, which for all cases above is velocity weakening.

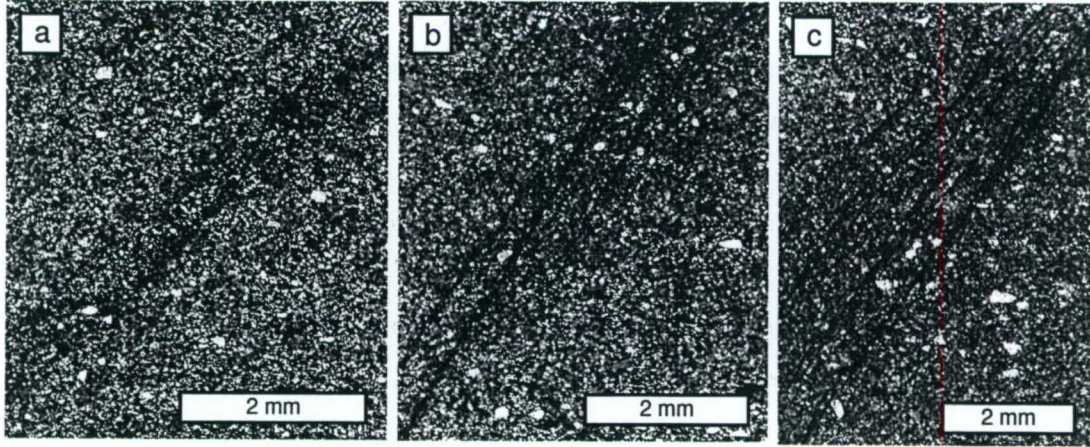


Figure 4-7: Photo micrographs of experiments deformed at (a) $T = 800^{\circ}\text{C}$, $P_{\text{eff}} = 200$ MPa (OF-06), (b) $T = 800^{\circ}\text{C}$, $P_{\text{eff}} = 50$ MPa (OF-05), and (c) $T = 1000^{\circ}\text{C}$, $P_{\text{eff}} = 200$ MPa (OF-07).

curve (e.g. Figure 4-2). During the second stage, deformation occurred at a nearly constant differential stress and the compaction rate slowed. Increasing P_{eff} resulted in an increased duration of stage one at the expense of stage two. The third stage was characterized by a strength decrease coincident with an increase or a plateau in volumetric strain. Stage three was observed between $2 \leq d \leq 4$ mm (12-15% axial strain) at high P_{eff} , compared to $d \approx 1.5$ mm ($\sim 8.5\%$ axial strain) for the lowest pressure tests (Figure 4-6). The final stage of deformation proceeded at a nearly constant stress and a small amount of dilation was observed in many samples. For low P_{eff} experiments, stage four resulted in increased instability, in which the samples exhibited periodic stick-slip events (Figure 4-6a).

4.4 Discussion

All experiments demonstrated shear localization in initially homogeneous olivine aggregates. The mechanism driving this localization may be similar to that envisioned by *Rudnicki and Rice* [1975]. An instability in the constitutive description of homogeneous deformation results in localized sliding along a shear plane within a homogeneously deforming medium. Our observations of velocity-weakening behavior superimposed on work-hardening curves (Figures 4-2, 4-3, & 4-6), suggest that the localization process initiated during the first stage of deformation when the sample was still compacting. The nucleation of localized sliding surfaces within a homogeneously compacting sample, prior to yielding at peak stress

is consistent with *Rudnicki and Rice's* constitutive model. Their description allows for localization of deformation either prior to or after the sample reaches a peak stress. We speculated that the continued localization of deformation onto a single shear plane occurred during the post-peak strain weakening. The formation of localized yielding surfaces is common to rock friction experiments, especially those at low effective pressures [e.g. *Paterson, 1978; Reches and Lockner, 1994; Wong et al., 1997*]. Additional microstructural work is necessary to better constrain the localization process, but the microstructures that we do have (Figure 4-7) indicate greater degrees of localization are obtained as deformation progresses and as compaction ceases.

The effects of pressure, temperature, and loading rate on olivine friction are systematic and are well described by the classic models of friction [e.g. *Bowden and Tabor, 1950; Greenwood and Williamson, 1966; Dieterich and Kilgore, 1996*]. In particular, our results are consistent with *Bowden and Tabor's* asperity hypothesis, which describes strong asperities that deform through both elastic and inelastic mechanisms [*Bowden and Tabor, 1950, 1966*], resulting in a linear pressure dependence of shear strength that is independent of temperature. Plastic yielding processes are inferred to dominate at high temperature [*Evans et al., 1990*], where the yield stress at the asperity contact is approximately a constant material property that is dependent on single crystal strengths. In our high temperature experiments, the onset of yielding occurs at a lower stress than for lower temperature tests, and from this we conclude that the early onset of yielding is due to plastic deformation at the asperity contacts.

Deformation of the asperity is hypothesized to occur according to flow laws determined from creep tests on olivine single crystals [*Kohlstedt and Goetze, 1974; Durham and Goetze, 1977; Goetze, 1978; Evans and Goetze, 1979; Bai et al., 1991*]. For the temperatures and strain rates used in the lab, single crystal strengths are about a factor of two to four greater than frictional strengths at the same conditions. Following the adhesion theory of friction, [*Bowden and Tabor, 1950, 1966*], this discrepancy can be explained by significant differences in the ratio of the real area of contact, A_R , to the nominal sample area, A . For single crystals the ratio $A_R/A = 1$, while for our samples of olivine aggregates $A_R/A < 1$, as depicted in the cartoon in Figure 4-8. We obtain estimates of A_R for our deformed samples, by assuming

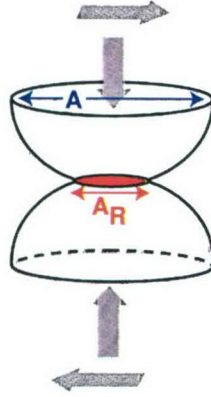


Figure 4-8: Cartoon of an asperity contact, where A is the nominal area of the sample and A_R is the real area of contact. Thick arrows denote the normal and shear forces loading the asperity (red).

that the pressure-dependent strengths we observe follow the relation,

$$\frac{\sigma_1 - \sigma_3}{\sigma_A} = \frac{A_R}{A}, \quad (4.1)$$

where the yield stress at the asperity, σ_A , is the single crystal strength. We estimate σ_A with the low-temperature plasticity flow law of *Goetze* [1978]:

$$\sigma_A = \sigma_P \left[1 - \left(\frac{-RT}{H} \ln \frac{\dot{\epsilon}}{B} \right)^{1/q} \right], \quad (4.2)$$

where the Peierl's stress $\sigma_P = 8500$ MPa, the gas constant $R = 8.3144$ J/mol/K, the activation enthalpy $H = 5.4 \times 10^5$ J/mol, the empirical constant $B = 5.7 \times 10^{11}$ s⁻¹, and the exponent $q = 2$. Equation 4.2 predicts that A_R/A will increase with temperature due to a decrease in σ_A for samples with approximately the same strength. This is what we find for the three $P_{\text{eff}} = 100$ MPa experiments shown in Figure 4-3 with the values of A_R/A : ~ 0.10 for $T = 600^\circ\text{C}$, ~ 0.16 for $T = 800^\circ\text{C}$, and ~ 0.25 for $T = 1000^\circ\text{C}$.

Assuming A_R is significantly less than A and deformation of the asperity controls the frictional behavior of the bulk sample, the velocity-weakening/strengthening transition should occur when σ_A reaches a critical value such that plastic yielding becomes the favored deformation mechanism at the asperity. For our experiments, where the transition in frictional behavior is observed at about $T = 1000^\circ\text{C}$, the critical value of σ_A is predicted in the approximate range of 800-1200 MPa. We assume that the critical value of σ_A is at the

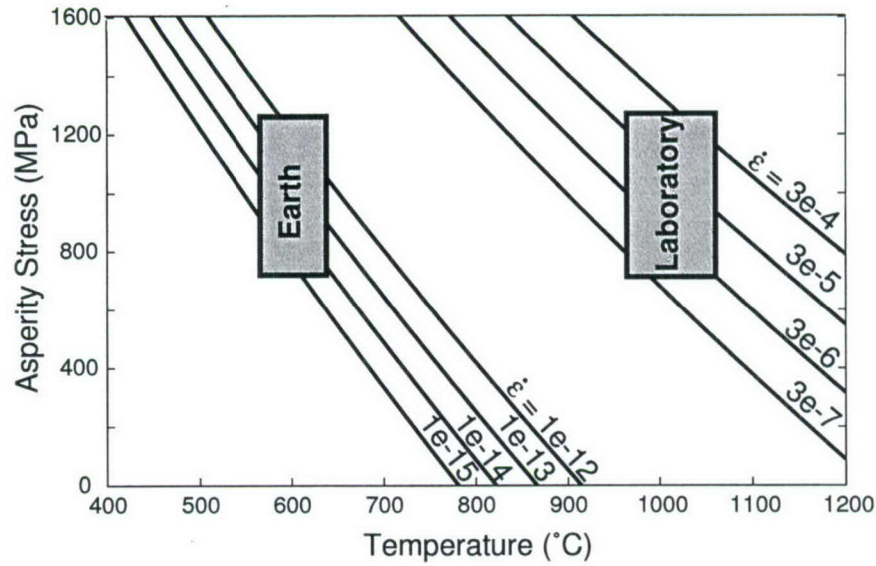


Figure 4-9: Scaling between laboratory experiments and natural conditions assuming the stress at the asperity is a constant material property. Curves calculated with equation 4.2 are shown for tectonic strain rates and for the strain rates used in laboratory experiments. Boxes indicate observed (laboratory) and calculated (Earth) conditions at which a transition between velocity weakening and strengthening behavior will occur.

brittle-plastic stability transition of the asperity and is a constant material property. Using equation 4.2, which is dependent on both temperature and strain rate, we scale the experimental conditions to conditions appropriate for the Earth (Figure 4-9). Using tectonic deformation rates $10^{-15}\text{s}^{-1} \leq \dot{\epsilon} \leq 10^{-12}\text{s}^{-1}$, we predict a transition temperature between $550\text{--}650^\circ\text{C}$, marking the base of the velocity-weakening layer. Note that at very high pressures ($P_{\text{eff}} \approx 1\text{ GPa}$) the differential stress will approach the strength of the asperity and according to equation 4.1, the real area of contact will then approach the full sample area. Therefore, under high pressure conditions ductile rather than frictional processes are expected to control deformation.

The above extrapolation of our experimental results, i.e. that the 600°C isotherm is the approximate base of the seismogenic zone in oceanic lithosphere, is consistent with observations from both seismic and aseismic deformation. Earthquake focal depths calculated from ocean bottom seismic studies [Wilcock *et al.*, 1990] and teleseismic studies using waveform modeling and slip inversions [Abercrombie and Ekström, 2001, 2003], are correlated with temperatures of $T \leq 600^\circ\text{C}$. Mylonites collected from the Shaka fracture zone on the South West Indian Ridge provide additional evidence for location of the boundary between

seismic and aseismic deformation. The microstructures preserved in the mylonites indicate that they formed during localized aseismic deformation at temperatures in the range of 600-800°C [Warren *et al.*, 2005]. Thus, our experiments, seismological observations, and microstructures from oceanic dredge samples all point to approximately 600°C as the bounding isotherm for seismic activity on oceanic transform faults.

4.5 Conclusions

Simple uniaxial compression tests of olivine powders display fundamental processes relating to fault formation and seismogenic slip. Each experiment resulted in the formation of a localized shear zone of fine-grained particles within a relatively undeformed matrix. Four characteristic stages of deformation resulted in systematic behavior of strength and volumetric strain with changes in pressure, temperature, and loading rate. The increase in strength with increasing effective pressure was observed independent of temperature. Our results spanned the frictional regimes from the velocity-weakening (potentially seismogenic) to the velocity-strengthening (stable creep), with a transition at approximately 1000°C for our laboratory conditions. As temperature increases asperity strength decreases, as determined by low-temperature plasticity flow laws, until a critical value is reached and plastic flow becomes the dominant deformation mechanism. With enhanced plastic deformation of the asperities the bulk sample becomes velocity-strengthening. Using flow laws derived from deformation tests of olivine single crystals we scale our results to conditions appropriate for the Earth. This procedure leads to the prediction that the 600°C isotherm is the approximate limit of the seismogenic zone in the oceanic lithosphere.

Chapter 5

Effects of Normal-Stress Variation on the Strength and Stability of Creeping Faults*

Abstract

A central problem in studies of fault interaction and earthquake triggering is that of quantifying changes in frictional strength and the constitutive response caused by dynamic stressing. We imposed normal-stress vibrations on creeping, laboratory shear zones to investigate the process of dynamic weakening and the conditions under which resonant frictional behavior occurs. Layers of quartz powder were sheared at room temperature in a double-direct shear geometry at normal stress $\bar{\sigma}_n = 25 - 200$ MPa, vibration amplitude $A = 0.1 - 10$ MPa, period $T = 0.1 - 200$ s, and loading rate $V = 1 - 1000$ $\mu\text{m/s}$. Frictional response varied systematically with A , T , & V . Small-amplitude, short-period vibrations had no effect on frictional strength, but large-amplitude, short-period vibrations reduced shear-zone strength by about 1%. Intermediate periods caused phase lags between shear strength and imposed vibrations. During long-period vibrations frictional strength varied sinusoidally, in phase with vibrations, and with an amplitude consistent with a constant coefficient of friction. Our data show that friction exhibits a critical vibration period as predicted by theory. At long periods the Dieterich (aging) friction law, with the Linker and Dieterich modification to describe step changes in normal stress, provides a good fit to our experimental results for all A and V . At short periods, however, theory predicts more dynamic weakening than we observed experimentally, suggesting that existing rate and state friction laws do not account for the full physics of our laboratory experiments. Our data show that normal-force vibrations can weaken and potentially destabilize steadily-creeping fault zones.

*Published as: M. S. Boettcher and C. Marone, Effects of normal-stress variation on the strength and stability of creeping faults, *J. Geophys. Res.*, v. 109, B12302, doi:10.29/2004JB003110.

Reproduced with permission from the American Geophysical Union.

Effects of normal stress variation on the strength and stability of creeping faults

M. S. Boettcher

Marine Geology and Geophysics, Massachusetts Institute of Technology/Woods Hole Oceanographic Institution Joint Program, Woods Hole Oceanographic Institution, Woods Hole, Massachusetts, USA

C. Marone

Department of Geosciences, Pennsylvania State University, University Park, Pennsylvania, USA

Received 2 October 2003; revised 30 December 2003; accepted 6 January 2004; published 11 March 2004.

[1] A central problem in studies of fault interaction and earthquake triggering is that of quantifying changes in frictional strength and the constitutive response caused by dynamic stressing. We imposed normal stress vibrations on creeping laboratory shear zones to investigate the process of dynamic weakening and the conditions under which resonant frictional behavior occurs. Layers of quartz powder were sheared at room temperature in a double-direct shear geometry at normal stress $\bar{\sigma}_n = 25\text{--}200$ MPa, vibration amplitude $A = 0.1\text{--}10$ MPa, period $T = 0.1\text{--}200$ s, and loading rate $V = 1\text{--}1000$ $\mu\text{m/s}$. Frictional response varied systematically with A , T , and V . Small-amplitude, short-period vibrations had no effect on frictional strength, but large-amplitude, short-period vibrations reduced shear zone strength by about 1%. Intermediate periods caused phase lags between shear strength and imposed vibrations. During long-period vibrations, frictional strength varied sinusoidally, in phase with vibrations and with an amplitude consistent with a constant coefficient of friction. Our data show that friction exhibits a critical vibration period, as predicted by theory. At long periods, the Dieterich (aging) friction law, with the Linker and Dieterich modification to describe step changes in normal stress, provides a good fit to our experimental results for all A and V . At short periods, however, theory predicts more dynamic weakening than we observed experimentally, suggesting that existing rate and state friction laws do not account for the full physics of our laboratory experiments. Our data show that normal-force vibrations can weaken and potentially destabilize steadily creeping fault zones.

INDEX TERMS: 7209 Seismology: Earthquake dynamics and mechanics; 8123 Tectonophysics: Dynamics, seismotectonics; 8168 Tectonophysics: Stresses—general; **KEYWORDS:** friction, earthquakes, vibrations

Citation: Boettcher, M. S., and C. Marone (2004), Effects of normal stress variation on the strength and stability of creeping faults, *J. Geophys. Res.*, 109, B03406, doi:10.1029/2003JB002824.

1. Introduction

[2] Natural fault zones are continuously subject to variations in normal stress, affecting both their strength and stability. Earthquakes alter the static stress field surrounding their rupture and send transient and potentially destabilizing seismic waves thousands of kilometers into the distance. For example, dynamic stress changes from the 1992 M_w 7.3 Landers, California earthquake are known to have increased the seismicity rates both near [Gomberg *et al.*, 1997; Wyss and Wiemer, 2000; Kilb *et al.*, 2000, 2002] and far from the fault rupture [Hill *et al.*, 1993; Gomberg and Bodin, 1994; Spudich *et al.*, 1995; Gomberg, 1996; Gomberg and Davis, 1996; Gomberg *et al.*, 1997; Harris, 1998], with the most aftershocks in the direction of rupture propagation where the dynamic stresses were largest [Hill *et al.*, 1993; Kilb *et*

al., 2000, 2002]. The strength of the Landers fault zone itself increased continuously from 1992 to 1999 until shaking from the nearby M_w 7.1 Hector Mine earthquake disrupted the healing process [Vidale and Li, 2003]. Periodic stressing from ocean and Earth tides also alter stress on faults [Brodsky *et al.*, 2003; Scholz, 2003]. Small-amplitude tidal stressing of the solid Earth did not effect seismicity rates in Southern California [Vidale *et al.*, 1998], but both Wilcock [2001] and Tolstoy *et al.* [2002] observed correlations between the larger-amplitude ocean tidal cycles and microseismicity rates on the Juan de Fuca Ridge.

[3] Much insight into the process of dynamic earthquake triggering has come from previous laboratory experiments and numerical simulations. Laboratory work of Lockner and Beeler [1999] and Beeler and Lockner [2003] showed that triggering of stick-slip events is both amplitude- and frequency-dependent. A threshold nucleation time was observed, and it was found that only large-amplitude stress perturbations triggered seismicity when the period of the

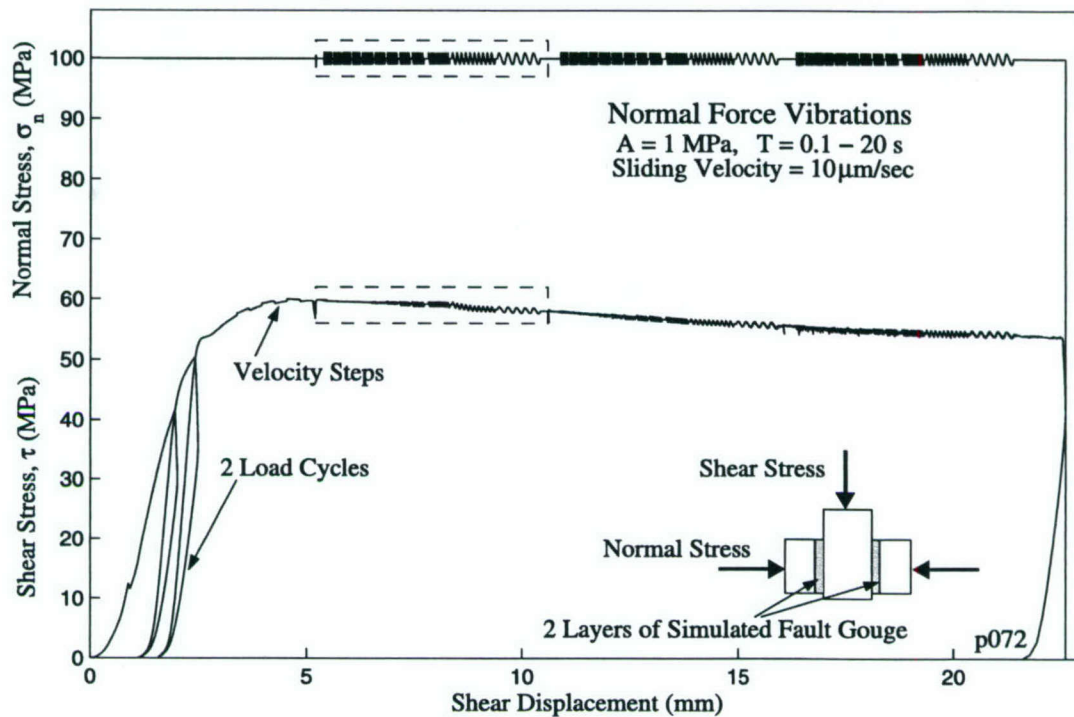


Figure 1. Imposed normal stress (σ_n) and resultant frictional strength (τ) of quartz powder during a full experimental run. The inset shows double-direct shear geometry. The central block was driven at a rate (V) of 10 $\mu\text{m/s}$, under a mean normal load ($\bar{\sigma}_n$) of 100 MPa, to a shear strain of 15. Sinusoidal σ_n vibrations, with an amplitude (A) of 1 MPa and a range of periods (T), were preceded by two load cycles and six velocity steps (10–20 $\mu\text{m/s}$). The number in the bottom right (shown here and in the figures to follow) refers to the experiment number (Table 1). Dashed boxes indicate data shown in Figure 2.

perturbations was shorter than the nucleation time [Beeler and Lockner, 2003]. Furthermore, the results of Lockner and Beeler [1999] and Beeler and Lockner [2003] are consistent with observed earthquake rates in Southern California: higher-frequency, moderate- to large-amplitude shaking from the Landers earthquake triggered seismicity, and long-period, low-amplitude, tidal stressing did not.

[4] Tworzydło and Hamzeh [1997] note that the inclusion of normal-force vibrations in models of rock friction can cause stably sliding simulations to go unstable. The work of Voisin [2001, 2002] shows that dynamic stressing of finite fault models, which obey either linear or nonlinear slip-dependent friction laws, can result in a stability/instability transition and may trigger earthquakes. Normal-force vibrations increased the healing rate of Richardson and Marone's [1999] laboratory shear zones, which when combined with the observations of Vidale and Li [2003] indicate that stress changes can both increase and decrease the rate of fault zone strengthening. Theoretical work of Perfettini *et al.* [2001] suggest a resonant response of shear zone strength, involving strong amplification of the shear stress and velocity response for a small range of friction parameters and a critical loading stiffness.

[5] Normal stress variation may also play an important role in rupture propagation. On the basis of early thoughts

on acoustic fluidization by Melosh [1979], Heaton [1990] suggested intense compressional waves could locally decrease the confining pressure ahead of a slip pulse. In the laboratory experiments of Bodin *et al.* [1998] a dynamic reduction in normal stress was observed during stick-slip events. Because normal stress should couple to slip anytime a fault has nonplanar geometry or nonhomogeneous materials, changes in normal stress are likely to be integral to both earthquake nucleation and rupture propagation.

[6] Rate and state friction laws, which have successfully modeled frictional sliding and earthquake phenomena for over two decades, were originally developed for constant normal stress conditions. In one formulation, termed the Dieterich or aging law, friction evolves during stationary contact [Dieterich, 1978, 1979], while in another, the Ruina or slip law, friction will only change with slip [Ruina, 1983]. These micromechanically distinct constitutive laws show macroscopically similar behavior under constant normal stress, but predict significantly different shear strength behavior when the steady state conditions are perturbed. Thus Perfettini *et al.* [2001] suggested laboratory experiments subject to normal stress vibrations to probe various formulations of the friction law.

[7] In this paper we report on laboratory experiments designed to investigate the effect of normal stress vibrations

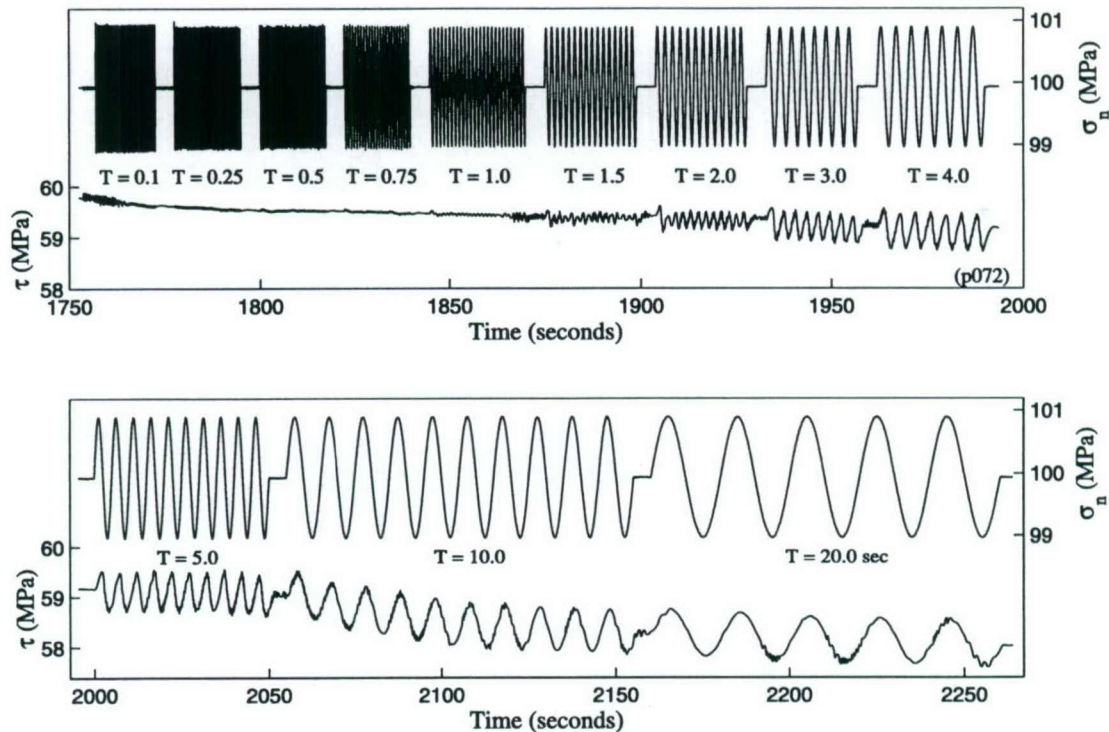


Figure 2. Frictional response (τ) of quartz powder to imposed normal stress (σ_n) vibrations during steady creep. τ oscillations increased in amplitude with vibration period (T). The character of τ oscillations evolved from no response at the shortest periods tested, to small-amplitude, sawtooth-shaped oscillations, to large-amplitude, symmetric sinusoids at the longest periods. The data are from the first vibration set of Figure 1 (dashed boxes).

on the strength and stability of steadily creeping shear zones. We show that shear zone strength varies systematically with vibration period, amplitude, and loading rate, in some cases resulting in dynamic fault weakening. We investigate the ability of the Dieterich and Ruina rate/state friction laws to model our laboratory observations and find that the Dieterich law provides the best fit.

2. Experimental Procedure

[8] Experiments were conducted in a biaxial loading apparatus at room temperature using double-direct shear geometry (inset to Figure 1) [see *Mair and Marone, 1999; Karner and Marone, 2001; Frye and Marone, 2002*]. In each experiment two, 3-mm-thick layers of quartz powder (U.S. Silica Co. F-110) were sandwiched between three steel forcing blocks. The two outer blocks have dimensions of $5.25 \times 5.0 \times 2.5 \text{ cm}^3$ and the central block measures $7.5 \times 5.25 \times 3.75 \text{ cm}^3$. The central block is longer than the side blocks and thus the nominal area of contact is constant during sliding. All blocks have grooves perpendicular to shear that constrain sliding to within the gouge layer, rather than along the gouge/steel interface.

[9] Vertical motion of the central forcing block was servo-controlled by displacement feedback and horizontal stress was maintained with constant load feedback. The

force applied to each block as well as its position was measured and recorded by displacement transducers and load cells mounted on the driving rams just above the forcing blocks. Gouge layer thickness was calculated from displacement of the horizontal ram using the calibrated apparatus stiffness and elastic corrections. In some experiments, three Belleville disc springs were inserted into the standard load column to reduce the system stiffness from its intrinsic value of $k = 0.5 \text{ KN}/\mu\text{m}$. Together the springs are rated to support 300 kN, which is the shear force necessary for sliding at 57 MPa normal stress. The springs were therefore most effective at low loads, reducing k to 0.041, 0.047, and 0.052 $\text{KN}/\mu\text{m}$ at normal stresses of 25, 50, and 100 MPa, respectively.

[10] Significant shear strain is required to obtain steady state frictional behavior in laboratory experiments [e.g., *Beeler et al., 1996; Mair and Marone, 1999*]. To reduce the net displacement needed to establish steady state shear zone fabric, and thus steady state frictional behavior [Marone, 1998], we began each experiment with load cycles and velocity steps following the procedure of *Frye and Marone [2002]* (Figure 1).

[11] We ran experiments at a constant load point velocity V in the range 1–1000 $\mu\text{m/s}$ and a $\bar{\sigma}_n$ between 25 and 200 MPa (Table 1). Sinusoidal oscillations of the normal load were imposed on the sample by summing on

Table 1. Experimental Parameters

Experiment ^a	σ_n , MPa	T , s	A , MPa	V , $\mu\text{m/s}$
m479	25	0.1–10	1,2,3	10
m480	25,35	0.1–10	2,3	10
m481	25,35	0.1–10	2,3	10
m484	25,100	0.1–10	4,10	10
m485	25,200	0.1–10	1,2	100
m489	100	0.1–10	5	100
m491	100	0.1–2	1.08	100
m494	100	0.1–2	1.10	100
m495	100	0.1–2	0.5	100
m520	100	0.1–4	1.0	100
m521	100	0.1–0.7	0.945	100
m522	100	0.1–0.75	0.95	100
m523	100	0.1–2	0.94	50
m526	100	0.1–2	1.0	10
p062	100	0.1–2	10.0	50
p063	100	0.1–2	10.0	50
p064	100	0.1–2	1.0	50
p065	100	0.1–2	1.0	50
p066	100	0.1–2	1.0	50
p067	50	0.1–2	0.5	50
p068	100	0.1–2	1.0	50
p069	25	0.1–2	0.25	50
p070	100	0.1–2	1.0	100
p071	100	0.1–20	1.0	10
p072	100	0.1–20	1.0	10
p081	100	0.1–20	0.25	10
p082	100	0.1–20	0.1	10
p083	100	0.1–4	1.0	100
p084	100	0.1–0.5	1.0	1000
p085	100	0.1–10	1.0	50
p086	100	0.1–20	2.0	10
p087	100	0.1–20	0.5	10
p088	100	0.1–200	1.0	1.0,50
p089	100	0.25–0.75	0.25–2.0	100
p090	100	0.1–20	5.0	10
p091	100	2,3	1.0	10
p092	150	0.1–2	1.5	50

^aBelville disc springs were inserted into the load column for experiments p066–p092.

external signal with a constant voltage reference that was used to maintain the mean normal stress. Vibration periods T ranged from 0.1 to 200 s and amplitudes A ranged from 0.1 to 10 MPa. Experiments were conducted at room temperature (22°–25°C) and humidity (9–33%), with the exception of m485, m489, m491, and m494, which were saturated with water prior to shearing. The maximum displacement, d , obtained during an experiment was 28 mm, a shear strain of about 19.

3. Results

[12] We evaluated the effect of normal stress vibrations by comparing to periods of constant normal stress (Figures 1 and 2). Vibration period had the greatest effect of all tested parameters, including vibration amplitude, loading rate, and mean normal stress. At short periods ($T = 0.1$ – 0.75 s) the effect of vibrations was negligible. Intermediate-period vibrations ($T = 1.0$ – 5.0 s) weakened the shear zone, producing an irregular (often sawtooth-shaped) response that phase lagged the σ_n vibrations. At long periods ($T \geq 5$ s) the frictional response was sinusoidal and in phase, such that the coefficient of friction remained approximately constant. Normal stress vibrations always began with an increase in σ_n and the first peak in τ was often larger than subsequent strength oscillations (Figure 2).

[13] Figure 3 shows the technique used to quantify observed frictional response for two cases with different amplitude vibrations ($\epsilon = A/\sigma_n = 0.01$ and 0.05). We measured three quantities for each vibration interval: (1) the steady state frictional strength variation during vibrations, $\Delta\tau$; (2) the change in peak yield strength, $\Delta\tau_{\text{yield}}$, which is the difference between the shear strength prior to vibrations, τ_{ss} , and the steady state peak strength during vibrations, τ_{peak} ; and (3) the phase delay, $\Delta\phi$, which is defined as the time difference between peaks in the σ_n and τ oscillations normalized by the vibration period. Figures 4–6 illustrate the variation in $\Delta\tau$, $\Delta\tau_{\text{yield}}$, and $\Delta\phi$.

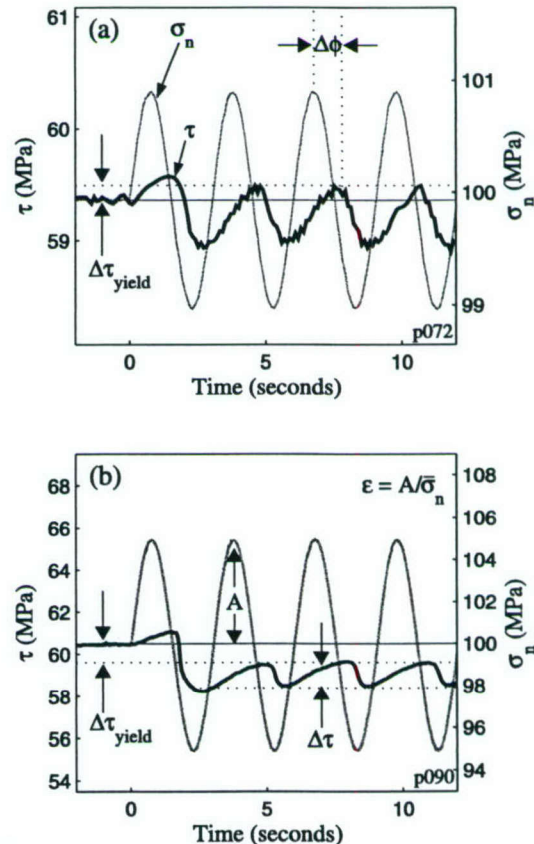


Figure 3. Quantification of the friction response to σ_n vibrations. (a) $T = 5$ s and $A = 1$ MPa. (b) $T = 5$ s and $A = 5$ MPa. The change in peak yield strength ($\Delta\tau_{\text{yield}}$) is the difference between the steady state peak τ and the initial level prior to vibrations. Note that $\Delta\tau_{\text{yield}}$ can be positive or negative, indicating induced strengthening (Figure 3a) or weakening (Figure 3b), respectively. $\Delta\tau$ is the peak-to-peak amplitude frictional strength response to σ_n vibrations. Phase lag ($\Delta\phi$) is the time difference between the peaks of the σ_n and τ oscillations converted to angular units. Figures 3a and 3b show 1.0 and 1.65 s time shifts, corresponding to $\Delta\phi = (2/5)\pi$ and $(2/3)\pi$, respectively.

with normalized amplitude ϵ , loading rate V , mean normal stress $\bar{\sigma}_n$, and vibration period T .

3.1. Reproducibility and Noise

[14] Experimental noise, such as small stick-slip events caused by grain breakage, can obscure systematic frictional strength variation. To minimize these effects we removed noise from our data before reporting $\Delta\tau$ and $\Delta\tau_{\text{yield}}$ measurements. The full amplitude of the noise was typically between 0.05–0.5 MPa, with a median of 0.25 MPa (Figure 2). We measured the noise level prior to each vibration set and subtracted it from the full range of yield strength values to get $\Delta\tau$. Background stick-slip events have little effect on peak strength levels, thus we subtracted half of the measured noise level to obtain $\Delta\tau_{\text{yield}}$.

[15] The uncertainty in determining $\Delta\tau$ was tested using a nonlinear least squares technique. For each experiment we fit the sinusoidal function $\tau = \hat{A} \sin(2\pi(t + \Delta\phi)/T)$ to an observed time series of τ . We chose long-period time series because of their sinusoidal shape. Estimates of \hat{A} and $\Delta\phi$ and the corresponding 95% confidence intervals were obtained from a nonlinear least squares regression. The amplitude estimate \hat{A} was then transformed into a noise estimate by subtracting \hat{A} from the measured peak-to-peak amplitude of the shear stress oscillations, i.e., the peak-to-trough distance including excursions due to noise. The 95% confidence interval included our measured noise values for the long-period vibrations. This simple test could not be successfully applied to shorter-period vibrations, because a sine wave is not a good approximation to the shape of the frictional response. The good agreement between the estimated and measured values of τ at long periods indicates that our method of removing experimental noise is effective.

[16] Bars at the lower right of each panel of Figures 4–6 show the span of experimental results obtained for vibration sets conducted with the range of slip rates, normal stresses, and vibration periods listed in Table 1. These bars represent the experimental reproducibility, and thus are considered the experimental uncertainty for our data.

3.2. Effect of Vibration Period, T

3.2.1. Variation of Frictional Strength, $\Delta\tau'$

[17] A normalized frictional strength variation of $\Delta\tau' = \Delta\tau/(2A\mu_{ss}) = 1$ represents the expected τ response to σ_n vibrations, assuming a constant coefficient of friction. Figures 4a, 5a, and 6a show that for all tested vibration amplitudes, loading rates, and normal stresses, the frictional response was not able to “keep up” with short-period vibrations, resulting in values of $\Delta\tau'$ near zero. In contrast, the coefficient of friction remained nearly constant for long-period vibrations, i.e., $\Delta\tau'$ approached 1.0.

3.2.2. Dynamic Weakening/Strengthening, $\Delta\tau'_{\text{yield}}$

[18] Figures 4b, 5b, and 6b show the effect of T on the degree of dynamic weakening or strengthening, i.e., the normalized change in peak yield strength, $\Delta\tau'_{\text{yield}} = \Delta\tau_{\text{yield}}/(A\mu_{ss})$. Short-period vibrations either did not affect the peak strength or caused dynamic weakening ($\Delta\tau'_{\text{yield}} \leq 0$). In contrast, long-period vibrations always increased the peak

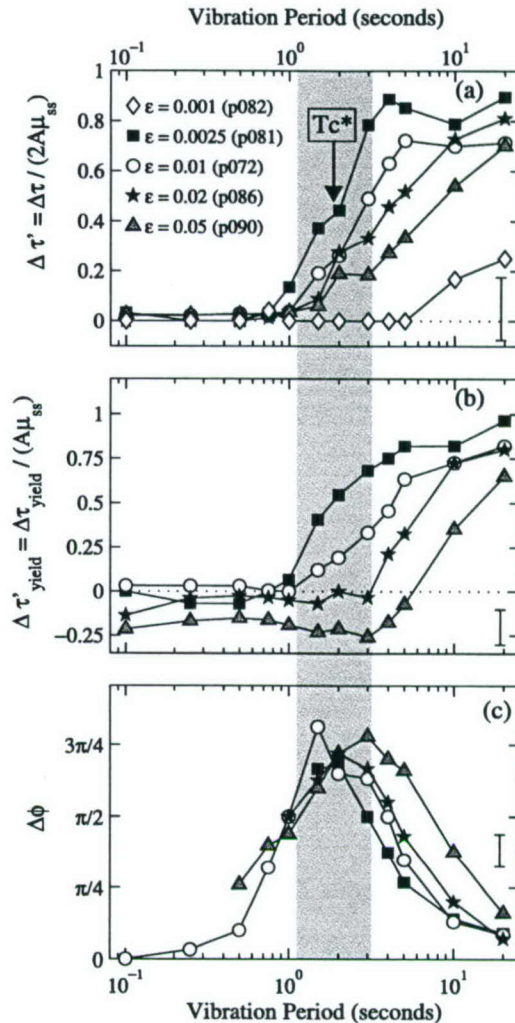


Figure 4. Effect of vibration amplitude and period on frictional strength. (a) A critical period (T_c^*), defined at $\Delta\tau' = 0.2$ (shaded bar), increased with normalized vibration amplitude (ϵ). Near T_c^* , frictional strength transitioned from a constant level ($\Delta\tau' = 0$) to having large-amplitude oscillations ($\Delta\tau' = 1$). (b) Note that dynamic weakening ($\Delta\tau'_{\text{yield}} < 0$) resulted from large-amplitude, short-period vibrations. (c) The largest phase lags ($\Delta\phi$) were observed near T_c^* , and in-phase responses were seen at both long and short periods. For some vibration sets, $\Delta\phi$ was incoherent and could not be measured. The bars in the lower right of each panel (here and in figures to follow) show experimental reproducibility. Note that $\epsilon = 0.001$ data are at the limit of our measurement resolution and are only plotted in Figure 4a. All data are from experiments run at $V = 10 \mu\text{m/s}$ and $\bar{\sigma}_n = 100 \text{ MPa}$, with $d = 6.5\text{--}10 \text{ mm}$ (strains of 4.3–6.7).

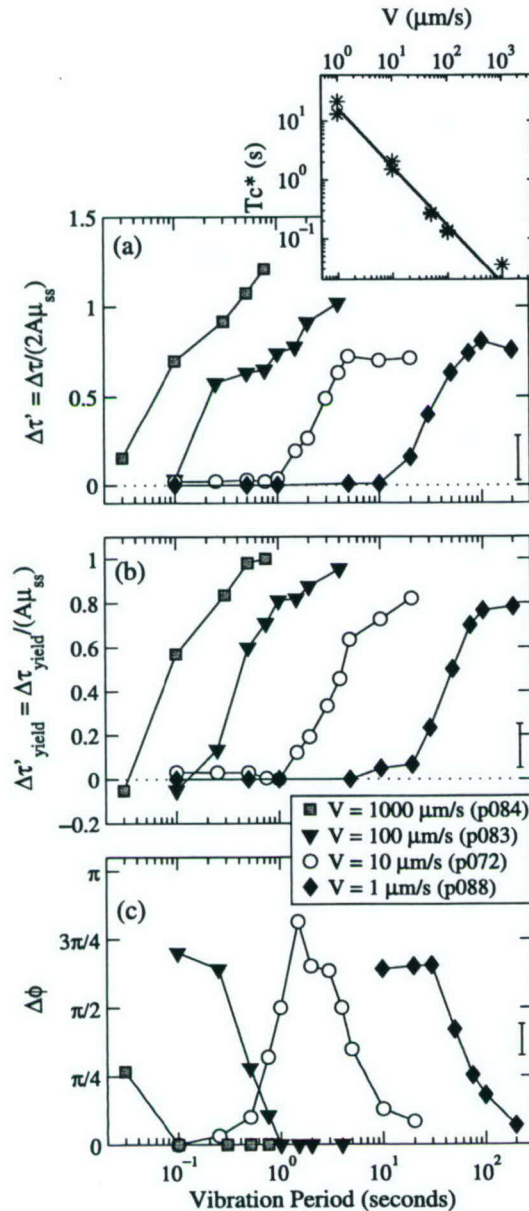


Figure 5. Effect of loading rate and vibration period on frictional strength. $\Delta\tau'$, $\Delta\tau'_{\text{yield}}$, and $\Delta\phi$ behaved systematically for all loading rates: Near T_c^* , strength oscillations increased in amplitude and phase lag reached a maximum. T_c^* decreased linearly with V , as shown in the inset. (a) Note that $\Delta\tau' > 1$ was observed for long-period tests with $V \geq 100 \mu\text{m/s}$. (b) Also note that only the fastest runs showed dynamic weakening ($\Delta\tau'_{\text{yield}} < 0$). (c) Only the $V = 10 \mu\text{m/s}$ test showed coherent short-period $\Delta\phi$ data. All experiments were conducted with $\bar{\sigma}_n = 100 \text{ MPa}$, $\epsilon = 0.01$, and $d = 6$ – 20 mm (strains of 4–13.5).

yield strength ($\Delta\tau'_{\text{yield}} > 0$). At the longest periods τ oscillated around τ_{ss} without causing an alteration in the time-averaged strength of the shear zone.

3.2.3. Phase Lag, $\Delta\phi$

[19] Phase lag $\Delta\phi$, shown in Figures 4c, 5c, and 6c, corresponds to a time or displacement scale needed to change frictional strength. When $\Delta\phi = 0$, the time or slip needed to effect a change in friction is short compared to the vibration period for a given loading rate. We find a peak in $\Delta\phi$ near the minimum $\Delta\tau'_{\text{yield}}$. At short periods, $\Delta\phi$ could not always be obtained because either τ oscillated with a period that was a multiple or fraction of σ_n , or no systematic $\Delta\phi$ was observable. The few short-period oscillations for which $\Delta\phi$ was measured suggest a tendency toward an in-phase response at short periods.

3.2.4. Critical Period, T_c^*

[20] A transition in $\Delta\tau'$, $\Delta\tau'_{\text{yield}}$, and $\Delta\phi$ occurs at a critical period T_c^* dependent on experimental parameters (shaded bar in Figure 4). We define T_c^* as the period at which $\Delta\tau' = 0.2$. This corresponds to the minimum $\Delta\tau'_{\text{yield}}$ and the maximum $\Delta\phi$. T_c^* is minimally affected by vibration amplitude and normal stress, but varies systematically with loading rate (see inset of Figure 5).

3.3. Effect of Epsilon, ϵ

[21] We studied the effect of vibration amplitudes $\epsilon = A/\bar{\sigma}_n$ between 0.001 and 0.05 (Figure 4). The total shear strength variation, $\Delta\tau$, increased linearly with ϵ (compare amplitudes shown in Figure 3). In Figure 4 we plot normalized quantities, which remove the first-order effect of amplitude. The normalization enables direct comparison of the ϵ tests at the same scale. T_c^* was near 2 s for all ϵ , with a slight, systematic increase in T_c^* with ϵ . Short-period, large-amplitude vibrations significantly affected $\Delta\tau'_{\text{yield}}$, producing the weakening shown in Figure 4b. All experiments shown in Figure 4 were loaded at $V = 10 \mu\text{m/s}$ under a mean normal stress of $\bar{\sigma}_n = 100 \text{ MPa}$. The effect of very small ϵ vibrations (< 0.0025) was below our detection limit (e.g., $\epsilon = 0.001$ in Figure 4a). Therefore only runs with $\epsilon \geq 0.0025$ were included in our analysis and in Figures 4b and 4c. Owing to the normalization of $\Delta\tau'$ and $\Delta\tau'_{\text{yield}}$ by ϵ , the two smallest-amplitude experiments shown in Figure 4 ($\epsilon < 0.01$) have larger uncertainties than those shown with the bars, and the large-amplitude tests ($\epsilon > 0.01$) have smaller uncertainties.

3.4. Effect of Sliding Rate, V

[22] We studied the effect of loading rate V between 1–1000 $\mu\text{m/s}$ and found that T_c^* decreases systematically with V (Figure 5). More subtle effects of V on $\Delta\tau'$ and $\Delta\tau'_{\text{yield}}$ were also observed. Long-period vibrations at the faster loading rates ($V = 100, 1000 \mu\text{m/s}$) resulted in $\Delta\tau' > 1$ and $\Delta\tau'_{\text{yield}} \approx 1.0$ and short periods caused slightly negative $\Delta\tau'_{\text{yield}}$ values, suggestive of dynamic weakening. At the slower loading rates ($V = 1, 10 \mu\text{m/s}$), neither $\Delta\tau'$ nor $\Delta\tau'_{\text{yield}}$ reached 1.0, indicating that the coefficient of friction varied even during long-period vibrations. The inset in Figure 5 displays the linear variation in T_c^* with V . Measurements are from the four experiments shown in Figures 5a–5c as well as additional

vibration tests at the same conditions. Performing a least squares regression, we found $T_c^* = 16.6/V$.

3.5. Effect of Normal Stress, $\bar{\sigma}_n$

[23] We explored the effect of the stiffness ratio k/k_c by conducting experiments with and without springs in the load column (Table 1) and using mean normal stress of $\bar{\sigma}_n = 50, 100$, and 150 MPa (Figure 6). The springs reduce k , the

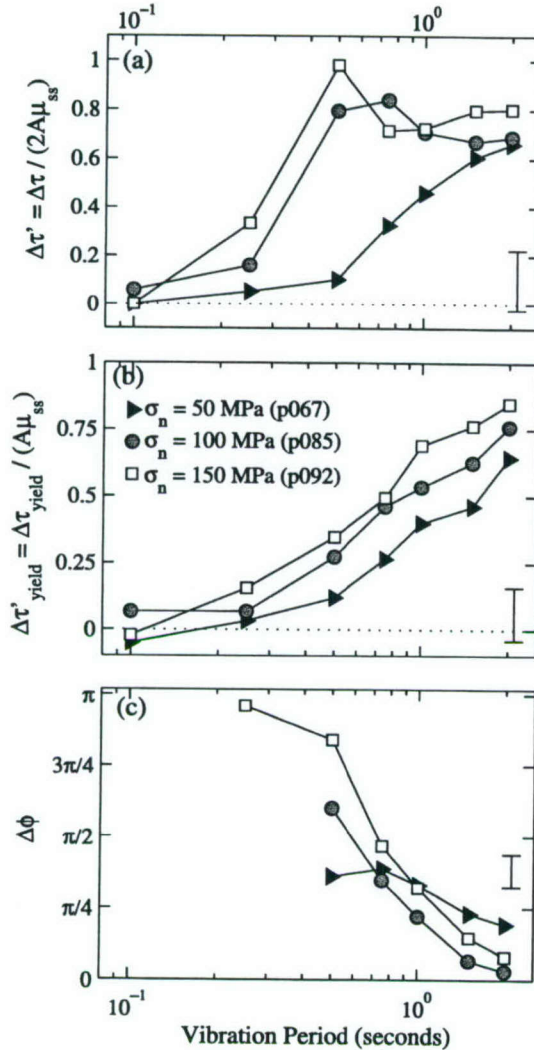


Figure 6. Effect of normal load and vibration period on frictional strength. The period at which $\Delta\tau' = 0.2$ (T_c^*) decreased slightly with $\bar{\sigma}_n$. (a) Note the peak in $\Delta\tau'$ at $T = 0.5$ s for $\bar{\sigma}_n = 150$ MPa. (b) The relative amplitude of $\Delta\tau'_{\text{yield}}$ for the three tests shows the decrease in T_c^* with $\bar{\sigma}_n$. (c) At the highest $\bar{\sigma}_n$ the shear stress response was fully out of phase with the σ_n vibrations. All experiments were conducted with $V = 50$ $\mu\text{m/s}$, $\epsilon = 0.01$, and $d = 7$ – 14 mm (strains of 4.7 – 9.3).

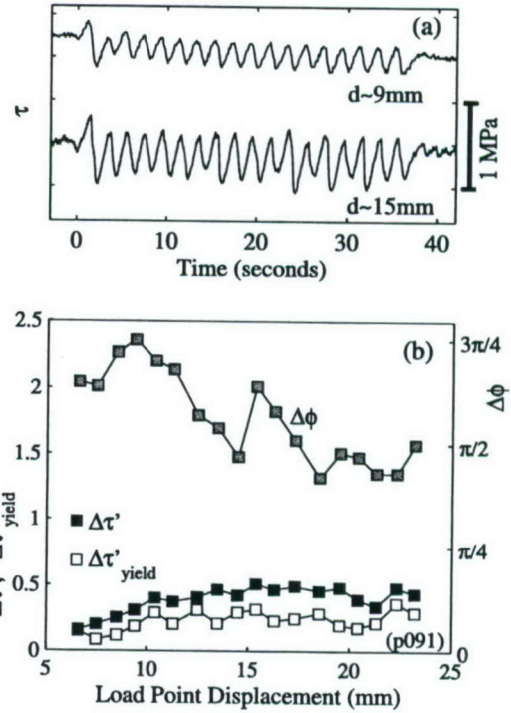


Figure 7. Effect of net shear strain on frictional strength. (a) Time series from $d = 9$ mm and $d = 15$ mm vary slightly in amplitude of both the frictional response and experimental noise. (b) $\Delta\tau'$, $\Delta\tau'_{\text{yield}}$, and $\Delta\phi$ are plotted as a function of load point displacement (e.g., Figures 4–6). Note that both $\Delta\tau'$ and $\Delta\tau'_{\text{yield}}$ changed very little after $d \approx 10$ mm (shear strain of about 6.6). Phase lag was the least stable quantity, but it remained high (near $\pi/2$) for all displacements. All data are from a single experiment with parameters $\bar{\sigma}_n = 100$ MPa, $\epsilon = 0.01$, $V = 10$ $\mu\text{m/s}$, and $T = 2$ s.

stiffness of our testing apparatus, by approximately an order of magnitude, and k increases with σ_n (as described in the experimental procedure). k_c , the critical stiffness, is given by

$$k_c = \frac{\sigma_n(b-a)}{D_c} \left(1 + \frac{mV^2}{a\sigma_n D_c} \right), \quad (1)$$

[Rice and Ruina, 1983], where a , b , and D_c are empirical friction parameters (and are discussed further below), and m is the mass of the system. A change in $\bar{\sigma}_n$ produces a greater effect on k_c than on k . Thus an increase in $\bar{\sigma}_n$ decreases k/k_c , bringing the system closer to the critical state, $k = k_c$.

[24] Figure 6 shows that the highest-normal stress (lowest k/k_c) resulted in the least systematic frictional behavior. The response to $T = 0.5$ s vibrations with $\bar{\sigma}_n = 150$ MPa is suggestive of the resonance seen in the numerical simulations of Perfettini et al. [2001]. The frictional strength oscillations, at vibration periods near T_c^* and the lowest k/k_c , were fully out of phase with σ_n . Both the large phase lags and the amplified shear strength response, indicate that

the system was closer to a critical state during low k/k_c experiments. The use of the Belleville disc springs and elevated σ_n conditions both helped to reduce the difference between the actual system stiffness and the theoretical critical stiffness, however our apparatus remained intrinsically too stiff to observe strong resonant behavior.

3.6. Effect of Displacement, d

[25] One limitation of these experiments was the small range of displacement available for study. In larger-displacement experiments [e.g., *Beeler et al.*, 1994; *Mair and Marone*, 1999] significant evolution of the shear zone was observed during initial slip, depending on σ_n . We attempted to minimize the displacement needed to obtain a steady state shear zone fabric by imposing load cycles and velocity steps at the start of each run. While the preconditioning helped, our shear zones continued to evolve at a reduced rate throughout the experiment.

[26] Data obtained from vibration sets at equal displacements were compared whenever possible. In Figures 4 and 6, where $V = 10$ and $50 \mu\text{m/s}$, respectively, we have displayed results from the first set of σ_n vibrations. However, in order to compare experiments conducted at different loading rates (Figure 5), it was necessary to use measurements from the entire range of displacement. The second and third vibration sets (see Figure 1, $d > 11$ mm) show the same systematics as the first set, however the increased frequency and amplitude of stick-slip events, which occur both during vibrations and under constant normal load, made obtaining precise measurements more difficult.

[27] In Figure 7a we show two shear stress time series taken from a single experiment with $V = 10 \mu\text{m/s}$, $\epsilon = 0.01$, $\sigma_n = 100$ MPa, and $T = 2$ s. The first is from 9 mm of displacement, and the second, with large-amplitude oscillations and an elevated noise level, is from 15 mm of displacement. Figure 7b illustrates measurements from the entire range of obtainable displacements. Very little change occurs in either $\Delta\tau'$ or $\Delta\tau'_{\text{yield}}$ past $d = 9$ mm. The $\Delta\phi$ measurements are less stable than those of shear strength. The period shown in Figure 7, $T = 2$ s, is near T_c^* for the displacement rate $V = 10 \mu\text{m/s}$ (see Figure 5d). Phase lag measurements in all experiments are observed to fluctuate most strongly near T_c^* . The variation in $\Delta\phi$ shown in Figure 7b is not large when compared with variation in $\Delta\phi$ observed for different vibration periods. Thus although displacement does have an effect on the values we report, it is minimal when compared to the effects of T , V , and ϵ .

3.7. Effect of Humidity

[28] Water content is known to affect frictional behavior [*Frye and Marone*, 2002]. We conducted four experiments under saturated conditions with $V = 100 \mu\text{m/s}$ and $\bar{\sigma}_n = 100$ MPa. Stable sliding at constant frictional strength was observed during short-period vibrations and sinusoidal oscillations resulted from long periods. Between the simple behaviors observed at short and long periods, the response at intermediate periods ($0.25 \leq T \leq 0.75$ s) was complex. Large drops in frictional strength, which approached a magnitude equal to A , occurred regularly with periods both above and below the vibration period. These large-amplitude instabilities are consistent with a more evolved shear zone and intrinsically more unstable frictional behavior.

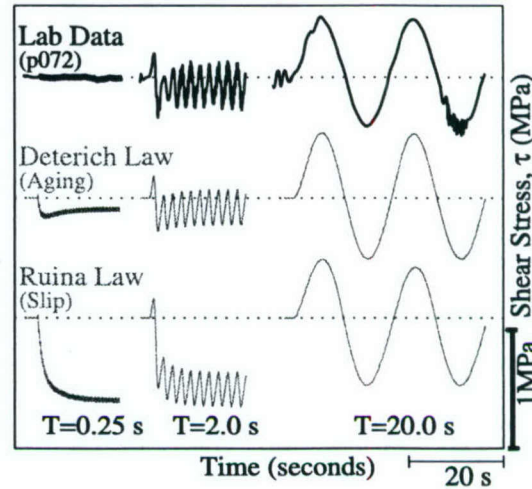


Figure 8. Time series of frictional strength for both laboratory data (black line) and Dieterich and Ruina rate/state friction models (gray lines). Note the discrepancy at $T = 0.25$ s between the predicted weakening in the models (greatest for the Ruina law) and the constant strength observed in the experimental data. The Ruina law also predicted weakening at $T = 2.0$ s. The parameters used in both models (as well as the simulations shown in the following figures) are $V = 10 \mu\text{m/s}$, $\epsilon = 0.01$, $\bar{\sigma}_n = 100$ MPa, $k/k_c = 4$, $a = 0.0015$, $b = 0.0065$, $D_c = 60 \mu\text{m}$, and $\alpha = 0.3$. The laboratory experiment was run at $V = 10 \mu\text{m/s}$, $\epsilon = 0.01$, and $\bar{\sigma}_n = 100$ MPa.

Although much can be learned from experiments in which the sample is near a critical stability transition, for this initial study we chose to focus on the systematic behavior of the more stable, low-water-content conditions.

4. Discussion

[29] The effects of normal stress vibrations on creeping shear zones are systematic and can be modeled through numerical simulations with a single set of friction parameters. We use rate and state constitutive friction laws of the standard form [e.g., *Ruina*, 1983; *Marone*, 1998]:

$$\mu = \mu_0 + a \ln\left(\frac{V}{V_0}\right) + b \ln\left(\frac{V_0 \theta}{D_c}\right), \quad (2)$$

where μ_0 is the coefficient of friction during steady sliding at velocity V_0 , V is the slip rate, θ is a state variable that evolves with either time or slip, a and b are empirical constants that respectively correspond to a direct effect and the state evolution following a change of velocity or normal stress, and D_c is the critical slip distance needed for μ to evolve to a new steady state following a change in loading conditions. In the following numerical simulations (Figures 8–15), we used values of $a = 0.0015$, $b = 0.0065$, and $D_c = 60 \mu\text{m}$, which were chosen from the range of behaviors found from modeled velocity steps in our experiments. We

compare laboratory data directly to our model results and discuss the numerical simulations of *Perfettini et al.* [2001], whose work predicts much of the systematic behavior we observe.

4.1. Evolution of the State Variable

[30] The two most often cited formulations for the friction state evolution are indistinguishable when linearized around steady state, but predict different behavior when subject to normal stress perturbations [*Linker and Dieterich*, 1992; *Richardson and Marone*, 1999; *Bureau et al.*, 2000; *Perfettini et al.*, 2001]. The Dieterich law,

$$\frac{d\theta}{dt} = 1 - \frac{V\theta}{D_c} - \alpha \frac{\dot{\sigma}}{b\sigma}, \quad (3)$$

in which the state evolves with time as well as slip [*Dieterich*, 1979; *Ruina*, 1983], predicts stable behavior for all cases of $k > k_c$, while the Ruina law,

$$\frac{d\theta}{dt} = \frac{-V\theta}{D_c} \ln\left(\frac{V\theta}{D_c}\right) - \alpha \frac{\dot{\sigma}}{b\sigma}, \quad (4)$$

in which the state changes only with slip [*Ruina*, 1983], predicts conditional stability for $k > k_c$. The above formulations include an extension of the standard rate and state equations to include changes in normal stress [*Linker and Dieterich*, 1992; *Richardson and Marone*, 1999; *Perfettini et al.*, 2001]. The term α describes the evolution of state and friction following a normal stress change from σ to σ_0 . Increasing α results in a decreased instantaneous response of the system. *Linker and Dieterich* [1992] observed a significant step in τ immediately following a sudden change in σ_n . *Richardson and Marone* [1999] also observed a step change in τ with a step in σ_n and found $\alpha = 0.3$ best fit their experimental data. We adopt $\alpha = 0.3$ for our numerical modeling and are able to model our data reasonably well with this value (Figures 8–15).

[31] We compare our experimental results to both formulations of the state evolution. Equation (3) or (4) is coupled with equation (2) and with a description of elastic interaction with our testing machine:

$$\frac{d\mu}{dt} = k'(V_p - V), \quad (5)$$

where k' is defined in terms of friction per displacement as $k' = k/(\sigma_n A_{\text{sample}})$, A_{sample} is the sample area, V_p is the load point velocity, and V is the shearing velocity along the fault surface.

4.2. Theory and Observations

[32] Figure 8 shows comparisons between experimental and theoretical time series from three sets of vibrations with periods of $T = 0.25, 2.0, 20.0$ s, loaded at $V = 10 \mu\text{m/s}$, under a mean normal stress of $\bar{\sigma}_n = 100$ MPa. Both the Dieterich and Ruina laws fit the data well at long and intermediate periods, but neither law correctly predicts the shortest period response. Both laws overpredict the magnitude of vibration-induced weakening, however the Dieterich law is much closer to the observed values.

[33] The steady frictional strength observed experimentally for short-period vibrations (e.g., the response to $T = 0.25$ s vibrations in Figure 8) implies that vibrations may not always result in an immediate step change in τ , as we have assumed with $\alpha = 0.3$. A higher value of α , i.e., $\alpha = 0.6$, is consistent with a smooth evolution to a new steady state frictional strength, rather than an immediate change in τ . However, $\alpha > 0.3$ underpredicts the amplitude of the frictional response at all vibration periods and overpredicts the phase lag for long-period vibrations. Additionally, the Dieterich law with $\alpha > 0.4$ predicts an overall strengthening of the shear zone with high-frequency vibrations, not the weakening that is experimentally observed.

[34] *Prakash* [1998] observed a continuous evolution of frictional strength following a step change in normal stress in his high-velocity ($1 \leq V \leq 30$ m/s) friction experiments. His experiments, conducted on metals and without gouge, could not be described using equations (3) and (4), and instead *Prakash* proposed a system with two state variables. While we did not observe an immediate change in τ with all normal stress vibrations, those at large amplitudes and short periods did produce an immediate effect. We proceed here with equations (3) and (4), the formulations derived from rock friction experiments, to probe the usefulness of the *Linker and Dieterich* [1992] modification to the standard rate and state equations.

[35] In Figure 9 we compare laboratory measurements and predicted values of $\Delta\tau'$, $\Delta\tau'_{\text{yield}}$, and $\Delta\phi$. Both the Dieterich and Ruina laws provide a good fit to the $\Delta\tau'$ data and the long-period response $\Delta\tau' = 1$ is indeed predicted when long-enough-period vibrations are imposed. The Dieterich law approximates the $\Delta\tau'_{\text{yield}}$ measurements, but the Ruina law dramatically underpredicts the observed values. Neither the Dieterich nor the Ruina law fits the few short-period phase lag measurements shown in Figure 9c. Both laws predict a plateau of large phase lag at short periods, while our limited $\Delta\phi$ data suggest an in-phase response at short periods. The analytical solutions of *Perfettini et al.* [2001] predict the same behavior as our numerical simulations for a system with $k/k_c = 4$ and $\alpha = \mu_{ss}/2$. They show that at long periods, $\Delta\phi \rightarrow 0$ and at short periods, $\Delta\phi$ ramps up to $\pi/2$. Phase lag measurements at $T < T_c^*$ are difficult to obtain and additional, well-resolved measurements are necessary to verify our short-period observations.

[36] While neither friction evolution law predicts all details of our observations, the Dieterich law provides a close fit. Additionally, the amplitude of the frictional response increases continuously with vibration amplitude, following the predictions of the Dieterich law [*Perfettini et al.*, 2001, Figure 4]. This continuous increase can be seen when the $\Delta\tau'$ values shown in Figure 4a are multiplied by the vibration amplitude of the test. Thus our data suggest that friction evolves with time as opposed to slip.

4.3. Dynamic Weakening

[37] Certain experimental conditions (e.g., $V \geq 50 \mu\text{m/s}$, $T < T_c^*$, $\epsilon > 0.01$) reduce the peak yield strength of the shear zone. We refer to the lowered strength as dynamic weakening, where the maximum strength reached during vibrations was reduced below the level for steady frictional sliding ($\Delta\tau'_{\text{yield}} < 0$). This weakening effect is most pronounced with large ϵ vibrations at high frequencies

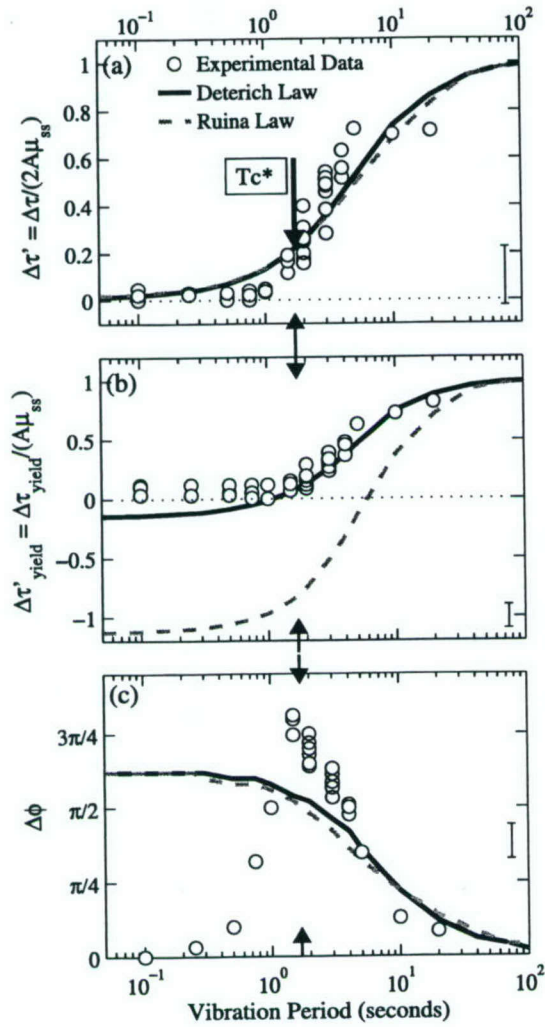


Figure 9. Effect of vibration period on frictional strength observed in laboratory data (circles) and predicted by the Dieterich (solid black line) and Ruina (dashed gray line) rate/state friction models. (a) $\Delta\tau'$ increased with T for both data and models. (b) T_c^* (indicated by arrows) corresponds to the period at which $\Delta\tau_{\text{yield}} = 0$ for both experimental data and the Dieterich law. The extreme weakening predicted by the Ruina law was not observed in the data. (c) Note that at short periods the data showed τ in phase with σ_n , while both models predicted large $\Delta\phi$. The model parameters are given in Figure 8 and the experiments were run at $V = 10 \mu\text{m/s}$, $\bar{\sigma}_n = 100 \text{ MPa}$, and $\epsilon = 0.01$.

and the weakening is well modeled with the Dieterich law (Figure 10).

[38] Using a numerical model with rate-dependent and state-dependent friction, *Perfettini et al.* [2003] found dynamic earthquake triggering to be most effective when the faults experienced high-frequency, large-amplitude

stress transients. *Bureau et al.* [2000] found similar results in their laboratory experiments of a sliding interface subject to high-frequency ($f = 120 \text{ Hz}$) σ_n vibrations. The strength reduction in their experiments was enhanced with increased vibration amplitude, providing as much as a 20% decrease in the average coefficient of friction for $\epsilon = 0.5$. The largest normal stress perturbations imposed in our experiments were an order of magnitude smaller than those of *Bureau et al.* [2000] and yielded a reduction in peak yield strength of about 1% (Figure 11).

[39] In our experiments, dynamic weakening was observed only when a large stress drop occurred during the initial decrease in normal stress. Figure 11 shows the effect of large-amplitude σ_n vibrations on the slip rate, shear strength, and layer thickness of our sample. Close to a 45-fold increase in shear zone slip rate occurs simultaneously with the 2.7 MPa stress drop during the first σ_n cycle. This stress drop was a 4.5% decrease in the shear zone strength, but over the full vibration set, the peak strength drop was only about 1%, which corresponds to $\Delta\tau_{\text{yield}} = -0.24$.

[40] Four stages of frictional behavior can be observed in Figure 11. In stage I the shear zone loses strength during a fast slip event accompanied by dilation of the shear zone. Stage I may be thought of as a seismic event that resets the state of the shear zone, i.e., $\theta = \theta_0$. During stage II the shear zone's strength is partially recovered. Figure 11c shows that strength increases over three normal stress oscillations following the initial stress drop. During the recovery period, the slipping speed remains near the background loading rate and the frictional state evolves toward a more mature level. The layer compacts following the slip event (Figure 11d) and then dilates and again compacts as σ_n cycles during stage II. While the vibrations continue the shear zone remains thinned compared to its original thickness under constant σ_n . Stage III begins where the shear strength is no longer climbing steadily and each drop in σ_n induces a small slip event (at approximately 5 s for the example shown in

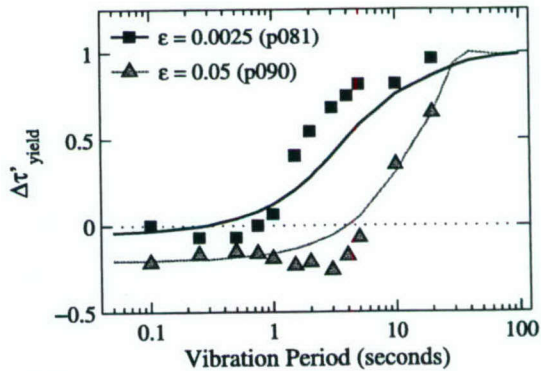


Figure 10. Effect of vibration amplitude and period on level of frictional strength observed in laboratory data (symbols) and predicted by the Dieterich rate/state friction model (lines). Large-amplitude vibrations ($\epsilon > 0.01$) caused dynamic weakening in both experimental and numerical tests. Model parameters are listed in Figure 8 with $\epsilon = 0.0025$ and 0.05 .

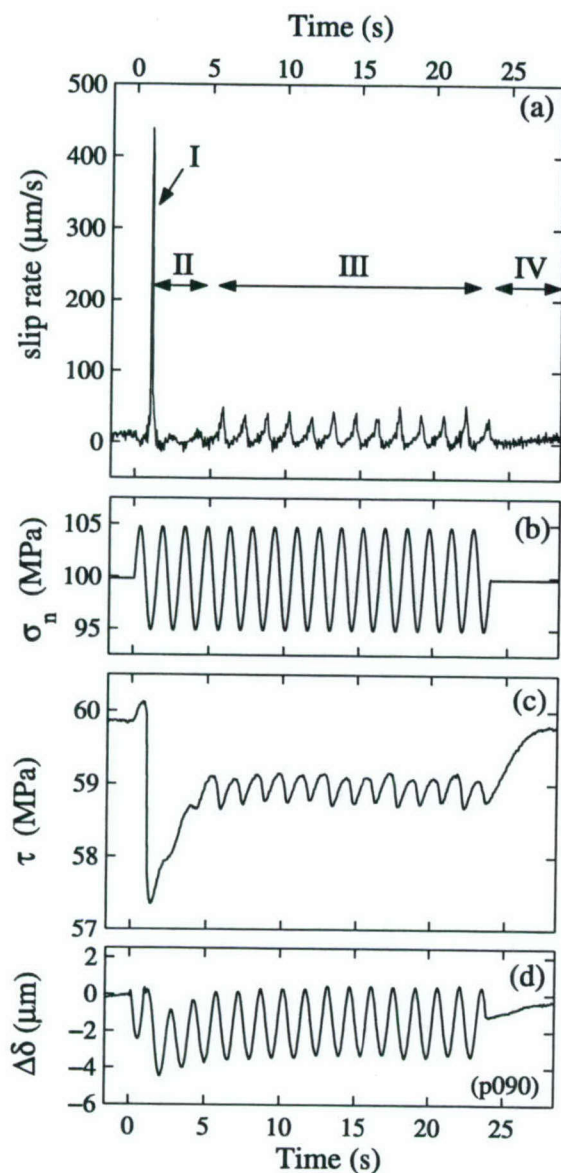


Figure 11. Time series of slip rate, normal stress, frictional strength, and layer thickness changes ($\Delta\delta$) for large amplitude ($\epsilon = 0.05$) vibrations near T_c^* ($T = 1.5$ s). Note (a) the large slip rate events, (c) the stress drops and dynamic weakening, and (d) compaction observed during vibrations. (b) Imposed vibrations started at time 0 and continued for 24 s through the four stages of frictional behavior described in the text.

Figure 11). We suspect that each slip event disrupts the particle packing, and thus reduces the frictional state of the system, such that the shear strength remains lower than the nonvibrated τ_{ss} . The compacted layer, however, is not in steady state, but instead continues to expand slowly

toward its original thickness. Finally, after the vibrations stop, a full recovery takes place during stage IV. The shear strength evolves to τ_{ss} , the layer dilates to its original value (when corrected for compaction due to geometric loss of gouge), and the slip rate returns to the background forcing rate of 10 $\mu\text{m/s}$.

[41] The difference between vibration sets that result in dynamic weakening and those that do not lies in the occurrence of the slip events. When we do not observe stage I, i.e., a large stress drop accompanied by a period of fast slip, then no dynamic weakening takes place (e.g., Figure 8). Strain delocalization, similar to that described by Sleep *et al.* [2000], accompanies these slip events. Smaller slips that occur during the continued σ_n vibrations of stage III also appear to be important in the weakening process. Thus we suspect that the earthquake-like slip events, which may reset the state variable to a less developed state, play a significant role in accommodating shear zone weakening.

[42] We note that the strength of the sample during stage III remained approximately constant, independent of the duration of vibrations (e.g., Figure 11c). This observation supports the theory presented by Sleep *et al.* [2000] that the observed healing during vibrated slide-hold-slide tests is due to a time-dependent process, rather than through mechanical consolidation, as was suggested by Nakatani [2001].

[43] Dynamic weakening appears to depend primarily on the amplitude and frequency of vibrations, rather than the number of vibrations or background creep rate of the shear zone. Figure 12 shows that a small amount of dynamic weakening is predicted at short periods for all loading rates ($1 \leq V \leq 1000$ $\mu\text{m/s}$). The model parameters are fixed to the values used in the previous numerical simulations, and again the Dieterich formulation of the rate and state theory systematically predicts the experimental data. The period at which the peak yield strength becomes positive is inversely proportional to V .

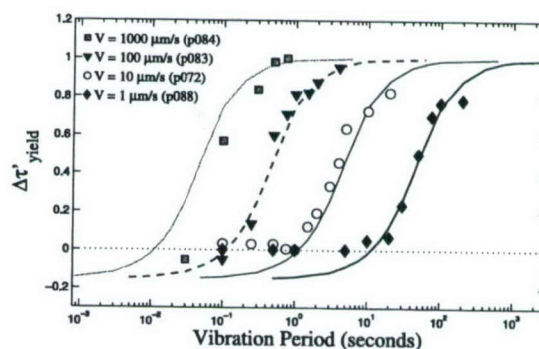


Figure 12. Effect of loading rate and vibration period on frictional strength observed in laboratory data (symbols) and predicted by the Dieterich rate/state friction model (lines). Note that while the theory matched the experimental data at long periods and the systematic variation with velocity, the predicted weakening at short periods was not observed. Model parameters are given in Figure 8 with loading rates of 1–1000 $\mu\text{m/s}$.

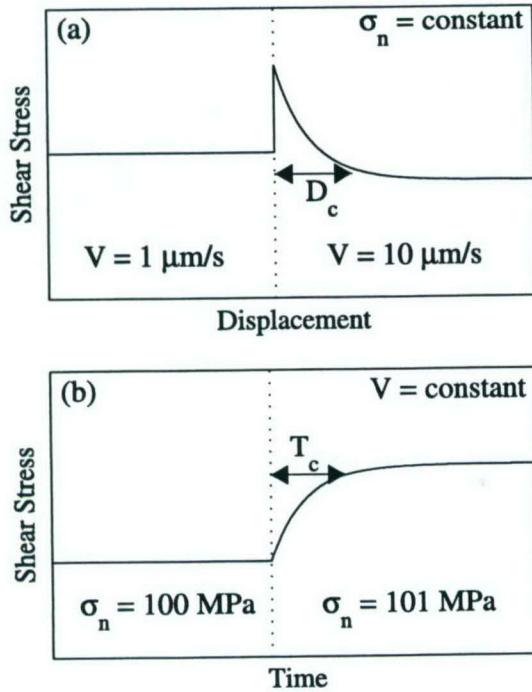


Figure 13. Critical length scales necessary to obtain a steady state frictional strength following a step in V or σ_n . (a) Under constant normal stress conditions, D_c is the critical slip distance needed to obtain a new steady state shear strength with a step in V . (b) Analogous to D_c , T_c is a critical time over which the frictional strength will evolve to a new steady state following a step in σ_n , assuming a constant loading rate. T_c is thus a critical period, below which the shear zone is continuously evolving as it attempts to respond to changes in σ_n .

The data scatter more at short periods than at long periods. The main discrepancy between data and theory is that the predicted dynamic weakening at short periods is not observed in our experiments. This may be due to inadequacies in the rate and state theory, such as the immediate response to a sudden change in normal stress.

[44] In this study we mainly focus on the destabilizing and weakening effects of vibrations, however, we see from Figure 12 that a common result of vibrations is to strengthen our samples. For most cases, the peak yield strength $\Delta\tau'_{\text{yield}}$ is positive, indicating that a dynamic strengthening processes is in affect. This is consistent with the laboratory results of *Richardson and Marone* [1999], which focused on the healing process. They found that σ_n vibrations caused increased strengthening during interseismic intervals. We emphasize that under certain conditions σ_n vibrations increase the absolute strength of a creeping shear zone while others result in dynamic weakening. In particular, high-frequency σ_n perturbations of sufficiently large amplitude will tempo-

rally reduce the strength of the shear zone, potentially bringing it closer to failure.

4.4. Resonant Conditions

[45] The stability of our experimental shear zones is dependent on three parameters: (1) the critical period, T_c , which was shown by *Rice and Ruina* [1983] to be

$$T_c = 2\pi\sqrt{a/(b-a)}(D_c/V); \quad (6)$$

(2) the critical vibration amplitude to destabilize slip, ϵ_c , that is approximately [*Perfettini et al.*, 2001]

$$\epsilon_c \approx \frac{b-a}{\mu_{ss}} \frac{1-k/k_c}{\sqrt{1+(1-\alpha/\mu_{ss})^2(b-a)/a}}; \quad (7)$$

and (3) the critical stiffness, k_c (see equation (1)). In order for our stiffness-stabilized system ($k > k_c$) to become unstable, T/T_c and k/k_c must both be very close to 1.0, and ϵ must exceed ϵ_c [*Perfettini et al.*, 2001].

[46] Figure 13 illustrates the meaning of T_c in terms of the time necessary for shear strength to evolve to a new steady state level following a single step in normal stress. As expressed in equation (6), T_c scales as D_c/V . Thus for a given loading rate, T_c scales directly with D_c , and both quantities describe a critical length scale necessary to obtain a new shear strength level. When a system is subject to periodic normal stress perturbations, rather than a simple normal stress step, we see that the vibration period strongly controls the response of the system. At vibration periods of T_c or longer, frictional strength is able to adjust continuously, allowing the layer thickness and the coefficient of friction to remain constant. Periods below T_c result in large-amplitude layer thickness changes that phase lag normal stress oscillations. The layer rapidly dilates and compacts in an attempt to compensate the imposed σ_n changes. At periods less than $T_c/10$, layer thickness fluctuations allow the shear strength to remain constant while σ_n rapidly changes. Variations in the layer thickness indicate that interparticle friction can not keep pace with the changes in normal stress. Thus periods less than T_c , in particular, $T < T_c/10$, are susceptible to instabilities such as the earthquake-like stress drops described above.

[47] Experimentally, $T = T_c$ can easily be achieved with the loading rates we used. The critical vibration amplitude $\epsilon_c = 0.0022$, obtained by inserting the friction parameters used in Figures 8–15 into equation (7), was exceeded in nearly all of our experiments. However, to achieve unstable resonant behavior, k/k_c must be reduced to near 1.0, and as shown in Figure 14 this is currently unachievable with our testing apparatus.

[48] Figure 14a, a reproduction of Figure 6 in *Perfettini et al.* [2001], shows the effect of changing k/k_c for a set of estimated friction parameters. Figure 14b is the same plot calculated using our laboratory measurements as the model parameters with our experimental data (open circles) plotted over the curves. The experimental data follow the lowermost curve, $k/k_c = 5$. We therefore conclude that the stiffness of our testing apparatus is well above the critical stiffness, and we are unable to attain resonant conditions. Additionally, the calculated frictional response for our

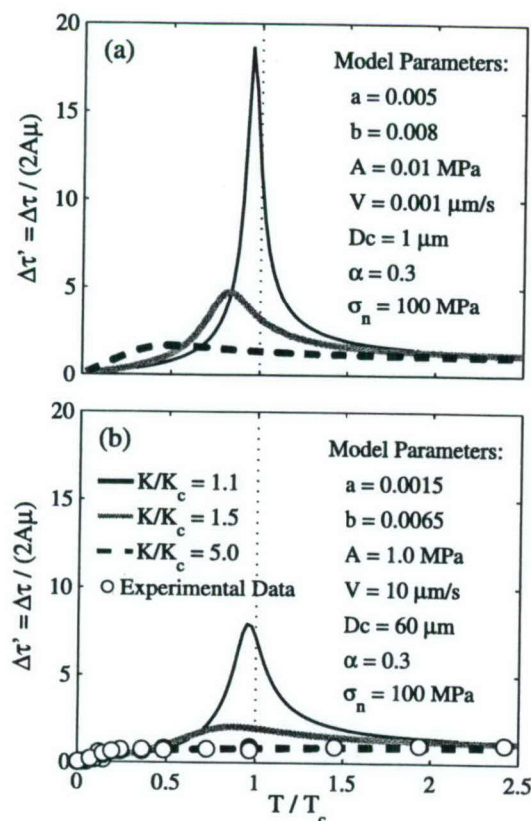


Figure 14. Analytical solutions for the effect of stiffness on frictional strength. (a) Critical parameter values that resulted in a peak response at $T = T_c$ [after Perfettini *et al.*, 2001, Figure 6]. (b) Parameters appropriate for our laboratory conditions. Note the reduced amplitude of the resonant peak at $T = T_c$ for the laboratory parameters. Superimposed on the calculated strength curves in Figure 14b are the experimental data (circles), which approximately follow the $K/K_c = 5$ curve. Equation (24) of Perfettini *et al.* [2001] was used to compute the predicted strength values.

laboratory conditions are minimal compared with the expectations for the conditions given in Figure 14a.

[49] While we do not observe resonance, Figure 15 shows that the theoretical critical period, below which the shear strength response is not sufficient to maintain a constant coefficient of friction, is consistent with our observed critical period, below which the shear strength response is completely unable to follow σ_n vibrations. We find that $T_c \approx 10T_c^*$, which allows us to extrapolate T_c through T_c^* and thus predict T_c for potentially more critical systems (i.e., $k/k_c \approx 1$).

4.5. Relevance to Natural Faults

[50] Making simple assumptions about the friction parameters of natural faults ($D_c = 0.1$ m and $b \approx 2a$), we can interpret our laboratory results in the context of earth-

quake processes. Equation (6) predicts that a critical vibration period of $T = 1$ s, which is near the microseism peak, will excite a resonant response on a stable fault, slipping at a rate of about a m/s. Our findings remain the same when the range of assumed values for a , b , and D_c is broadened to include $1.1a \leq b \leq 3a$ and $0.01 \text{ m} \leq D_c \leq 1.0 \text{ m}$. Microseismic energy will only excite a resonant response on stable faults sliding at speeds between a few cm/s and tens of m/s, much more rapidly than is typically observed in the Earth.

[51] On a fault creeping at $V = 10$ mm/yr, resonance should occur during vibrations with a period of between a few years and a few thousands of years for the range of parameters given above. Stable slip at the rates of rupture propagation may therefore be affected by coseismic vibrations, but tectonic loading rates are too slow to be influenced by high-frequency seismic shaking. Earth tides, which oscillate at a period of 12 hours, may destabilize a fault slipping between 1 $\mu\text{m/s}$ and 0.5 mm/s; rates intermediate between tectonic loading and coseismic slip. Roy and Marone [1996] estimated that similar slip rates (1–100 mm/s) are necessary for a static stress perturbation to trigger inertia-driven motion and nucleate earthquakes. Thus we find that the resonant response to normal stress vibrations does not appear to trigger earthquakes on creeping faults.

[52] Normal-force perturbations appear to have a greater effect on fault strength than stability. Our results show that a fault subject to large-amplitude, short-period vibrations, at $T < 0.1T_c$, will exhibit dynamic weakening. Therefore transient stressing from tidal forcing, seismic waves, or other periodic normal stress fluctuations of sufficient amplitude ($\epsilon > 0.01$) with periods less than a few years (for faults creeping at $V = 10$ mm/yr with the friction parameters given above) may all result in fault zone weakening.

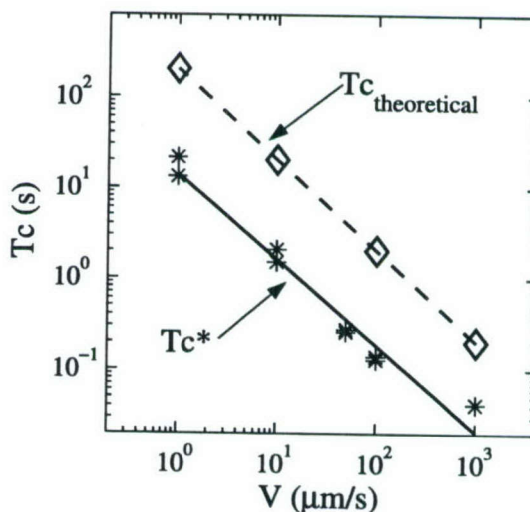


Figure 15. Theoretical definitions of critical period using the friction parameters given in Figure 8 compared with our laboratory-derived values of T_c^* . The relationship, $T_c \approx 10 T_c^*$, enabled us to convert T_c^* to T_c .

[53] Some differences are observed between the dynamic weakening process seen in our experiments and the documented cases of dynamic triggering observed in nature. We do not observe a delay in the weakening of our laboratory shear zone, as is suggested by observations of dynamic triggering following the Landers earthquake [Hill *et al.*, 1993]. Gombert *et al.* [1997] and Kilb *et al.* [2002] discuss the possibility of permanent weakening or creation of new fractures due to dynamic stressing. They suggest that "extra" seismicity occurs on new fault surfaces and it may be delayed significantly from the onset of dynamic stressing. No permanent damage from the imposed normal stress vibrations is evident in our experiments, yet our shear zone is not lithified rock and fractures do not form. Sleep *et al.* [2000] suggest that the observed healing in the slide-hold-slide experiments of Richardson and Marone [1999] may be due to the disruption of smooth, sliding surfaces during the imposed vibrations. It is important to note that our experiments are conducted on short timescales and cannot be expected to see long-term, time-dependent weakening or strengthening.

[54] Once the systematics of σ_n vibrations on creeping shear zones are well determined, it will be advisable to investigate the effect of fluids within the stressed shear zone. Fluid-filled regions such as volcanic and hydrothermal systems are most often affected by dynamic stresses [e.g., Hill *et al.*, 1993; Gombert and Davis, 1996]. In laboratory experiments conducted by Frye and Marone [2002] enhanced healing is observed in samples with higher water content and the theoretical work of Segall and Rice [1994] shows that the effect of dilatancy on slip instability is strongly influenced by fault zone porosity. It is likely that shaking would cause changes in fluid levels, altering the pore pressure and creating a more critical system.

5. Summary and Conclusion

[55] Laboratory experiments testing the effect of normal stress vibrations on steadily creeping shear zones show systematic variation with vibration period, amplitude, and loading rate. Large-amplitude, short-period vibrations result in a small (~1%) dynamic weakening of the shear zone that persists throughout the vibrations, with stress drops of ~4.5% during the onset of vibrations. The weakening is accompanied by dilation and a sharp increase in shear zone slip rate. At periods longer than the critical period, which is a well-defined quantity for each set of experimental conditions, vibrations produce sinusoidal shear strength oscillations that are in phase with the periodic forcing. Small-amplitude vibrations have a negligible effect on mean shear zone strength at all periods. While a resonant response was not observed in our experiments and we do not expect that resonance causes instabilities on many natural faults, we do predict that periodic vibrations will temporarily weaken fault zones.

[56] The Dieterich (aging) friction evolution law reproduces the experimental data more closely than does the Ruina (slip) law. At intermediate and long periods, the Linker and Dieterich formulation for the effect of a step change in normal stress successfully predicts the shear strength behavior, but at short periods no immediate response is observed. It appears that while the Dieterich law

together with the Linker and Dieterich parameter predict much of our observed shear strength behavior, they do not adequately account for the effect of high-frequency normal stress vibrations.

[57] **Acknowledgments.** We would like to thank K. Frye for giving his technical expertise and J. Rice for helpful discussions. This paper benefited from constructive reviews by J. Gombert, H. Perfettini, and N. Sleep. This research was supported by NSF grant EAR 01-96570 and USGS grant 02HQGR0156, and M.B. was supported by a NSF Graduate Research Fellowship. Contribution 11032 of Woods Hole Oceanographic Institution.

References

- Beeler, N. M., and D. A. Lockner (2003), Why earthquakes correlate weakly with the solid Earth tides: Effects of periodic stress on the rate and probability of earthquake occurrence, *J. Geophys. Res.*, **108**(B8), 2391, doi:10.1029/2001JB001518.
- Beeler, N. M., T. E. Tullis, and J. D. Weeks (1994), The roles of time and displacement in the evolution effect in rock friction, *Geophys. Res. Lett.*, **21**(18), 1987–1990.
- Beeler, N. M., T. E. Tullis, M. L. Blanpied, and J. D. Weeks (1996), Frictional behavior of large displacement experimental faults, *J. Geophys. Res.*, **101**(B4), 8697–8715.
- Bodin, P., S. Brown, and D. Matheson (1998), Laboratory observations of fault-normal vibrations during stick slip, *J. Geophys. Res.*, **103**(12), 29,931–29,944.
- Brodsky, E. E., E. Rocofofs, D. Woodcock, I. Gall, and M. Manga (2003), A mechanism for sustained groundwater pressure changes induced by distant earthquakes, *J. Geophys. Res.*, **108**(B8), 2390, doi:10.1029/2002JB002321.
- Bureau, L., T. Baumberger, and C. Caroli (2000), Shear response of a frictional interface to a normal load modulation, *Phys. Rev. E*, **62**(5), 6810–6820.
- Dieterich, J. H. (1978), Time-dependent friction and the mechanics of stick-slip, *Pure Appl. Geophys.*, **116**, 790–806.
- Dieterich, J. H. (1979), Modeling of rock friction: 1. Experimental results and constitutive equations, *J. Geophys. Res.*, **84**(B5), 2161–2168.
- Frye, K. M., and C. Marone (2002), The effect of humidity on granular friction at room temperature, *J. Geophys. Res.*, **107**(B11), 2309, doi:10.1029/2001JB000654.
- Gombert, J. (1996), Stress/strain changes and triggered seismicity following the M_w 7.3 Landers, California, earthquake, *J. Geophys. Res.*, **101**(B1), 751–764.
- Gombert, J., and P. Bodin (1994), Triggering of the M_s = 5.4 Little Skull Mountain, Nevada, earthquake with dynamic strains, *Bull. Seismol. Soc. Am.*, **84**(3), 844–853.
- Gombert, J., and S. Davis (1996), Stress/strain changes and triggered seismicity at The Geysers, California, *J. Geophys. Res.*, **101**(B1), 733–750.
- Gombert, J., M. L. Blanpied, and N. M. Beeler (1997), Transient triggering of near and distant earthquakes, *Bull. Seismol. Soc. Am.*, **87**(2), 294–309.
- Harris, R. A. (1998), Introduction to special section: Stress triggers, stress shadows, and implications for seismic hazard, *J. Geophys. Res.*, **103**(B10), 24,347–24,358.
- Heaton, T. H. (1990), Evidence for and implications of self-healing pulses of slip in earthquake rupture, *Phys. Earth Planet. Inter.*, **64**, 1–20.
- Hill, D., *et al.* (1993), Seismicity remotely triggered by the magnitude 7.3 Landers, California, earthquake, *Science*, **260**, 1617–1623.
- Karner, S. L., and C. Marone (2001), Frictional restrengthening in simulated fault gouge: Effect of shear load perturbations, *J. Geophys. Res.*, **106**(B9), 19,319–19,337.
- Kilb, D., J. Gombert, and P. Bodin (2000), Triggering of earthquake aftershocks by dynamic stresses, *Nature*, **408**, 570–574.
- Kilb, D., J. Gombert, and P. Bodin (2002), Aftershock triggering by complete Coulomb stress changes, *J. Geophys. Res.*, **107**(B4), 2060, doi:10.1029/2001JB000202.
- Linker, M. F., and J. H. Dieterich (1992), Effects of variable normal stress on rock friction: Observations and constitutive equations, *J. Geophys. Res.*, **97**(B4), 4923–4940.
- Lockner, D. A., and N. M. Beeler (1999), Premonitory slip and tidal triggering of earthquakes, *J. Geophys. Res.*, **104**(B9), 20,133–20,151.
- Mair, K., and C. Marone (1999), Friction of simulated fault gouge for a wide range of velocities and normal stresses, *J. Geophys. Res.*, **104**(B12), 28,899–28,914.
- Marone, C. (1998), Laboratory derived friction laws and their application to seismic faulting, *Annu. Rev. Earth Planet. Sci.*, **26**, 643–696.
- Melosh, H. J. (1979), Acoustic fluidization: A new geologic process?, *J. Geophys. Res.*, **84**(B13), 7513–7520.

- Nakatani, M. (2001), Conceptual and physical clarification of rate and state friction: Frictional sliding as a thermally activated rheology, *J. Geophys. Res.*, 106(B7), 13,347–13,380.
- Perfettini, H., J. Schmittbuhl, J. R. Rice, and M. Cocco (2001), Frictional response induced by time-dependent fluctuations of the normal loading, *J. Geophys. Res.*, 106(B7), 13,455–13,472.
- Perfettini, H., J. Schmittbuhl, and A. Cochard (2003), Shear and normal load perturbations on a two-dimensional continuous fault: 2. Dynamic triggering, *J. Geophys. Res.*, 108(B9), 2409, doi:10.1029/2002JB001805.
- Prakash, V. (1998), Frictional response of sliding interfaces subjected to time varying normal pressures, *J. Tribology*, 120, 97–102.
- Rice, J. R., and A. L. Ruina (1983), Stability of steady frictional slipping, *J. Appl. Mech.*, 105, 343–349.
- Richardson, E., and C. Marone (1999), Effects of normal stress vibrations on frictional healing, *J. Geophys. Res.*, 104(B12), 28,859–28,878.
- Roy, M., and C. Marone (1996), Earthquake nucleation on model faults with rate- and state-dependent friction: Effects of inertia, *J. Geophys. Res.*, 101(B6), 13,919–13,932.
- Ruina, A. (1983), Slip instability and state variable friction laws, *J. Geophys. Res.*, 88(B12), 10,359–10,370.
- Scholz, C. H. (2003), Good tidings, *Nature*, 425, 670–671.
- Segall, P., and J. R. Rice (1994), Dilatancy, compaction, and slip instability of a fluid-infiltrated fault (abstract), *Eos Trans. AGU*, 75(44), Fall Meet. Suppl., 425.
- Sleep, N. H., E. Richardson, and C. Marone (2000), Physics of friction and strain rate localization in synthetic fault gouge, *J. Geophys. Res.*, 105(B11), 25,875–25,890.
- Spudich, P., L. Steck, M. Hellweg, J. Fletcher, and L. Baker (1995), Transient stresses at Parkfield, California, produced by the *M* 7.4 Landers earthquake of June 28, 1992: Observations from the UPSAR dense seismograph array, *J. Geophys. Res.*, 100(B1), 675–690.
- Tolstoy, M., F. Vernon, J. Orcutt, and F. Wyatt (2002), Breathing of the seafloor: Tidal correlations of seismicity at Axial volcano, *Geology*, 30(6), 503–506.
- Tworzydło, W. W., and O. N. Hamzeh (1997), On the importance of normal vibrations in modeling of stick slip in rock sliding, *J. Geophys. Res.*, 102(B7), 15,091–15,103.
- Vidale, J. E., and Y.-G. Li (2003), Damage to the shallow Landers fault from the nearby Hector Mine earthquake, *Nature*, 421, 524–526.
- Vidale, J. E., D. C. Agnew, M. J. S. Johnston, and D. H. Oppenheimer (1998), Absence of earthquake correlation with Earth tides: An indication of high preseismic fault stress rate, *J. Geophys. Res.*, 103(B10), 24,567–24,572.
- Voisin, C. (2001), Dynamic triggering of earthquakes: The linear slip-dependent friction case, *Geophys. Res. Lett.*, 28(17), 3357–3360.
- Voisin, C. (2002), Dynamic triggering of earthquakes: The nonlinear slip-dependent friction case, *J. Geophys. Res.*, 107(B12), 2356, doi:10.1029/2001JB001121.
- Wilcock, W. S. D. (2001), Tidal triggering of microearthquakes on the Juan de Fuca Ridge, *Geophys. Res. Lett.*, 28(20), 3999–4002.
- Wyss, M., and S. Wiemer (2000), Change in the probability for earthquakes in southern California due to the Landers magnitude 7.3 earthquake, *Science*, 290, 1334–1338.

M. S. Boettcher, Marine Geology and Geophysics, MIT/WHOI Joint Program, Woods Hole Oceanographic Institution, Woods Hole, MA 02543, USA. (margaret@whoi.edu)

C. Marone, Department of Geosciences, Pennsylvania State University, University Park, PA 16802, USA. (cjm@geosc.psu.edu)

Chapter 6

A Synoptic Model of Ridge Transform Fault Seismicity

Abstract

Earthquake processes on mid-ocean ridge transform faults (RTFs) can be better understood through a synoptic model that unites the rheology and geology with the seismicity of these faults. Few large earthquakes occur on RTFs and these events are followed by a relatively small number of aftershocks. On average, the area ruptured by the largest earthquake scales with the area above the 600°C isotherm to the one-half power. Faulting on RTFs is primarily aseismic, i.e. only ~15% of the tectonic offset is accommodated by earthquakes and the remaining 85% occurs through steady aseismic creep or slow earthquakes. This aseismic loading may trigger the abundance of foreshocks that precede the larger RTF earthquakes. Olivine friction experiments and studies of earthquake focal depths both suggest a thermally controlled depth extent of oceanic earthquakes, with the 600°C isotherm marking the approximate lower limit. RTFs are characterized by relatively simple compositional and thermal structures. These, together with the extensive data on high-temperature olivine deformation, allow us to construct a layered rheological model that includes (1) a significant amount of serpentine with velocity and temperature dependent strength and stability, (2) a potentially seismogenic layer of peridotite, (3) a zone of peridotite characterized by pressure-dependent strength and stable creep in which mylonites are formed, and (4) a weak, ductile mantle. To better understand the physical processes that give rise to the observed seismic characteristics we integrate this rheological characterization with seismic properties of RTFs. Depending on the RTF length, slip rate, fault segmentation, and pore pressure gradient our model predicts that RTFs will yield at high maximum shear strengths ($\tau \geq 100$ MPa), consistent with indications of high strength obtained from mylonites fabrics. Earthquake stress drops, however, appears to be low ($\Delta\sigma < 1$ MPa), suggesting an apparent stress paradox between the fault yield strengths and low stress release during earthquakes. We show that when the rheology is combined with RTF geology and seismicity, we can start to understand the spatial and size distribution of earthquakes along the fault and identify target locations and problems for future study.

6.1 Introduction

In the previous chapters we focused on specific aspects of fault slip, primarily pertaining to oceanic ridge transform fault (RTF) settings. From our olivine friction experiments, we found that on RTFs the 600°C isotherm corresponds to the frictional stability boundary, dividing the potentially seismogenic region at lower temperatures from the region of higher temperature where stable sliding prevails. Studies of earthquake catalogs from the global set of RTFs indicate that only about 15% of the total slip above the 600°C isotherm on RTFs is accommodated seismically. Despite large fault areas, the biggest events on RTFs are small ($M_W \leq 7.1$) and their rupture area scales as the total fault area to the 1/2 power. In this chapter, we seek a more complete understanding of deformation on RTFs, and thus we combine the observational and experimental findings from this thesis and previous studies with the regional seismology and geology of individual transform faults. We present new thermal modeling that includes intra-transform spreading centers to better reflect the observed structural complexities of RTFs. The goal of combining these components is to construct a synoptic model that presents a comprehensive view of the current state of knowledge of RTFs, similar to models constructed by previous authors for continental strike-slip faulting [Sibson, 1984; Scholz, 1998, 2002].

In the absence of ocean bottom seismometers on RTFs, now is an appropriate time to develop a synoptic model to guide up coming deployments (e.g. NEPTUNE, which is soon to be deployed on the Juan de Fuca Ridge) and direct future investigations of earthquake processes on RTFs. In our model we unite the global observations from RTF seismicity with the rheological laws that describe deformation of oceanic lithosphere. We compute regions of high and low yield strength as well as locations of seismogenic and stable slip. By comparing observed patterns of seismicity to predicted yield strength and frictional behavior, we evaluate our synoptic model for the case studies of the Blanco and Romanche ridge transform faults. Finally, we end with some predictions of expected seismicity patterns based on our synoptic model.

6.2 The Rheology of Oceanic Transform Faults

The mechanical behavior of oceanic transform faults is largely controlled by the rheology of upper mantle rocks, which support the highest stresses. Beneath the oceans, the lithosphere

is composed of rocks emplaced at mid-ocean ridges that cooled from high-temperatures under high pressures. As such, these rocks are not likely to have been fractured or altered prior to earthquake rupture. Their chemical composition is relatively well constrained from analysis of peridotites and basalts that have been collected from ophiolites and oceanic dredges [e.g. *Johnson and Dick*, 1992; *Kelemen et al.*, 1997; *Niu et al.*, 1997; *Salters and Dick*, 2002]. Seismic refraction experiments indicate that RTFs are often characterized by thinned oceanic crust, only 2-3 km thick in some places, with abundant outcrops of gabbro and serpentinized peridotite [*Sinha and Loudon*, 1983; *Detrick and Purdy*, 1980; *Whitmarsh and Calvert*, 1986; *White et al.*, 1984].

We use data from experimental tests on olivine, the primary component of the oceanic lithosphere, and its alteration phase, serpentine, to determine the deformation mechanisms likely to be active on oceanic transform faults. We also review the strength and frictional stability of gabbro. The experimental flow laws are then extrapolated from the laboratory to the Earth and cross-checked using microstructures preserved in dredged samples of the oceanic lithosphere. Thermal models allow us to apply these rheologic laws to individual faults and construct spatially-varying cross sections of both fault strength and frictional stability.

6.2.1 Brittle Deformation I: Olivine

In the brittle deformation field, we predict the yield strength of an RTF using rock densities, pore pressures, coefficients of friction, a thermal structure, and the following assumptions. First, given the strike-slip tectonic setting, we assume the vertical stress due to the overlying rock is the intermediate principle stress, which follows a law of effective stress,

$$\sigma_2 = \rho g z - \alpha P_p, \quad (6.1)$$

where ρ is the density of the rock ($\rho = 3.300 \text{ g/m}^3$ for peridotite), g is the gravitational acceleration, z is the depth, P_p is the pore pressure, and the coefficient $\alpha \approx 1$ [*Paterson*, 1978]. To calculate the remaining principal stresses, we follow *Zoback and Townsend* [2001]. We start with the assumption that the intermediate principle stress is the mean of the maximum and minimum principle stresses, $\sigma_2 = (\sigma_1 + \sigma_3)/2$. Next we utilize four relations that are all easily seen with a Mohr Circle given the assumptions above: (1) $\mu = \tan \phi$,

where μ is the coefficient of friction and ϕ is the friction angle, (2) $\sigma_1 - \sigma_2 = \sigma_2 \sin \phi$, (3) $\sigma_1 - \sigma_3 = 2\sigma_2 \sin \phi$, and (4) $\tau = (\sigma_1 - \sigma_3)/2$, where τ is the maximum shear strength on the fault [Jaeger and Cook, 1977]. Finally, using the identity $\sin \phi = \mu/\sqrt{\mu^2 + 1}$, the differential stress can be written as, $\sigma_1 - \sigma_3 = 2\sigma_2\mu/\sqrt{\mu^2 + 1}$, and the maximum shear strength, which is shown in the figures throughout this chapter, becomes,

$$\tau = \frac{\sigma_2\mu}{\sqrt{\mu^2 + 1}}. \quad (6.2)$$

Prior to the data presented in this thesis (Chapter 4), few data on the frictional strength of olivine existed. The work of *Stesky et al.* [1974] and *Stesky* [1978a] showed that the frictional strength of olivine approximately followed Byerlee's Law [Byerlee, 1978]. The coefficient of friction, $\mu \approx 0.5$, found for the experiments described in Chapter 4 is slightly lower than expected, but is consistent with the strengths given in the earlier studies. As discussed in Section 4.3, complexities due to stress orientation during deformation of the load column may be the cause of a somewhat low apparent coefficient of friction.

While the strengths recorded in our experiments were similar to those of *Stesky*, the results of frictional stability differ significantly. We found that the frictional stability of olivine aggregates is directly related to temperature, with velocity weakening behavior (potentially seismogenic) at temperatures up to 1000°C for a range of effective pressures and laboratory strain rates. Scaling from laboratory to tectonic strain rates, we find that this transition to velocity strengthening (stable) frictional behavior occurs near 600°C in the Earth. In contrast, the findings of *Stesky* [1978a] indicate that stable sliding should occur at all temperatures above 200°C. This discrepancy is most likely due to the presence of small amounts of alteration phases in *Stesky's* samples [Hirth, 2002]. Therefore, in our model we assume that earthquakes can nucleate within the olivine layer to depths corresponding to $T \leq 600^\circ\text{C}$.

6.2.2 Brittle Deformation II: Serpentine

Serpentinites, formed during the interaction of water with peridotites, are known to be an important component of the shallow oceanic lithosphere, especially in transform fault settings [e.g. *Bonatti*, 1976; *Francis*, 1981; *Tucholke and Lin*, 1994; *Cannat et al.*, 1995]. We discuss the variations in both strength and frictional stability of the three serpentine poly-

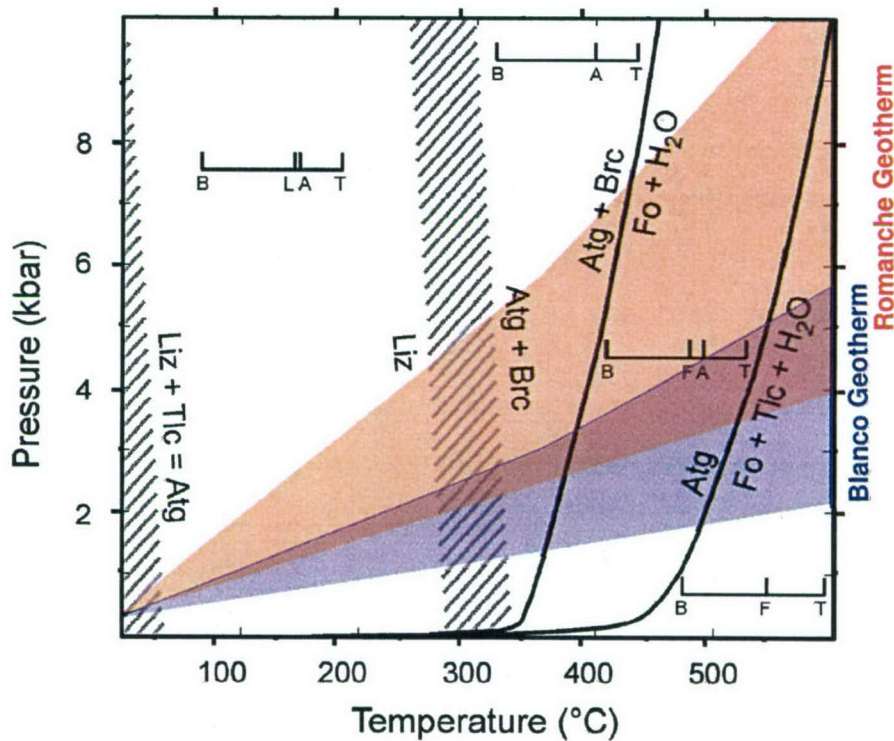


Figure 6-1: A possible phase diagram from *Evans* [2004] for the poorly constrained serpentine system. The original caption is, "A possible stable diagram for the system MSH [$\text{MgO} - \text{SiO}_2 - \text{H}_2\text{O}$]. To emphasize the uncertainty in their locations, the two steep H_2O -conserved reactions are shown as shaded areas." The mineral names and chemical formulas for the abbreviations are: "Liz" and "L" = Lizardite = $\text{Mg}_3\text{Si}_2\text{O}_5(\text{OH})_4$; "Tlc" and "T" = Talc = $\text{Mg}_3\text{Si}_4\text{O}_{10}(\text{OH})_2$; "Atg" and "A" = Antigorite = $\text{Mg}_{48}\text{Si}_{34}\text{O}_{85}(\text{OH})_{62}$; "Brc" and "B" = Brucite = $\text{Mg}(\text{OH})_2$; and "Fo" and "F" = Fosterite = Mg_2SiO_4 . Antigorite is stable to higher temperatures with increased silica activity (to the right on the above diagram). A range of possible geotherms for the Blanco Transform Fault (blue) and the Romanche Transform Fault (red) are shown in the shaded regions, which span the range from hydrostatic to lithostatic pressures and are calculated assuming serpentine from the surface to the 350°C isotherm with peridotite below.

types: lizardite, chrysotile, and antigorite. The transitions between the polytypes, as well as olivine and other hydrous phases, are illustrated in *Evans's* [2004] phase diagram shown in Figure 6-1. Both lizardite and chrysotile have the chemical composition $\text{Mg}_3\text{Si}_2\text{O}_5(\text{OH})_4$. Lizardite, which is stable between 50°C and 300°C, replaces olivine and enstatite during hydration of low porosity and low permeability rocks [*Evans*, 2004]. After hydration is complete, chrysotile is likely to form in cracks and voids, especially along fault planes and in regions previously subject to shear deformation [*O'Hanley et al.*, 1989; *Moore et al.*, 1997; *Evans*, 2004]. Chrysotile is present at temperatures from 0°C to 350°C, but is never the most stable polytype. Antigorite, $\text{Mg}_{48}\text{Si}_{34}\text{O}_{85}(\text{OH})_{62}$, is the highest temperature polytype, with a stability field between about 250°C and 500°C [*Evans*, 2004].

Laboratory studies have shown that chrysotile serpentinites have a significantly lower coefficient of friction than unserpentinized peridotites [*Reinen et al.*, 1994; *Moore et al.*, 1996a, 1997] and that even a small amount of serpentinization ($< 10\%$) will reduce the strength to near that of fully serpentinized rocks [*Escartin et al.*, 2001]. Most of the existing strength data for serpentine has been collected at room temperature [e.g. *Moore et al.*, 1997]. These data span a wide range of observed strengths, from very low coefficients of friction for chrysotile to values that follow Byerlee's Law for lizardite and antigorite. Because serpentine is stable at temperatures up to at least 500°C [*O'Hanley et al.*, 1989], it is problematic to extrapolate data from room temperature experiments to the hydrothermal conditions of the Earth. Thus, in our synoptic model, we focus on the results obtained by *Moore et al.* [1996b, 2004] at hydrothermal conditions. For chrysotile they found a very low coefficient of friction, $\mu < 0.2$ at low pressures and temperatures. At higher temperatures and pressures (above $T = 280^\circ\text{C}$ and $P_{\text{eff}} = 150 \text{ MPa}$) the samples lost some of their bound water and strengthened to $\mu \approx 0.5$.

Here we assume water, necessary for the formation of serpentine, does not penetrate deeper than about 10-15 km in the mantle rocks. We choose the 350°C isotherm as the base of the hydrostatic layer and thus 350°C also marks the extent of the serpentinized zone. We also assume that chrysotile, the weakest serpentine polytype controls the strength of the shallow lithosphere on RTFs. Following the experimental data of *Moore et al.* [2004], we use a linear gradient of μ from 0.2 to 0.5 between the surface and the 350°C isotherm. We incorporate this frictional gradient and a serpentine density of $\rho = 2.55 \times 10^{-6} \text{ g/m}^3$ into the fault strength calculated with equations 6.1 and 6.2.

Serpentine has also been shown to be more frictionally stable than olivine-rich rocks and has thus been suggested as the cause for aseismic slip on the San Andreas Fault and in other regions of strike-slip fault slip [e.g. *Allen*, 1968; *Francis*, 1981; *Reinen et al.*, 1991; *Reinen*, 1993, 2000b; *Moore et al.*, 2004]. In the hydrothermal tests conducted by *Moore et al.* [2004] stable sliding was observed for chrysotile gouge at low strength, and the frictional behavior became velocity weakening as the coefficient of friction increased towards $\mu = 0.5$ at temperatures above 200-300°C. Therefore, we assume stable velocity-strengthening frictional behavior is prevalent in the shallowest lithosphere and that the serpentinized layer becomes seismogenic (velocity-weakening) at temperatures above 250°C.

6.2.3 Brittle Deformation III: Gabbro

A number of studies have investigated the strength and stability of gabbro, the primary component of the lower oceanic crust away from fracture zones. At loading rates of less than ~ 1 m/s, most samples exhibit $\mu \geq 0.6$ [*Stesky et al.*, 1974; *Marone and Cox*, 1994; *Tsutsumi and Shimamoto*, 1997]. However a wide range of values was reported, $0.4 \leq \mu \leq 0.9$, with the lowest values obtained with roughened sliding surfaces [*Marone and Cox*, 1994] and increased temperatures ($T = 400^\circ\text{C}$) [*Montesi et al.*, 1999]. At slow loading rates the velocity-dependence of friction varied between experiments and with surface roughness, suggesting that gabbro may be velocity-strengthening or weakening depending on conditions. At co-seismic slip rates, a dramatic switch in behavior to velocity-weakening is observed [*Tsutsumi and Shimamoto*, 1997]. The complexity in these data sets suggests that a simple temperature and pressure dependent relation describing the strength of gabbro does not accurately convey the laboratory results. As previously mentioned, the oceanic crust is thinned at RTFs and variations in the coefficient of friction at such shallow depths has almost no effect on the predicted strengths. In our synoptic model, we have assumed a simple layered lithospheric rheology, using experimental data from tests on serpentine and olivine, and at present we have not included details of the crustal structure.

6.2.4 Ductile Flow

Extensive suites of experiments have been conducted to determine flow laws for the ductile deformation of olivine at high pressures and/or temperatures. Experiments on olivine single crystals have shown plastic deformation is even possible at room temperature if stresses are

Table 6.1: Flow Law Parameter Values from *Hirth and Kohlstedt* [2003]

Flow Law	A^a	n	p	E^* (kJ/mol)	V^* (m ³ /mol)
Grain Boundary Sliding	6500	3.5	2	400	18×10^{-6}
Diffusion Creep	1.5×10^9	1	3	375	6×10^{-6}
Dislocation Creep	1.1×10^5	3.5	0	530	18×10^{-6}

^a For stress in MPa and grain size in μm .

high enough (approaching 5-6 GPa) [*Evans and Goetze*, 1979]. The yield stress found in these indentation experiments can be predicted with the low-temperature plasticity flow law [*Goetze*, 1978],

$$\sigma = \sigma_P \left[1 - \left(\frac{-RT}{H} \ln \frac{\dot{\epsilon}}{B} \right)^{1/q} \right], \quad (6.3)$$

where the Peierl's stress $\sigma_P = 8500$ MPa, the gas constant $R = 8.3144$ J/mol/K, the absolute temperature is denoted T , the activation enthalpy $H = 5.4 \times 10^5$ J/mol, the strain rate is $\dot{\epsilon}$, the empirical constant $B = 5.7 \times 10^{11}$ s⁻¹, and the exponent $q = 2$.

At high temperatures the strength of the deforming rock mass is well described by a creep law of the form,

$$\sigma = \left(\dot{\epsilon} A^{-1} d^p \exp \left[\frac{E^* + PV^*}{RT} \right] \right)^{1/n}, \quad (6.4)$$

where A , n , and p are constants that depend on the deformation mechanism, d is the grain size, E^* and V^* are the activation energy and activation volume respectively, and P is the pressure. In our model we include the effects of low-temperature plasticity, grain boundary sliding, diffusion creep, and dislocation creep in addition to frictional sliding. Everywhere on the fault surface we calculate the value of stress given by each deformation mechanism and choose the one that yields at the lowest stress. For grain boundary sliding, diffusion creep, and dislocation creep, we use the parameter values of *Hirth and Kohlstedt* [2003] that are listed in Table 6.1.

6.2.5 Thermal Modeling

To apply the rheological laws described above to individual faults, a temperature distribution is needed to convert pressure- and temperature-dependent properties into spatially-dependent ones. There are multiple standard methods for calculating the thermal structures of ridge transform faults, including (1) averaging the temperatures of the bounding plates

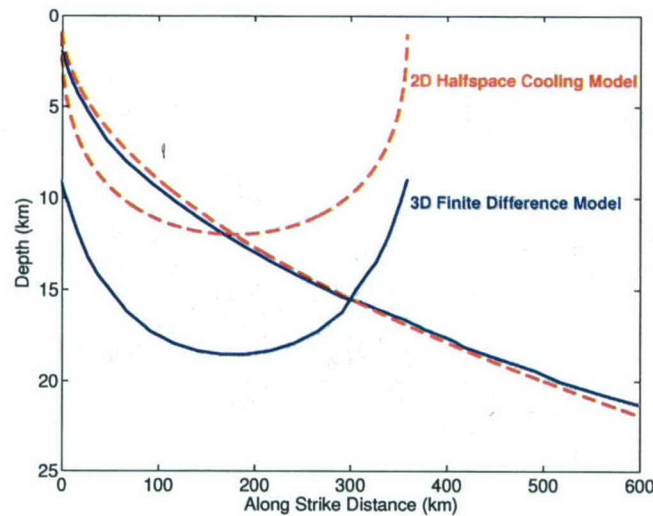


Figure 6-2: Profiles of the 600°C isotherm moving from a ridge segment off axis and along a transform fault calculated both with a three-dimensional (3D) finite difference technique (solid blue curves) and with a two-dimensional (2D) halfspace cooling model (dashed red curves) for a ridge spreading at a half rate of 30 mm/yr. For comparison the area above the 600°C isotherm is 3660 km² and 6062 km² for the 2D and 3D models respectively. See text for model details.

computed from a two-dimensional half-space cooling model [e.g. *Engeln et al.*, 1986; *Okal and Langenhorst*, 2000; *Abercrombie and Ekström*, 2001; *Boettcher and Jordan*, 2004] and (2) using a finite difference method to calculate heat transport in a three-dimensional passively upwelling mantle flow field that is driven by diverging plates [*Phipps Morgan and Forsyth*, 1988; *Shaw and Lin*, 1996; *Behn et al.*, 2002]. The two-dimensional half-space cooling model accounts for vertical conductive cooling away from a ridge and approximates the effect of lateral heat conduction across the RTF (see Chapter 2, Figure 1). The finite difference method, on the other hand, incorporates both the effects of heat conduction and advection in a three-dimensional volume. The finite difference method models perturbations to the mantle flow field near segment ends, and thus produces a much cooler thermal structure than is obtained with the simple averaging technique. Figure 6-2 shows cross-sectional profiles of the 600°C isotherm calculated with both methods. Figure 6-2 illustrates the significant differences predicted for a RTF, as well as the similarity of the model solutions far from transform fault segments. We use the two techniques to obtain upper and lower bounds on RTF thermal models and strength profiles. However, in the remainder of the chapter we primarily present the more realistic results of the finite difference solution that

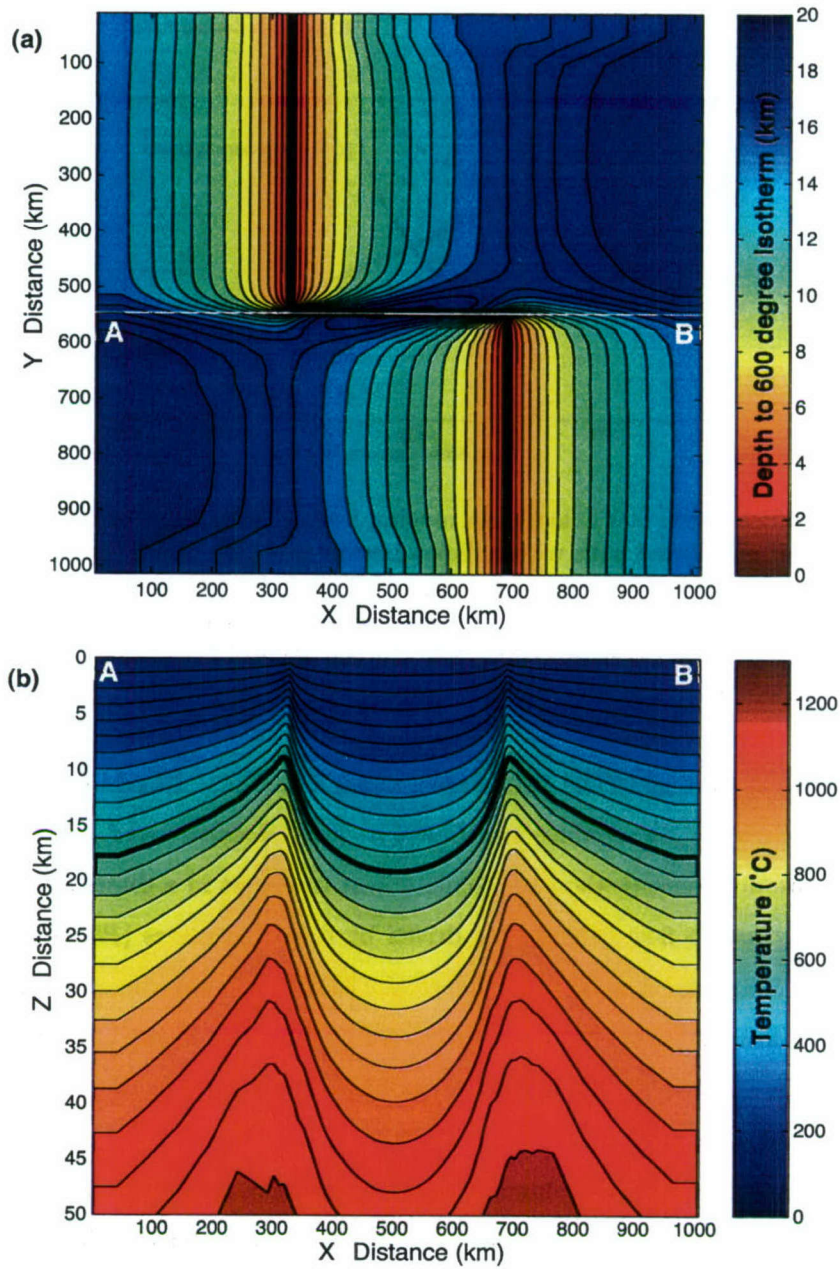


Figure 6-3: Three-dimensional finite difference model calculation of the thermal structure of a ridge-transform-ridge system spreading at a half rate of 30 mm/yr with a 360 km-long continuous transform fault segment. (a) Map view of the system with contoured depths to the 600°C isotherm. Transect AB overlies the transform. (b) Cross sectional view of the thermal structure of AB with the 600°C isotherm denoted with the thick line.

is discussed in more detail below.

We use the finite difference technique of *Phipps Morgan and Forsyth* [1988], which consists of a two-part solution. First, using a Fourier series flow decomposition the flow velocities \mathbf{v} are calculated in a uniform viscosity mantle half-space beneath a ridge-transform-ridge plate geometry. The thermal problem is then solved using an upwind finite differencing technique to solve the steady-state energy conservation equation. Thus the net heat advected (convected) and diffused (conducted) into and out of a volume surrounding each grid point is zero, which written in terms of temperature for each grid point is,

$$\mathbf{v} \cdot \nabla T = \kappa \nabla^2 T. \quad (6.5)$$

The thermal diffusivity is set to $\kappa = 0.01 \times 10^{-6} \text{ m}^2/\text{s}$. Equation 6.5 is then solved assuming that the surface temperature everywhere is $T_s = 0^\circ\text{C}$, the mantle temperature at the base of the solution space is $T_m = 1300^\circ\text{C}$, and mantle flow is driven by surface plates. The model space we used varied with fault length L , from $1024 \times 1024 \text{ km}^2$ for $L = 360 \text{ km}$ to $2048 \times 2048 \text{ km}^2$ for $L = 920 \text{ km}$, with 100 km depth for all cases. To resolve the details of the thermal structure in the most complex regions of the model, the finite difference grid is the densest within 15 km of ridge transform intersections and in the upper 20 km of the lithosphere. Figure 6-3 illustrates the result of applying the spectral flow solution and finite difference technique to ridge segments offset by a RTF of length $L = 360 \text{ km}$ and assuming a half spreading rate $U = 30 \text{ mm/yr}$. The 600°C isotherm extends to approximately 20 km depth in the center of the RTF. The strength profile described in the next section is calculated from the geotherm corresponding to the center of the RTF.

6.2.6 Maximum Fault Strength

Combining the calculated thermal structures with our layered rheological model, we obtain a cross sectional distribution of maximum fault strength. In all the cases illustrated in this chapter we assume that the mantle is serpentized from the surface to the 350°C isotherm due to the presence of water. In the serpentized layer, we assume a density of $\rho = 2.55 \times 10^{-6} \text{ g/m}^3$, a coefficient of friction that follows a linear gradient from 0.2 to 0.5 with increasing temperature, and hydrostatic pore fluid pressure. Serpentine is assumed to be velocity-strengthening from the surface to 250°C and to progressively become more

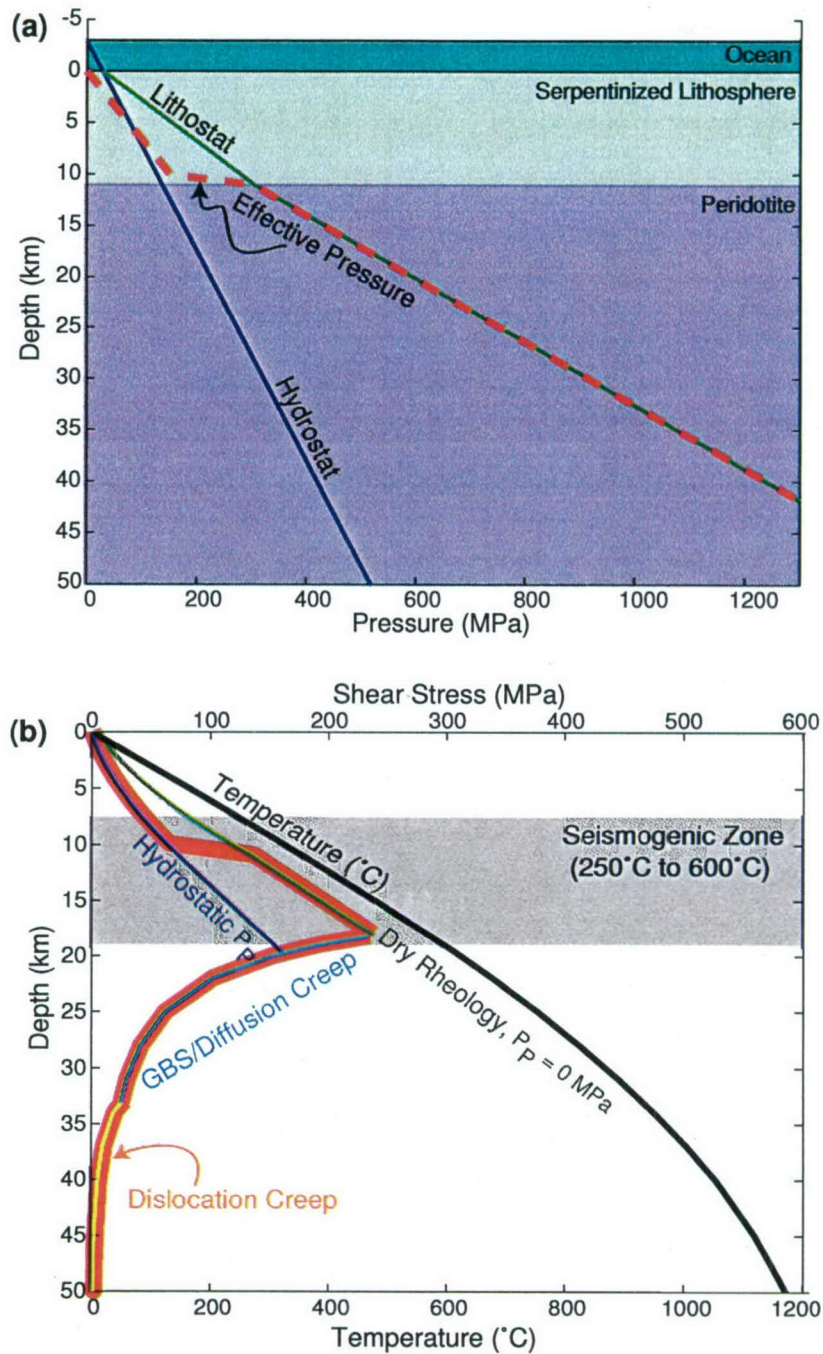


Figure 6-4: (a) Effective pressure for a section of oceanic lithosphere under a 3 km ocean with hydrostatic pore fluid pressure throughout a serpentinized lithosphere that extends from the surface to the 350°C isotherm and with a dry peridotitic mantle below. (b) Strength envelope (red) using the geotherm (black) from the center of the transform fault in Figure 6-3 and the effective pressure curve from panel (a). Note that pore fluid pressure strongly influences the yield strength in the frictional regime, resulting in the blue curve with hydrostatic pore pressure and the green curve with dry pore space. The seismogenic zone lies between the 250°C and 600°C isotherms.

velocity weakening as temperature increases. Below the serpentine-dominated layer we assume a dry, olivine-rich mantle with a density of $\rho = 3.30 \times 10^{-6} \text{ g/m}^3$. At shallow depths olivine deforms through frictional sliding and follows Byerlee's Law with a coefficient of friction of $\mu = 0.5$.

A transition from frictional behavior to ductile creep occurs at higher temperatures when the ductile flow laws predict lower yield stress than Byerlee's law. Grain boundary sliding and diffusion creep both depend on grain size, which we derive by calculating the grain size necessary to obtain the same strength with both grain-size dependent laws for a given strain rate [Warren *et al.*, 2005]. We equate equation (6.4) for the two laws using the parameters in Table 6.1 and obtain values in the range $2 \text{ } \mu\text{m} \leq d \leq 20 \text{ } \mu\text{m}$. At the highest temperatures the dislocation creep flow law has the lowest yield strength and becomes the dominant deformation mechanism. The one-dimensional strength envelope shown in Figure 6-4b was computed with a strain rate of $\dot{\epsilon} = 1 \times 10^{-12} \text{ s}^{-1}$, which implies 1-2 km wide deformation zone at depth for a spreading rate of $U = 30 \text{ mm/yr}$. While $\dot{\epsilon}$ has no effect on the brittle behavior, it does have a modest effect on the ductile flow laws. In particular, decreasing $\dot{\epsilon}$ by a factor of 1000, which encompasses the range of expected tectonic strain rates, enhances creep processes at lower temperatures. This leads to a shallower intersection between the brittle and ductile flow laws (15.8 km compared to 18.2 km), and therefore results in a decrease of the maximum shear stress from $\tau_{\text{max}} = 239 \text{ MPa}$ to $\tau_{\text{max}} = 205 \text{ MPa}$, which is a stress decrease of $\sim 14\%$.

A region of high stress ($\tau \geq 100 \text{ MPa}$) is found near the transition from brittle to ductile behavior. It occurs in the depth range of approximately 10-20 km and has a maximum shear strength of about 200 MPa. These values depend on the assumptions made for the values of the variables μ , $\dot{\epsilon}$, T , and pore fluid pressure. As noted above, we have assumed that water does not penetrate below the 350°C isotherm, which we have chosen as the divide between the hydrostatic pore fluid pressures and the dry mantle rheology below. The effective pressure curve shown in Figure 6-4a illustrates this model. Alternatively, assuming hydrostatic pore fluid pressure throughout the brittle layer, the resultant maximum strength is lower by about 25% (see the hydrostatic curve in Figure 6-4b). Oceanic mantle rocks that have never been broken are dry, and assuming very little water has penetrated the upper crust, a dry rheology may be appropriate for the entire brittle layer. The dry rheology would follow the lithostat in Figure 6-4a and the curve labeled "dry rheology" in Figure 6-4b, which

would give the same value of maximum shear strength, $\tau \approx 200$ MPa. The values given here represent upper bounds for shear strength; with pore fluid pressures closer to lithostatic, the yield stress could be significantly reduced. Additionally, variation in other parameters, e.g. a lower coefficient of friction, lower strain rates, and warmer thermal structures will all reduce the predicted yield strengths. While the stresses shown in Figure 6-4 are high, they are in the range estimated for the formation of mylonitic fabrics [Warren *et al.*, 2005], suggesting that they are not unreasonable. In the following two sections we apply these rheological laws and thermal structure calculations to two RTFs: the Blanco Transform Fault that offsets the Juan de Fuca Ridge and the Romanche Transform Fault that offsets the Mid Atlantic Ridge.

6.3 Case Study I: The Blanco Transform Fault System

The Blanco Transform Fault (BTF), located off the coast of Oregon, is about 360 km long and is slipping at an intermediate rate of 59 mm/yr. Unlike most other oceanic transform faults, the Blanco is located near a high-quality, on-shore, seismic array. The relative accessibility of the Blanco has allowed for multiple seismic and morphologic studies over the past 40 years [McManus, 1965; Hyndman and Weichert, 1983; Embley and Wilson, 1992; Dziak *et al.*, 1991, 2000; Karson *et al.*, 2002]. Embley and Wilson [1992] mapped a series of extensional basins and complex tectonic features, likely due to a recent episode of plate reorganization. Dziak *et al.* [1991, 2000] found that the Cascadia Depression, a short spreading center near the center of the transform, acts as a barrier to continuous earthquake ruptures, separating the 150 km long Blanco Ridge on the east from a system of short strike-slip faults to the west.

6.3.1 Blanco Seismicity

Origin times, hypocenter locations, and travel time picks from the International Seismological Center On-line Bulletin (1965-1996) were used to relocate 458 Blanco earthquakes. This ISC data set was augmented with moment tensor solutions from the Harvard Centroid Moment Tensor (Harvard CMT) Project (1976-2005) [Dziewonski *et al.*, 1981] and Oregon State University (OSU) Moment-Tensors Solutions (1990-1996) [Nabelek and Xia, 1995]. Only the reported centroid depth determinations from OSU, which were calculated with

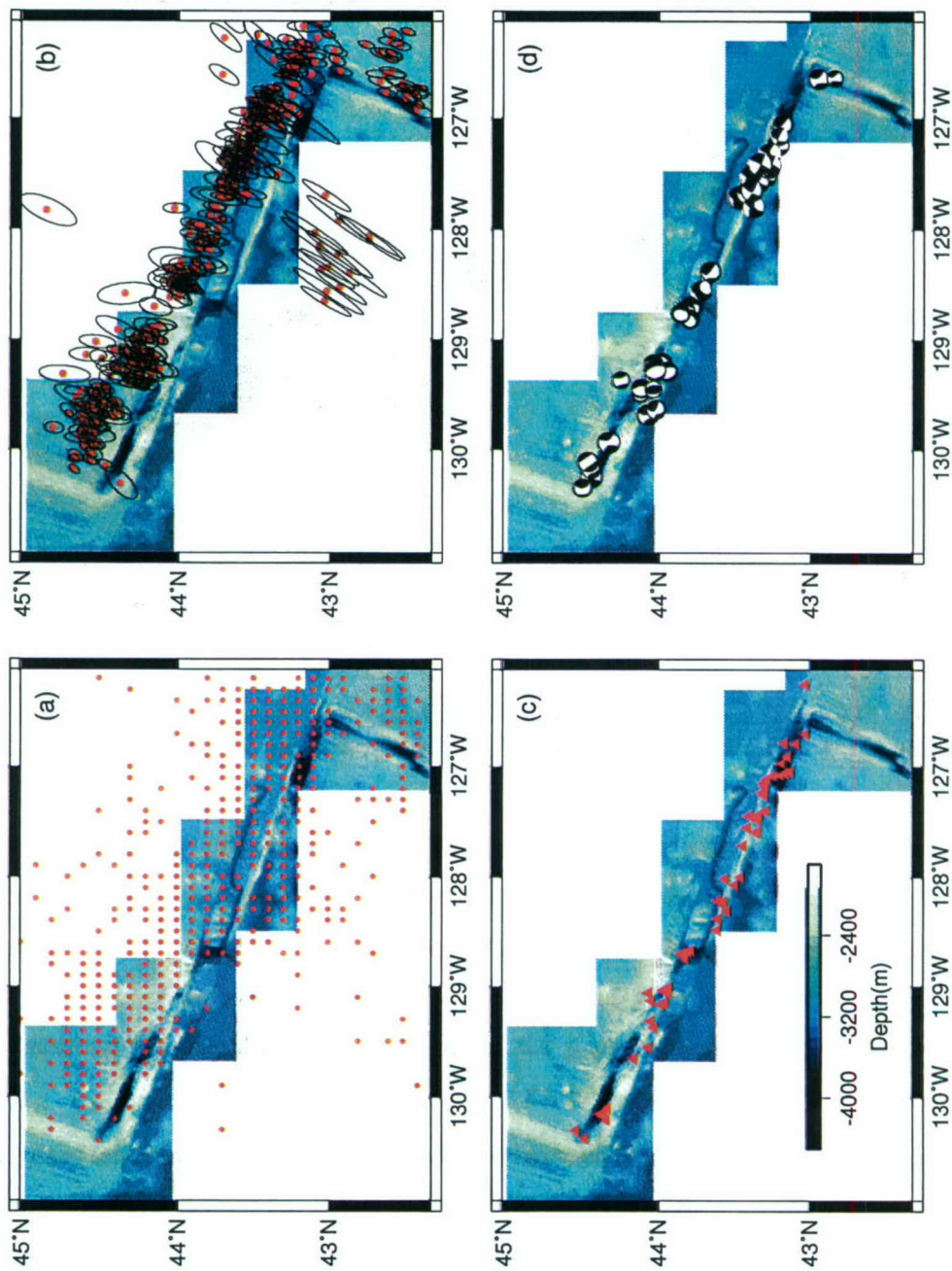


Figure 6-5: Blanco Transform Fault seismicity with regional bathymetry from the *Ridge Multibeam Synthesis Project* [1999]. (a) Event locations as reported by the International Seismological Centre, (b) events relocated using the method of *Jordan and Sverdrup* [1981] with 95% confidence ellipses, (c) locations of SOSUS events [*Dziak, 1999*], and (d) locations of focal mechanisms from OSU and Harvard CMT shifted as described in the text.

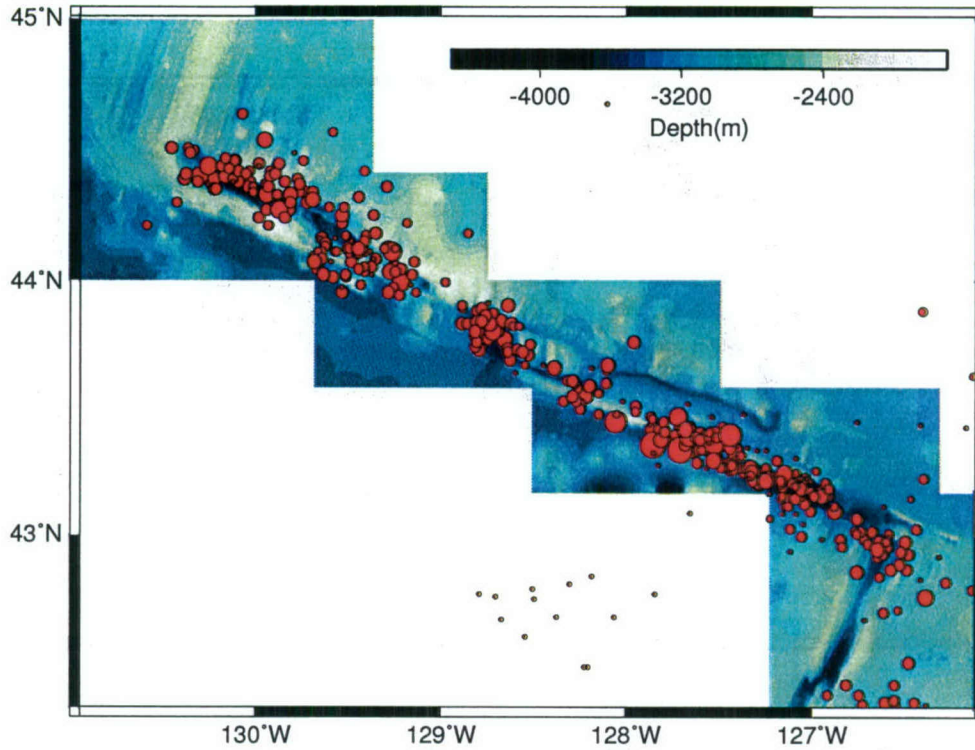


Figure 6-6: Relocated events on the Blanco Transform Fault. Symbol size represents event magnitude ($M \leq 6.4$). Bathymetry is from the *Ridge Multibeam Synthesis Project* [1999].

a regional seismic array and a regional velocity model, were used in our analysis. Additional seismic data were obtained from the U.S. Navy Sound Surveillance System (SOSUS) of underwater hydrophones [Dziak *et al.*, 1996, 2000; Dziak, 1999]. The SOSUS data are T-phases, which are produced by the conversion of body waves to acoustic waves, and allow for the detection of small events, $m_b \geq 2.0$, at great distances with radiator locations that are estimated to be accurate to within ± 3 km [Dziak *et al.*, 2000].

The original ISC locations for Blanco earthquakes are shown with the regional bathymetry in Figure 6-5a. In order to improve these locations, we used the hypocentroidal decomposition algorithm [Jordan and Sverdrup, 1981]. The advantage of this technique is that for a limited source region, the ray paths between many events and a single station are all very similar. Thus, this multiple-event relocation program accurately constrains relative locations of events within the cluster.

The area surrounding the Blanco was divided into 13 regions to minimize the effect of velocity heterogeneity along the ray path from events located more than ~ 60 km apart. The

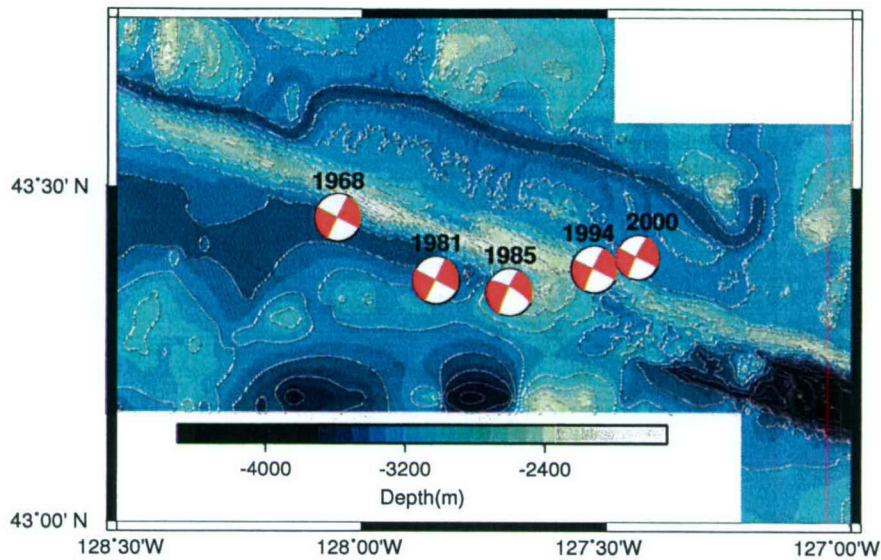


Figure 6-7: Relocated positions of five of the largest events on the Blanco Transform Fault from 1964-2005 (Table 6.2). Beachball symbols from the Harvard CMT catalog represent the best double-couple earthquake focal mechanisms. Bathymetry is countered at 200 m intervals and is obtained from the *Ridge Multibeam Synthesis Project* [1999].

depths of all events were fixed at 10 km due to the poor depth resolution of the teleseismic P-waves. Each earthquake with a minimum of 25 picks was relocated relative to others in the same region using the IASP91 velocity model. New event epicenter locations were determined relative to the centroid of the regional event cluster and poorly constrained events with inadequate azimuthal coverage were removed from the data set. The procedure was repeated until all events with sufficient data were relocated and had location uncertainties of less than 20 km as shown in Figure 6-5b.

The relocated epicenters define a linear feature to the north of the Blanco. This offset is most likely due to asymmetric station coverage (most stations are located to the north east on the west coast of America, *Johnson and Jones* [1978]) and to inaccuracies in the velocity model [*Bergman and Solomon*, 1988]. To remove the northward bias, we determined the average vector between each earthquake reported by the SOSUS hydrophone array (Figure 6-5c) and the relocated epicenter for the same event (Figure 6-5b). We then applied a uniform shift to the relocated data set, yielding the locations displayed in Figure 6-6.

The character of the seismicity along the Blanco Transform Fault changes from more localized on the eastern half, to more diffuse to the west, consistent with observations of *Dziak et al.* [1991]. A large seismic gap, 40 km long, is located near the eastern end

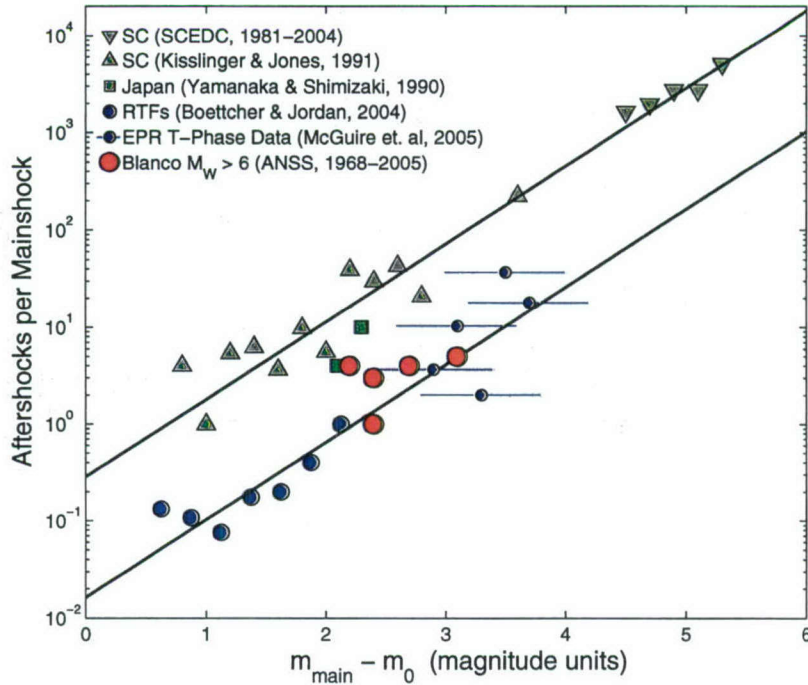


Figure 6-8: Aftershocks per mainshock, plotted against the magnitude difference ΔM between the mainshock magnitude m_{main} and the catalog completeness threshold m_0 . Red circles represent data for the five large earthquakes on the Blanco Transform Fault listed in Table 6.2. For the Blanco events, aftershocks are counted from the ANSS catalog within two weeks and 100 km of the relocated mainshock position and m_0 was estimated based on the magnitude range of the events within the preceding two months. Information on the other oceanic (blue) and continental (green) data sets can be found in the captions of Figures 2-4 and 3-3.

of the Cascadia Depression, which is depicted in Figure 6-5d by the normal faulting focal mechanism. The western segment appears complex, with a mixture of strike-slip and normal faulting events, while the eastern segment consistently shows right-lateral strike-slip focal mechanisms. A few intra-plate earthquakes are also observed in the vicinity of the Blanco.

Five of the largest earthquakes on the Blanco ($6.1 \leq M_W \leq 6.4$) initiated within 50 km of each other. The parameters of these events are listed in Table 6.2 and the relocated epicenters are shown in Figure 6-7. We searched the Advanced National Seismic System (ANSS) composite earthquake catalog for aftershocks within 100 km and two weeks of each mainshock and estimated the threshold magnitude of completeness for the Blanco region at the time of each mainshock. The results shown in Figure 6-8 illustrate that aftershocks of the large earthquakes on the Blanco fit well with the global statistics presented in Chapters 2 and 3.

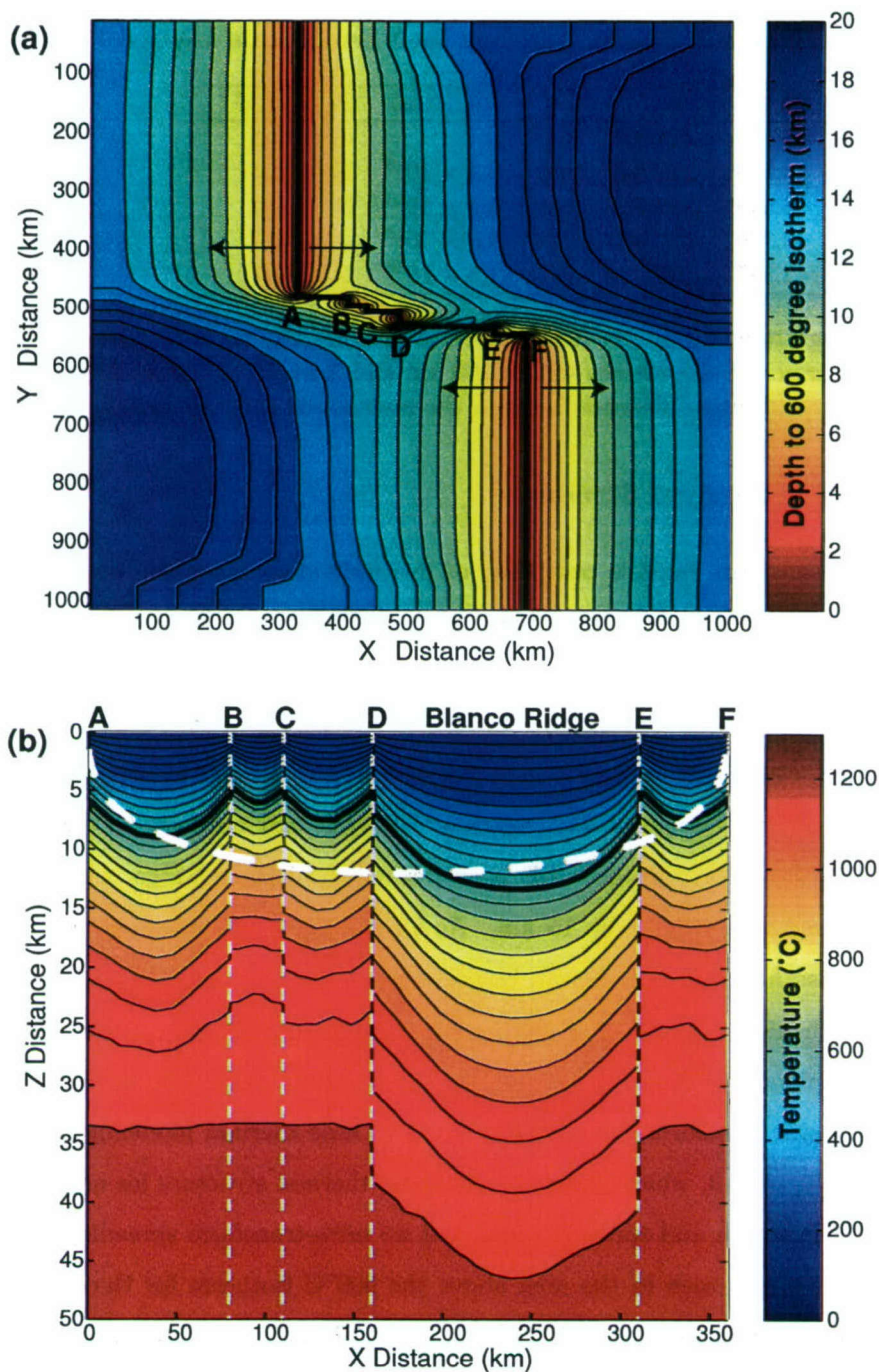


Figure 6-9: Three-dimensional finite difference model calculation of the thermal structure surrounding the Blanco Transform Fault. The ridge-transform-ridge system is spreading at a half rate of 30 mm/yr and has a total of length 360 km, divided among five fault segments. (a) Map view of the system with contoured depths to the 600°C isotherm. Letters mark transform segment endpoints. (b) Cross sectional view of the thermal structure of the strike-slip segments projected onto a single plane. The 600°C isotherm denoted with the thick black curve. For comparison the dashed white curve shows the 600°C isotherm calculated with the half-space cooling model.

Table 6.2: Blanco Transform Fault Earthquakes $M_W > 6.0$

yr/mo/day	lat	lon	M^*	M_0 (Nm)	N_a^*	ΔM^+
1968/05/08	43.455	-128.048	6.2	-	4	2.2
1981/11/03	43.363	-127.847	6.4	5.2×10^{18}	1	2.4
1985/03/13	43.345	-127.696	6.4	5.5×10^{18}	3	2.4
1994/10/27	43.379	-127.523	6.3	3.5×10^{18}	4	2.7
2000/01/20	43.397	-127.434	6.1	1.5×10^{18}	5	3.1

* M is the magnitude value: M_S for the 1968 event and M_W for the others.

* N_a is the number of aftershocks within 100 km and 2 weeks of the mainshock.

+ ΔM is the magnitude difference between the mainshock and the catalog completeness.

6.3.2 Blanco Thermal Structure

The Blanco Transform Fault is composed of five individual strike-slip segments that are shown in the morphologic and structural maps of *Embley and Wilson* [1992]. Using the finite difference modeling described above, we determined the three-dimensional thermal structure of the region surrounding the Blanco. The model geometry, shown in Figure 6-9, consists of five offset fault segments, with lengths given in Table 6.3. Segment AB is offset 15 km to the north of segment BC. Segment BC is 10 km north of CD, which ends at the Cascadia Depression. Segment DE is also called the Blanco Ridge, and is offset from the eastern-most segment EF by 15 km. As Chapter 4 has highlighted the importance of the 600°C isotherm in defining the base of the seismogenic lithosphere, we've mapped the depth to the 600°C isotherm in Figure 6-9a. Projecting all of the strike-slip segments onto a single plane, we determined the thermal structure along a cross section in depth for the composite transform fault (Figure 6-9b). These thermal modeling results can be compared to Figure 6-3, which shows the resultant thermal structure for an RTF with the same total fault length and spreading rate, but no intra-transform spreading segments. A dramatic difference is seen in the area above the 600°C isotherm for the segmented and unsegmented fault models, $A_T = 3256 \text{ km}^2$ and 6052 km^2 respectively, emphasizing the importance in using the correct segmentation geometry in calculating fault strength and seismogenic potential.

6.3.3 Strength of the Blanco RTF

For each point on the Blanco Transform Fault our model predicts the maximum strength

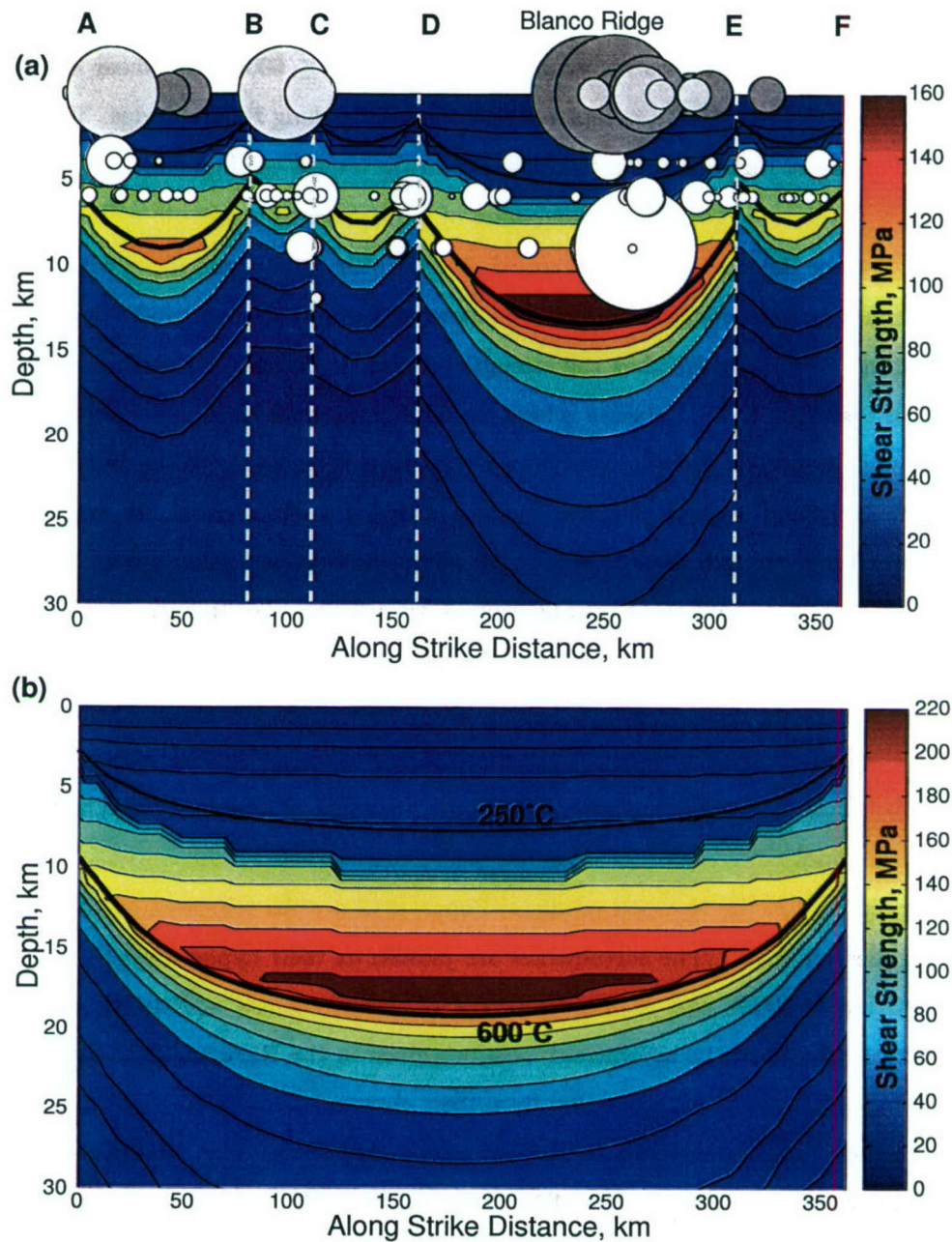


Figure 6-10: Maximum shear strength supported on the Blanco Transform Fault for the (a) segmented and (b) unsegmented fault models. Relocated earthquakes with depths from OSU (white) are shown at their hypocenters. Relocated earthquakes from the ISC catalog (dark gray) and unrelocated earthquakes with locations from the Harvard CMT catalog (light gray) are plotted at their epicenters. Circle sizes represent rupture areas calculated with a constant stress drop of $\Delta\sigma = 1$ MPa, assuming slip scales with the rupture area. The 250°C and 600°C isotherms are labeled with thick black lines, which enclose the seismogenic zone. Note that pressure-dependent rheology is indicated by relatively horizontal stripes above the region of peak strength and with temperature-dependent rheology the lines of constant strength follow isotherms.

shown in Figure 6-10. The fault is weak from the surface to the 350°C isotherm, yielding at $\tau \leq 50$ MPa. At depths corresponding to $350^\circ\text{C} \leq T \leq 600^\circ\text{C}$ the shear strength is found to be less than 100 MPa, except beneath the 150 km-long Blanco Ridge. The Blanco Ridge is the longest segment and is the site of both the largest earthquakes and the highest yield strength ($\tau_{\text{max}} \approx 160$ MPa). The region of high strength is narrow with dimensions of approximately 100 km along strike and 5 km down dip, and spans the predicted velocity weakening/strengthening transition. The average strength above the 600°C isotherm is $\bar{\tau} = 55$ MPa. We emphasize that the strengths shown in Figure 6-10 are maximum estimates. For example, if fluid pressure is high the fault zone could be significantly weaker. In addition we have used a relatively cool thermal structure calculated with the finite difference technique. If instead we had used the simple half-space cooling model, we would expect significantly lower strength levels. Because the simple half-space cooling model can not accurately model intra-transform spreading centers, we compare the strengths predicted with the unsegmented finite difference model of the Blanco shown in Figure 6-10b, which predicts $\bar{\tau} = 90$ MPa and $\tau_{\text{max}} = 240$ MPa, with the results of the half-space cooling method, $\bar{\tau} = 57$ MPa and $\tau_{\text{max}} = 160$ MPa. This comparison indicates that the half-space cooling model predicts strengths that are about two-thirds the value of those predicted by the finite difference method.

Superimposed on the strength profile of Figure 6-10 are the relocated earthquakes described in Section 6.3.1. The earthquakes are plotted at their hypocenters where depths from OSU are available and at the epicenters otherwise. A few additional events from 2001-2005 are shown at the epicentroid locations given in the Harvard CMT catalog. The depicted rupture areas A are calculated from their observed seismic moment $M_{\text{obs}} = \mu AD$, where μ is the shear modulus and D is the slip during the earthquake. We assume D scales with a constant stress drop $\Delta\sigma = 1$ MPa as, $D = (\Delta\sigma/\mu)A^{1/2}$. With these assumptions, the rupture area can be written as $A = (M_{\text{obs}}/\Delta\sigma)^{2/3}$ (see equations 2.12-2.14).

6.3.4 Fit of Blanco Seismicity to the Synoptic Model

To test our model we compare the size of the largest observed event on each segment to the size of the largest predicted earthquake. Taking the 600°C isotherm as the base of the seismogenic layer, scaling relation F of Table 2.1 gives an expression for the largest expected event, $M_C = C_1 A_T^{3/4}$, where the coefficient $C_1 = 2 \times 10^{16}$ N/km^{1/2} (values of C_1

Table 6.3: Blanco Transform Fault Segmentation and Seismicity

Segment ^a	L , km	A_T^b , km ²	ΣM^c , 10^{18} Nm/yr	m_{obs}^c	m_C^d	χ
AB	80	641	3.66	6.2	6.2	0.08
BC	30	178	3.84	6.2	5.9	0.30
CD	50	350	0.76	5.6	6.1	0.03
DE	150	1743	22.68	6.4	6.4	0.18
EF	50	344	0.35	5.4	6.1	0.01
Total ^b	360	3256	31.28	6.4	6.6	0.13

^a Segment names refer to the end points given in Figure 6-9.

^b Fault parameters assuming the segmented fault thermal model of Figure 6-9 with the base of the seismogenic zone at 600°C.

^c Moment and largest magnitude values from the Harvard CMT catalog 1977-Feb, 2005.

^d Largest expected event calculated from scaling relation F of Table 2.1 assuming a constant stress drop of $\Delta\sigma = 1$ MPa.

between 1.4×10^{16} N/km^{1/2} and 3.0×10^{16} N/km^{1/2} are within the 95% confidence limits from the maximum likelihood calculation given in Chapter 2) and A_T is the thermal area of contact for $T \leq 600^\circ\text{C}$ obtained from the thermal model shown in Figure 6-9. This scaling relation gives estimates of the magnitude of the largest expected event m_C on each segment to within approximately ± 0.1 magnitude unit.

Overall there is a good correlation between the observed and predicted event sizes listed in Table 6.3. We find that including accurate fault geometry and segmentation was essential to correctly predicting spatially-varying seismicity patterns. This is illustrated in the results shown for the segmented (Figure 6-10a) and unsegmented (Figure 6-10b) fault models. The 250°C and 600°C are highlighted on both models to mark the region of expected velocity-weakening frictional behavior, i.e. the seismogenic zone. The magnitudes of the observed and predicted events match exactly for segments AB and DE. Only segment BC had a significantly larger than predicted event. BC is both the smallest and morphologically the least well-defined segment, due to the transition into the Surveyor Depression on its western end. *Embley and Wilson* [1992] map segments AB and BC as a single western segment with a kink at the Blanco Depression. The predicted largest event for a connected 110 km-long segment AB-BC would be $m_C \approx 6.3$, providing a good fit to the reported magnitudes of the largest observed events on segments AB and BC listed in Table 6.2.

The Blanco and the sequence of large events on the Blanco Ridge provide an excellent opportunity to test the single-mode hypothesis discussed in Chapter 2. This hypothesis

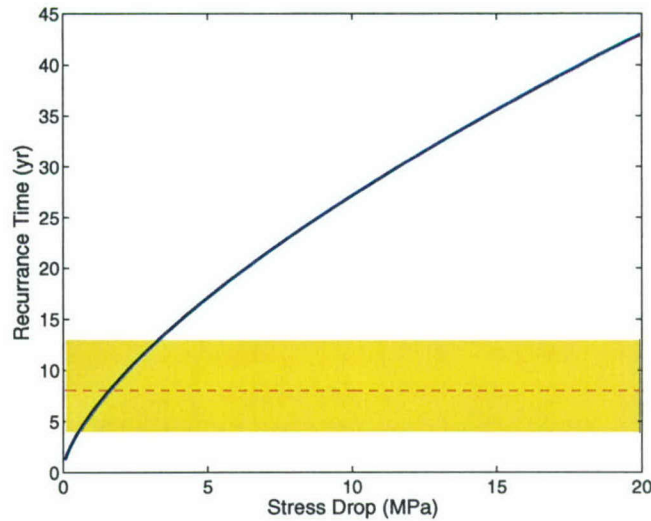


Figure 6-11: Trade off (blue curve) between stress drop and recurrence time of $M_W = 6.3$ earthquakes on a single patch on the Blanco Transform Fault. Yellow box shows the range of observed recurrence intervals of $M \geq 6.1$ earthquakes on the Blanco Ridge. Red dashed line indicates the mean recurrence interval.

suggests that a particular fault patch on an RTF slips either seismically or aseismically, but does not alternate between the two modes of deformation (see Figure 2-14). Below we show that the combined slip during the large Blanco Ridge earthquakes could accommodate the full plate motion on a small fault patch, depending on assumed earthquake stress drops. We then examine the remaining fault segments and find that other fault patches are likely to violate the single-mode hypothesis. We obtain this result by comparing the effective seismic area $A_E = \dot{M}/(\mu V)$, where \dot{M} is the moment release rate and V is the plate motion rate, to the total fault area from which seismic moment release occurs, A_S . If $A_S < A_E$, then it is possible that slip on the Blanco obeys the single-mode hypothesis. However, if $A_S > A_E$, then parts of the fault that sometimes slip seismically, must not be fully coupled, and thus follow the multi-mode hypothesis— deformation on a single fault patch will alternate between seismic and aseismic mechanisms. As there is a strong trade off between stress drop and rupture area, we determine the critical stress drop below which parts of the fault must obey the multimode hypothesis.

To test whether the section of the Blanco Ridge that ruptured in the large earthquakes could be fully coupled, we first assume all events ruptured the same fault patch. Without very accurate centroid locations we can not determine if the above assumption is true, or if the events occurred progressively further to the east, as is suggested by the epicenters

(Figure 6-7). However, for the purpose of testing the single-mode hypothesis we assume that the events did rupture the same patch of area, $A_{\text{patch}} = (M_0/\Delta\sigma)^{2/3}$. In Figure 6-11 we show the trade off between the stress drop of a $M_W = 6.3$ earthquake and the recurrence time necessary to keep the fault patch fully coupled, $t_R = M_0/(\mu V A_{\text{patch}})$. With a shear modulus $\mu = 44.1$ GPa and the tectonic slip rate across the Blanco of $V = 59$ mm/yr, stress drops of $0.5 \text{ MPa} \leq \Delta\sigma \leq 3.5 \text{ MPa}$ give recurrence intervals consistent with those of the observed events that are listed in Table 6.2. Therefore if the large events on the Blanco Ridge did rupture the same fault patch, then with reasonable stress drops a small patch ($100 \text{ km}^2 \leq A_{\text{patch}} \leq 350 \text{ km}^2$ depending on stress drop) will be fully seismic ($\chi = 1.0$).

To justify a speculation that the single-mode hypothesis applies all along the Blanco Transform Fault, we must show that all portions of the fault could be either fully seismic or fully aseismic. We can assume that the entire Blanco Ridge segment obeys the single-mode hypothesis, with a small fully-seismic patch and the remainder of the segment fully aseismic. For the other four strike-slip segments, we calculate a combined effective area of $A_E = 254 \text{ km}^2$ from the past 28 years of earthquakes from the Harvard CMT catalog. We can also determine an estimate of A_S from the along-strike seismicity distribution (Figures 6-6 & 6-10a). To be conservative, we estimate A_S using only the $M_W > 6.0$ earthquakes. In addition to the events on the Blanco Ridge, two $M_W = 6.2$ events occurred on non-overlapping patches. We find that for stress drops less than 5.5 MPa, $A_S > A_E$, suggesting that at least some fault patches slip both seismically and aseismically. Alternatively, if the stress drops of the two large earthquakes are greater than 5.5 MPa, and thus larger than the stress drops of the Blanco Ridge events, then $A_S < A_E$ and the single-mode hypothesis could describe slip on the Blanco RTF.

6.4 Case Study II: The Romanche Transform Fault

The Romanche Transform Fault is a prominent, approximately 920 km-long, feature that offsets the slowly spreading Mid-Atlantic Ridge at a half rate of 16 mm/yr just south of the equator. The Romanche is bounded by anomalous transverse ridges (transform-parallel highs) and a deep valley, which descends to 7.8 km below sea level in the deepest basin. The active transform valley is continuous, but not straight, with a number of bends that have been associated with changes in plate motion [Bonatti *et al.*, 1994; Searle *et al.*, 1994]. The

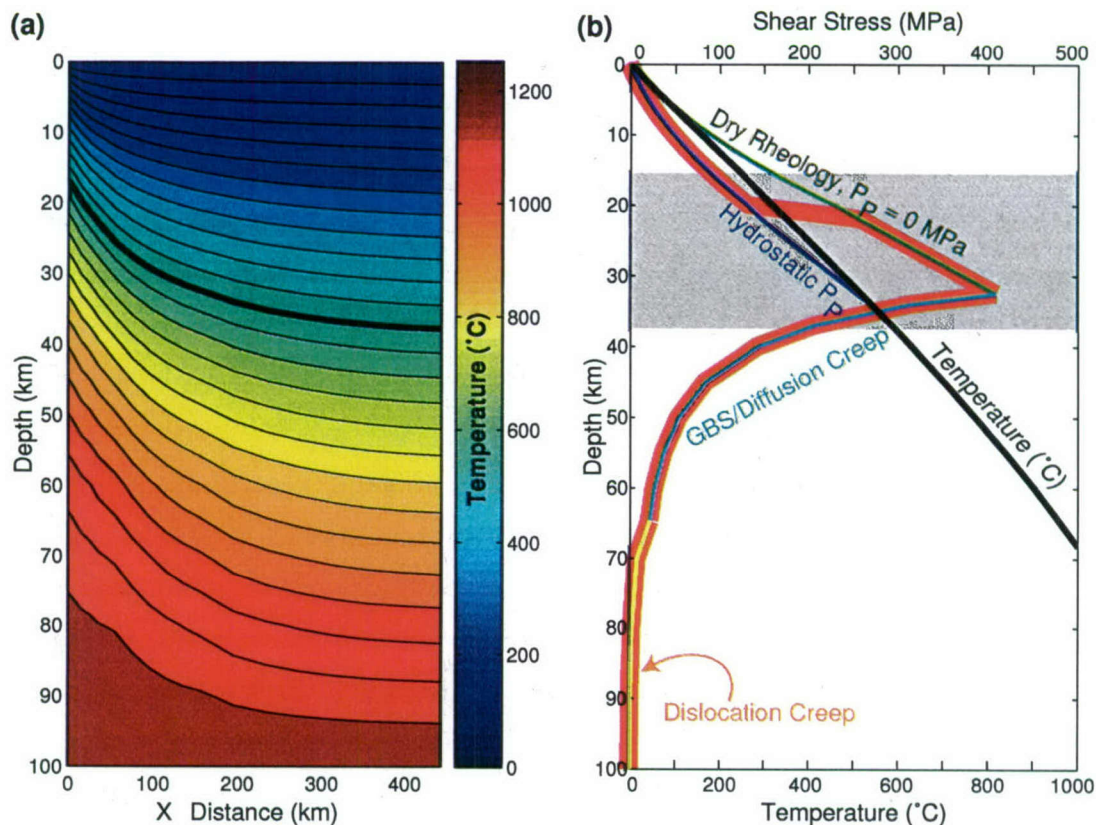


Figure 6-12: (a) Cross-sectional view of the 3D finite difference solution for the thermal structure of the Romanche, with a half-spreading rate $U = 16$ mm/yr and a total length of 920 km. The full solution is symmetric around $x = 460$ km. (b) Predicted strength envelope (red) using the geotherm (black) from the center of the transform ($x = 460$ km) and hydrostatic pore pressure to the 350°C isotherm and a dry rheology below. The seismogenic zone (250°C to 600°C) is marked with a gray stripe. Note the strengths shown here are significantly higher than those of Figure 6-4.

occurrence of 140 ma pelagic limestone within 120 ma oceanic crust indicates that plate boundary reorganization must have been common throughout the history of the Romanche [Bonatti *et al.*, 1996].

The Romanche is the second longest RTF (after the Chile Transform in the eastern Pacific Ocean) and is the site of many of the largest RTF earthquakes over the past 41 years, including the largest, $M_W = 7.1$, that occurred on January 3rd, 1982. Another large earthquake, $M_W = 7.0$ on March 14th, 1994, has been studied extensively. McGuire *et al.* [1996] show that the 1994 event was preceded by a slow (~ 100 s) episode of moment release prior to the P-wave arrival, although this result has been contested by Abercrombie and

Ekström [2001, 2003]. Events recorded in the Harvard CMT catalog from 1976-2005 are shown in Figure 6-13, with rupture areas calculated from the observed moments assuming constant stress drop scaling ($\Delta\sigma = 1$ MPa) as was done for earthquakes on the Blanco Transform Fault.

The three-dimensional thermal structure of the region surrounding the Romanche was calculated using the finite difference technique described in Section 6.2.4. We use a simple model geometry of a single RTF of length 920 km. Because the Romanche is one of the longest RTFs and is on a slow spreading ridge, it has one of the coolest thermal structures. In our model the 600°C isotherm reaches depths of $z_{\max} = 38$ km on the Romanche (Figure 6-12a). This is significantly deeper than the maximum depth of the 600°C isotherm on the Blanco, for either the segmented ($z_{\max} = 14$ km) or unsegmented ($z_{\max} = 20$ km) models. Moreover, the earthquake centroid depths calculated by *Abercrombie and Ekström* [2003] have a maximum depth of 20 km.

Estimates of the maximum strength for each point on the Romanche are shown in Figure 6-13. These strengths are obtained by combining the thermal and rheological models, which are shown in Figures 6-12a & 6-12b respectively. In the crust and uppermost mantle (0-10 km beneath the seafloor), the Romanche appears to be weak, yielding at maximum shear stresses of $\tau \leq 50$ MPa. The shear strength increases gradually down to ~ 20 km, reaching $\tau \geq 100$ MPa. In the center of the Romanche, the 350°C isotherm is located at a depth of about 20 km, which is where our model predicts a switch from a hydrostatic serpentine rheology to dry peridotite. Consequently a dramatic stress increase is also predicted at ~ 20 km, due to the significant depth of the transition from hydrostatic to dry conditions (see the pressure difference between the hydrostat and lithostat in Figure 6-4a).

The highest shear strengths predicted on the Romanche reach values of up to $\tau_{\max} \approx 400$ MPa, with an overall average strength above the 600°C isotherm of $\bar{\tau} = 154$ MPa. Again, we emphasize that the strengths shown in these plots are maximum predictions based on our relatively simple thermal and rheological models. Using the half-space cooling model the 600°C isotherm is still very deep, approaching 25 km, as is shown with the white-dashed line in Figure 6-13, and we still obtain high shear stresses, with a maximum strength of $\tau_{\max} = 300$ MPa and an average strength of $\bar{\tau} = 115$ MPa. Faults such as the Romanche, which are extreme in their size, are most likely affected by unmodeled processes, such as thermal weakening from continued localized shearing. Thus the Romanche is a good

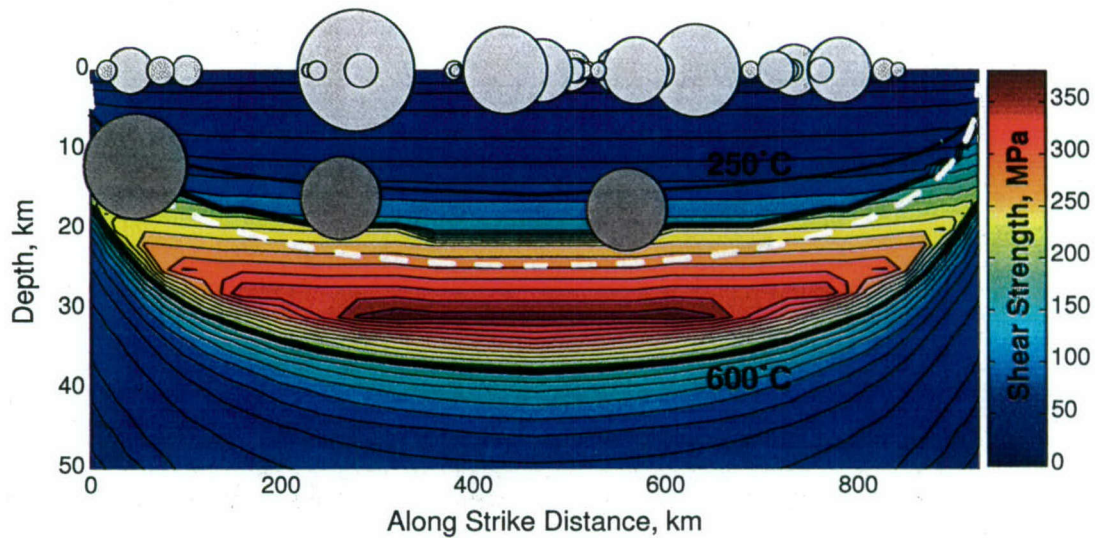


Figure 6-13: Maximum yield strength along the Romanche Transform Fault. Earthquakes from the Harvard CMT catalog (1976-2005) are plotted at their epicenters (light gray) and three events with depths from *Abercrombie and Ekström* [2003] are shown at their hypocenters. Circle sizes represent rupture areas calculated with a constant stress drop of $\Delta\sigma = 1$ MPa, assuming slip scales with the rupture area. The 250°C and 600°C isotherms are labeled with thick black lines and delineate the seismogenic zone. For comparison the white dashed line shows the 600°C isotherm as calculated with the half-space cooling model.

candidate for future modeling studies to better understand what processes could be active on RTFs, to produce warmer thermal structures and more reasonable stress levels.

6.4.1 Fit of Romanche Seismicity to the Synoptic Model

Our synoptic model for the Romanche Transform Fault indicates a continuous seismogenic zone (between the 250°C and 600°C isotherms), approximately 900 km \times 20 km in total area. If this area were to rupture in a single event with a stress drop of $\Delta\sigma = 1$ MPa, it would be equivalent to approximately a $M_W = 8.2$ earthquake. However, such large earthquakes are not consistent with the scaling relations derived in Chapter 2 and are not observed on RTFs. Using the relation given in Section 6.3.4, we obtain a prediction for the magnitude of the largest expected event, $M_C \approx 7.0$, which correlates well with the largest observed event $M_W = 7.1$. The three events for which *Abercrombie and Ekström* [2003] have published centroid estimates all fall just below the 250°C isotherm in Figure 6-13 and into the predicted seismogenic zone. Using the half-space cooling model, these events are still located within the seismogenic zone, but in this case they fall just above the 600°C

isotherm (Figure 6-13, which is the result reported by *Abercrombie and Ekström* [2003]). As the Romanche is a single, massive fault structure, it is difficult to evaluate the distribution of seismicity relative to our model. Our model is certainly not unique and with only three earthquake depths, we have few constraints on how well our model fits the seismicity data.

6.5 Synoptic Model Evaluation and Implications

This synoptic model raises a question that is integral to the mechanics of faulting— how to resolve the apparent paradox between the high yield strength in the seismogenic zone as predicted by extrapolation of rock mechanics data and the low earthquake stress drops. Like on the San Andreas Fault, our synoptic model for RTFs suggests a difference of one to two orders of magnitude between shear stresses on the fault and stress drops during earthquakes. In particular, the largest earthquakes observed on the Blanco are located near the region of highest predicted shear strength ($\tau \approx 150$ MPa). These events include the 1994 earthquake, for which the very low stress drop $\Delta\sigma \approx 0.1$ MPa was estimated from aftershock locations (Table 2.2).

A possible resolution to the apparent stress paradox for RTFs is that actual fault strength is low. This is suggested by the work of *Behn et al.* [2002], who through numerical modeling, found that RTFs require coupling coefficients of only about 5% to match stress rotations of earthquake focal mechanisms and abyssal hill fabric near transform faults. With hydrostatic pore fluid conditions throughout the seismogenic zone the predicted shear strengths would be significantly reduced from what we have previously shown, reducing strengths by 25-40%, yielding values of $\bar{\tau} = 33$ MPa and $\tau_{\max} = 125$ MPa on the Blanco, and $\bar{\tau} = 113$ MPa and $\tau_{\max} = 275$ MPa on the Romanche. The difficulty in obtaining high pore fluid pressures at seismogenic depths, is in somehow allowing water to penetrate through a serpentized layer to reach the peridotite below. The fluids that do make it into the peridotite layer are likely to be trapped at depth, due to the non-dilatant brittle behavior of serpentine [*Escartin et al.*, 1997]. Once trapped, these fluids could be over pressurized, reducing the shear strength to values even lower than those given above.

Warmer thermal structures would also lead to lower maximum yield strengths, as discussed with the two thermal modeling techniques used in this chapter. While our finite difference calculations include both convection and advection of heat due to the mantle

flow field near ridges, transforms, and intra-transform spreading segments, our models do not include the effects of hydrothermal cooling or shear heating. Hydrothermal cooling will likely cool the shallow lithosphere, but is not likely to effect the seismogenic regions where the stresses are highest. Thermal weakening, however, does provide another mechanism for lowering fault strength.

Both steady-state shear heating from continuous plate loading and thermal weakening during fast slip in an earthquake are likely to effect faults that support high stress. The predicted mean strengths of the two RTFs considered here are very high, $55 \text{ MPa} \leq \bar{\tau} \leq 155 \text{ MPa}$, significantly exceeding the value of $\bar{\tau} = 20 \text{ MPa}$ determined by *Brune et al.* [1969] and *Lachenbruch and Sass* [1973] for the San Andreas Fault based on the heat flow data. *Chen* [1988] predicted that slow-slipping, long-offset faults could produce enough shear heating to raise the thermal structure by 200-400°C. Rapid earthquake slip could result in flash heating and thermal softening of the asperities, or in local melting on narrow slip surfaces. All of these effects would result in warmer thermal structures, which would enhance creep processes in the upper mantle, resulting in a reduced strength profile. However, there is direct evidence from mylonites collected on the Shaka Transform Fault on the Southwest Indian Ridge [*Jaroslow et al.*, 1996], for relatively high stresses in the viscously deforming region just below the seismogenic zone. *Warren et al.* [2005] determined that the mylonites were formed through grain boundary sliding at shear stresses near 100 MPa and temperatures between 600°C-800°C, consistent with the region of peak strength at the base of the seismogenic zone shown for the Blanco. Thus, while the actual strengths supported by RTFs are most-likely lower than what we have calculated for the Romanche, they must reach levels near what we predict for the Blanco (~100 MPa) in order to form mylonitic structures.

If the actual stress on RTFs does reach high values, then alternate mechanism are required to resolve the apparent stress paradox on RTFs. One possibility is that earthquake stress drops only partially relieve the accumulated shear stress. This suggestion is consistent with laboratory experiments on rock friction, which show relatively low magnitude stick-slip events (e.g. those shown in Chapters 4 & 5). A second possibility is that the average stress, $\bar{\tau}$ on the fault is low. In such a model, isolated patches of high fault strength are surrounded by steadily creeping, low strength material. This last suggestion has been offered as an explanation for the repeating earthquakes observed in the creeping section of

the San Andreas [Nadeau and McEvilly, 1999] and on the Japanese subduction zone interface [Matsuzawa *et al.*, 2002; Igarashi *et al.*, 2003]. While the stress paradox remains an unsolved problem for both the San Andreas and oceanic RTFs, our synoptic model suggests tests of some of the possible resolutions. If shear strengths are high, then we would expect variable heat flow along segmented faults, corresponding to variation in mean stress between the segments. On the Blanco, our model predicts high heat flow on the Blanco Ridge and low values on the shortest segments. With more earthquake relocations and with additional centroid locations, we can also evaluate whether there are strong asperities with repeating earthquakes on RTFs.

An outcome of our synoptic model is the prediction of a number of aspects of seismicity and faulting that will hopefully be tested in the future. As discussed previously, our model specifies the magnitude of largest expected event on each segment and that this quantity varies as a function of the area above the 600°C isotherm. For segmented faults it also predicts heat flow variation along strike. We speculate that isolated fault patches may be fully seismically coupled, and with more location information and longer earthquake catalogs it will be possible to determine if most of the fault slip on RTFs obeys the single-mode or multi-mode hypothesis.

Our synoptic model yields depth-dependent predictions of focal mechanism orientation on RTFs. These predictions are based on the study of Bokelmann and Beroza [2000], who investigated earthquake focal mechanisms in Northern California and found that their principle axes were well oriented with the vertical and horizontal in the upper few kilometers, which they suggested was due to the free surface boundary condition. Between about 4-8 km depth the slip vectors rotated, indicating an increase in shear traction on the fault. At greater depths the focal mechanism re-aligned with the horizontal and vertical, which the authors speculated was due to a weak lower crust, and therefore a second free surface boundary condition. In our model, we predict a gradual strengthening throughout the shallow lithosphere, followed by a rapid strengthening at the transition from hydrostatic to dry conditions, and a subsequent weakening in the ductile mantle. Applying the analysis of Bokelmann and Beroza [2000] to RTFs, we expect a rotation of the earthquake slip vectors by the top of the seismogenic zone at 250°C in response to increasing shear stress. As no weak lower crustal layer is expected, our model predicts that the focal mechanisms will remain rotated at all seismogenic depths.

6.6 Summary

In this chapter we present a synoptic model that incorporates many aspects of the current knowledge of faulting on oceanic ridge transform faults to better understand characteristics of RTF seismicity that have been investigated throughout this thesis. We include a relatively weak layer of serpentinized rock in the shallow lithosphere, with a coefficient of friction that increases from 0.2 up to typical values for olivine at depth. At tectonic creep rates the serpentinized region is likely to be velocity strengthening at temperatures $T \leq 250^\circ\text{C}$, and thus will limit earthquake nucleation at shallow depths. Our model includes a transition in frictional behavior at 250°C to velocity weakening (i.e. seismogenic) conditions. At 350°C our model switches from hydrostatic pore pressures and a serpentinite lithology to dry peridotite with a coefficient of friction of $\mu \approx 0.5$. The peridotite layer exhibits velocity weakening behavior that gives way to stable sliding near the 600°C isotherm. The shallowest portion of temperature-dependent ductile rheology is dominated by grain boundary sliding and diffusion creep, where mylonites are formed. Diffusion creep transitions to dislocation creep at depth and the yield stress decreases rapidly.

The inclusion of small-scale structures and fault segmentation are integral to obtaining reasonable estimates of fault strength and predicting the location and maximum size of earthquakes on ridge transform faults. We find scaling relations derived in Chapter 2 from a global distribution of large RTFs are successful predictors of seismicity on small transform segments, such as those on the Blanco Transform Fault. Five of the largest earthquakes ($M_W \leq 6.4$) on the Blanco are located within 50 km of each other and may represent an example of a fully-coupled fault patch on an RTF. However, much of the Blanco has a low coupling coefficient and some segments appear to violate the single-mode hypothesis, which states that a fault patch with either slip seismically or aseismically, but will not alternate.

The largest earthquakes appear to be spatially correlated with the highest stresses. This relationship indicates an apparent paradox between high fault yield strengths and low earthquake stress drops. Our model predicts especially high stresses ($\tau \geq 300 \text{ MPa}$) in a narrow region near the base of the seismogenic zone on the Romanche Transform Fault. Such high stress levels do not appear sustainable and thus indicate that unmodeled effects, such as shear heating, may play an important role in determining the thermal structure of long-offset, slow-slipping RTFs. We speculate focal mechanism orientations will be uniform

with depth, and we predict that maximum earthquake size and heat flow will vary along strike on segmented RTFs. To test these predictions and address other unresolved problems discussed in this thesis a high-quality array of ocean bottom seismometers that are located on an RTF is essential.

References

- Abercrombie, R., and G. Ekström, Earthquake slip on oceanic transform faults, *Nature*, 410, 74–77, 2001.
- Abercrombie, R., and G. Ekström, A reassessment of the rupture characteristics of oceanic transform earthquakes, *J. Geophys. Res.*, 108, 2003.
- Abercrombie, R., and J. Mori, Occurrence patterns of foreshocks to large earthquakes in the western united states, *Nature*, 381, 303–307, 1996.
- Aki, K., Some problems in statistical seismology, *Zisin*, 8, 205–228, 1956.
- Aki, K., Maximum likelihood estimate of b in the formula $\log n = a - bm$ and its confidence limits, *Bull. Earthquake Res. Inst. Tokyo Univ.*, 43, 237–239, 1965.
- Aki, K., Seismic displacements near a fault, *J. Geophys. Res.*, 73, 5959–5976, 1968.
- Allen, C. R., *Proceedings of a Conference on the Geologic Problems of the San Andreas Fault System*, chap. The tectonic environments of seismically active and inactive areas along the San Andreas fault system, pp. 70–82, Stanford University Press, 1968.
- Anderson, J. G., and J. E. Luco, Consequences of slip rate constraints on earthquake occurrence relation, *Bull. Seism. Soc. Am.*, 73, 471–496, 1983.
- Aviles, C. A., C. H. Scholz, and J. Boatwright, Fractal analysis applied to characteristic segments of the San Andreas Fault, *J. Geophys. Res.*, 92, 331–344, 1987.
- Bai, Q., S. Mackwell, and D. Kohlstedt, High-temperature creep of olivine single crystals 1. mechanical results for buffered samples, *J. Geophys. Res.*, 96, 2441–2463, 1991.
- Bäth, M., Lateral inhomogeneities in the upper mantle, *Tectonophys.*, 2, 483–514, 1965.
- Beeler, N., and D. Lockner, Why earthquakes correlate weakly with the solid Earth tides: Effects of periodic stress on the rate and probability of earthquake occurrence, *J. Geophys. Res.*, 108, 2391, doi:10.1029/2001JB001518, 2003.
- Beeler, N., T. Tullis, and J. Weeks, The roles of time and displacement in the evolution effect in rock friction, *Geophys. Res. Lett.*, 21, 1987–1990, 1994.
- Beeler, N., T. Tullis, M. Blanpied, and J. Weeks, Frictional behavior of large displacement experimental faults, *J. Geophys. Res.*, 101, 8697–8715, 1996.
- Behn, M. D., J. Lin, and M. T. Zuber, Evidence for weak oceanic transform faults, *Geophys. Res. Lett.*, 29, 10.1029/2002GL015612, 2002.
- Bender, B., Maximum likelihood method estimation of b values for magnitude grouped data, *Bull. Seism. Soc. Am.*, 73, 831–851, 1983.
- Bergman, E. A., and S. C. Solomon, Transform fault earthquakes in the North Atlantic: Source mechanisms and depth of faulting, *J. Geophys. Res.*, 93, 9027–9057, 1988.
- Beroza, G., Near-source modeling of the Loma Prieta earthquake: Evidence for heterogeneous slip and implications for earthquake hazard, *Bull. Seism. Soc. Am.*, 81, 1603–1621, 1991.
- Beroza, G. C., and T. H. Jordan, Searching for slow and silent earthquakes using free oscillations, *J. Geophys. Res.*, 95, 2485–2510, 1990.
- Bird, P., Y. Y. Kagan, and D. D. Jackson, Plate tectonics and earthquake potential of spreading ridges and oceanic transform faults, *Amer. Geophys. Un. Geodyn. Monog.*, 30, 203–218, 2002.

- Bodin, P., and J. M. Brune, On the scaling of slip with rupture length for shallow strike-slip earthquakes: quasi-static models and dynamic rupture propagation, *Bull. Seism. Soc. Am.*, **86**, 1292–1299, 1996.
- Bodin, P., S. Brown, and D. Matheson, Laboratory observations of fault-normal vibrations during stick slip, *J. Geophys. Res.*, **103**, 29,931–29,944, 1998.
- Boettcher, M. S., and T. H. Jordan, Earthquake scaling relations for mid-ocean ridge transform faults, *J. Geophys. Res.*, p. submitted, 2004.
- Boettcher, M. S., G. Hirth, and B. Evans, Olivine friction at the base of the seismogenic zone, *Eos Trans. AGU*, **84**, Fall Meet. Suppl., Abstract T41C-0231, 2003.
- Bohnenstiehl, D. R., M. Tolstoy, R. P. Dziak, C. G. Fox, and D. K. Smith, Aftershock sequences in the mid-ocean ridge environment: an analysis using hydroacoustic data, *Tectonophysics*, **354**, 49–70, 2002.
- Bohnenstiehl, D. R., M. Tolstoy, and E. Chapp, Breaking into the plate: a mega fracture-zone earthquake adjacent to the Central Indian Ridge, *Geophys. Res. Lett.*, **31**, L02,615, doi:10.1029/2003GL018,981, 2004.
- Bokelmann, G. H. R., and G. C. Beroza, Depth-dependent earthquake mechanism orientation: Evidence for a weak zone in the lower crust, *J. Geophys. Res.*, **105**, 21,683–21,695, 2000.
- Bonatti, E., Serpentinite protrusions in the oceanic crust, *Earth Planet. Sci. Lett.*, **32**, 107–113, 1976.
- Bonatti, E., M. Ligi, L. Gasperini, A. Peyve, Y. Raznitsin, and Y. Chen, Transform migration and vertical tectonics at the Romanche fracture zone, equatorial Atlantic, *J. Geophys. Res.*, **99**, 21,779–21,802, 1994.
- Bonatti, E., M. Ligi, A. Borsetti, L. Gasperini, A. Negri, and R. Sartori, Lower Cretaceous deposits trapped near the equatorial Mid-Atlantic Ridge, *Nature*, **380**, 518–520, 1996.
- Bouchon, M., N. Toksoz, H. Karabulut, M.-P. Bouin, M. Dietrich, M. Aktar, and M. Edie, Seismic imaging of the Izmit rupture inferred from near-fault recordings, *Geophys. Res. Lett.*, **27**, 3013–3016, 2000.
- Bowan, J., and R. S. White, Variation with spreading rate of oceanic crustal thickness and geochemistry, *Earth Planet. Sci. Lett.*, **121**, 435–449, 1994.
- Bowden, F., and D. Tabor, *The friction and lubrication of solids*, p. 374, Oxford University Press, 1950.
- Bowden, F., and D. Tabor, Friction, lubrication and wear: a survey of work during the last decade, *Brit. J. Appl. Phys.*, **17**, 1521–1544, 1966.
- Brace, W. F., B. W. P. Jr., and C. Scholz, Dilatancy in the fracture of crystalline rocks, *J. Geophys. Res.*, **71**, 3939–3953, 1966.
- Brodsky, E. E., E. Roeloffs, D. Woodcock, I. Gall, and M. Manga, A mechanism for sustained groundwater pressure changes induced by distant earthquakes, *J. Geophys. Res.*, **108**, 2390, doi:10.1029/2002JB002,321, 2003.
- Brune, J. N., Seismic moment, seismicity, and rate of slip along major fault zones, *J. Geophys. Res.*, **73**, 777–784, 1968.
- Brune, J. N., T. L. Henyey, and R. F. Roy, Heat flow, stress and rate of slip along San Andreas fault, California, *J. Geophys. Res.*, **74**, 3821–3827, 1969.
- Bureau, L., T. Baumberger, and C. Caroli, Shear response of a frictional interface to a normal load modulation, *Physical Review E*, **62**, 6810–6820, 2000.
- Burr, N. C., and S. C. Solomon, The relationship of source parameters of oceanic transform earthquakes to plate velocity and transform length, *J. Geophys. Res.*, **83**, 1193–1205, 1978.
- Byerlee, J., Friction of rocks, *Pure Appl. Geophys.*, **116**, 615–626, 1978.
- Cande, S., J. LaBrecque, R. Larson, W. Pitman, III, X. Golovchenko, , and W. Haxby, Magnetic lineations of world's ocean basins (map), *Tech. rep.*, Amer. Ass. Petrol. Geol., OK, 1989.
- Cannat, M., et al., Thin crust, ultramafic exposures, and rugged faulting patterns at the mid-atlantic ridge (22 deg – 24 degn), *Geology*, **23**, 49–52, 1995.
- Chen, Y., Thermal model of oceanic transform faults, *J. Geophys. Res.*, **93**, 1988.

- Cowie, P. A., Normal fault growth in three-dimensions in continental and oceanic crust, *Faulting and Magmatism at Mid-Ocean Ridges*, AGU Monograph, 106, 325-348, 1998.
- Cowie, P. A., and C. H. Scholz, Physical explanation for displacement-length relationship for faults using a post-yield fracture mechanics model, *J. Struct. Geol.*, 14, 1133-1148, 1992.
- Davies, G. F., and J. N. Brune, Regional and global fault slip rates from seismicity, *Nature Phys. Sci.*, 229, 101-107, 1971.
- DeMets, C., R. G. Gordon, D. F. Angus, and S. Stein, Current plate motions, *Geophys. J. Int.*, 101, 425-478, 1990.
- Detrick, R. S., and G. M. Purdy, The crustal structure of the Kane fracture zone from seismic refraction studies, *J. Geophys. Res.*, 85, 3759-3777, 1980.
- Dieterich, J., and B. Kilgore, Implications of fault constitutive properties for earthquake prediction, *Proc. Natl. Acad. Sci. USA*, pp. 3787-3794, 1996.
- Dieterich, J. H., Time-dependent friction and the mechanics of stick-slip, *Pure Appl. Geophys.*, 116, 790-806, 1978.
- Dieterich, J. H., Modeling of rock friction: 1 experimental results and constitutive equations, *J. Geophys. Res.*, 84, 2161-2168, 1979.
- Dodge, D. A., G. C. Beroza, and W. Ellsworth, Detailed observations of California foreshock sequences: Implications for the earthquake initiation process, *J. Geophys. Res.*, 101, 22,371-22,392, 1996.
- Dragert, H., K. Wang, and T. S. James, A silent slip event on the deeper Cascadia subduction interface, *Science*, 292, 1525-1528, 2001.
- Durham, W. B., and C. Goetze, Plastic flow of oriented single crystals of olivine, 1, mechanical data, *J. Geophys. Res.*, 82, 5737-5753, 1977.
- Dziak, R., C. Fox, R. Embley, J. Lupton, G. Johnson, W. Chadwick, and R. Koski, Detection of and response to a probable volcanogenic T-wave event swarm on the western Blanco Transform Fault Zone, *Geophys. Res. Lett.*, 23, 873-876, 1996.
- Dziak, R. P., SOSUS locations for events on the Western Blanco Transform Fault, 1999, personal Communication.
- Dziak, R. P., C. G. Fox, and R. W. Embley, Relationship between the seismicity and the geologic structure of the Blanco Transform Fault Zone., *Marine Geophysical Researches*, 13, 203-208, 1991.
- Dziak, R. P., C. Fox, R. Embley, J. Nabelek, J. Braunmiller, and R. Koski, Recent tectonics of the Blanco Ridge, eastern Blanco transform fault zone, *Marine Geophys. Res.*, 21, 423-450, 2000.
- Dziewonski, A. M., T.-A. Chou, and J. H. Woodhouse, Determination of earthquake source parameter from waveform data for studies of global and regional seismicity, *J. Geophys. Res.*, 86, 2825-2852, 1981.
- Ekström, G., and A. M. Dziewonski, Evidence of bias in estimations of earthquake size, *Nature*, 332, 319-323, 1988.
- Elliott, D., The energy balance and deformation mechanisms of thrust sheets, *Phil. Trans. Roy. Soc. Lond.*, A283, 289-312, 1976.
- Ellsworth, W. L., and G. Beroza, Observation of the seismic nucleation phase in the ridgecrest, California, earthquake sequence, *Geophys. Res. Lett.*, 25, 401-404, 1998.
- Embley, R. W., and D. S. Wilson, Morphology of the Blanco Transform-Fault Zone-NE Pacific: Implications for its tectonic evolution, *Marine Geophys. Res.*, 14, 25, 1992.
- Engeln, J. F., D. A. Weins, and S. Stein, Mechanisms and depths of Atlantic transform earthquakes, *J. Geophys. Res.*, 91, 548-577, 1986.
- Escartin, J., G. Hirth, and B. Evans, Non-dilatant brittle deformation of serpentinites: Implications for Mohr-Coulomb theory and the strength of faults, *J. Geophys. Res.*, 102, 2897-2913, 1997.
- Escartin, J., G. Hirth, and B. Evans, Strength of slightly serpentinitized peridotites: Implications for the tectonics of oceanic lithosphere, *Geology*, 29, 1023-1026, 2001.
- Evans, B., and C. Goetze, The temperature variation of hardness of olivine and its implications for polycrystalline yield stress, *J. Geophys. Res.*, 84, 5505-5524, 1979.

- Evans, B., J. T. Frederich, and T.-F. Wong, The brittle-ductile transition in rocks: Recent experimental and theoretical progress, in *The Brittle-ductile Transitions in Rocks: The Heard Volume*, vol. 56 of *Geophysical Monograph*, pp. 1–20, 1990.
- Evans, B. W., The serpentinite multisystem revisited: chrysotile is metastable, *Int. Geol. Rev.*, *46*, 479–506, 2004.
- Feltzer, K. R., R. Abercrombie, and G. Ekström, A common origin for aftershocks, foreshocks, and multiplets, *Bull. Seism. Soc. Am.*, *94*, 88–98, 2004.
- Felzer, K. R., T. W. Becker, R. E. Abercrombie, G. Ekström, and J. Rice, Triggering of the 1999 M_w 7.1 Hector Mine earthquake by aftershocks of the 1992 M_w 7.3 Landers earthquake, *J. Geophys. Res.*, *107*, 10.1029/2001JB000911, 2002.
- Forsyth, D. W., Y. Yang, and M. D. Mangriotis, Coupled seismic slip on adjacent oceanic transform faults, *Geophys. Res. Lett.*, *30*, 10.1029/2002GL016454, 2003.
- Fox, C. G., H. Matsumoto, and T. K. Lau, Monitoring pacific ocean seismicity from an autonomous hydrophone array, *J. Geophys. Res.*, *163*, 4183–4206, 2001.
- Francis, T. J. G., The detailed seismicity of mid-ocean ridges, *Earth Planet. Sci. Lett.*, *4*, 39–46, 1968.
- Francis, T. J. G., Serpentinization faults and their role in the tectonics of slow spreading ridges, *J. Geophys. Res.*, *86*, 11,616–11,622, 1981.
- Frohlich, C., and K. D. Apperson, Earthquake focal mechanisms, moment tensors, and the consistency of seismic activity near plate boundaries, *Tectonics*, *11*, 279–296, 1992.
- Frohlich, C. F., and S. D. Davis, Teleseismic b -values: Or, much ado about 1.0, *J. Geophys. Res.*, *98*, 631, 1993.
- Frye, K. M., and C. Marone, The effect of humidity on granular friction at room temperature, *J. Geophys. Res.*, *107*, 2309, doi:10.1029/2001JB000654, 2002.
- Gardner, J., and L. Knopoff, Is the sequence of earthquakes in Southern California, with aftershocks removed, Poissonian?, *Bull. Seism. Soc. Am.*, *64*, 1363–1367, 1974.
- Gladwin, M. T., R. L. Gwyther, R. H. G. Hart, and K. S. Breckenridge, Measurements of the strain field associated with episodic creep events on the San Andreas Fault at San Juan Bautista, California, *J. Geophys. Res.*, *99*, 4559–4565, 1994.
- Goetze, C., Mechanisms of creep in olivine, *Phil. Trans. Roy. Soc. of London Series A*, *288*, 99–119, 1978.
- Gomberg, J., Stress/strain changes and triggered seismicity following the M_w 7.3 Landers, California, earthquake, *J. Geophys. Res.*, *101*, 751–764, 1996.
- Gomberg, J., and P. Bodin, Triggering of the $M_s = 5.4$ Little Skull Mountain, Nevada, earthquake with dynamic strains, *Bull. Seism. Soc. Am.*, *84*, 844–853, 1994.
- Gomberg, J., and S. Davis, Stress/strain changes and triggered seismicity at the Geysers, California, *J. Geophys. Res.*, *101*, 733–750, 1996.
- Gomberg, J., M. L. Blanpied, and N. M. Beeler, Transient triggering of near and distant earthquakes, *Bull. Seism. Soc. Am.*, *87*, 294–309, 1997.
- Greenwood, J., and J. Williamson, Contact of nominally flat surfaces, *Proc. R. Soc. London Ser. A*, *295*, 300–319, 1966.
- Guo, Z., and Y. Ogata, Statistical relations between the parameters of aftershocks in time, space, and magnitude, *J. Geophys. Res.*, *102*, 2857–2873, 1997.
- Hanks, T. C., and W. H. Bakun, A bilinear source-scaling model for $m - \log a$ observations, *Bull. Seism. Soc. Am.*, *92*, 1841–1846, 2002.
- Harris, R. A., Introduction to special section: Stress triggers, stress shadows, and implications for seismic hazard, *J. Geophys. Res.*, *103*, 24,347–24,358, 1998.
- Harris, R. A., and P. Segall, Detection of a locked zone at depth on the Parkfield, California, segment of the San Andreas Fault, *J. Geophys. Res.*, *92*, 7945–7962, 1987.
- Harvard Centroid-Moment Tensor Project, <http://www.seismology.harvard.edu/projects/CMT>, 1976–2002.

- Heaton, T. H., Evidence for and implications of self-healing pulses of slip in earthquake rupture, *Phys. Earth Planet. Inter.*, **64**, 1–20, 1990.
- Heki, K., S. Miyazake, and H. Tsuji, Silent fault slip following an interplate thrust earthquake at the Japan trench, *Nature*, **386**, 595–598, 1997.
- Helmstetter, A., Is earthquake triggering driven by small earthquakes?, *Phys. Rev. Lett.*, **91**, 2003.
- Helmstetter, A., and D. Sornette, Subcritical and supercritical regimes in epidemic models of earthquake aftershocks, *J. Geophys. Res.*, **107**, 2002.
- Helmstetter, A., and D. Sornette, Båth's law derived from the Gutenberg-Richter law and from aftershock properties, *Geophys. Res. Lett.*, **30**, 2003.
- Helmstetter, A., Y. Kagan, and D. D. Jackson, Importance of small earthquakes for stress transfers and earthquake triggering, *in press J. Geophys. Res.*, 2005.
- Hill, D., et al., Seismicity remotely triggered by the magnitude 7.3 Landers, California, earthquake, *Science*, **260**, 1617–1623, 1993.
- Hirata, T., Fractal dimension of fault systems in Japan; fractal structure in rock fracture geometry at various scales, *Pure Appl. Geophys.*, **131**, 157–170, 1989.
- Hirose, H., K. Hirahara, F. Kimata, N. Fujii, and S.-I. Miyazake, A slow thrust slip event following the two 1996 Hyuganada earthquakes beneath the Bungo Channel, Southwest Japan, *Geophys. Res. Lett.*, **26**, 3237–3240, 1999.
- Hirth, G., Laboratory constraints on the rheology of the upper mantle, in *Plastic Deformation of Minerals and Rocks*, edited by S. Karato and H. R. Wenk, vol. 51, pp. 97–120, Reviews in Mineralogy and Geochemistry, 2002.
- Hirth, G., and D. L. Kohlstedt, Rheology of the upper mantle and the mantle wedge: A view from the experimentalists, in *The Subduction Factory*, Geophysical Monograph, p. ??, AGU, 2003.
- Hyndman, R. D., and D. H. Weichert, Seismicity and rates of relative plate motion on the plate boundaries of Western North America, *Geophys. J. R. astr. Soc.*, **72**, 59–82, 1983.
- Igarashi, T., T. Matsuzawa, and A. Hasegawa, Repeating earthquakes and interplate aseismic slip in the northeastern Japan subduction zone, *J. Geophys. Res.*, pp. 8–1, 2003.
- Ihmlé, P. F., and T. H. Jordan, Teleseismic search for slow precursors to large earthquakes, *Science*, **266**, 1547–1551, 1994.
- Ihmlé, P. F., P. Harabaglia, and T. H. Jordan, Teleseismic detection of a slow precursor to the Great 1989 Macquari Ridge Earthquake, *Science*, **261**, 177–182, 1993.
- International Seismological Center On-line Bulletin, <http://www.isc.ac.uk>, 1964 - 1999.
- Jackson, D. D., The case for huge earthquakes, *Seism. Res. Lett.*, **67**, 3–5, 1996.
- Jaeger, J. C., and N. Cook, *Fundamentals of Rock Mechanics*, Chapman and Hall, 1977.
- Jaroslów, G. E., G. Hirth, and H. J. B. Dick, Abyssal peridotite mylonites: implications for grain-size sensitive flow and strain localization in the oceanic lithosphere, *Tectonophysics*, **256**, 17–37, 1996.
- Johnson, K. T. M., and H. J. B. Dick, Open system melting and temporal and spatial variation of peridotite and basalt at the atlantis ii fracture zone, *J. Geophys. Res.*, **97**, 9219–9241, 1992.
- Johnson, S. H., and P. R. Jones, Microearthquakes located on the Blanco Fracture Zone with sonobuoy arrays, *J. Geophys. Res.*, **83**, 255–261, 1978.
- Jordan, T. H., and K. Sverdrup, Teleseismic location techniques and their application to earthquake clusters in the South-Central Pacific, *Bull. Seismol. Soc. Am.*, **71**, 1105–1130, 1981.
- Kagan, Y. Y., Seismic moment distribution, *Geophys. J. Int.*, **106**, 123–134, 1991.
- Kagan, Y. Y., Statistics of characteristic earthquakes, *Bull. Seism. Soc. Am.*, **83**, 7–24, 1993.
- Kagan, Y. Y., Seismic moment distribution revisited: I. Statistical results, *Geophys. J. Int.*, **148**, 520–541, 2002a.
- Kagan, Y. Y., Seismic moment distribution revisited: II. Moment conservation principle, *Geophys. J. Int.*, **149**, 731–754, 2002b.
- Kagan, Y. Y., and D. D. Jackson, Probabilistic forecasting of earthquakes, *Geophys. J. Int.*, **143**, 438–453, 2000.

- Kagan, Y. Y., and L. Knopoff, Stochastic synthesis of earthquake catalogs, *J. Geophys. Res.*, **86**, 2853–2862, 1991.
- Kagan, Y. Y., and S. Wesnousky, The Gutenberg-Richter or characteristic earthquake distribution, Which is it? Discussion and reply, *Bull. Seism. Soc. Am.*, **86**, 274–291, 1996.
- Kanamori, H., The energy release in great earthquakes, *J. Geophys. Res.*, **82**, 2981–2987, 1977.
- Kanamori, H., and J. J. Cipar, Focal process of the Great Chilean Earthquake May 22, 1960, *Phys. Earth Planet. Int.*, **9**, 128–136, 1974.
- Kanamori, H., and E. Hauksson, A slow earthquake in the Santa Maria basin, California, *Bull. Seism. Soc. Am.*, **82**, 2087–2096, 1992.
- Kanamori, H., and G. Stewart, Mode of strain release along the Gibbs Fracture Zone, Mid-Atlantic Ridge, *Phys. Earth Planet. Inter.*, **11**, 312–332, 1976.
- Karner, S. L., and C. Marone, Frictional restrengthening in simulated fault gouge: Effect of shear load perturbations, *J. Geophys. Res.*, **106**, 19,319–19,337, 2001.
- Karson, J. A., M. A. Tivey, and J. R. Delaney, Internal structure of uppermost oceanic crust along the Western Blanco Transform Scarp: Implications for subaxial accretion and deformation at the Juan de Fuca Ridge, *J. Geophys. Res.*, **107**, 2181, doi:10.1029/2000JB000051, 2002.
- Kawaski, I., Y. Kawahara, I. Takata, and N. Kosugi, Mode of seismic moment release at transform faults, *Tectonophysics*, **118**, 313–327, 1985.
- Kelemen, P. B., G. Hirth, N. Shimizu, M. Spiegelman, and H. J. Dick, A review of melt migration processes in the adiabatically upwelling mantle beneath oceanic spreading ridges, *Phil. Trans. of the Roy. Soc. of Lon., Series A- Mathematical Physical and Engineering Sciences* **355**, 283–318, 1997.
- Kilb, D., and J. Gomberg, The initial subevent of the 1994 northridge, california, earthquake: Is earthquake size predictable?, *J. Seis.*, **3**, 409–420, 1999.
- Kilb, D., J. Gomberg, and P. Bodin, Triggering of earthquake aftershocks by dynamic stresses, *Nature*, **408**, 570–574, 2000.
- Kilb, D., J. Gomberg, and P. Bodin, Aftershock triggering by complete Coulomb stress changes, *J. Geophys. Res.*, **107**, 2002.
- King, G. C. P., R. S. Stein, and J. B. Rundle, The growth of geological structures by repeated earthquakes: 1. conceptual framework, *J. Geophys. Res.*, **93**, 13,307–13,318, 1988.
- Kiratzzi, A. A., A study on the active crustal deformation of the North and East Anatolian fault zones, *Tectonophysics*, **225**, 191–203, 1993.
- Kisslinger, C., and L. M. Jones, Properties of aftershock sequences in Southern California, *J. Geophys. Res.*, **96**, 11,947–11,958, 1991.
- Knopoff, L., Statistics of earthquakes in Southern California, *Bull. Seism. Soc. Am.*, **54**, 1871–1873, 1964.
- Kohlstedt, D. L., and C. Goetze, Low-stress high-temperature creep in olivine single crystals, *J. Geophys. Res.*, **79**, 2045–2051, 1974.
- Lachenbruch, A., and H. Sass, Thermo-mechanical aspects of the San Andreas fault system, in *Proceedings of the Conference on Tectonic Problems of the San Andreas Fault System*, edited by R. L. Kovach and A. Nur, Stanford University Publications in Geological Sciences **13**, pp. 192–205, 1973.
- Langenhorst, A. R., and E. A. Okal, Correlation of beta-value with spreading rate for strike-slip earthquakes of the mid-oceanic ridge system, *Amer. Geophys. Un. Geodyn. Monog.*, **30**, 191–202, 2002.
- Langer, J. S., J. M. Carlson, C. R. Myers, and B. E. Shaw, Slip complexity in dynamic models of earthquake faults, *Proc. Natl. Acad. Sci.*, **93**, 3825–3829, 1996.
- Ligi, M., E. Bonatti, L. Gasperini, and A. N. Poliakov, Oceanic broad multifault transform plate boundaries, *Geology*, **30**, 11–14, 2002.
- Lilwall, R., and R. Kirk, OBS observations on the Charlie Gibbs Fracture zone, *Geophys. J. of Roy. Ast. Soc.*, **80**, 195–208, 1985.
- Linde, A. T., M. T. Gladwin, M. J. Johnson, R. L. Gwyther, and R. G. Bilham, A slow earthquake sequence on the San Andreas Fault, *Nature*, **383**, 65–68, 1996.

- Lindh, A. G., and D. M. Boore, Control of rupture by fault geometry during the 1966 Parkfield earthquake, *Bull. Seism. Soc. Am.*, **71**, 95–116, 1981.
- Linker, M., and J. H. Dieterich, Effects of variable normal stress on rock friction: observations and constitutive equations, *J. Geophys. Res.*, **97**, 8441–8452, 1992.
- Lockner, D. A., and N. M. Beeler, Premonitory slip and tidal triggering of earthquakes, *J. Geophys. Res.*, **104**, 20,133–20,151, 1999.
- Mai, P. M., and G. Beroza, Source scaling properties from finite-fault rupture models, *Bull. Seism. Soc. Am.*, **90**, 604–615, 2000.
- Main, I. G., and P. W. Burton, Information theory and the earthquake frequency-magnitude distribution, *Bull. Seism. Soc. Am.*, **74**, 1409–1426, 1984.
- Mair, K., and C. Marone, Friction of simulated fault gouge for a wide range of velocities and normal stresses, *J. Geophys. Res.*, **104**, 28,899–28,914, 1999.
- Marone, C., Laboratory derived friction laws and their application to seismic faulting, *Annu. Rev. Earth Planet. Sci.*, **26**, 643–696, 1998.
- Marone, C., and S. J. D. Cox, Scaling of rock friction constitutive parameters: The effects of surface roughness and cumulative offset of friction of gabbro, *Pure Appl. Geophys.*, **143**, 359–385, 1994.
- Matsuzawa, T., T. Igarashi, and A. Hasegawa, Characteristic small-earthquake sequence off Sanriku northeastern Honshu, Japan, *Geophys. Res. Lett.*, **29**, 2002.
- McGuire, J. J., and T. H. Jordan, Further evidence for the compound nature of slow earthquakes: The Prince Edward Island Earthquake of April 28, 1997, *J. Geophys. Res.*, **105**, 7819–7827, 2000.
- McGuire, J. J., P. F. Ihmlé, and T. H. Jordan, Time-domain observations of a slow precursor to the 1994 Romache Transform Earthquake, *Science*, **274**, 82–85, 1996.
- McGuire, J. J., T. H. Jordan, and J. Lin, Complexities of transform fault plate boundaries in the oceans, *Amer. Geophys. Un. Geodyn. Monog.*, **30**, 219–241, 2002a.
- McGuire, J. J., L. Zhao, and T. H. Jordan, Predominance of unilateral rupture for a global catalog of large earthquakes, *Bull. Seism. Soc. Am.*, **92**, 3309–3317, 2002b.
- McManus, D. A., Blanco Fracture Zone, Northeast Pacific Ocean, *Marine Geology*, **3**, 429–455, 1965.
- Melosh, H. J., Acoustic fluidization: A new geologic process?, *J. Geophys. Res.*, **84**, 7513–7520, 1979.
- Miller, M. M., T. Melbourne, D. J. Johnson, and W. Q. Sumner, Periodic slow earthquakes from the Cascadia subduction zone, *Science*, **295**, 2423, 2002.
- Molnar, P., Earthquake recurrence intervals and plate tectonics, *Bull. Seism. Soc. Am.*, **69**, 115–133, 1979.
- Montesi, L., C. Marone, G. Hirth, and S. L. Karner, Frictional properties and microstructure of simulated diabase gouge at temperatures up to 400°C, *EOS*, 1999.
- Moore, D., D. A. Lockner, M. Shengli, R. Summers, and J. Byerlee, Strengths of serpentinite gouges at elevated temperatures, *J. Geophys. Res.*, **102**, 14,787–14,801, 1997.
- Moore, D. E., D. A. Lockner, R. Summers, J. D. Byerlee, and S. Ma, Sample characterization and strength measurements of serpentinite gouges, *U.S. Geol. Surv. Open File Rep.*, **96-702**, 88, 1996a.
- Moore, D. E., D. A. Lockner, R. Summers, M. Shengli, and J. D. Byerlee, Strength of chrysotile-serpentinite gouge under hydrothermal conditions: Can it explain a weak San Andreas fault?, *Geology*, **24**, 1041–1044, 1996b.
- Moore, D. E., D. A. Lockner, H. Tanaka, and K. Iwata, The coefficient of friction of chrysotile gouge at seismogenic depths, *Int. Geol. Rev.*, **46**, 385–398, 2004.
- Mori, J., and H. Kanamori, Initial rupture of earthquakes in the 1995 ridgecrest, California sequence, *Geophys. Res. Lett.*, **23**, 2437–2440, 1996.
- Muller, J., Earthquake source parameters, seismicity, and tectonics of North Atlantic Transform Faults, Ph.D. thesis, Massachusetts Institute of Technology, Cambridge, Massachusetts, 1983.
- Nabelek, J., and G. Xia, Moment-tensor analysis using regional data; application to the March 25, 1993, Scotts Mills, Oregon, earthquake, *Geophysical Research Letters*, **22**, 13–16, 1995.

- Nadeau, R. M., and L. R. Johnson, Seismological studies at parkfield vi: Moment release rates and estimates of source parameters for small repeating earthquakes, *Bull. Seism. Soc. Am.*, **88**, 790–814, 1998.
- Nadeau, R. M., and T. McEvilly, Fault slip rates at depth from recurrence intervals of repeating microearthquakes, *Science*, **285**, 718–721, 1999.
- Nakatani, M., Conceptual and physical clarification of rate and state friction: Frictional sliding as a thermally activated rheology, *J. Geophys. Res.*, **106**, 13,347–13,380, 2001.
- Niu, Y., C. H. Langmuir, and R. J. Kinzler, The origin of abyssal peridotites: a new perspective, *Earth Planet. Sci. Lett.*, **152**, 251–265, 1997.
- Ogata, Y., Estimation of the parameters in the modified Omori formula for aftershock frequencies by maximum likelihood procedure, *J. Phys. Earth*, **31**, 115–124, 1983.
- Ogata, Y., Statistical models for earthquake occurrence and residual analysis for point processes, *J. Am. Stat. Assoc.*, **83**, 9–27, 1988.
- O'Hanley, D. S., J. V. Chernosky, and F. J. Wicks, The stability of lizardite and chrysotile, *Canad. Mineral.*, **27**, 483–493, 1989.
- Okal, E. A., and A. R. Langenhorst, Seismic properties of the Eltanin Transform System, South Pacific, *Phys. Earth Planet. Inter.*, **119**, 185–208, 2000.
- Okal, E. A., and S. Stein, The 1942 Southwest Indian Ocean Ridge earthquake: Largest ever recorded on an oceanic transform, *Geophys. Res. Lett.*, **14**, 147–150, 1987.
- Okal, E. A., and L. M. Stewart, Slow earthquakes along oceanic fracture zones: evidence for asthenospheric flow away from hotspots?, *Earth Planet. Sci. Lett.*, **57**, 75–87, 1982.
- Oppenheimer, D., et al., The Cape Mendocino, California, earthquakes of April 1992: Subduction at the triple junction, *Science*, **261**, 433–438, 1993.
- Ouilleon, G., C. Castaing, and D. Sornette, Hierarchical geometry of faulting, *J. Geophys. Res.*, **101**, 5477–5487, 1996.
- Paterson, M., Rock deformation experimentation, in *The Brittle-ductile Transitions in Rocks: The Heard Volume*, vol. 56 of *Geophysical Monograph*, pp. 187–194, 1990.
- Paterson, M. S., *Experimental Rock Deformation—the Brittle Field*, Berlin: Springer-Verlag, 1978.
- Pegler, G., and S. Das, Analysis of the relationship between seismic moment and fault length for large crustal strike-slip earthquakes between 1977–92, *Geophys. Res. Lett.*, **23**, 209–208, 1996.
- Perfettini, H., J. Schmittbuhl, J. R. Rice, and M. Cocco, Frictional response induced by time-dependent fluctuations of the normal loading, *J. Geophys. Res.*, **106**, 13,455–13,472, 2001.
- Perfettini, H., J. Schmittbuhl, and A. Cochard, Shear and normal load perturbations on a two-dimensional continuous fault: 2. Dynamic triggering, *J. Geophys. Res.*, **108**, 2409, doi:10.1029/2002JB001,805, 2003.
- Phipps Morgan, J., and D. W. Forsyth, Three-dimensional flow and temperature perturbations due to a transform offset: Effects on oceanic crustal and upper mantle structure, *J. Geophys. Res.*, **93**, 2955–2966, 1988.
- Pinkston, J., and S. H. Kirby, Experimental deformation of dunite under conditions appropriate to the lithosphere, *EOS Trans. Am. Geophys. Union*, **63**, 1094, 1982.
- Pockalny, R., R. Detrick, and P. Fox, Morphology and tectonics of the Kane transform from Sea Beam bathymetry data, *J. Geophys. Res.*, **93**, 3907–3939, 1988.
- Power, W. L., and T. E. Tullis, A review of the fractal character of natural fault surfaces with implications for friction and the evolution of fault zones, in *Fractals in The Earth Sciences*, edited by P. Lapointe and C. Barton, Plenum, pp. 89–105, New York, 1995.
- Prakash, V., Frictional response of sliding interfaces subjected to time varying normal pressures, *J. Tribology*, **120**, 97–102, 1998.
- Reasenber, P. A., and L. M. Jones, Earthquake hazard after a mainshock in California, *Science*, **243**, 1173–1176, 1989.
- Reches, Z., and D. A. Lockner, Nucleation and growth of faults in brittle rocks, *J. Geophys. Res.*, **99**, 18,159–18,173, 1994.

- Reinen, L. A., The frictional behavior of serpentinite: Experiments, constitutive models, and implications for natural faults, Ph.D. thesis, Brown Univ., 1993.
- Reinen, L. A., Slip styles in a spring-slider model with a laboratory-derived constitutive law for serpentinite, *Geophys. Res. Lett.*, **27**, 2037–2040, 2000a.
- Reinen, L. A., Seismic and aseismic slip indicators in serpentinite gouge, *Geology*, **28**, 135–138, 2000b.
- Reinen, L. A., J. D. Weeks, and T. E. Tullis, The frictional behavior of serpentinite: Implications for aseismic creep on shallow crustal faults, *Geophys. Res. Lett.*, **18**, 1921–1924, 1991.
- Reinen, L. A., J. D. Weeks, and T. E. Tullis, The frictional behavior of lizardite and antigorite serpentinites: Experiments, constitutive models, and implications for natural faults, *Pure Appl. Geophys.*, **143**, 317–385, 1994.
- Rice, J. R., Spatio-temporal complexity of slip on a fault, *J. Geophys. Res.*, **98**, 9885–9907, 1993.
- Rice, J. R., and A. L. Ruina, Stability of steady frictional slipping, *J. of Appl. Mecha.*, **105**, 1983.
- Richardson, E., and C. Marone, Effects of normal stress vibrations on frictional healing, *J. Geophys. Res.*, **104**, 28,859–28,878, 1999.
- Ridge Multibeam Synthesis Project, <http://coast.ldeo.columbia.edu/general/html/home.html>, 1999.
- Romanowicz, B., Strike-slip earthquakes on quasi-vertical transcurrent faults: Inferences for general scaling relations, *Geophys. Res. Lett.*, **19**, 481–484, 1992.
- Romanowicz, B., Comment on “A Reappraisal of large earthquake scaling” by C. Scholz, *Bull. Seism. Soc. Am.*, **84**, 1675–1676, 1994.
- Romanowicz, B., and L. J. Ruff, On moment-length scaling of large strike-slip earthquakes and the strength of faults, *Geophys. Res. Lett.*, **29**, 45–1, 45–4, 2002.
- Roy, M., and C. Marone, Earthquake nucleation on model faults with rate- and state-dependent friction: Effects of inertia, *J. Geophys. Res.*, **101**, 13,919–13,932, 1996.
- Rudnicki, J., and J. Rice, Conditions for the localization of deformation in pressure-sensitive dilatant materials, *J. Mech. Phys. Solids*, **23**, 371–394, 1975.
- Ruina, A. L., Slip instability and state variable friction laws, *J. Geophys. Res.*, **88**, 10,359–10,370, 1983.
- Rundquist, D., and P. Sobolev, Seismicity of mid-ocean ridges and its geodynamic implications: A review, *Earth-Sci. Rev.*, **58**, 143–161, 2002.
- Sacks, I., S. Suyehiro, A. T. Linde, and J. A. Snoke, Slow earthquakes and stress redistribution, *Nature*, **275**, 599–602, 1978.
- Salter, V., and H. Dick, Minerology of the mid-ocean-ridge basalt source from neodymium isotopic composition of abyssal peridotites, *Nature*, **418**, 68–72, 2002.
- Sammis, C. G., and J. R. Rice, Repeating earthquakes as low-stress-drop events at a border between locked and creeping fault patches, *Bull. Seism. Soc. Am.*, **91**, 532–537, 2001.
- Scholz, C. H., Scaling laws for large earthquakes: Consequences for physical models, *Bull. Seism. Soc. Am.*, **72**, 1–14, 1982.
- Scholz, C. H., *Fault Mechanics and Transport Properties of Rocks*, chap. 21: Paradigms or Small Change in Earthquake Mechanics, pp. 505–517, Academic Press Ltd, 1992.
- Scholz, C. H., A reappraisal of large earthquake scaling, *Bull. Seism. Soc. Am.*, **84**, 215–218, 1994a.
- Scholz, C. H., Reply to comments on “A reappraisal of large earthquake scaling” by C. Scholz, *Bull. Seism. Soc. Am.*, **84**, 1677–1678, 1994b.
- Scholz, C. H., Earthquakes and friction laws, *Nature*, **391**, 37–42, 1998.
- Scholz, C. H., *The Mechanics of Earthquakes and Faulting*, second ed., Cambridge University Press, 2002.
- Scholz, C. H., Good tidings, *Nature*, **425**, 670–671, 2003.
- Schulz, S. S., G. M. Mavko, R. O. Burford, and W. D. Stuart, Long-term fault creep observations in central California, *J. Geophys. Res.*, **87**, 6977–6982, 1982.
- Schwartz, D., The case against huge earthquakes, *Seism. Res. Lett.*, **67**, 3–5, 1996.

- Schwartz, D. P., and K. J. Coppersmith, Fault behavior and characteristic earthquakes: Examples from the Wasatch and San Andreas Fault zones, *J. Geophys. Res.*, 1984.
- Searle, R., M. Thomas, and E. Jones, Morphology and tectonics of the Romanche transform fault and its environs, *Mar. Geophys. Res.*, 16, 427, 1994.
- Segall, P., and J. Rice, Dilatancy, compaction, and slip instability of a fluid-infiltrated fault, *Eos Trans. AGU*, 75, 1994.
- Shaw, B. E., and J. R. Rice, Existence of continuum complexity in the elastodynamics of repeated fault ruptures, *J. Geophys. Res.*, 105, 791–810, 2000.
- Shaw, B. E., and C. H. Scholz, Slip-length scaling in large earthquakes: Observations and theory and implications for earthquake physics, *Geophys. Res. Lett.*, 28, 2991–2994, 2001.
- Shaw, W. J., and J. Lin, Models of ocean ridge lithospheric deformation: Dependence on crustal thickness, spreading rate, and segmentation, *J. Geophys. Res.*, 101, 17,977–17,993, 1996.
- Shimada, M., A. Cho, and H. Yukatake, Fracture strength of dry silicate rocks at high confining pressures and activity of acoustic emission, *Tectonophysics*, 96, 159–172, 1983.
- Shimazaki, K., *Small and large earthquakes: The effects of the thickness of the seismogenic layer and the free surface*, pp. 209–216, Earthquake Source Mechanics, AGU Monograph 37, 1986.
- Sibson, R. H., Continental fault structure and the shallow earthquake source, *J. Geol. Soc. Lond.*, 140, 741–767, 1983.
- Sibson, R. H., Roughness at the base of the seismogenic zone: Contributing factors, *J. Geophys. Res.*, 89, 5791–5799, 1984.
- Sinha, M., and K. Louden, The Oceanographer fracture zone— i. Crustal structure from seismic refraction studies, *Geophys. J. R. Astr. Soc.*, 75, 713–736, 1983.
- Sleep, N., E. Richardson, and C. Marone, Physics of friction and strain rate localization in synthetic fault gouge, *J. Geophys. Res.*, 105, 25,875–25,890, 2000.
- Sleep, N. H., Formation of the oceanic crust: some thermal constraints, *J. Geophys. Res.*, 80, 4037–4042, 1975.
- Smith, D. K., and T. H. Jordan, Seamount statistics in the Pacific Ocean, *J. Geophys. Res.*, 93, 2899–2918, 1988.
- Smith, W. H. F., and D. T. Sandwell, Global seafloor topography from satellite altimetry and ship depth soundings, *Science*, 277, 1957–1926, 1997.
- Sobolev, P., and D. V. Rundquist, Seismicity of oceanic and continental rifts— a geodynamic approach, *Phys. Earth Planet. Inter.*, 111, 253–266, 1999.
- Solomon, S. C., and N. C. Burr, The relationship of source parameters of ridge-crest and transform earthquakes to the thermal structure of oceanic lithosphere, *Tectonophysics*, 55, 107–126, 1979.
- Spudich, P., L. Steck, M. Hellweg, J. Fletcher, and L. Baker, Transient stresses at Parkfield, California, produced by the m7.4 Landers earthquake of June 28, 1992: Observations from the upsar dense seismograph array, *J. Geophys. Res.*, 100, 675–690, 1995.
- Stein, R. C., and T. C. Hanks, $M \geq 6$ earthquakes in Southern California during the twentieth century: No evidence for a seismicity or moment deficit, *Bull. Seism. Soc. Am.*, 88, 635–652, 1998.
- Stein, S., and A. Pelayo, Seismological constraints on stress in the oceanic lithosphere, *Phil. Trans. R. Soc. Lond. A*, 337, 53–72, 1991.
- Stesky, R. M., Rock friction-effect of confining pressure, temperature, and pore pressure, *PAGEOPH*, 116, 690–704, 1978a.
- Stesky, R. M., Mechanisms of high temperature frictional sliding in wet granite, *Canadian Journal of Earth Sciences*, 15, 361–375, 1978b.
- Stesky, R. M., W. F. Brace, D. K. Riley, and P.-Y. F. Robin, Friction in faulted rock at high temperature and pressure, *Tectonophysics*, 23, 177–203, 1974.
- Stirling, M. W., S. G. Wesnousky, and K. Shimazaki, Fault trace complexity, cumulative slip, and the shape of the magnitude-frequency distribution for strike-slip faults: A global survey, *Geophysical Journal International*, 124, 833–868, 1996.

- Stoddard, P. R., On the relation between transform fault resistance and plate motion, *J. Geophys. Res.*, **97**, 17,637–17,650, 1992.
- Thatcher, W., Present-day crustal movements and the mechanics of cyclic deformation, in San Andreas Fault System, California, in *U. S. Geological Survey Professional Paper 1515*, edited by R. Wallace, pp. 189–205, 1990.
- Thurber, C., and R. Sessions, Assessment of creep events as potential earthquake precursors: Application to the creeping section of the San Andreas Fault, California, *Pure Appl. Geophys.*, **152**, 685–705, 1998.
- Tolstoy, M., F. Vernon, J. Orcutt, and F. Wyatt, Breathing of the seafloor: Tidal correlations of seismicity at Axial volcano, *Geology*, **30**, 503–506, 2002.
- Trehu, A., and S. Solomon, Earthquakes in the Orozco Transform Zone: Seismicity, source mechanism, and tectonics, *J. Geophys. Res.*, **88**, 8203–8225, 1983.
- Tsutsumi, A., and T. Shimamoto, High-velocity frictional properties of gabbro, *Geophys. Res. Lett.*, **24**, 699–702, 1997.
- Tucholke, B. E., and J. Lin, A geological model for the structure of ridge segments in slow-spreading ocean crust, *J. Geophys. Res.*, **99**, 11,937–11,958, 1994.
- Turcotte, D. L., A fractal model for crustal deformation, *Tectonophysics*, **132**, 261–269, 1986.
- Turcotte, D. L., and G. Schubert, *Geodynamics, Application of Continuum Physics to Geological Problems*, Cambridge University Press, New York, NY, 2001.
- Tworzydło, W. W., and O. N. Hamzeh, On the importance of normal vibrations in modeling of stick slip in rock sliding, *J. Geophys. Res.*, **102**, 15,091–15,103, 1997.
- Umino, N., T. Okada, and A. Hasegawa, Detailed distribution of accelerating foreshocks before a m 5.1 earthquake in Japan, *Bull. Seism. Soc. Am.*, **92**, 2465–2477, 2002.
- Utsu, T., A statistical study on the occurrence of aftershocks, *Geophys. Mag.*, **30**, 521–605, 1961.
- Utsu, T., Aftershocks and earthquake statistics I, Some parameters which characterize an aftershock sequence and their interaction, *J. Fac. Sci. Hokkaido Univ., Ser. 7*, 129–195, 1969.
- Vidale, J. E., and Y.-G. Li, Damage to the shallow Landers fault from the nearby Hector Mine earthquake, *Nature*, **421**, 524–526, 2003.
- Vidale, J. E., D. C. Agnew, M. J. S. Johnston, and D. H. Oppenheimer, Absence of earthquake correlation with earth tides: An indication of high preseismic fault stress rate, *J. Geophys. Res.*, **103**, 24,567–24,572, 1998.
- Voisin, C., Dynamic triggering of earthquakes: the linear slip-dependent friction case, *Geophys. Res. Lett.*, **28**, 3357–3360, 2001.
- Voisin, C., Dynamic triggering of earthquakes: The nonlinear slip-dependent friction case, *J. Geophys. Res.*, **107**, 2356, doi:10.1029/2001JB001121, 2002.
- Wald, D., T. Heaton, and K. Hudnut, The slip history of the 1994 Northridge, California, earthquake determined from strong-motion, teleseismic, GPS, and leveling data, *Bull. Seism. Soc. Am.*, **86**, S49–S70, 1996.
- Waldhauser, F., and W. L. Ellsworth, Fault structure and mechanics of the Hayward Fault, California, from double-difference earthquake locations, *J. Geophys. Res.*, **107**, art. no. 2054, 2002.
- Wang, J.-H., and S.-S. Ou, On scaling of earthquake faults, *Bull. Seism. Soc. Am.*, **88**, 758–766, 1998.
- Ward, S. N., More on m_{max} , *Bull. Seism. Soc. Am.*, **87**, 1199–1208, 1997.
- Warren, J., G. Hirth, and H. J. Dick, Grain size sensitive deformation mechanisms in naturally deformed peridotites, *submitted to Earth and Planet. Sci. Lett.*, 2005.
- Wesnousky, S. G., Seismicity as a function of cumulative geologic offset: Some observations from Southern California, *Bull. Seism. Soc. Am.*, **80**, 1374–1381, 1990.
- Wesnousky, S. G., The Gutenberg-Richter or Characteristic Earthquake Distribution, which is it?, *Bull. Seism. Soc. Am.*, **84**, 1940–1959, 1994.
- Wesson, R. L., Dynamics of fault creep, *J. Geophys. Res.*, **93**, 8929–8951, 1988.
- White, R., R. Detrick, M. Sinha, and M. H. Cormier, Anomalous seismic crustal structure of oceanic fracture zones, *Geophys. J. R. Astr. Soc.*, **79**, 779–798, 1984.